

**A Study of Inter- and Intramolecular  
Interactions through Neutron Compton  
Scattering and Low Temperature Matrix  
Isolation Infrared Spectroscopy**

Lee Iverson

PhD Thesis

School of Chemistry, University of East Anglia,

Norwich Research Park, Norwich, Norfolk,

NR3 7TJ

Original Submission December 2013,

Final Submission June 2014

©This copy of the thesis has been supplied on condition that anyone who consults it is understood to recognise that its copyright rests with the author and that use of any information derived there from must be in accordance with current UK Copyright Law. In addition, any quotation or extract must include full attribution.

## **Declaration**

The work contained in this Thesis and submitted for the degree of Doctor of Philosophy is my own, except where reference has been made to other authors, and no part of it has been previously submitted for a degree at this or any other university.

## Abstract

Matrix Isolation Infrared Spectroscopy has been proposed as an alternative for detection and quantification of site-specific isotopic signals. 4-hydroxy-3-methoxy benzaldehyde (vanillin) is used in an attempt to make use of its asymmetry and distinguish between the vibrations of its three functional groups, assigning structural effects to specific locations in the molecule. After achieving an apparent near-isolated state, the role of isotopic signals in the resulting splitting effects of the predicted isolated-peak structure are discussed, as well as possible significant contributions from conformational, aggregation and steric effects from the matrix on the guest molecule. Density Functional Theory is considered as a method of simulating and predicting the behaviour of the molecule in the isolated phase, and simulated spectra are produced to attempt to replicate and assign the observed phenomena, predicting the positions and intensities of isotopic peaks based on natural isotopic abundances, and estimated conformer populations calculated from the energy levels of each structure.

In a novel experiment to observe changes in momentum distributions in a solution of poly-N-isopropyl acrylamide (pNIPAAm) passing through a temperature-induced phase change, deuterated polymer/ solvent mixtures were studied on the VESUVIO instrument at the ISIS RAL facility, and the analysis of that data is presented. pNIPAAm and related compounds display a critical temperature for solvation *above* which they precipitate due to competition between solvent-polymer H-bonding verses internal H-bonding structure; though better stabilised by the additional hydrophobic effects of methanol, pure water solvation shows this behaviour. It is additionally seen that the mixture of water and methanol results in a depression of this Lower Critical Solution Temperature (LCST) relative to the pure solvents, thought to be due to solvent-solvent interactions limiting solvent availability to the polymer. Deuterium labels were introduced in neutron scattering experiments, and expected to show significant momentum change with this collapse of hydrogen bonding.

300 Words

# Contents

<b>Declaration</b>	i
<b>Abstract</b>	ii
<b>Contents</b>	iii
<b>List of Figures</b>	viii
<b>List of Tables</b>	xiii
<b>List of Equations</b>	xv
<b>Acknowledgements</b>	xviii
<b>Citation of the Gaussian 09 Program</b>	xix
<b>Preface</b>	xx
<b>Part One: Matrix Isolation Infrared Spectroscopy Study of Vanillin in a Low- Temperature Argon Matrix</b>	
• Chapter 1: Isolation of Vanillin in an Inert Argon Matrix	Page 1
1-1: Introduction	Page 2
1-1-1: Overview of this Work	Page 2
1-1-2: Isotopic Splitting in the Matrix	Page 4

1-1-3: Why Matrix Isolation?	Page 5
1-1-4: Packing in the Matrix	Page 7
1-1-5: Vanillin as a Target Analyte	Page 10
1-2: Experimental	Page 11
1-2-1: Equipment	Page 11
1-2-2: Argon Backgrounds and System Integrity	Page 18
1-3: Results and Analysis	Page 19
1-3-1: A Note on the Quality of Spectra	Page 19
1-3-2: Experimental IR Spectra of Vanillin Isolated in an Ar Matrix	Page 22
1-4: Discussion and Conclusions	Page 69
1-4-1: Vanillin Intensity in Matrix Isolated Spectra	Page 69
1-4-2: Discussion of Splitting Effects in the Matrix Isolated Spectra	Page 71
1-4-3: Conclusions and Further Development	Page 74
<b>Part Two: Fundamentals of Density Functional Theory and the Simulation of Vanillin in both the Solid and Isolated Phase</b>	Page 76
• Chapter 2: Fundamentals of Density Functional Theory	Page 77
2-1: Introduction	Page 77

2-1-1: Isotopic Labelling in High Resolution Vibrational Spectra	Page 77
2-1-2: Density Functional Theory (DFT) Modelling of Vibrational Spectra	Page 78
2-2: Density Functional Theory	Page 81
2-2-1: Origins of Density Functional Theory	Page 81
2-2-2: The Kohn-Sham Approximation	Page 88
2-2-3: The Local Density Approximation and Modern DFT Methods	Page 89
2-3: Basis Set Construction	Page 92
• Chapter 3a: Gaussian Simulation Results Part I- Solid Phase Vanillin	Page 94
3a-1: Determination of the Optimised Molecular Structure for Vibrational Calculation	Page 94
3a-2: Vibrational Spectra Calculation and Evaluation for 4-Hydroxy-3-Methoxy Benzaldehyde	Page 99
3a-2-1: Simulated Raman Spectra	Page 103
3a-2-2: Simulated Infrared Spectra	Page 131
3a-3: Conclusions and Application to Experimental Systems	Page 140
• Chapter 3b: Gaussian Simulation Results Part II- Isolated Vanillin	Page 151
3b-1: Determination of the Optimised Molecular Structure for Vibrational Calculation	Page 151

3b-2: Vibrational Spectra Calculation and Evaluation for 4-Hydroxy-3-Methoxy Benzaldehyde	Page 160
3b-2-1: Energy Level Distribution for Rotational Conformers	Page 160
3b-2-2: Vibrational Frequency Scaling	Page 162
3b-2-3: Simulation Results	Page 163
3b-2-4: Examination of Calculated Vibrational Modes	Page 185
3b-3: Conclusions and Application to Experimental Systems	Page 223
<b>Part Three: Neutron Compton Profiles of Hydrogen and Deuterium through Inelastic Neutron Scattering on the VESUVIO Instrument</b>	Page 230
• Chapter 4: Neutron Compton Scattering of the Poly-N-Isopropyl Acrylamide Co-Nonsolvency Effect	Page 231
4-1: Introduction	Page 231
4-1-1: Neutron Scattering on Solvated Systems	Page 231
4-1-2: The Lower Critical Solution Temperature and the Co-Nonsolvency Effect	Page 233
4-1-3: Water-Methanol Systems	Page 236
4-2: The VESUVIO Spectrometer	Page 238
4-2-1: The Impulse Approximation and the Neutron Compton Scattering Profile	Page 238
4-2-2: Neutron Detection on VESUVIO	Page 244

4-2-3: Generating the Time-of-Flight Count Data	Page 249
4-2-4: Predictions for the Neutron Compton Scattering Profile in the Poly-N-Isopropyl Acrylamide Co-Nonsolvency System	Page 254
• Chapter 5: Results of Neutron Compton Scattering Study of Mixed Water, Methanol and Poly-N-Isopropyl Acrylamide Systems	Page 256
5-1: Introduction	Page 256
5-2: Experiment I: Neutron Scattering Momentum Distribution Study of Deuterated Poly-N-Isopropyl Acrylamide Displaying the Co-Nonsolvency Effect in Mixed D <sub>2</sub> O and CH <sub>3</sub> OD Solvents	Page 257
5-2-1: The Poly-N-Isopropyl Acrylamide Co-Nonsolvency System	Page 257
5-2-2: Experimental I	Page 258
5-2-3: Results and Analysis I	Page 260
5-2-4: Analysis and Conclusions I	Page 264
5-3: Experiment II: Neutron Scattering Momentum Distribution Study of Deuterated Solvent-Only Systems (Inverse Labelling)	Page 272
5-3-1: Samples Used in Experiment II	Page 272
5-3-2: Experimental and Results II	Page 272
5-3-3: Analysis and Conclusions II	Page 274
5-4: Re-Analysis of Data from Experiment I Using the Revised Multiple Scattering Calculation	Page 276

5-4-1: Results and Analysis	Page 276
5-4-2: Conclusions	Page 282
5-5: Final Conclusions about the System and Future Development on VESUVIO	Page 286
<b><u>Part Four: Conclusions</u></b>	Page 288
• Chapter 6: Final Conclusions	Page 289
<b><u>References</u></b>	Page 292
<b><u>List of Figures</u></b>	
▪ Figure 1-1: 4-hydroxy-3-methoxy benzaldehyde, or Vanillin	Page 2
▪ Figure 1-2: Structure of CO <sub>2</sub>	Page 4
▪ Figure 1-3: Structures of N <sub>2</sub> O	Page 4
▪ Figures 1-4a and b: The Connolly Solvent excluded Volume of the vanillin molecule	Page 9
▪ Figure 1-5: Diagram of experimental gas management system	Page 12
▪ Figures 1-6a, b and c: Vacuum system glassware and sample chamber	Pages 14-15
▪ Figures 1-7a to h: Sample 1 Infrared Spectra	Pages 22-29

- Figures 1-8a to h: Sample 2 Infrared Spectra  
Pages 32-39
- Figures 1-9a to h: Sample 3 Infrared Spectra  
Pages 42-49
- Figures 1-10a to h: Sample 4 Infrared Spectra  
Pages 51-58
- Figure 1-11a to h: Sample 5 Infrared Spectra  
Pages 60-67
- Figure 3a-1a and b: ORTEP display of the repeating four-molecule asymmetric unit of solid phase vanillin  
Page 95
- Figure 3a-2: Solid phase vanillin configuration  
Page 98
- Figure 3a-3: Experimentally obtained solid phase Raman spectrum for reference data  
Page 100
- Figure 3a-4: Approximate linear relationship between simulated data set (B3LYP) and experimentally obtained Raman data points  
Page 120
- Figure 3a-5: Approximate linear relationship between simulated data set (B3LYP +) and experimentally obtained Raman data points  
Page 120
- Figure 3a-6: Approximate linear relationship between simulated data set (B3LYP d) and experimentally obtained Raman data points  
Page 121
- Figure 3a-7: Approximate linear relationship between simulated data set (B3LYP +d) and experimentally obtained Raman data points  
Page 121

- Figure 3a-8: Approximate linear relationship between simulated data set (B3PW91) and experimentally obtained Raman data points

Page 122

- Figure 3a-9: Approximate linear relationship between simulated data set (B3PW91 +) and experimentally obtained Raman data points

Page 122

- Figure 3a-10: Approximate linear relationship between simulated data set (B3PW91 d) and experimentally obtained Raman data points

Page 123

- Figure 3a-11: Approximate linear relationship between simulated data set (B3PW91 +d) and experimentally obtained Raman data points

Page 123

- Figure 3a-12: Vanillin Raman simulated spectrum, solid phase (B3LYP)

Page 129

- Figure 3a-13: Vanillin Raman simulated spectrum, solid phase (B3PW91)

Page 130

- Figure 3a-14: Experimentally obtained solid phase infrared spectrum for reference data

Page 131

- Figure 3a-15: Linear relationship between Raman and infrared solid phase spectra

Page 133

- Figure 3a-16: Vanillin infrared simulated spectrum, solid phase (B3LYP)

Page 138

- Figure 3a-17: Vanillin infrared simulated spectrum, solid phase (B3PW91)

Page 139

- Figure 3a-18: B3LYP simulated infrared spectrum vs solid phase infrared reference

Page 141

- Figure 3a-19: B3LYP simulated Raman spectrum vs solid phase Raman reference  
Page 142
- Figure 3a-20: B3PW91 simulated infrared spectrum vs solid phase infrared reference  
Page 143
- Figure 3a-21: B3PW91 simulated Raman spectrum vs solid phase Raman reference  
Page 144
- Figure 3a-22a and b: Charge separation diagrams of vanillin using B3LYP and B3PW91 calculation methods  
Page 149
- Figures 3b-1a to d: Change in absolute energy of vanillin molecule with rotation of functional groups  
Pages 153-156
- Figure 3b-2a to i: The eight lowest-energy rotational configurations of the functional groups of vanillin  
Pages 158-159
- Figure 3b-3: Initial simulation of isolated phase vanillin infrared spectrum (B3LYP +d)  
Page 168
- Figure 3b-4: Initial simulation of isolated phase vanillin Raman spectrum (B3LYP +d)  
Page 169
- Figure 3b-5: Initial simulation of isolated phase vanillin infrared spectrum (B3PW91 +d)  
Page 170
- Figure 3b-6: Initial simulation of isolated phase vanillin Raman spectrum (B3PW91 +d)  
Page 171
- Figure 3b-7: Atomic number assignment in simulations  
Page 174
- Figure 3b-8: Final simulation of isolated phase vanillin infrared spectrum (B3LYP +d)  
Page 181

- Figure 3b-9: Final simulation of isolated phase vanillin Raman spectrum (B3LYP +d)
  - Page 182
- Figure 3b-10: Final simulation of isolated phase vanillin infrared spectrum (B3PW91 +d)
  - Page 183
- Figure 3b-11: Final simulation of isolated phase vanillin Raman spectrum (B3PW91 +d)
  - Page 184
- Figure 3b-12a and b: Reference Sample 5 vs. Final infrared simulation (B3LYP +d)
  - Page 223-224
- Figure 3b-13a and b: Reference Sample 5 vs. Final infrared simulation (B3PW91 +d)
  - Page 225-226
- Figure 4-1: Lower Critical Solution Temperature for a mixture of water and methanol
  - Page 234
- Figure 4-2: Exterior photograph of the VESUVIO spectrometer
  - Page 238
- Figure 4-3: Schematic diagram of the VESUVIO spectrometer
  - Page 244
- Figure 4-4: Illustration of the process of cycling the secondary gold foil
  - Page 247
- Figure 5-1: Example raw output for Time of Flight data for backward scattering detectors for pure D<sub>2</sub>O
  - Page 261
- Figure 5-2: Example raw output for Time of Flight data for forward scattering detectors for pure D<sub>2</sub>O
  - Page 261
- Figure 5-3: Fitted output for Time of Flight data for backward scattering detectors for pure D<sub>2</sub>O
  - Page 262

- Figure 5-4: Fitted output for Time of Flight data for forward scattering detectors for pure D<sub>2</sub>O  
Page 262
- Figures 5-5, 5-6, 5-7 and 5-8: Predicted deuterium momentum variances for component concentrations  
Pages 269-270
- Figures 5-9, 5-10, 5-11 and 5-12: Revised data points for the deuterium variances calculated from Experiment I  
Pages 278-279
- Figures 5-13, 5-14, 5-15 and 5-16: Data points for the hydrogen and deuterium variances calculated from the -OD and -OH samples used in Experiment II  
Pages 280-282
- Figure 5-17: Overlaid deuterium momentum variances for re-analysed Experiment I verses Experiment II  
Page 284

### List of Tables

▪ Table 1-1	▪ Table 1-7
	Page 8
▪ Table 1-2	▪ Table 3a-1
	Page 21
▪ Table 1-3	▪ Table 3a-2
	Page 30
▪ Table 1-4	▪ Table 3a-3
	Page 40
▪ Table 1-5	▪ Table 3a-4
	Page 50
▪ Table 1-6	▪ Table 3a-5
	Page 59
	Page 101
	Page 104

▪ Table 3a-6	Page 106	▪ Table 3b-3	Page 161
▪ Table 3a-7	Page 108	▪ Table 3b-4	Page 163
▪ Table 3a-8	Page 110	▪ Table 3b-5	Page 164
▪ Table 3a-9	Page 112	▪ Table 3b-6	Page 165
▪ Table 3a-10	Page 114	▪ Table 3b-7	Page 166
▪ Table 3a-11	Page 116	▪ Table 3b-8	Page 172
▪ Table 3a-12	Page 118	▪ Table 3b-9	Page 173
▪ Table 3a-13	Page 124	▪ Table 3b-10	Page 175
▪ Table 3a-14	Page 125	▪ Table 3b-11	Page 176
▪ Table 3a-15	Page 127	▪ Tables 3b-12a to c	Pages 187-193
▪ Table 3a-16	Page 132	▪ Tables 3b-13a to c	Pages 196-204
▪ Table 3a-17	Page 134	▪ Tables 3b-14a to c	Pages 205-213
▪ Table 3a-18	Page 136	▪ Tables 3b-15a to c	Pages 214-222
▪ Table 3a-19	Page 147	▪ Table 5-1	Page 258
▪ Table 3b-1	Page 151	▪ Table 5-2	Page 264
▪ Table 3b-2	Page 157	▪ Table 5-3	Page 272

▪ Table 5-4	▪ Table 5-5
Page 274	Page 276

### List of Equations

▪ Equation 1-1	▪ Equation 2-11
Page 70	Page 86
▪ Equation 1-2a and b	▪ Equation 2-12
Page 70	Page 86
▪ Equation 2-1	▪ Equation 2-13
Page 81	Page 86
▪ Equation 2-2	▪ Equation 2-14
Page 82	Page 86
▪ Equation 2-3	▪ Equation 2-15
Page 82	Page 87
▪ Equation 2-4	▪ Equation 2-16
Page 84	Page 87
▪ Equation 2-5	▪ Equation 2-17
Page 84	Page 87
▪ Equation 2-6	▪ Equation 2-18
Page 84	Page 87
▪ Equation 2-7	▪ Equation 2-19
Page 84	Page 88
▪ Equation 2-8	▪ Equation 2-20
Page 84	Page 89
▪ Equation 2-9	▪ Equation 2-21
Page 85	Page 90
▪ Equation 2-10	▪ Equation 2-22
Page 85	Page 90

▪ Equation 4-1	Page 240	▪ Equation 4-17	Page 250
▪ Equation 4-2	Page 240	▪ Equation 4-18	Page 251
▪ Equation 4-3	Page 240	▪ Equation 4-19	Page 251
▪ Equation 4-4	Page 241	▪ Equation 4-20	Page 251
▪ Equation 4-5	Page 241	▪ Equation 4-21	Page 251
▪ Equation 4-6	Page 241	▪ Equation 4-22	Page 252
▪ Equation 4-7	Page 242	▪ Equation 4-23	Page 252
▪ Equation 4-8	Page 246	▪ Equation 4-24	Page 252
▪ Equation 4-9	Page 246	▪ Equation 4-25	Page 253
▪ Equation 4-10	Page 246	▪ Equation 4-26	Page 253
▪ Equation 4-11	Page 246	▪ Equation 4-27	Page 253
▪ Equation 4-12	Page 247	▪ Equation 5-1	Page 263
▪ Equation 4-13	Page 248	▪ Equation 5-2	Page 263
▪ Equation 4-14	Page 248	▪ Equation 5-3	Page 265
▪ Equation 4-15	Page 249	▪ Equation 5-4	Page 265
▪ Equation 4-16	Page 250	▪ Equation 5-5	Page 267

- |                |          |                |          |
|----------------|----------|----------------|----------|
| ▪ Equation 5-6 | Page 267 | ▪ Equation 5-8 | Page 267 |
| ▪ Equation 5-7 | Page 267 | ▪ Equation 5-9 | Page 268 |

Appendices can be found on the accompanying disk in the form of five pdf files, one .cif file and one file folder. These appendices contain the data output of all Gaussian calculations performed in the course of this project, the x-ray crystallography data for solid phase vanillin, and all the raw data necessary to reconstruct the results obtained from the VESUVIO instrument, respectively.

## **Acknowledgements**

I would like to thank a number of people for their help during my PhD study here at the University of East Anglia, in particular my primary supervisor Dr U. A. Jayasooriya for his time, effort and patience in helping me reach my goal. I would also like to extend my thanks to Dr A. Mayes for his work on the pNIPAAm Co-Nonsolvancy investigation, Doctors V. Oganesyn and G. Jones for their help with the practical applications of Density Functional Theory (and for taking the time to proof read the relevant sections of this thesis), and to Dr R. Grinter for helping me get to grips with the Matrix Isolation Infrared process and the principles behind it. I would also like to thank Dr M. Cheesman for his help in organising my activities during the closing stages of my writing period. Special note should be made of the assistance of Doctors J. Mayers and A. Seel of the ISIS facility of the Rutherford Appleton Laboratory, both with the operation of the VESUVIO spectrometer and the lengthy analysis procedure afterwards. I would also like to offer my appreciation to Dr J. Peck, who has since moved on to work at the ISIS facility, for providing my initial introduction to the Gaussian DFT package and much of my early support during our time here as students.

All aspects of my PhD studies have been part-funded by a studentship provided by the School of Chemistry here at the University of East Anglia, while experimental work at the ISIS facility was funded by the Science and Technologies Facilities Council; I would like to express my appreciation to both.

Finally, I would like to thank my family, my parents and grandparents, for helping me along during my study period. I know I've sometimes been difficult to live with: thanks for putting up with me.

## Citation of the Gaussian 09 Program

This work makes extensive use of the Gaussian 09 program; where applicable this program should be cited as follows:

Gaussian 09, Revision C.01, M. J. Frisch, G. W. Trucks, H. B. Schlegel, G. E. Scuseria, M. A. Robb, J. R. Cheeseman, G. Scalmani, V. Barone, B. Mennucci, G. A. Petersson, H. Nakatsuji, M. Caricato, X. Li, H. P. Hratchian, A. F. Izmaylov, J. Bloino, G. Zheng, J. L. Sonnenberg, M. Hada, M. Ehara, K. Toyota, R. Fukuda, J. Hasegawa, M. Ishida, T. Nakajima, Y. Honda, O. Kitao, H. Nakai, T. Vreven, J. A. Montgomery, Jr., J. E. Peralta, F. Ogliaro, M. Bearpark, J. J. Heyd, E. Brothers, K. N. Kudin, V. N. Staroverov, T. Keith, R. Kobayashi, J. Normand, K. Raghavachari, A. Rendell, J. C. Burant, S. S. Iyengar, J. Tomasi, M. Cossi, N. Rega, J. M. Millam, M. Klene, J. E. Knox, J. B. Cross, V. Bakken, C. Adamo, J. Jaramillo, R. Gomperts, R. E. Stratmann, O. Yazyev, A. J. Austin, R. Cammi, C. Pomelli, J. W. Ochterski, R. L. Martin, K. Morokuma, V. G. Zakrzewski, G. A. Voth, P. Salvador, J. J. Dannenberg, S. Dapprich, A. D. Daniels, O. Farkas, J. B. Foresman, J. V. Ortiz, J. Cioslowski, and D. J. Fox, Gaussian, Inc., Wallingford CT, 2010.

## Preface

Several well-known techniques exist for the determination of isotopic ratios in samples, the most famous of which is undoubtedly Mass Spectrometry. Isotopic signals in MS are typically only recorded as a single total-population figure for the entire sample, but other techniques can make use of isotopic labels for the determination of structural and systematic features in a molecular system. Conversely, a technique such as Site-specific Natural Isotope Fractionation Nuclear Magnetic Resonance Spectrometry (SNIF-NMR) can provide some structural information, but is of notably low sensitivity requiring high concentrations of functional groups that can be modified to give an appropriate signal. This reliance on large concentrations of chemically modified functional groups makes NMR techniques<sup>1</sup> a complicated proposition in a conventional laboratory setting, and makes the technique of limited use in identifying naturally occurring levels of isotopic abundance.

Both mass spectrometry and SNIF-NMR require extensive training for operation and interpretation of results, and can come with a significant cost in both time and operating expense. This text builds on the ideas introduced in the earlier 2009 Master's Thesis to discuss Matrix Isolation Infrared Spectroscopy as a more accessible alternative. Infrared is an obvious choice for the detection of isotopic species because of the dependency of vibrational frequency on the masses of the vibrating atoms involved. Such measurements are not normally possible in the solid or liquid phases because of the degree of interaction between neighbouring molecules (hydrogen bonding, instantaneous interactions and so forth) giving a broadening effect on the bands observed. At the other extreme, gaseous samples show significant numbers of ro-vibrational transitions which when not fully resolved have a similar effect on the resulting peaks in the sample. Matrix isolation was proposed as a compromise between the two: effectively an extremely dilute 'frozen solution' of sample molecule held in a solid matrix of chemically inert atoms (argon,

in this case). The resulting structure should show the characteristic sharp peaks of the gas phase, but lack significant contributions from the ro-vibrational components of those spectra. The invention of this technique is credited to G.C. Pimentel, late of Berkley University California; a full library of his works can be found in reference<sup>2</sup>.

This thesis begins with a discussion of the potential effects generated in vibrational techniques such as infrared and Raman spectroscopy by matrix isolation. In the following experimental method and discussion we attempt to show the development of a Matrix Isolation system capable of resolving vibrational structure of the order necessary to distinguish between contributions of different isotopes in a common molecule of relatively small size. The principle target of this work is the molecule 4-hydroxy-3-methoxy benzaldehyde, more commonly known as Vanillin<sup>3</sup>. This species is comparatively small consisting of 19 atoms, and has three different functional groups (comprised entirely of carbon, hydrogen and oxygen) that are easily distinguished in the infrared. By attempting to refine the matrix isolation procedure it was hoped that samples showing signals attributable to isotopic populations in the functional groups of the molecule would be observable using IR spectra collected with a conventional laboratory instrument. Vanillin was initially chosen as a sample species as a compromise between being small enough to easily interpret the resulting vibrational data in the isolated phase and minimise the number of possible conformer contributions in the spectrum, and hopefully being large enough to avoid significant splitting effects in the signals produced by the packing arrangement of atoms in the argon lattice. As will be discussed later on in *Chapters 1, 3a and 3b*, neither of these properties proved to be ideal, and the resulting spectra were much more complex than was first anticipated.

In addition to the applications to static systems, matrix isolation techniques can be used to allow controlled rates of reaction between species by annealing the host material. Unlike the two techniques mentioned earlier, an isotopically substituted sample used in vibrational spectroscopy will retain almost identical chemical properties to the normal species (mass spectrometry fractionates the molecule, and SNIF-NMR relies on the derivitisation of functional groups with the

correct spin labelling for detection): the ability to scan a sample *in-situ*, and then to potentially observe it during a reaction process<sup>4</sup> is very valuable, and adds to the potential of matrix isolation IR by leaving the possibility of following reaction mechanisms by isotopic labelling of specific functional groups. This aspect of the technique has not been addressed in this thesis, but is worthy of future consideration.

Following this experimental work is an extensive section dealing with the simulation of the vibrational properties of vanillin, attempting to reconcile the peak distributions observed experimentally with the possible roles played by the restrictions found in the solid phase crystal structure, and in the apparent packing effects experienced in the matrix. These simulations were performed using the Gaussian 09<sup>5</sup> suite to calculate the properties of the molecular system using Density Functional Theory (DFT)<sup>6,7,8</sup>. It was hoped that, by combining the weighted results of vibrational spectrum simulations for the most common stable structures and isotopomers of vanillin it would be possible to determine the origin of each feature seen in the matrix isolated spectra. At present insufficient data is available to make such concrete assignments, but the system shows promise that with further refinement of the experimental technique assignments of peaks of natural isotopic abundance in such spectra may be a potential alternative to the more cumbersome methods available.

Vibrational techniques are not the only field in which isotopic information may be useful in the determination of sample structure properties; the VESUVIO Deep Inelastic Neutron Scattering instrument operated at the ISIS facility at Rutherford Appleton Laboratories in Oxfordshire<sup>9,10,11</sup> offers the chance to use targeted isotopic substitutions to explore the momentum distribution of atoms in samples. During collisions between particles of any given mass there is a transfer of both energy and momentum<sup>12,13,14</sup>: by measuring the characteristic time-of-flight for neutrons of a given energy scattering from different particles (i.e. atoms) in a sample, it is possible to calculate how much momentum they have *transferred*, and thus how much the atoms *have*. Conventional measurements on this instrument are typically made on samples containing only one isotopic species (hydrogen or deuterium), and

most frequently on samples in the solid phase (though not exclusively so<sup>15-18</sup>, given the extensive measurements that have been taken of water systems). In a break from this pattern the two experiments performed on the instrument detailed here involve liquid samples containing both H and D, in a novel application of this technique to try and observe the presumed change in momentum distribution caused by the temperature-induced phase change in solvated poly-N-isopropyl acrylamide (pNIPAAm), and to understand the properties of the mixed solvent system in which it takes place.

The phase change in question is an unusual one, frequently displayed by related compounds, known as the Lower Critical Solution Temperature (LCST)<sup>19</sup>. The polymer is believed to be held in solution by the combination of hydrophobic and hydrophilic interactions, and is thus fully solvated by methanol at all temperatures; the polymer is also well solvated by water below ~25°C, but above this temperature it is believed that the solvent-polymer hydrogen bonding interactions are weakened enough to be overcome by the polymer's own internal hydrogen bonding interactions<sup>20</sup>, and it then collapses immediately into a globular state and precipitates out of solution. What is most interesting in this system is that the combination of water and methanol displays a lower LCST value than the pure water, reaching a minimum at a methanol mole fraction of ~0.35- in effect, the mixture of the two is a poorer solvent than either alone. This property has been attributed to the 'dehydration' effect caused by cluster formation in the mixed H<sub>2</sub>O and CH<sub>3</sub>OH solvents<sup>21</sup>, and is known to be strongly affected by the concentration of ionic solutes in the mixture<sup>22</sup>. By labelling specific sites in the polymer and solvents expected to undergo hydrophilic interactions, the hydrogen and deuterium would be expected to show different behaviour before and after the phase change.

The possibility of 'tuning' the LCST by the combination of solvent composition, ionic solutes and copolymerisation<sup>23,24</sup> makes this class of polymers potentially useful in areas such as industry and medicine, with some applications being developed for targeted release of bound active species under certain environmental conditions. It was hoped that our time on the VESUVIO instrument

would shed further light on the hydrophobic and hydrophilic systems at work in these mixtures; because the time-of-flight and scattering cross sections (the degree to which the neutrons interact with the atomic nuclei of that species; derived from pure empirical measurement of prior neutron scattering experiments) of hydrogen and deuterium are different they produce separate peaks in the time-of-flight data from which momentum distributions are calculated. For the reasons explained in detail in *Chapter 5*, the final results of these two experiments are largely inconclusive thanks to a hitherto unknown experimental uncertainty in the measurements taken on this system<sup>25</sup>. Should this reproducibility issue be resolved, we remain hopeful about the eventual results of this investigation.

## **Part One:**

**Matrix Isolation Infrared Spectroscopy Study of Vanillin in  
a Low Temperature Argon Matrix.**

# **Chapter 1: Isolation of Vanillin in an Inert Argon Matrix.**

## **1-1: Introduction**

### **1-1-1: Overview of this Work**

This chapter is, in part, a continuation of the work submitted in my 2009 MSc thesis titled ‘Natural Isotope Abundance using Infra-Red Spectroscopy’. In my previous submission I conducted a number of experiments using the Matrix Isolation technique to form isolated/ pseudo-isolated structures of trapped carbon dioxide and/or molecular nitrogen in an inert matrix of argon atoms<sup>26</sup>, and then examined the results of their Infra-Red (IR) transmission spectra. Here I will show how I have expanded this work to focus on a much larger organic molecule, one which is of relevance to food authenticity- Vanillin, shown in *Figure 1-1* below, also known as 4-hydroxy-3-methoxybenzaldehyde, C<sub>8</sub>H<sub>8</sub>O<sub>3</sub><sup>1</sup>.

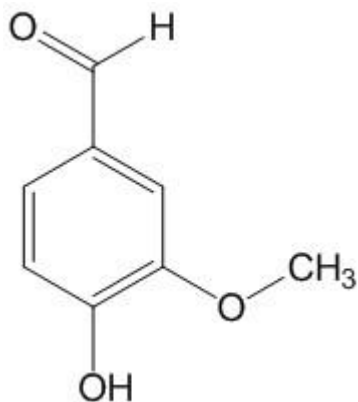


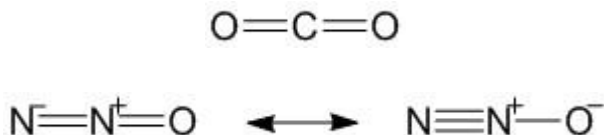
*Figure 1-1: 4-hydroxy-3-methoxy benzaldehyde, or Vanillin.*

As noted in earlier work, the driving force for these investigations is quality control, be it either academic or industrial in nature. It is a fact that many products of inferior quality are nonetheless cheaper and easier to produce, and it is always a temptation for the unscrupulous to substitute these items for those of higher grade in order to save both time and money. A very common place to see this is of course in the food industry (the typical example given is orange juice, where it is cheaper to reconstitute some or all of the product from washings of otherwise waste pulp<sup>27</sup>, than to buy and juice more fruit), but this may also extend to other fields such as pharmaceutical supplies. To this end, it is highly desirable to have access to a reliable technique that can potentially differentiate between the structural isomers<sup>26,28</sup> of an analyte in extremely small concentration, and which may be able to draw out data on the probable synthetic and geographical origins of the sample without excess cost. Data about the origins of a sample may also be found in the distribution of *isotopes* through the sample, thus a vibrational technique (providing information about both structure and mass) such as infrared is a strong contender; IR vibrational data is well understood, allowing us to explore the additional effects of isotopic substitution and compare the predicted values to the observed experimental results. Alternate synthetic methods can be expected to produce different (and characteristic) levels of isotopic fractionation between the possible sites in the product.

The objective of this investigation is to test the use of matrix isolation in conjunction with Density Functional Theory simulations to detect and differentiate isotopic signals in a sample. By developing a method that can quickly, cheaply and reliably measure this distribution in conjunction with reference data for the characteristic fractionation profiles for each known synthetic path, and/ or methods of predicting such distributions, this information may be used as another tool for determining the provenance of the sample examined.

### 1-1-2: Isotopic Splitting in the Matrix

The earlier Masters' thesis focused on the development of lab-based infrared spectra of Matrix Isolated compounds (shorthand MI-IR) in the targeted observation of naturally abundant populations of atypical isotopes (that is to say,  $^{13}\text{C}$  and  $^2\text{H}$  instead of the more common  $^{12}\text{C}$  and  $^1\text{H}$  atomic species) as a possible alternative to more expensive techniques. The results of this work- though clearly preliminary in nature- indicated that it was indeed possible to draw information about the relative population distribution of isotopes in the IR spectra of simple Matrix Isolated molecules, though such spectra suffered from a generally very poor signal-to-noise ratio. Additionally, in the case of the asymmetrical  $\text{N}_2\text{O}$  (*Figure 1-2*) it was possible to attribute  $^{14}\text{N}$  intensity to specific Nitrogen atoms in the total population, due to the difference in their normal modes of vibration<sup>29-45</sup>.



*Figures 1-2 and 1-3: Structures of  $\text{CO}_2$  and  $\text{N}_2\text{O}$ . Note that as a result of the asymmetry in  $\text{N}_2\text{O}$ , the molecule shows two distinct vibrational stretching modes (one mostly N-N in character, the other mostly N-O), as opposed to the degenerate bending modes observed in  $\text{CO}_2$ .*

This procedure was intended to be developed as a potential alternative for industrial-scale isotopic interrogation. The current state of technology uses two main techniques to accomplish this at present:

- Mass Spectrometry (MS, which has a high degree of sensitivity, but only results in one isotopic ratio over the whole compound)
- Site-Specific Natural Isotope Fractionation-Nuclear Magnetic Resonance (SNIF-NMR, low sensitivity but provides site-specific information).

Both MS and SNIF-NMR are limited in their availability by cost and resources, needing specialist training to perform. In addition of the two only SNIF-NMR has the ability to provide information about the position of the isotope in a molecule by modifying its functional groups<sup>1</sup>; this is of great importance here since a molecule of biological origin will have been produced by a very specific reaction pathway, and will not necessarily be the same as one produced synthetically. At the present time, it is not commercially viable to determine site specific isotopic abundances of a sample. The purpose of this investigation was to explore vibrational spectroscopy as a method of doing this, one that would be both scientifically and economically viable.

### **1-1-3: Why Matrix Isolation?**

The principle limiting factor in the use of infrared spectroscopy in the solid and liquid states for this kind of structural/ isotopic investigation is the widths of the individual resonances, mainly due to interactions between neighbouring molecules in the condensed phases. We naturally wish to observe the vibrational properties of the target molecule in isolation, without any interactions with neighbouring molecules that might affect the resulting spectrum (as it would be found in the ideal gas phase); unfortunately, in the gas phase the molecule is freely able to move around and rotate through its full range of ro-vibrational transitions. In a fairly bulky molecule like vanillin the rotational transitions within the ro-vibrational spectra cannot be easily resolved, resulting in the merging of the distinct rotational fine structure into a single broad continuum from which proportionately weak structure such as isotopic populations may not be easily distinguished.

A compromise is found in the use of the low temperature Matrix Isolation technique (written shorthand as MI, or MI-IR in conjunction with infrared

spectroscopy): a well-established technique developed principally by G. C. Pimentel during his career at the University of California, Berkley in the 1950s as a method of trapping, isolating and analysing short-lived volatile chemical species<sup>46</sup>. In this technique a very small concentration of the analyte molecule in the vapour phase is mixed with a bulk material that is spectroscopically inert in the observed range; this bulk material is chosen such that it is not expected to undergo any significant chemical interaction with the analyte (typically a noble gas such as argon, neon, krypton or xenon). This mixture is then sprayed onto a spectroscopically transparent window of sufficiently low temperature to freeze the mixture into a solid, trapping the analyte in a ‘solid solution’ of very low concentration, where it is either isolated or nearly so by the inert material. This solid matrix can then be treated in the same manner as a conventional IR sample while at low temperature. Argon has been used for all isolation experiments reported in this study.

The phrase *pseudo-isolated* is frequently used by this author to refer to the samples produced by this method because, while the matrix in question is believed to contain either isolated or near-isolated sample molecules, this is an assumption based on the changes observed in signal peak character and not a known fact. Although the concentration of the matrices was at the lowest possible level still able to achieve an observable signal in these experiments, the possibility still exists for some significant fraction molecules to interact. The term *pseudo-isolated* is instead used here to acknowledge the possibility of some residual intermolecular interactions in the matrices, and any signal structures that may be attributed to these aggregates will be commented upon where appropriate.

Later chapters in this thesis will show my attempts to model ideal ‘Isolated Phase’ spectra for vanillin using Density Functional theory. The experimental data presented in this chapter, along with solid and gas-phase IR spectra presented later, provide the ‘raw data’ against which these models are compared.

#### 1-1-4: Packing in the Matrix

As discussed in detail in my earlier work with CO<sub>2</sub> and N<sub>2</sub>O, the way in which the molecule fits into the argon matrix<sup>28</sup> is an important consideration. By the very nature of this technique there is a direct physical interaction between the two species as they condense together from the vapour phase into the solid. As a result, infrared peaks in a Matrix Isolated spectrum may be both shifted and/or split relative to the calculated spectrum of an isolated molecule to a degree dependent on the physical properties of the matrix material<sup>47-51</sup>. Ideal gas atoms are typically modelled as hard spheres of a given radius (almost always the van der Waals' radii of the atoms)<sup>52</sup>, meaning that the principal property of interest is their size relative to the sample molecules and the size of the resulting possible sites of substitution in the solid matrix. In my previous experimental data from the use of argon as a matrix material, this has typically given rise to repetitions of other existing structures (i.e. isotopic splitting structure) of lower intensity shifted either positively or negatively in position by ~7-8 cm<sup>-1</sup> for the prominent spectrum of the carbon dioxide sample, a phenomenon supported by behaviour reported in existing literature sources for other small species<sup>44</sup> in which larger matrix shifts and splits (of the order of 50-60 cm<sup>-1</sup> or even greater) have been reported. Argon has been observed to have an atomic radius of 1.88Å (see *Table 1-1* below), and is seen through diffraction studies to form a face-centred cubic lattice; it is the way this structure accommodates each atom and functional group of the isolated molecule that is of interest.

Using the x-ray determined crystal structure as a starting point, the volume of the vanillin molecule was calculated using the Connolly Solvent Exclusion method; this method calculates the volume of a molecular system from the van der Waals' radii of its constituent atoms and approximating this volume with a variety of integrated polyhedral functions. The Connolly method is also frequently used to calculate the surface area of a molecule that is accessible to solvents because it performs these calculations using a spherical 'probe' of arbitrarily determined radius (and thus volume). The probe used is typically of radius 1.4Å to simulate a water molecule, but in this text a probe of radius 1.88Å was used instead to simulate the

‘solvation’ by the argon matrix. Increasing the size of the probe usually has the effect of slightly increasing the calculated volume due to solvent inaccessibility, but in the case of the vanillin crystal structure both probe sizes return the same value of  $115.523\text{\AA}^3$  ( $\pm 1.156$ ) calculating the equivalent volume of the argon spheres to be  $37.612\text{\AA}^3$  each (and scaling this volume to account for the face centred cubic atomic packing factor of 0.74) results in the substitution of the equivalent of 3.071 Ar atoms in the matrix. As discussed later, although this simple picture of packing in the matrix suggests equivalent *volume* for direct substitution, it does not adequately account for the shape of the molecular volume itself as seen in *Figures 1-4a* and *b* below. While vanillin may only occupy the equivalent volume of 3.071 Ar atoms, further substitutions may be necessary in order to accommodate the actual size of the molecule, and each of these differences in the matrix will have an effect on the position of the resulting infrared peaks for the matrix isolated spectra.

Species	Solvent Excluded Volume/ $\text{\AA}^3$
Ar	37.612
Kr	34.526
Xe	42.213
OH	10.326
CHO	24.59
O-CH <sub>3</sub>	31.334
Vanillin (C <sub>8</sub> H <sub>8</sub> O <sub>3</sub> )	115.523

*Table 1-1: Relative atomic/ molecular volumes of Ar, Kr, Xe, the functional groups of Vanillin (OH, CHO and O-CH<sub>3</sub>), and Vanillin itself (C<sub>8</sub>H<sub>8</sub>O<sub>3</sub>) taken from the X-Ray Crystallographic data for the solid phase structure. Connolly Solvent Excluded Volume calculations for the functional groups use a probe of radius 1.88 $\text{\AA}$  to simulate the bulk phase argon, but are otherwise treated as groups in a vacuum with no accounting for the overlap with other vanillin atoms; Atomic species are spherical volumes from their respective van der Waals radii.*

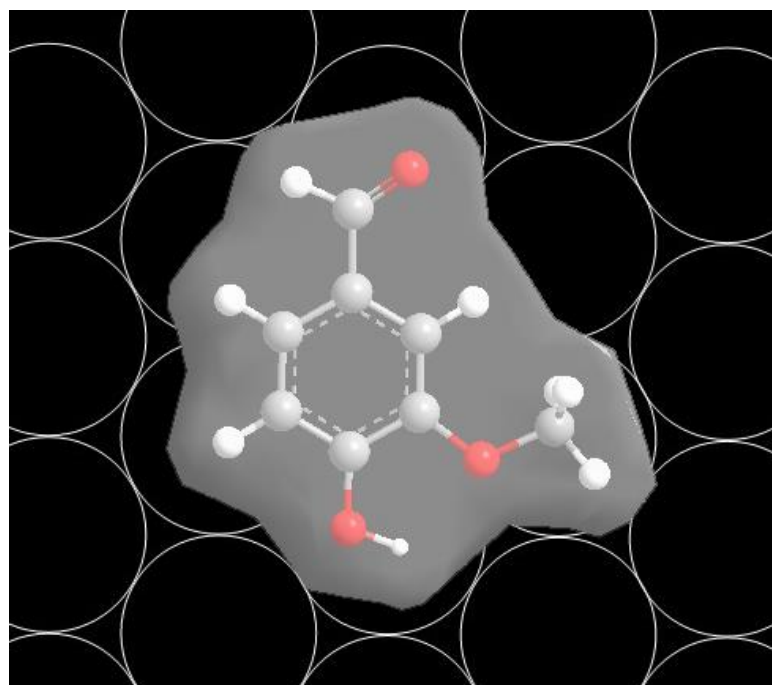
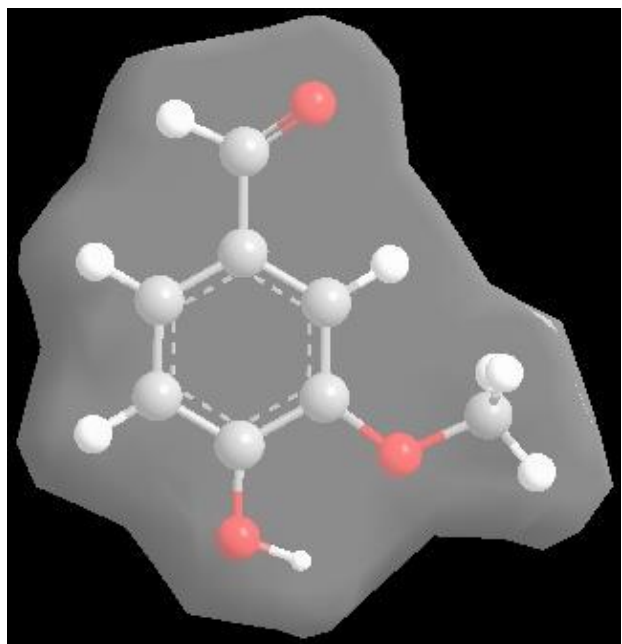


*Figure 1-4a and b: The Connolly Solvent excluded Volume of the vanillin molecule (crystal structure, top) and an example of how it may fit into the packing structure of the argon lattice (argon spheres represented by white outlines, bottom); argon structure extends into the z-axis in an ‘a-b-c’ layering formation, though the vanillin molecule is largely planar in this configuration with a ‘thickness’ less than the diameter of the Ar layer.*

### **1-1-5: Vanillin as a Target Analyte**

Vanillin was chosen as a target for this investigation for a number of reasons: firstly, the compound is a relatively small species, containing only nineteen atoms. This renders vanillin quite a volatile compound with a melting point of only 83°C, and makes it easy to sublime into the vapour phase for the purpose of Matrix Isolation experiments. In addition the calculation times required for the Density Functional Theory simulations (detailed later in this thesis) depend greatly on the number of particles involved; the nineteen atom system calculated to the 6-311+G (d) level of theory (see later) requires less than a day's processing time with the resources available on the UEA campus to produce a simulated vibrational spectrum. The second useful characteristic of vanillin is that it contains three different functional groups- all three of which contain oxygen. As outlined for nitrous oxide above, the differences in the vibrational frequencies of the functional groups allow for the possibility of assignment of isotopic population density between them. This leads to the third reason for choosing vanillin: availability. Vanillin is a very common compound in the food industry, produced both from naturally sourced pods from the Vanilla plant, and produced synthetically industrially<sup>53</sup>. Isotopes, because of different masses, are naturally subject to fractionation effects and thus the different methods of production will be expected to produce variations in isotopic population. This gives rise to the possibility of identifying the source of a sample based only on a characteristic isotopic population distribution, and the relative size and complexity of vanillin make it a (comparatively) simple target for such an exercise.

## **1-2: Experimental**

### **1-2-1: Equipment**

*Figure 1-5* shows the initial construction of the matrix isolation apparatus, including a gas handling system as well as a closed-cycle Helium expansion cryostat. This system has a minimum working temperature of approximately 15K, depending on the presence of radiation shielding around the window/temperature sensor. The gas system was fitted together using stainless steel pipes together with commercially available Swagelok fittings; the main ‘chassis’ of the system (the sample chamber itself, Parts E & G) was refitted from an older piece of equipment.

This system was refurbished for the purposes of the previously mentioned Master’s project during 2008/ 2009, and has undergone several minor adjustments and alterations as my work with vanillin has progressed- especially in regard to the direct introduction of sublimed solid samples into the path of the argon gas stream from specially constructed heated glassware (see *Figures 1-6 a and b*). The vanillin sample used was dried overnight in a 50°C oven then held under vacuum.

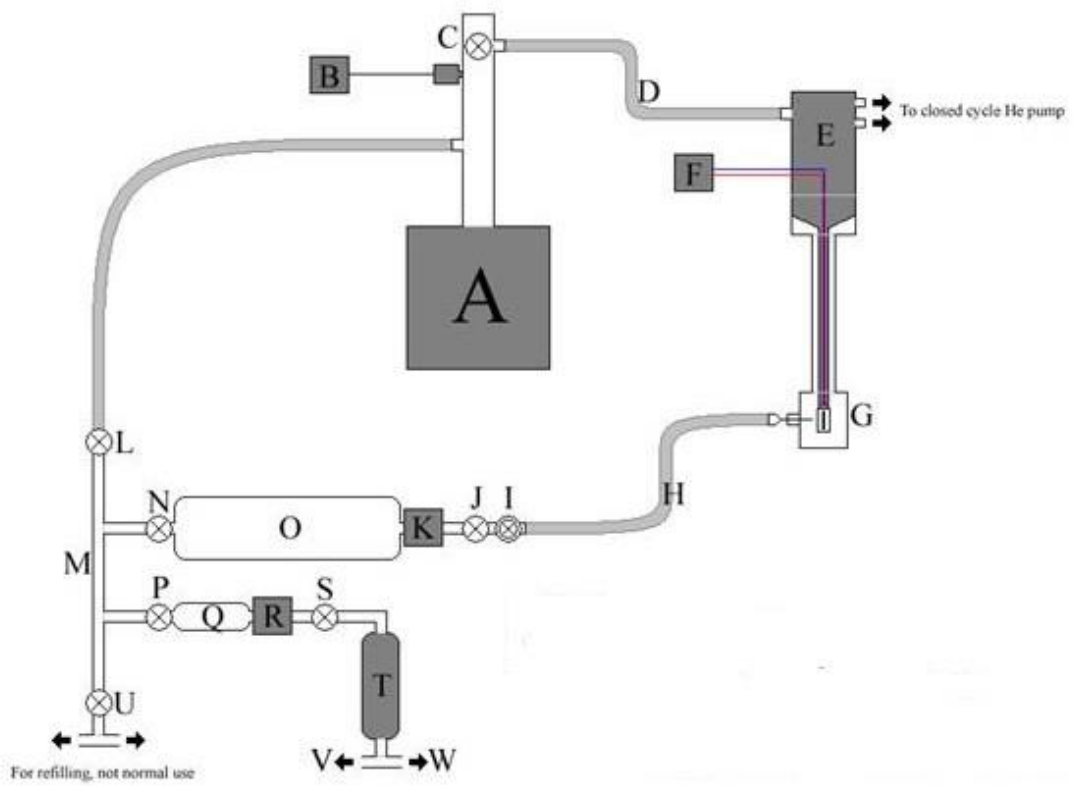


*Figure 1-5: Diagram of experimental gas management system, originally presented in MSc by research, same author.*

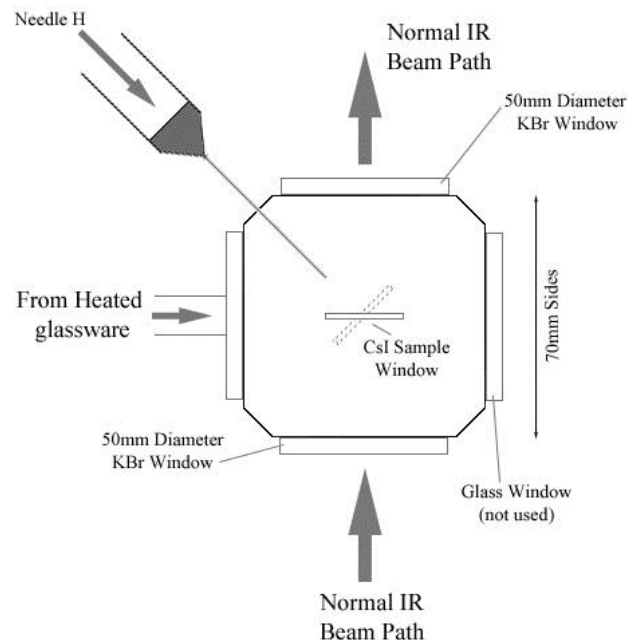
*Labelled parts are as follows:*

- A. Turbopump.
- B. Digital pressure sensor (HV emission detector).
- C. Master valve (closes off sample section when necessary).
- D. 0.5cm internal diameter flexible pipe.
- E. Double stage He expander cryostat (arm extends down to sample chamber G)
- F. Combination digital thermometer and heater.
- G. Sample chamber (Contains but does not make contact with bracket holding inert sample window in path of both sample spray and IR beam; walls in plane of view are IR transparent and chamber wall is penetrated by a needle that deposits sample gas spray ~1cm from the surface of the sample window).

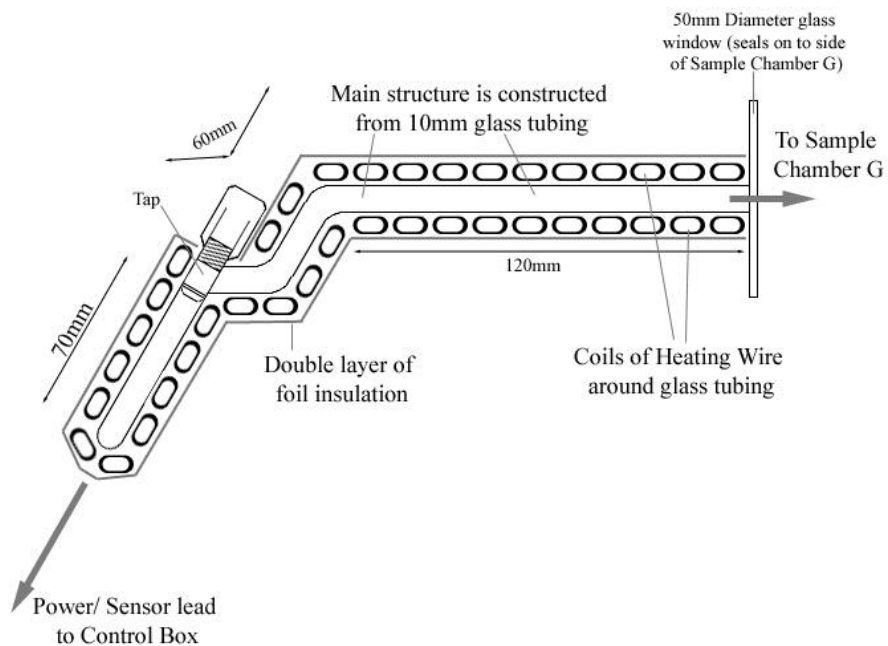
*An expanded view of Part G can be seen in Figure 1-6a; an expanded view of the glassware used to introduce vanillin vapour into Part G can additionally be found in Figure 1-6b.*

- H. 0.5cm internal diameter flexible pipe.
- I. Needle valve to control sample spray pressure.
- J. Tap.
- K. Analog pressure gauge, 0-1000mbar.
- L. Tap.
- M. 0.5cm internal diameter pipe.
- N. Tap.
- O. 2250cm<sup>3</sup> volume primary vessel.
- P. Tap.
- Q. 40cm<sup>3</sup> volume small vessel.
- R. Analog pressure gauge, 0-100mbar.
- S. Tap.
- T. Drying tube for Ar carrier gas containing powdered P<sub>2</sub>O<sub>5</sub>.
- U. Tap (seals off 'T' branch; only used outside of experiments).
- V. Ar gas supply.
- W. Secondary gas supply (CO<sub>2</sub> or N<sub>2</sub>O, used in earlier experiments).

### Top-Down View, Sample Chamber G



### Vanillin Sample Container





*Figures 1-6a, b and c: Orientation of temperature controlled glassware relative to Sample Chamber G showing relation of CsI window to incoming argon gas stream (greyed out) from needle H verses normal sample scanning orientation (solid line), detail view of glassware construction showing heating elements and insulation; photograph of glassware relative to sample chamber.*

The procedure for the collection of a Matrix Isolated Infrared Spectrum was as follows. The entire gas-handling system was evacuated to the minimum possible pressure with the Leybold BMH70 turbopump (typical working pressure approximately  $1 \times 10^{-7}$  mbar). The main reservoir cylinder (Part O) was filled to its maximum measured capacity of 1 bar with argon gas (dried after passing through the  $P_2O_5$  drying tube Part T), then the taps labelled L and N were left closed for the remainder of the experiment.

With the Sample Chamber G in the beam path of the IR spectrometer (a Bruker IFS-66 IR spectrometer operated by the OPUS v6.0 software package was used for these experiments) the CsI window was cooled using the double stage helium expander cryostat to a working temperature of ~15K. Measured temperatures for this system appear to be correct to within +/- 3K, meaning this value is safely below the melting point of argon of 83.78K. The upright section of the cryostat

assembly had a limited range of rotation (approximately 45°) and was initially placed perpendicular to the deposition needle at the end of tube H as it enters the sample chamber. Once at the working temperature (after a cooling period of approximately two hours) a small amount of argon was released from the primary vessel O through the needle valve out onto the cold window; a pressure drop of 20mbar in the vessel was used to quantify this gas release. This argon preferentially deposits on the cold window in the spray flight path, rather than the room temperature walls of the chamber- though given that the 2mm needle coats the entire 20mm diameter window and the metal bracket holding it with argon, diffusion effects make direct quantification of the volume deposited gas impossible without more sophisticated equipment. During deposition of material the pressure in the system increases from the normal resting value; in each case, this 20mbar of Ar gas was deposited at a target working pressure of  $\sim 1 \times 10^{-4}$  mbar (with the taps L and N sealed and argon flow controlled by I, meaning that the resting and working/ deposition pressures are measured only in the sample and pump sections of the gas system).

At this point the window was rotated to face the IR beam path, and a fine resolution background spectrum taken: this argon layer also acts as a system check, to ensure that the gas spray is targeted correctly and that the system does not show excess levels of moisture or atmospheric contamination. The resulting background contains signals from the ‘empty’ argon matrix (which should not show any bands if the gas-handling system is clean of all IR-active contaminants), the evacuated sample chamber, the spectrometer beam path and the instrument itself- all of which *should* be subtracted from the sample signal during later processing. The interior of the spectrometer was under a constant purge from a dry nitrogen gas supply, running at a constant pressure of  $\sim 750$ mbar; this was directed into the spectrometer to operate the air bearing for the interferometer scanner and to flush the spectrometer beam path- exact pressures are not known, but even though the spectrometer was covered by an improvised seal (to accommodate the gas system) stable background signals were observed  $\sim 15$  minutes from the start of operation, and allowances were made for ‘rest periods’ for signal stabilisation before measurements.

All infrared spectra using this system were collected using a deuterated triglycine sulphate (DTGS) detector at a range of numbers of scans and resolutions (specific values for each of these properties, as well as deposition pressures) can be found in *Table 1-2* later in this chapter for each individual sample spectrum collected. In each case the background was collected at the same resolution as the sample, and the S/N value quoted is for the data after background subtraction; all spectra were collected with a zero-filling factor of four, meaning spectra of resolution  $0.5\text{ cm}^{-1}$  contain 59156 data points (every fourth point being ‘real’), while those scans of resolution  $0.25\text{ cm}^{-1}$  contain 118312 points (29578 of which are ‘real’). A  $0.5\text{ cm}^{-1}$  spectrum from a total of 512 scans could be collected over some 2.5 hours, while a ‘full’ spectrum collected with 1024 scans at a resolution of  $0.25\text{ cm}^{-1}$  requires an approximate collection time of 7 hours on the IFS-66 instrument. Combined with a roughly 4-hour preparation time for the vacuum system and deposition of the matrix sample, this means that a complete experiment could be conducted in between 10 and 19 hours.

After the background was collected, sample deposition was then prepared: the CsI window was rotated back to face the needle for optimum spray angle and the vanillin sample glassware (see *Figure 1-6*) heated to the desired temperature. The opening for the vanillin glassware is much larger than that of the needle, but the contents were held at a much lower pressure (evacuated with the rest of the system while at room temperature, then sealed again during cooling); the free path of the vanillin vapour intersects with that of the argon, so that the two materials would co-deposit on the window at the same time. To begin deposition the argon stream was first re-started, then once a set quantity of pure Ar had been deposited the vanillin tap was opened; a set quantity (usually 100mbar pressure from the primary vessel O, but sometimes more depending on the desired experimental conditions) of argon was co-deposited with the heated vanillin vapour trace, forming the sample matrix together on the cold window. At this point the vanillin sample was re-sealed, and a further 10mbar of pure argon continued to deposit.

This procedure gave three experimentally controlled variables to each experiment: vanillin temperature (and thus vapour concentration), argon release pressure (and thus argon host gas concentration) and total deposition time (thus controlling overall signal-to-noise ratio). It should be noted that no automatic system was available to maintain set argon deposition pressure, so this value was regulated in each experiment by hand; this results in an uncertainty to all quoted argon deposition pressures of +/- 1x10<sup>-4</sup>mbar. Once deposition was complete, the system was allowed a ‘rest period’ of five minutes, then the window was rotated back to face the IR beam. Sample scans were then taken using the same settings and resolution as the earlier background.

### **1-2-2: Argon Backgrounds and System Integrity**

Nitrogen and argon gases were used in this experiment as supplied by BOC gases; nitrogen was listed as 100% pure (with no further data available), while ‘Pureshield’ Argon was listed as 99.998% pure. Both types of gas were passed through (separate) P<sub>2</sub>O<sub>5</sub> drying columns to remove trace water vapour. Detectable water signals in the result spectra described below are therefore attributed to two possible sources: atmospheric water vapour that has not been fully flushed from the spectrometer beam path, and trace water left in the vanillin powder sample (which was noted previously in the Solid Phase reference data).

Background spectra were collected before each isolation was performed, using the method described above.

## **1-3: Results and Analysis**

### **1-3-1: A Note on the Quality of Spectra**

Using the method detailed above, infrared spectra of pseudo-isolated vanillin were produced under conditions considered satisfactory (i.e. clear IR signals with minimised levels of atmospheric contamination). As the sample molecules are reduced in concentration to enter an isolated state, the signal intensity per matrix path length decreases; given that there is a limit to the amount of gas that can be held in the system for deposition, lower matrix concentrations (controlled by temperature as noted above) approach the limit of detection for the available IR spectrometer system. Because of this weakening of intensity only Samples 3 and 5 appear to show the peak width and separation characteristic of samples approaching true isolated conditions while still being of statistically quantifiable magnitude compared to background noise in the spectra. All five sample spectra obtained have, however, been reproduced below to demonstrate the iterative nature of the investigation. Sample 5 has been used as the reference for the later chapters of this thesis because of its superior resolution ( $0.25\text{ cm}^{-1}$  verses  $0.5\text{ cm}^{-1}$  in other spectra), though the three large features typically seen at  $\sim 3500\text{ cm}^{-1}$  are not actually observed here (see the later analysis section for comments on this behaviour).

It is clear from experimental evidence that the methods and equipment used in this investigation do not allow for the complete elimination of the rotational structure of molecules such as atmospheric carbon dioxide from the vacuum system or the resulting measured spectra, the presence of such lines in spectra of ‘pure’ samples confirming that this is a systematic issue. In addition it is sometimes possible to observe interference fringes in the spectra, fringes which may be used in such cases to calculate the thickness of the matrix deposited on the surface of the CsI window (and thus the experimental path length). Further to this behaviour, the instability of the spectrometer due to temperature changes both inside and out causes

minute band shifts that make it difficult to get an exact background subtraction; attempts to compensate for these band shifts by relative displacement of background and sample spectra before manual background subtraction have proven unsuccessful, as each band is displaced by a different non-linear value and produce only a very narrow range of proper background subtraction ( $\sim 50 \text{ cm}^{-1}$ ). Peaks outside this range in either direction can be seen to show sinusoidal subtraction artefacts at their extremities due to the equivalent data points being ‘out of phase’. As a result of these effects, the spectra obtained have high levels of noise and show a large number of subtraction artefacts which are easy to mistake for actual signals. Of note is the absence of visible peak structure typically seen between  $3200\text{-}3550 \text{ cm}^{-1}$  in Sample 5: these peaks are usually very strong, but in this case cannot be distinguished from local background noise and residual rotational structure from the hydrogen bonding band attributed to the hydroxyl group centred at  $\sim 3700 \text{ cm}^{-1}$ .

The peaks marked in the following spectra are true signals, as judged by their absence from the background scans of argon containing no vanillin vapour deposited prior to sample collection. These signals have been manually fitted with Gaussian curves using the OPUS software to determine their width and intensity; this data is presented in *Tables 1-3 to 1-5* below. The remainder of the structure observed has been dismissed as a mixture of background noise and artefacts of improper subtraction. A single distinct peak (of varying strength) is observed in the sample spectra at a wavenumber value of  $\sim 2712 \text{ cm}^{-1}$ ; this peak does not appear to show the same dependence on vanillin concentration as its neighbours, nor does it ever broaden or change shape with sample conditions, depending only on overall transmission intensity. For this reason, this peak is assigned as an artefact of the spectrometer, as are the known features that may be observed at  $\sim 748$ ,  $\sim 1496$  and  $\sim 2992 \text{ cm}^{-1}$ . Some of the sample spectra (specifically Samples 1, 2 and 3) show a clear signal peak at  $\sim 3750 \text{ cm}^{-1}$ : this peak is attributed to the asymmetric stretching mode of residual water trapped in the vanillin sample, showing as it does the same dependence on matrix concentration as the vanillin itself.

Absorbance spectra are shown below in *Figures 1-7 to 1-11 a, b, c, d, e, f, g* and *h* in ascending order from Sample 1 to Sample 5; in each case the entire spectrum is presented between 4000-500 cm<sup>-1</sup> on the first page, then in expanded views of 4000-3500 cm<sup>-1</sup>, 3500-3000 cm<sup>-1</sup>, 3000-2500 cm<sup>-1</sup>, 2500-2000 cm<sup>-1</sup>, 2000-1500 cm<sup>-1</sup>, 1500-1000 cm<sup>-1</sup> and 1000-500 cm<sup>-1</sup> on the subsequent four pages in direct comparison to the argon-only background spectrum taken for that range. In each case, peaks identified as genuine signals are tabulated on the following (ninth) page in *Tables 1-3 to 1-7*. For reference, the argon-only background spectra are presented alongside the sample spectra below, in order to confirm the assignment of peak values to real signals (as opposed to subtraction artefacts). Collection conditions for each sample are presented in *Table 1-2* immediately below:

<b>Sample</b>	<b>Vanillin Temperature (°C)</b>	<b>Mean Deposition Pressure (mbar)</b>	<b>Scan Resolution (cm<sup>-1</sup>)</b>	<b>Number of Scans</b>	<b>Calculated Signal/ Noise Ratio (RMS) Across Entire Spectral Range</b>
1	29	5.2x10 <sup>-5</sup>	0.5	512	0.757
2	28	1.2x10 <sup>-4</sup>	0.5	512	0.338
3	25	2.2x10 <sup>-4</sup>	0.5	512	0.537
4	22	2.2x10 <sup>-4</sup>	0.5	512	0.748
5	25	2.0x10 <sup>-4</sup>	0.25	1024	0.639

*Table 1-2: Collection/ deposition conditions for Samples 1 to 5.*

**1-3-2: Experimental IR Spectra of Vanillin Isolated in an Ar Matrix**

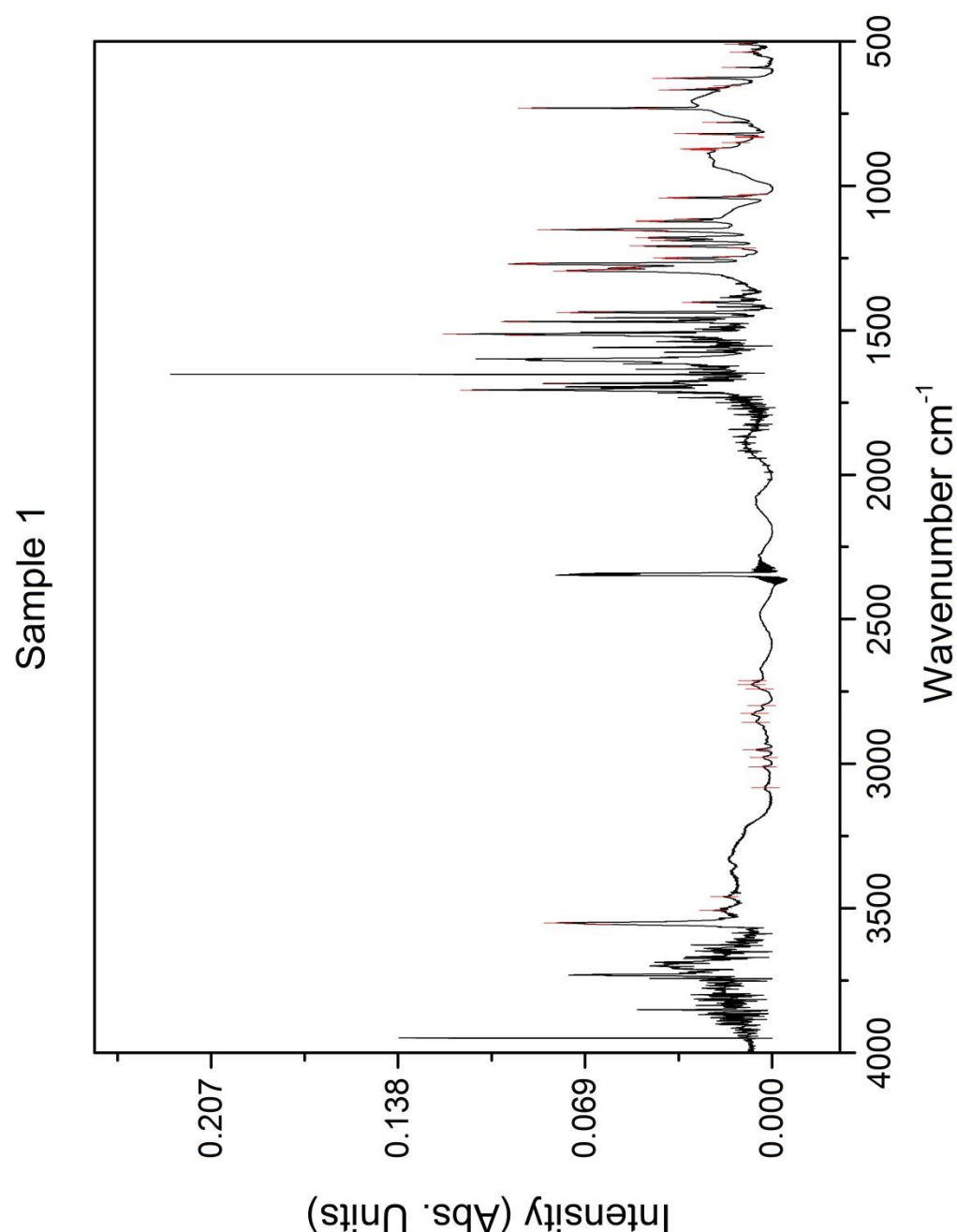


*Figure 1-7a: Overview of Sample 1 IR spectrum, 4000-500 cm<sup>-1</sup>.*

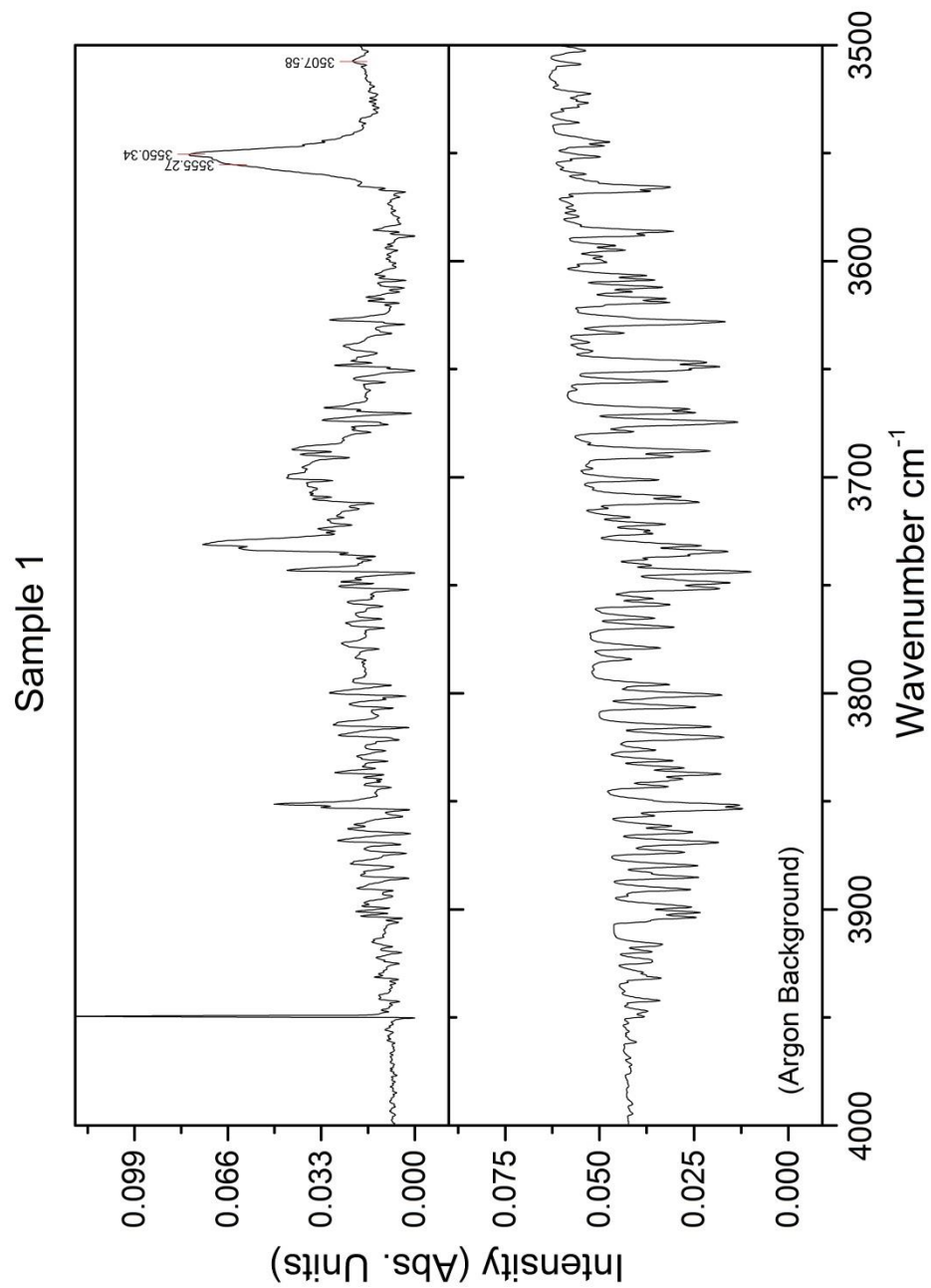


Figure 1-7b: Expanded view of Sample 1 IR spectrum,  $4000\text{-}3500 \text{ cm}^{-1}$ . Genuine signal peaks are marked to indicate position where present.

Sample 1

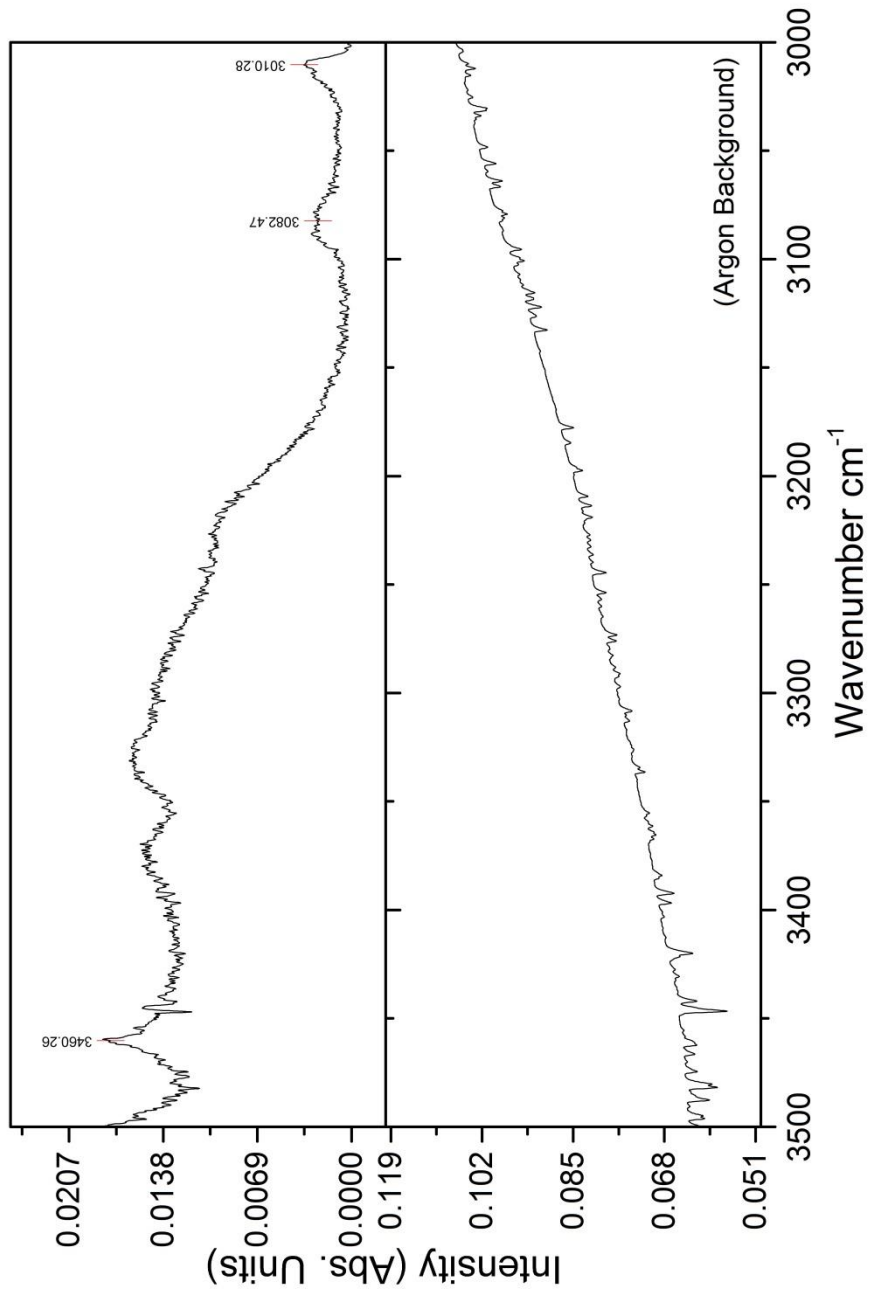


Figure 1-7c: Expanded view of Sample 1 IR spectrum,  $3500\text{-}3000 \text{ cm}^{-1}$ . Genuine signal peaks are marked to indicate position where present.

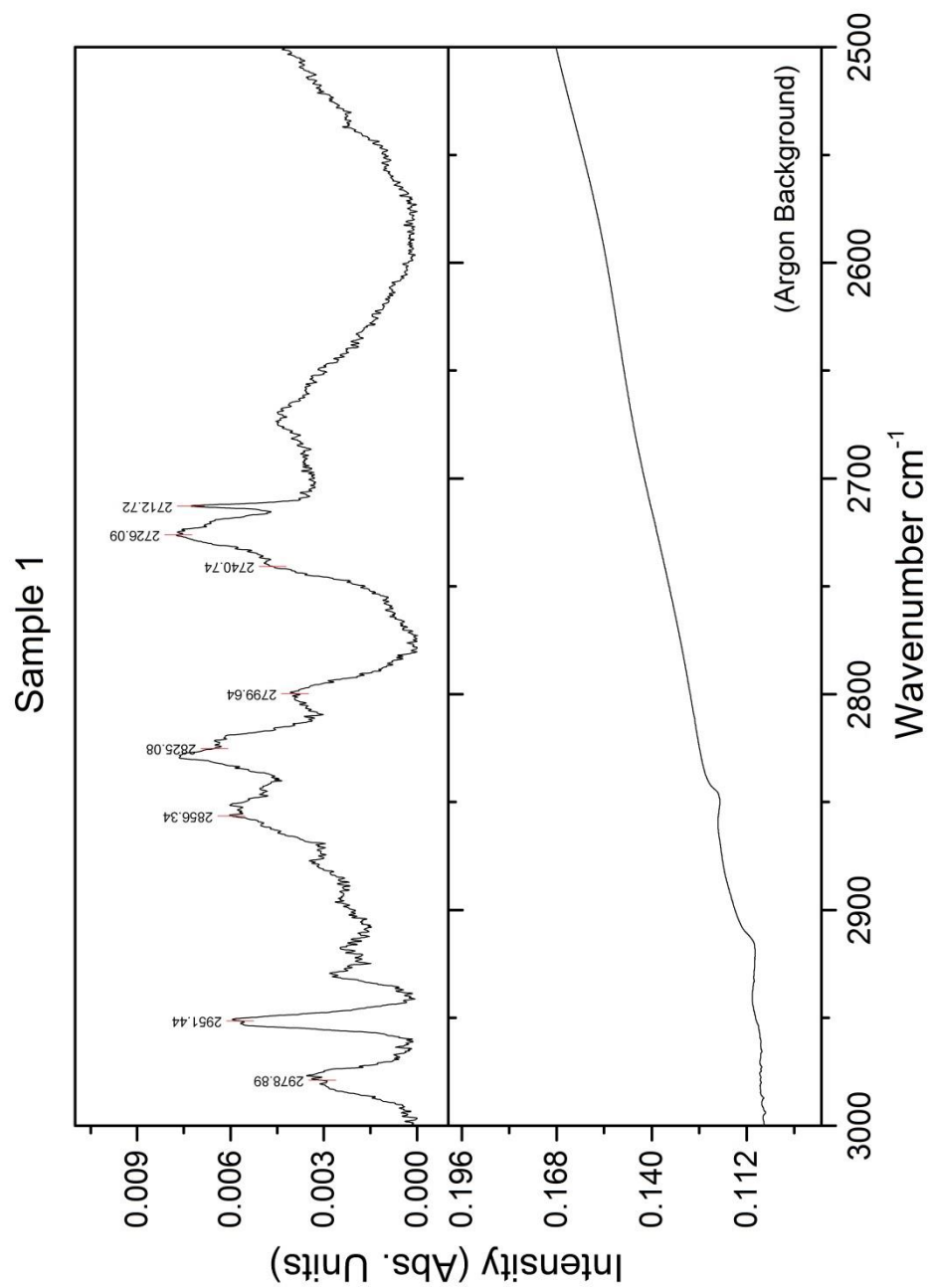


Figure 1-7d: Expanded view of Sample 1 IR spectrum,  $3000\text{-}2500 \text{ cm}^{-1}$ . Genuine signal peaks are marked to indicate position where present.

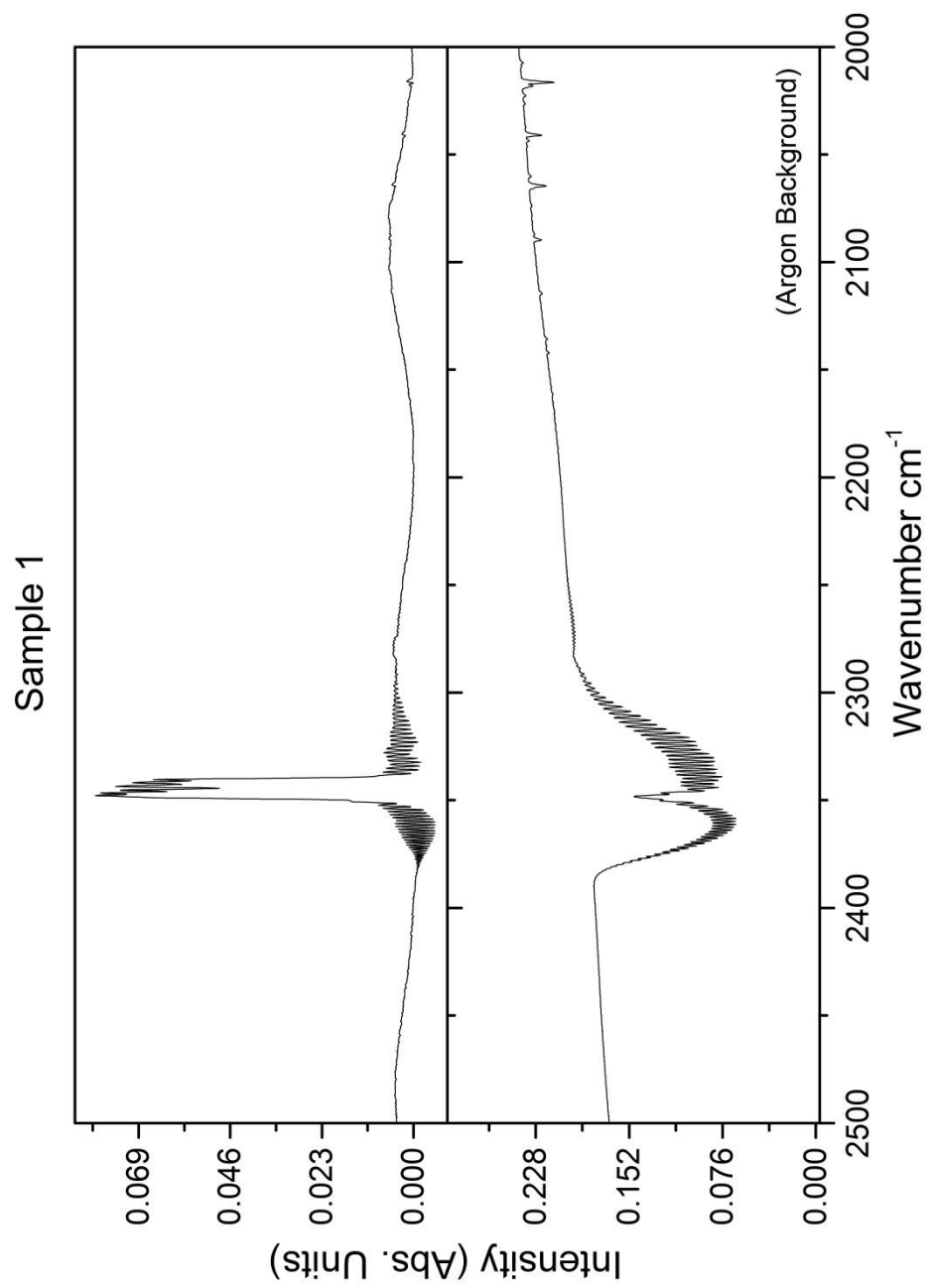


Figure 1-7e: Expanded view of Sample 1 IR spectrum,  $2500\text{-}2000 \text{ cm}^{-1}$ . Genuine signal peaks are marked to indicate position where present.

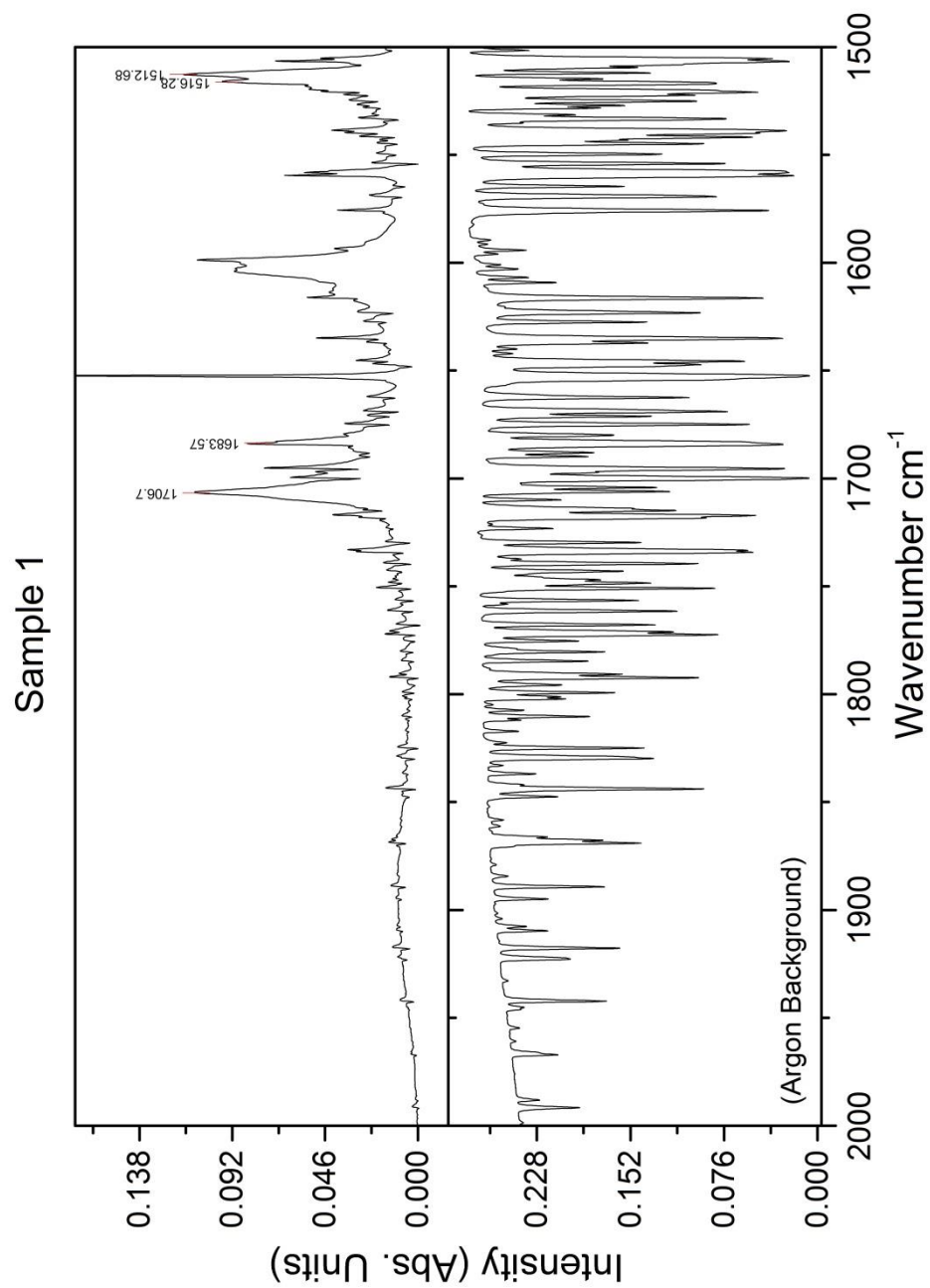
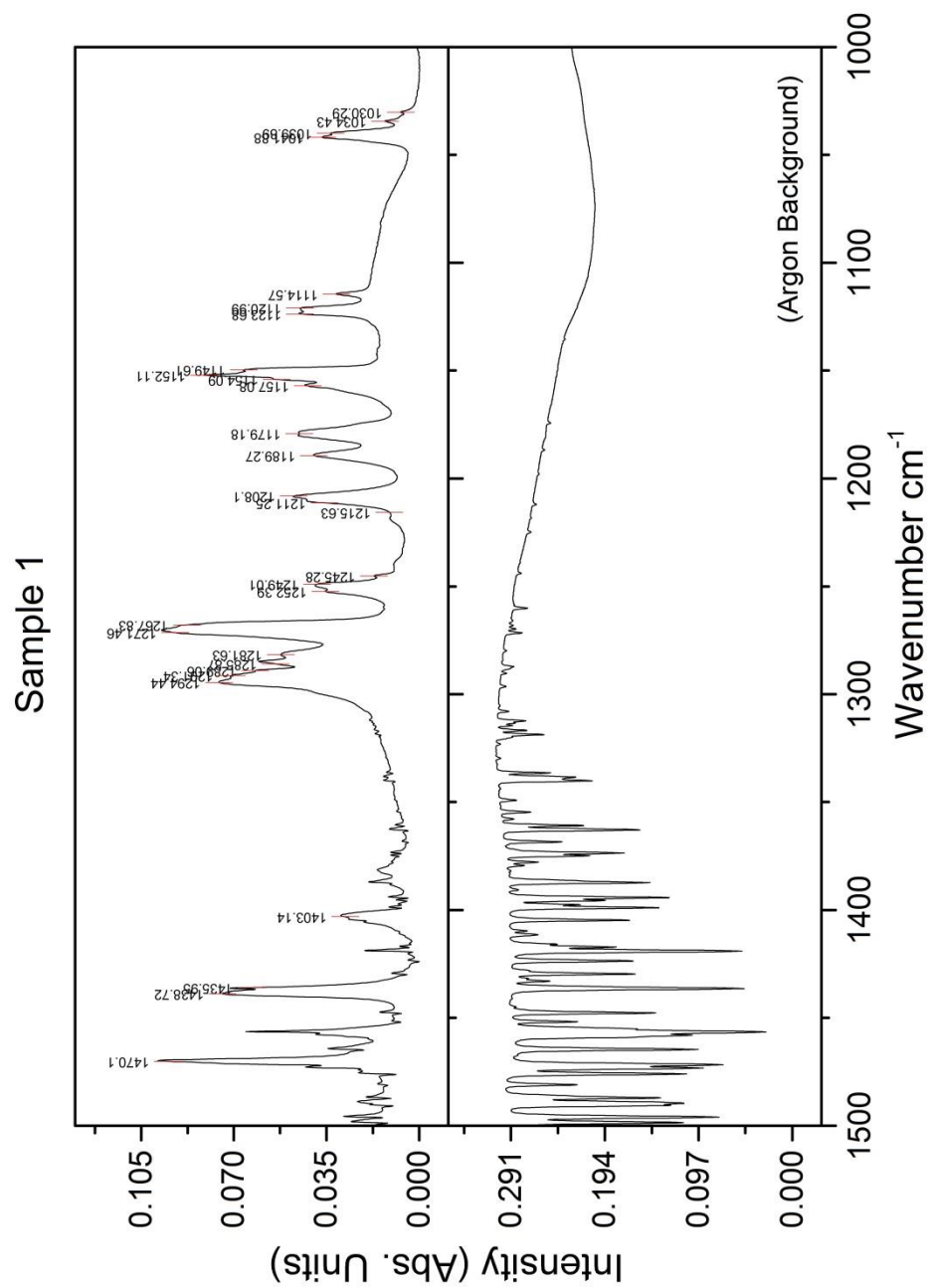


Figure 1-7f: Expanded view of Sample 1 IR spectrum,  $2000\text{-}1500\text{ }\text{cm}^{-1}$ . Genuine signal peaks are marked to indicate position where present.



*Figure 1-7g: Expanded view of Sample 1 IR spectrum, 1500-1000  $\text{cm}^{-1}$ . Genuine signal peaks are marked to indicate position where present.*

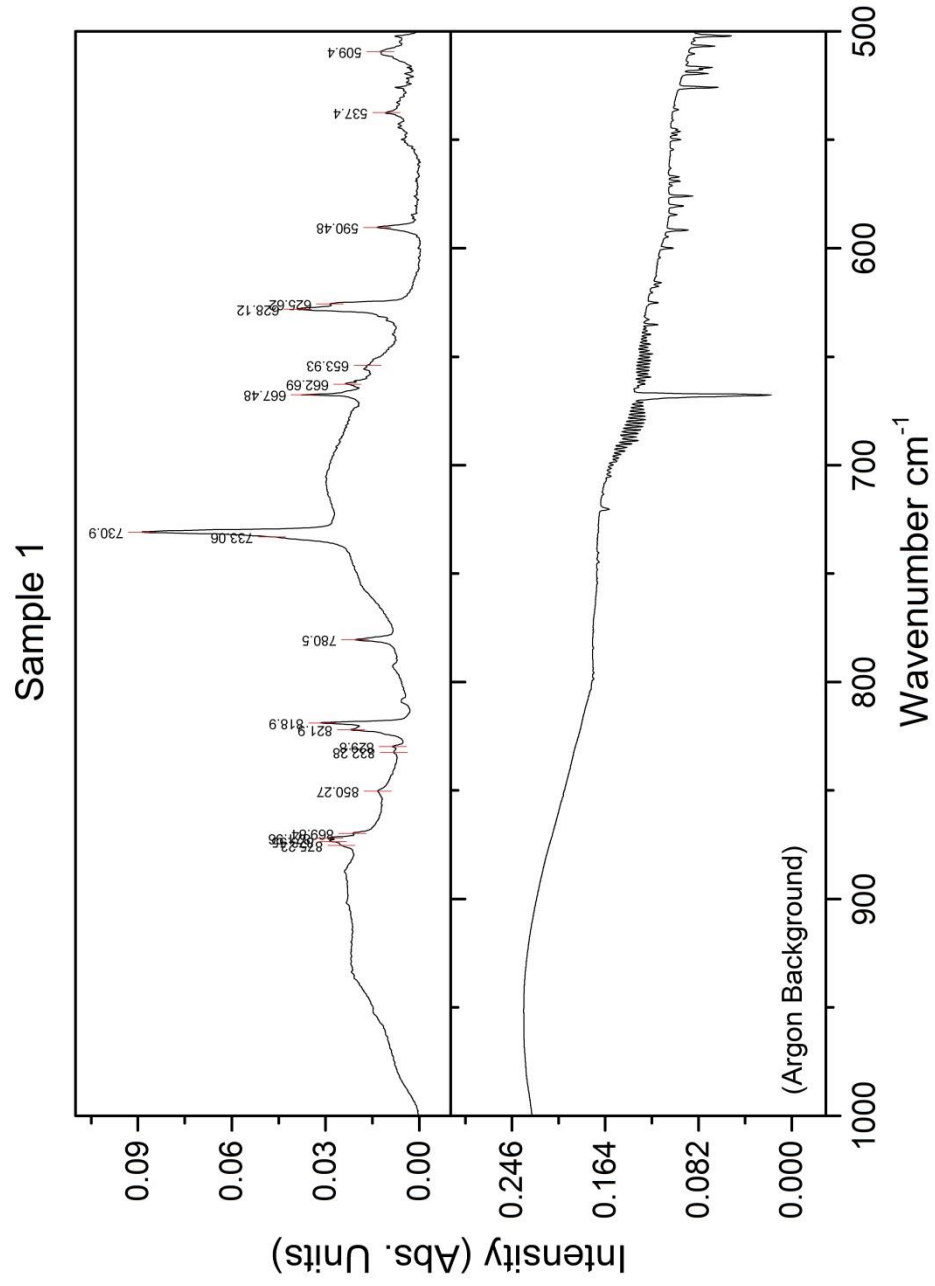


Figure 1-7h: Expanded view of Sample 1 IR spectrum,  $1000\text{-}500 \text{ cm}^{-1}$ . Genuine signal peaks are marked to indicate position where present.

<b>Position</b>	<b>FWHM (cm<sup>-1</sup>)</b>	<b>Intensity (Abs. Units)</b>
509.40	0.012	6.91
537.40	0.003	1.62
590.48	0.012	2.94
625.62	0.024	2.00
628.12	0.035	2.30
653.93	0.006	8.86
662.69	0.008	2.96
667.48	0.021	1.46
730.90	0.055	2.34
733.06	0.021	3.82
780.50	0.012	2.39
818.90	0.025	1.83
821.90	0.018	3.73
829.80	0.003	1.75
832.28	0.003	3.12
850.27	0.005	3.66
869.84	0.006	1.79
871.96	0.012	1.51
873.55	0.010	1.44
875.23	0.008	2.13
1030.29	0.006	2.74
1034.43	0.011	2.88
1039.89	0.017	4.66
1041.88	0.021	5.31
1114.57	0.016	2.63
1120.99	0.030	2.88
1123.68	0.027	2.40
1149.61	0.053	4.50
1152.11	0.064	2.06
1154.09	0.024	1.44
1157.08	0.031	4.82
1179.18	0.037	6.89
1189.27	0.031	5.96
1208.10	0.040	4.60
1211.25	0.018	2.24
1215.63	0.006	10.00
1245.28	0.010	2.30
1249.01	0.030	3.47
1252.39	0.026	3.78
1267.83	0.070	4.29
1271.46	0.076	4.23
1281.63	0.045	7.26
1285.87	0.033	3.24
1289.06	0.041	2.44
1291.34	0.024	2.24
1294.44	0.069	6.32
1403.14	0.030	5.58
1435.95	0.053	1.87
1438.72	0.074	3.56
1470.10	0.099	3.50
1512.68	0.114	3.68
1516.28	0.086	2.64
1683.57	0.062	2.50
1706.70	0.089	6.14

2726.09	0.003	10.41
2740.74	0.001	7.75
2799.64	0.003	14.87
2825.08	0.005	14.10
2856.34	0.002	18.54
2951.44	0.006	8.15
2978.89	0.003	14.39
3010.28	0.003	7.38
3082.47	0.002	16.91
3460.26	0.004	4.99
3507.58	0.007	17.26
3550.34	0.062	5.16
3555.27	0.048	4.98

*Table 1-3: Integrated Gaussian fitting parameters for signal peaks in Sample 1.*

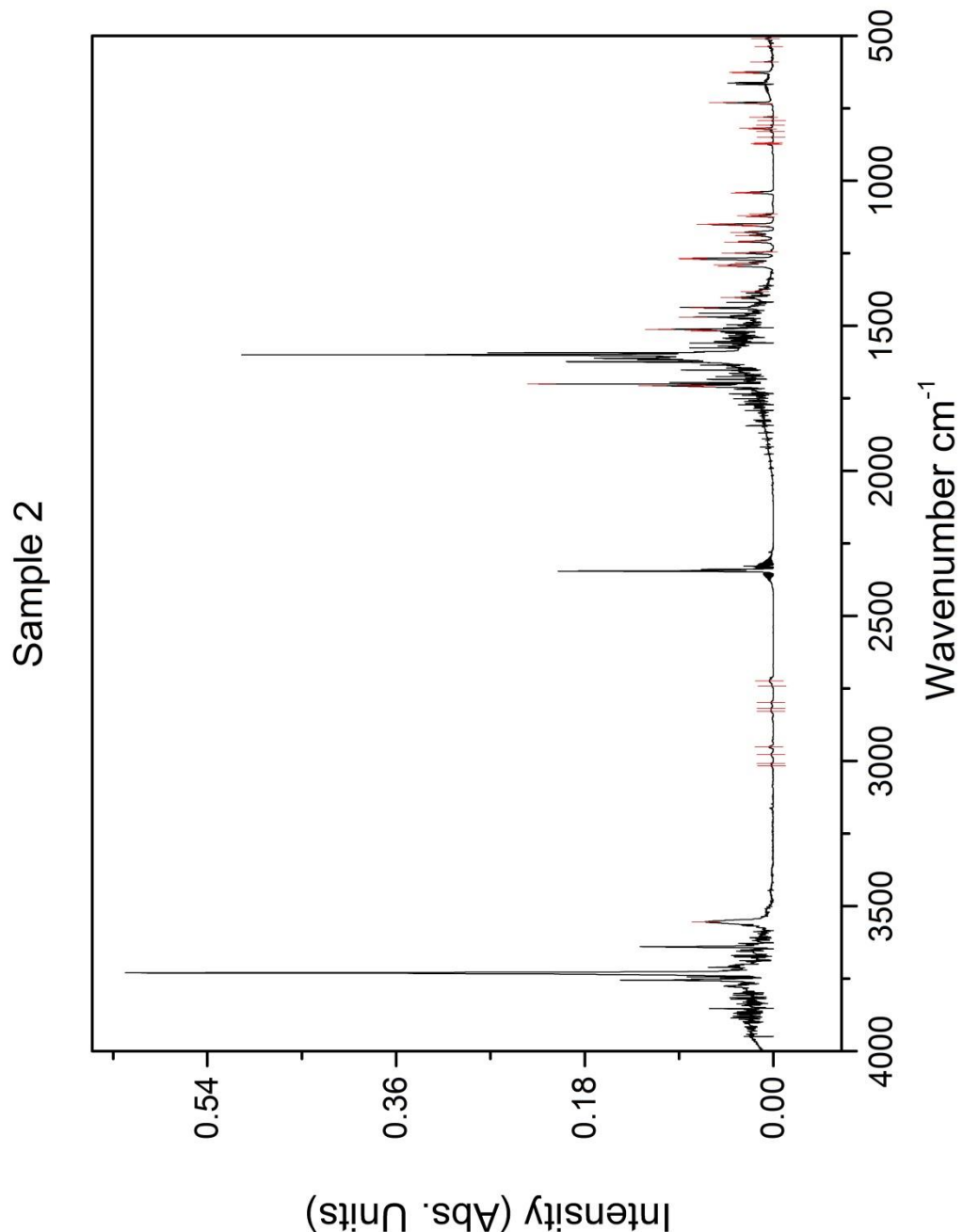


Figure 1-8a: Overview of Sample 2 IR spectrum, 4000-500 cm<sup>-1</sup>.

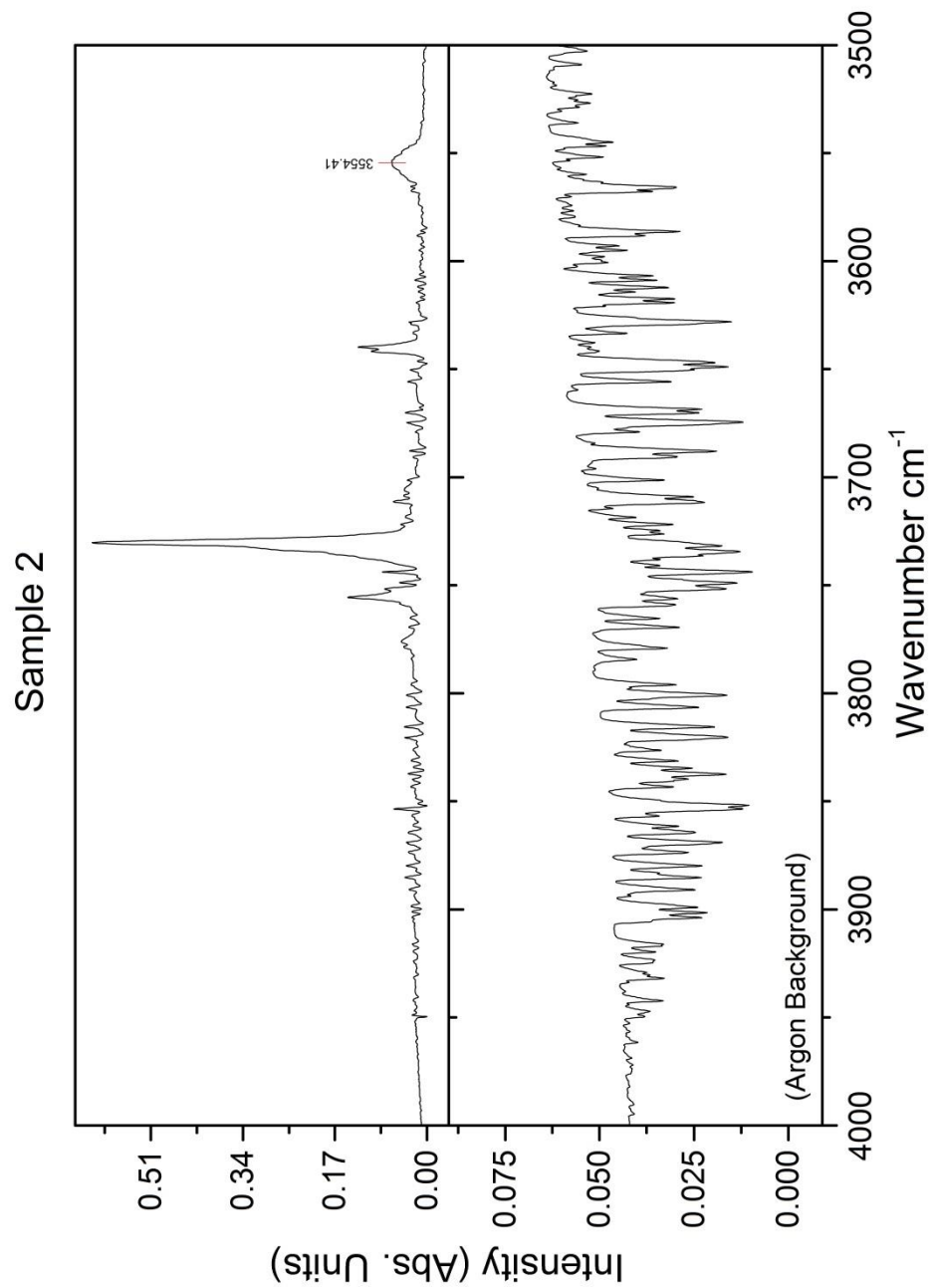


Figure 1-8b: Expanded view of Sample 2 IR spectrum,  $4000\text{-}3500 \text{ cm}^{-1}$ . Genuine signal peaks are marked to indicate position where present.

Sample 2

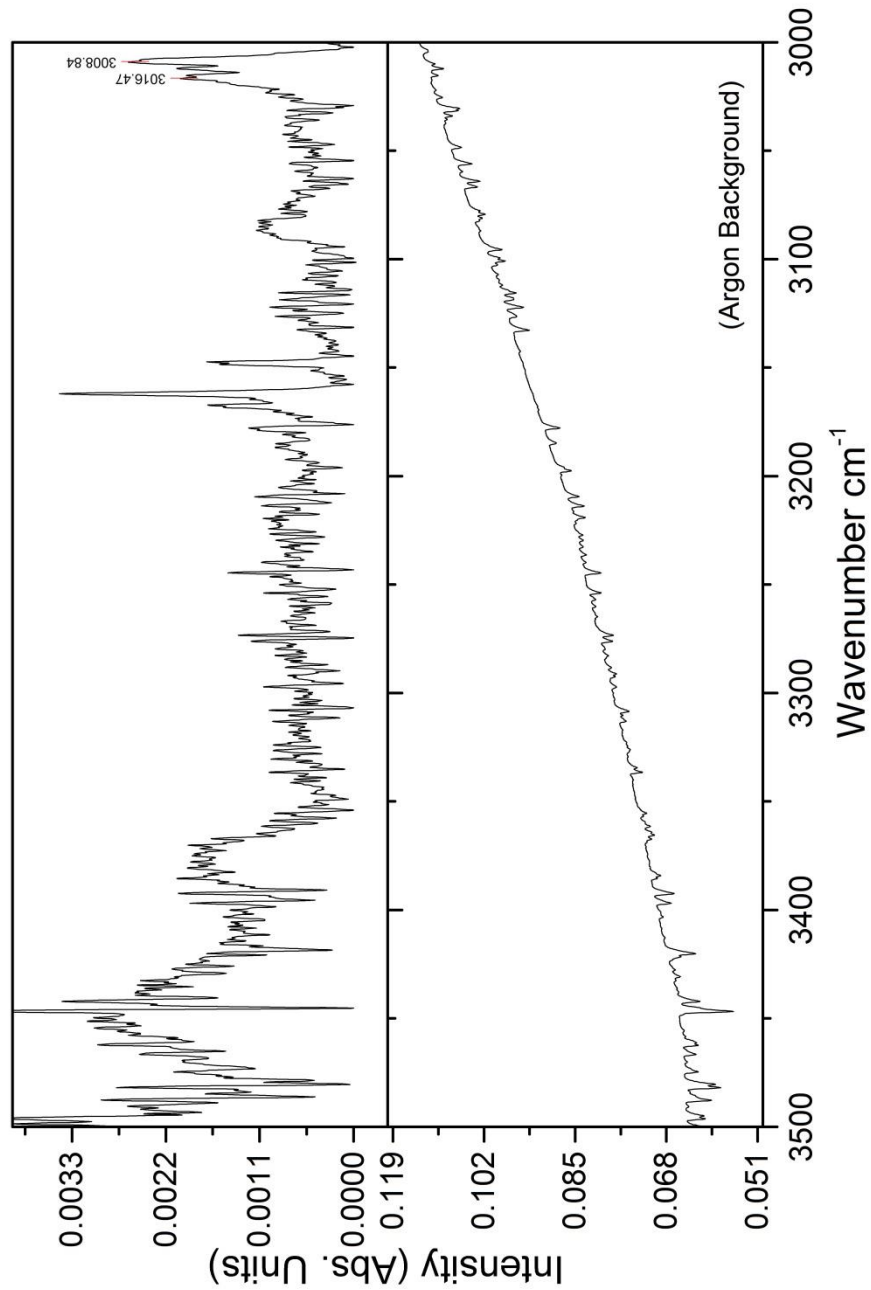


Figure 1-8c: Expanded view of Sample 2 IR spectrum, 3500-3000 cm<sup>-1</sup>. Genuine signal peaks are marked to indicate position where present.

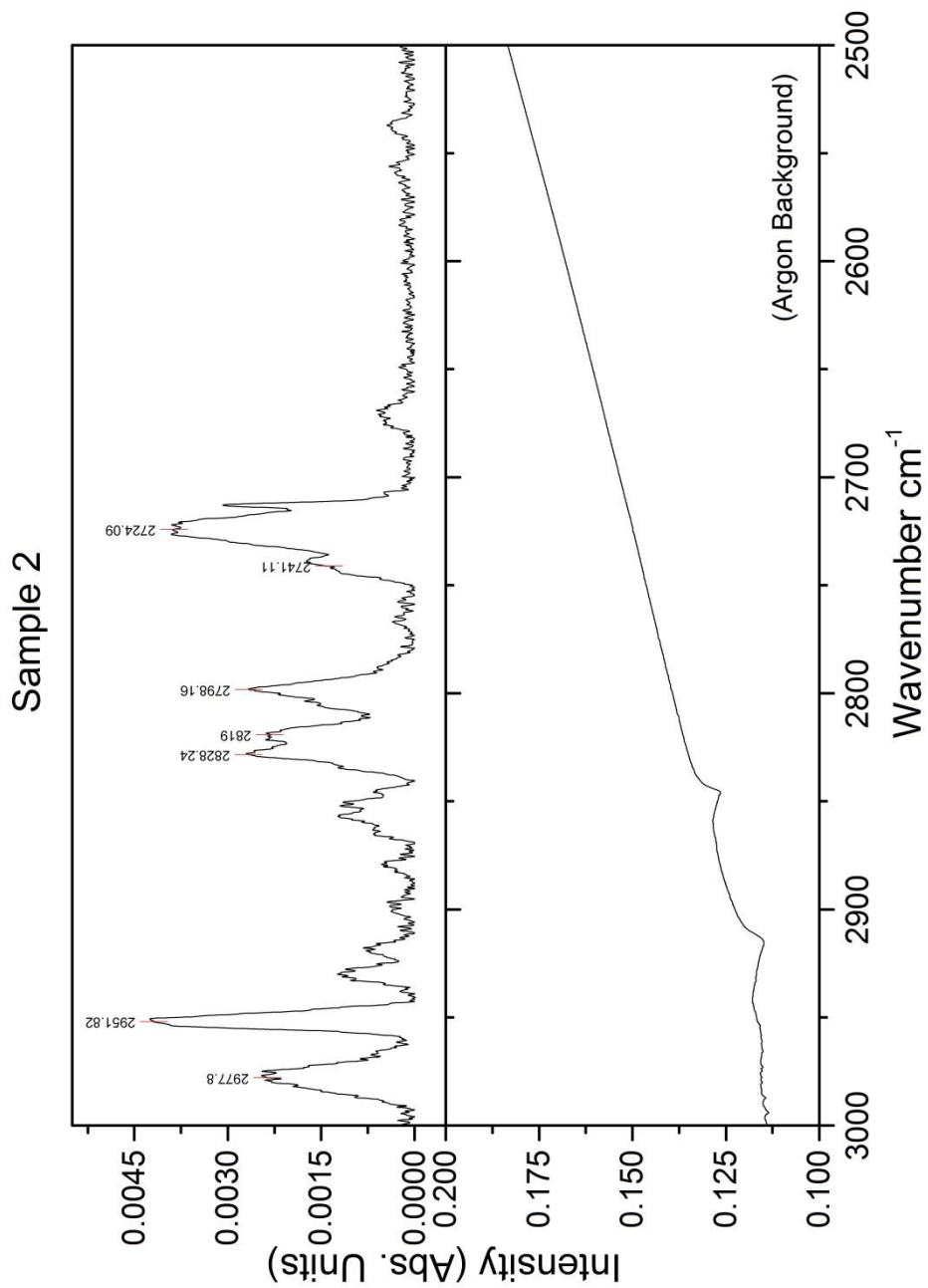


Figure 1-8d: Expanded view of Sample 2 IR spectrum,  $3000\text{-}2500 \text{ cm}^{-1}$ . Genuine signal peaks are marked to indicate position where present.

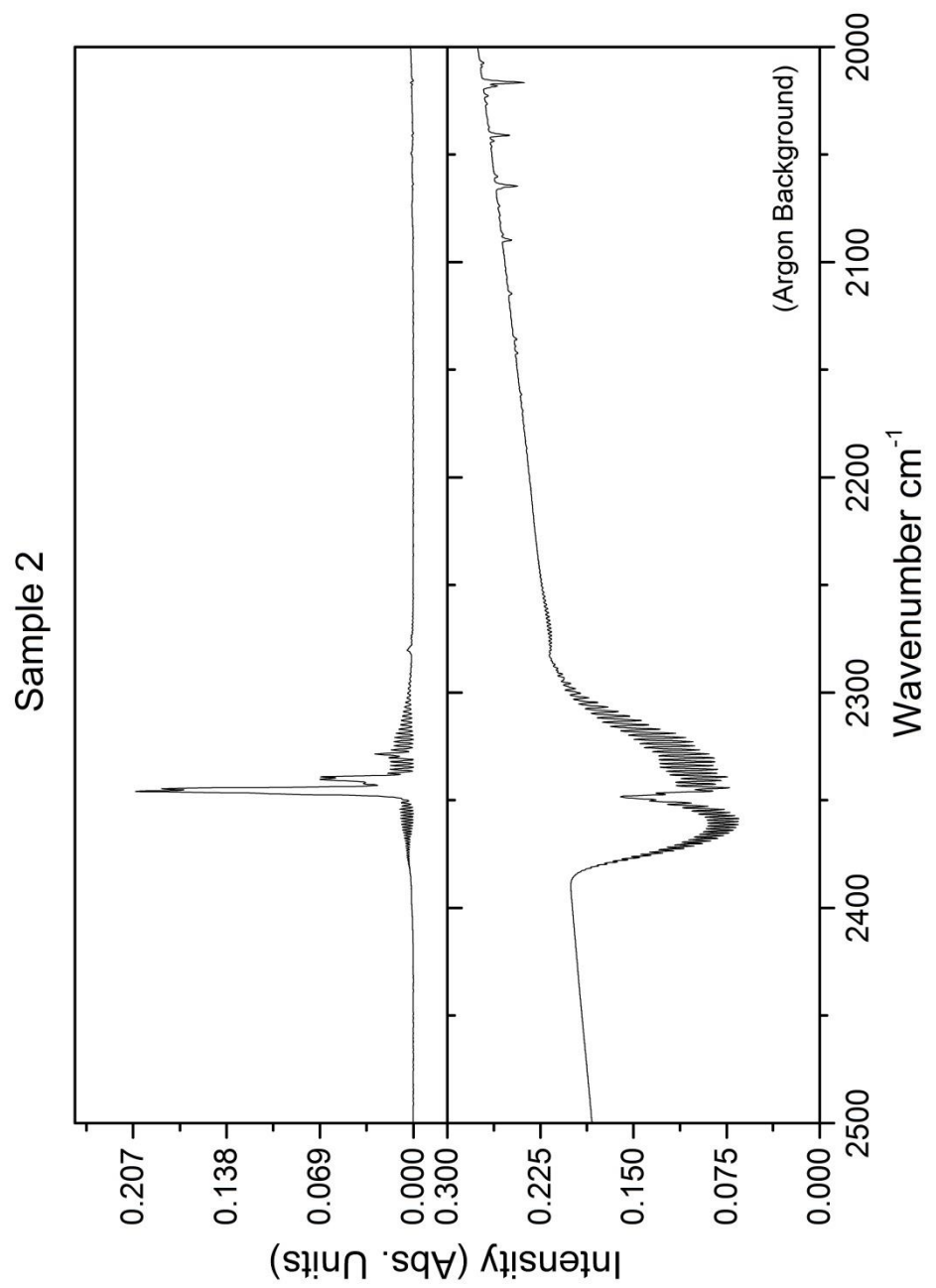


Figure 1-8e: Expanded view of Sample 2 IR spectrum,  $2500\text{-}2000 \text{ cm}^{-1}$ . Genuine signal peaks are marked to indicate position where present.

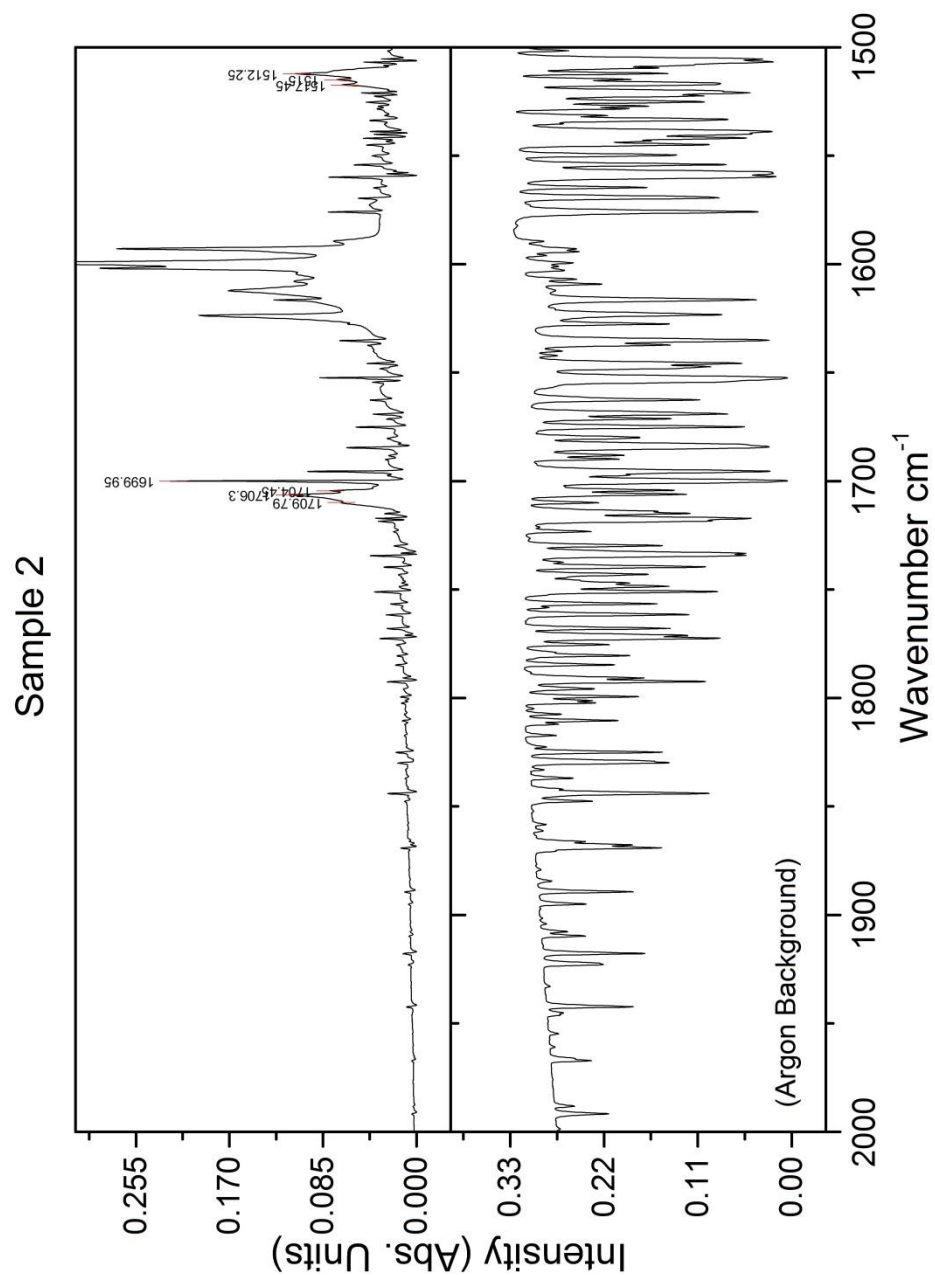
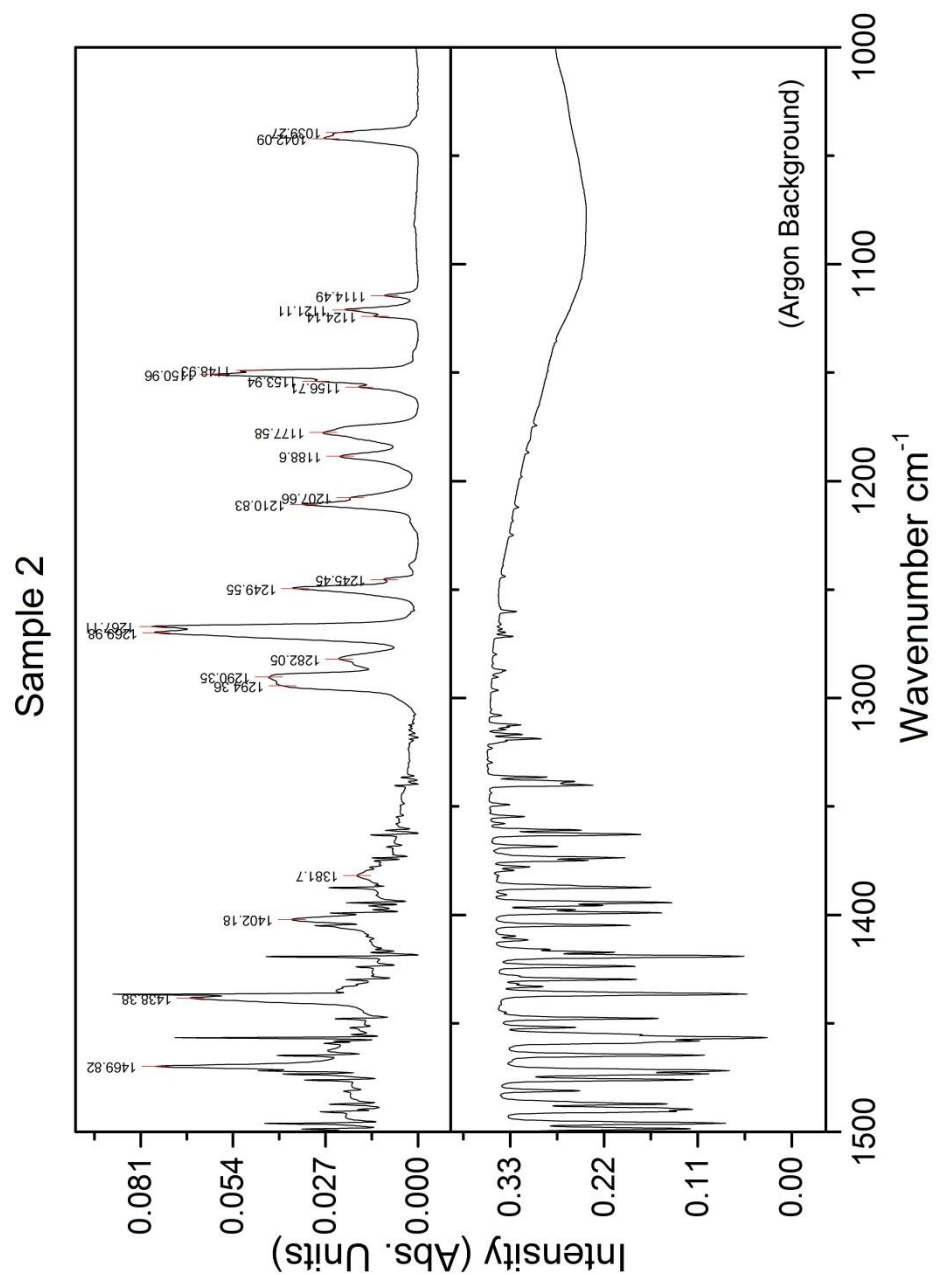
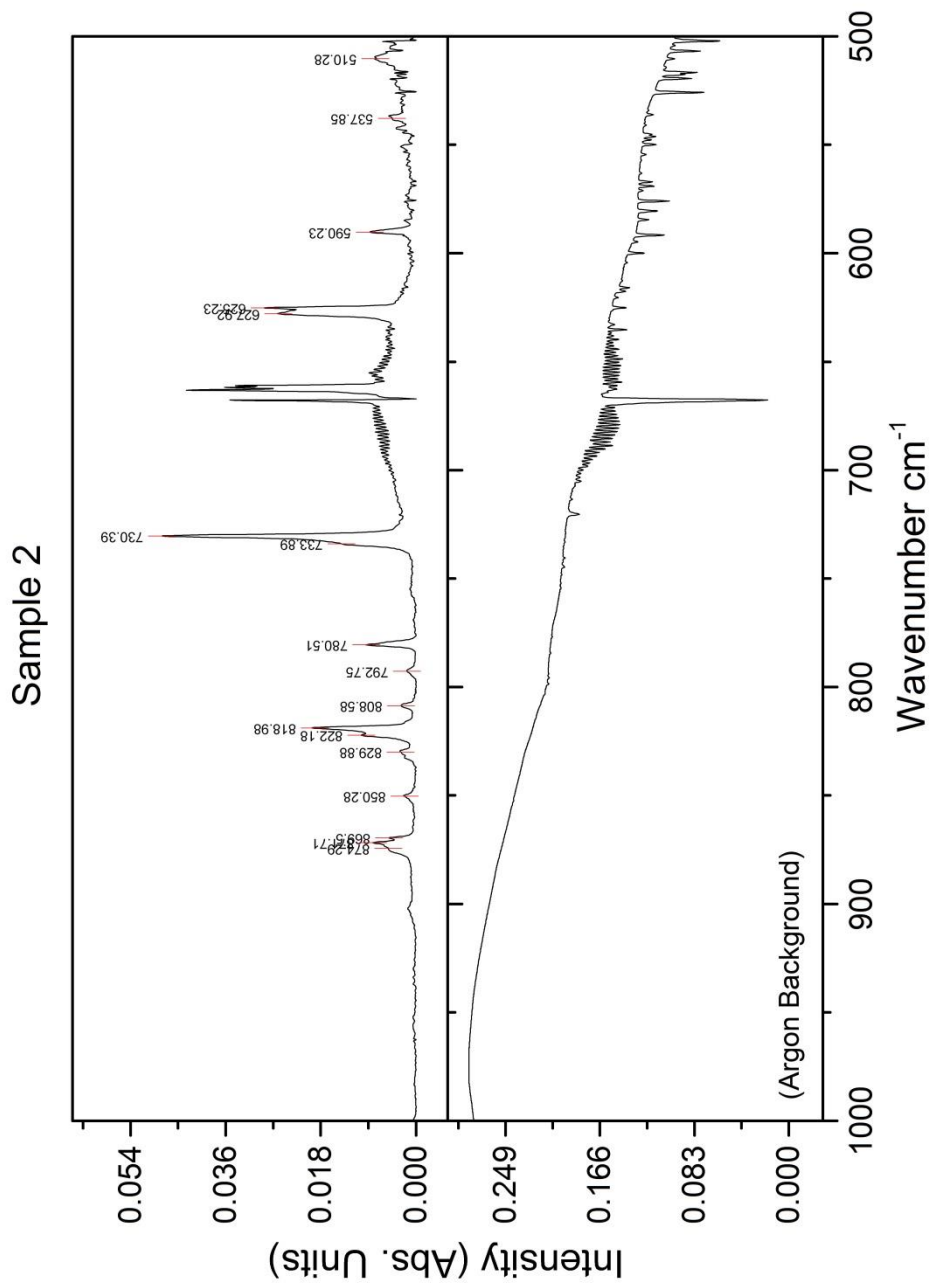


Figure 1-8f: Expanded view of Sample 2 IR spectrum,  $2000\text{-}1500 \text{ cm}^{-1}$ . Genuine signal peaks are marked to indicate position where present.



*Figure 1-8g: Expanded view of Sample 2 IR spectrum, 1500-1000  $\text{cm}^{-1}$ . Genuine signal peaks are marked to indicate position where present.*



*Figure 1-8h: Expanded view of Sample 2 IR spectrum, 1000-500  $\text{cm}^{-1}$ . Genuine signal peaks are marked to indicate position where present.*

<b>Position</b>	<b>FWHM (cm<sup>-1</sup>)</b>	<b>Intensity (Abs. Units)</b>
510.28	0.005	6.21
537.85	0.003	3.19
590.23	0.008	2.62
625.23	0.025	1.42
627.92	0.023	2.54
730.39	0.047	1.95
733.89	0.013	2.69
780.51	0.009	2.31
792.75	0.002	3.21
808.58	0.003	2.67
818.98	0.019	2.22
822.18	0.010	3.02
829.88	0.003	3.37
850.28	0.002	2.55
869.50	0.004	1.77
871.71	0.005	1.47
874.29	0.005	6.34
1039.27	0.018	2.20
1042.09	0.027	3.71
1114.49	0.009	2.48
1121.11	0.021	2.87
1124.14	0.011	1.89
1148.93	0.036	1.53
1150.96	0.059	2.72
1153.94	0.027	2.30
1156.71	0.016	2.12
1177.58	0.027	6.71
1188.60	0.023	4.26
1207.66	0.018	2.89
1210.83	0.032	2.70
1245.45	0.009	2.69
1249.55	0.036	3.42
1267.11	0.065	2.19
1269.98	0.074	3.31
1282.05	0.017	6.98
1290.35	0.037	4.27
1294.36	0.032	3.86
1381.70	0.008	5.77
1402.18	0.030	3.86
1438.38	0.054	4.54
1469.82	0.059	2.60
1512.25	0.083	2.45
1515.00	0.043	1.96
1517.45	0.041	1.80
1699.95	0.211	0.52
1704.45	0.065	1.31
1706.30	0.097	1.46
1709.79	0.057	3.58
2724.09	0.004	16.60
2741.11	0.002	8.01
2798.16	0.003	9.60
2819.00	0.002	9.10
2828.24	0.002	8.31
2951.82	0.004	8.10

2977.80	0.002	15.29
3008.84	0.003	5.31
3016.47	0.002	6.28
3554.41	0.057	14.71

Table 1-4: Integrated Gaussian fitting parameters for signal peaks in Sample 2.

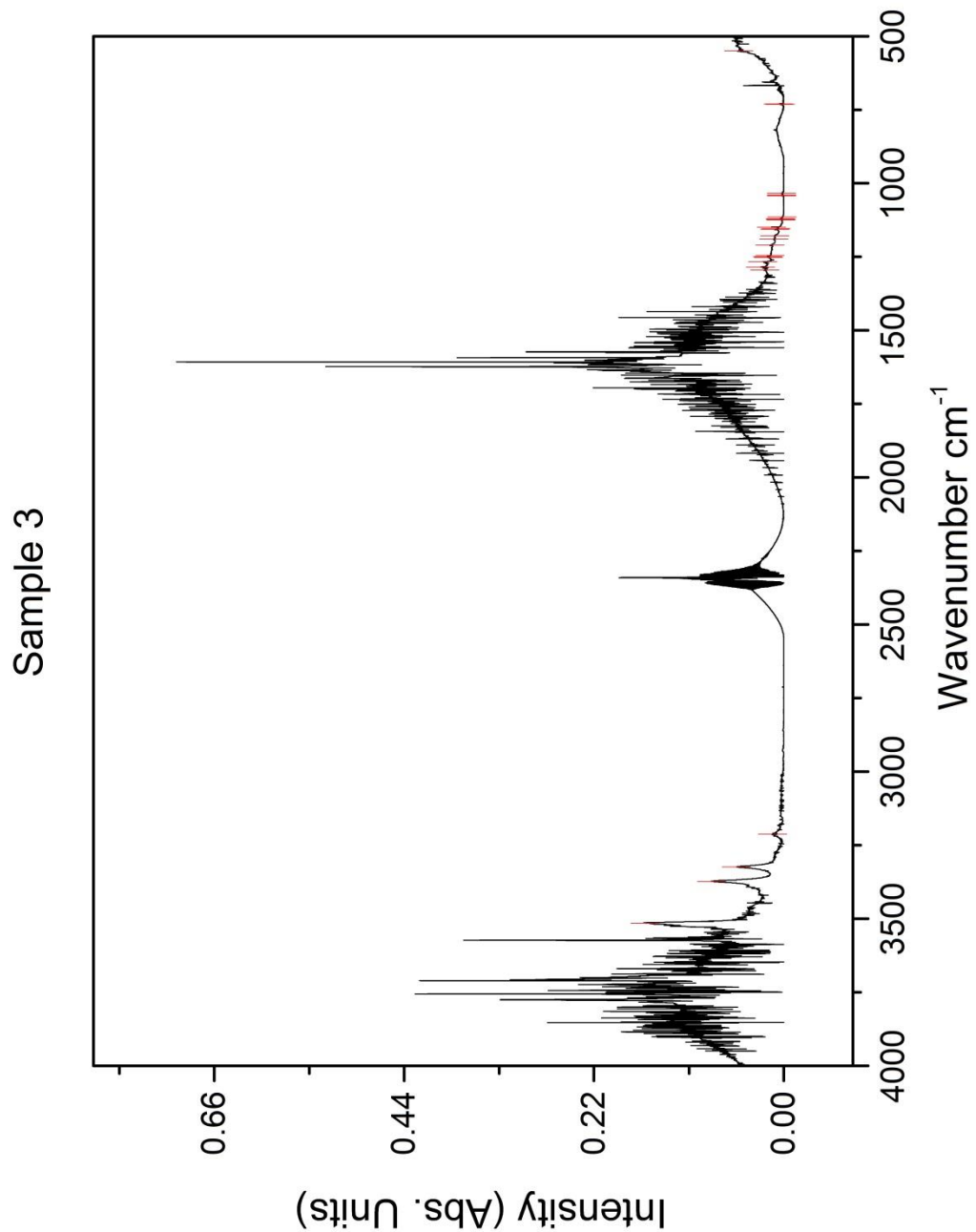
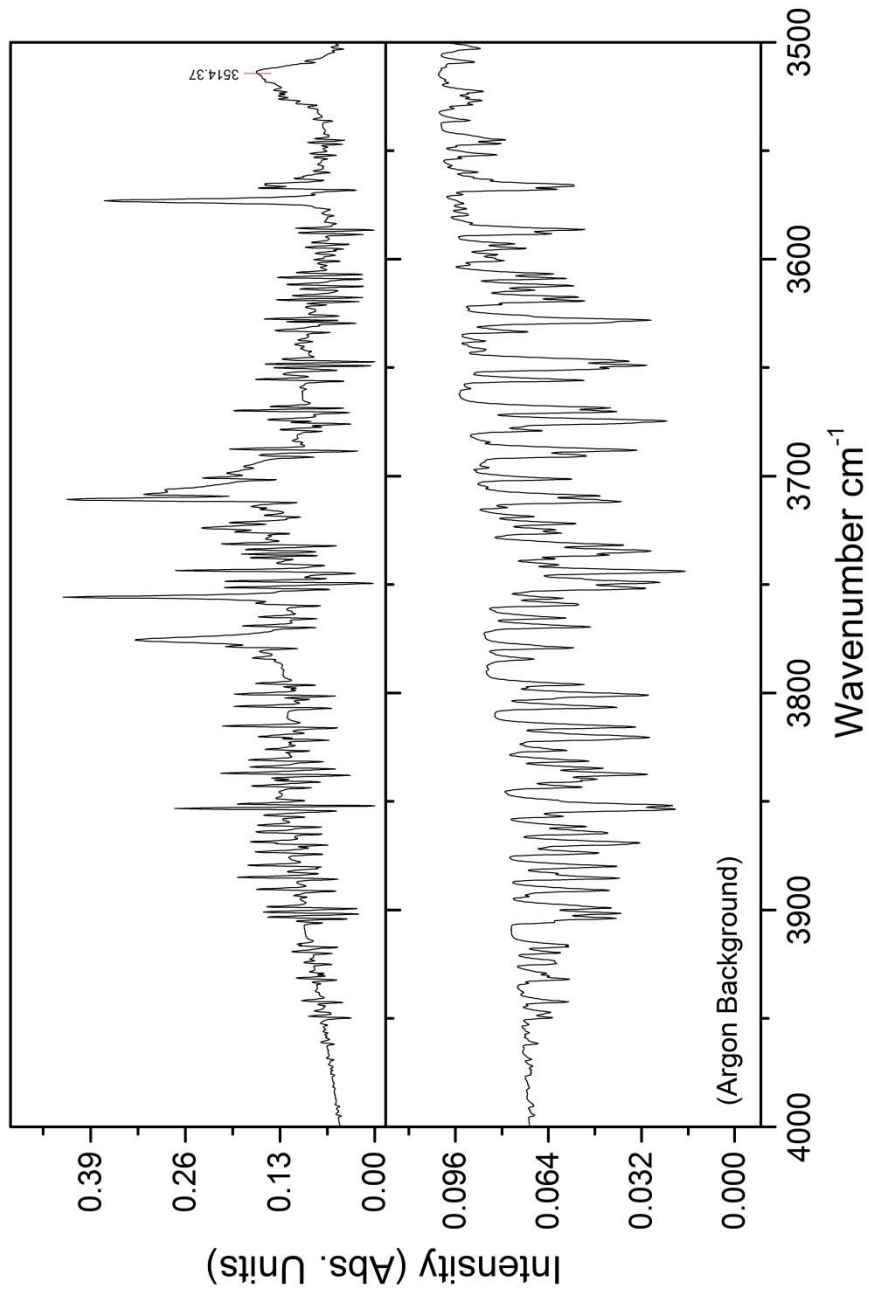


Figure 1-9a: Overview of Sample 3 IR spectrum, 4000-500 cm<sup>-1</sup>.

Sample 3



*Figure 1-9b: Expanded view of Sample 3 IR spectrum, 4000-3500 cm<sup>-1</sup>. Genuine signal peaks are marked to indicate position where present.*

Sample 3

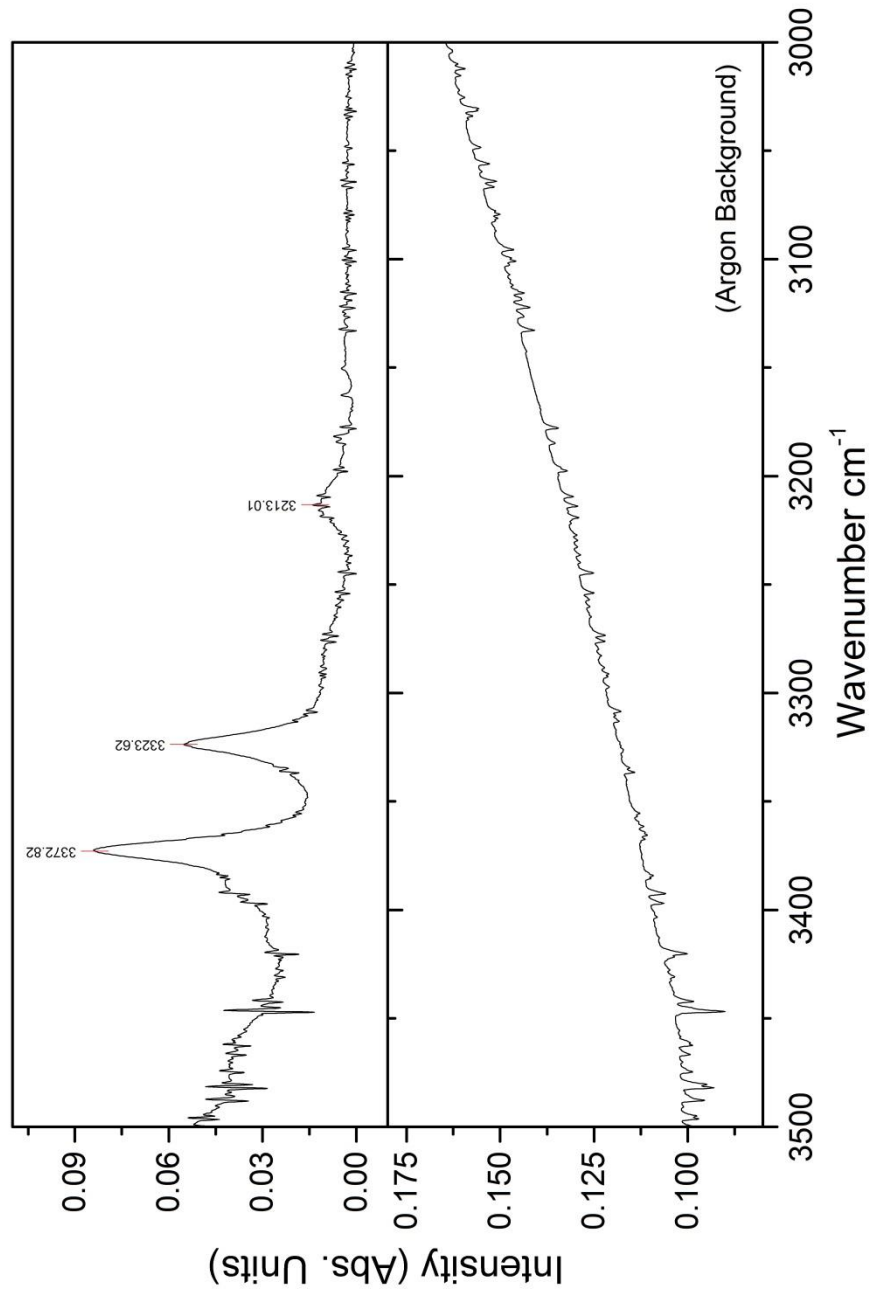
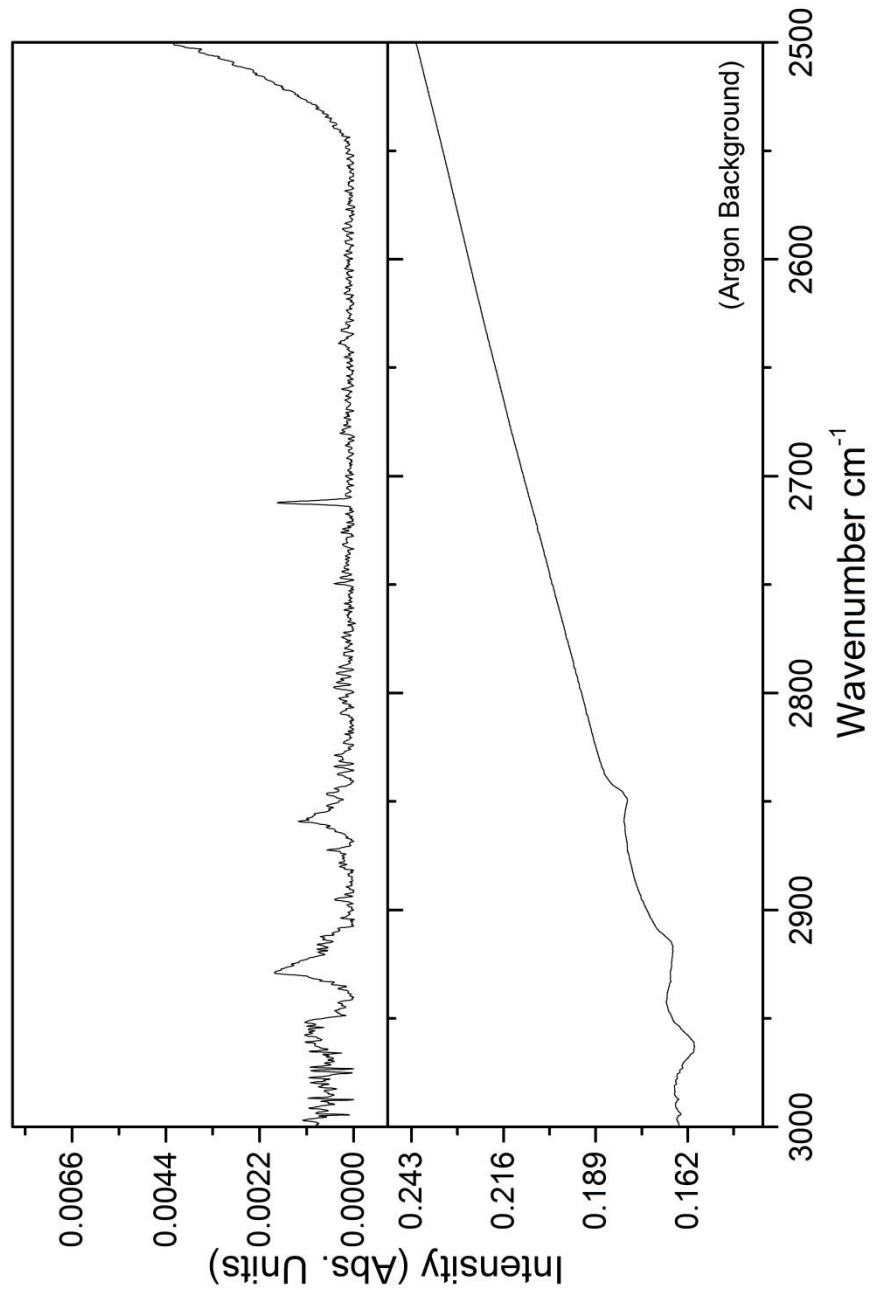


Figure 1-9c: Expanded view of Sample 3 IR spectrum,  $3500\text{-}3000 \text{ cm}^{-1}$ . Genuine signal peaks are marked to indicate position where present.

Sample 3



*Figure 1-9d: Expanded view of Sample 3 IR spectrum,  $3000\text{-}2500\text{ } \text{cm}^{-1}$ . Genuine signal peaks are marked to indicate position where present.*

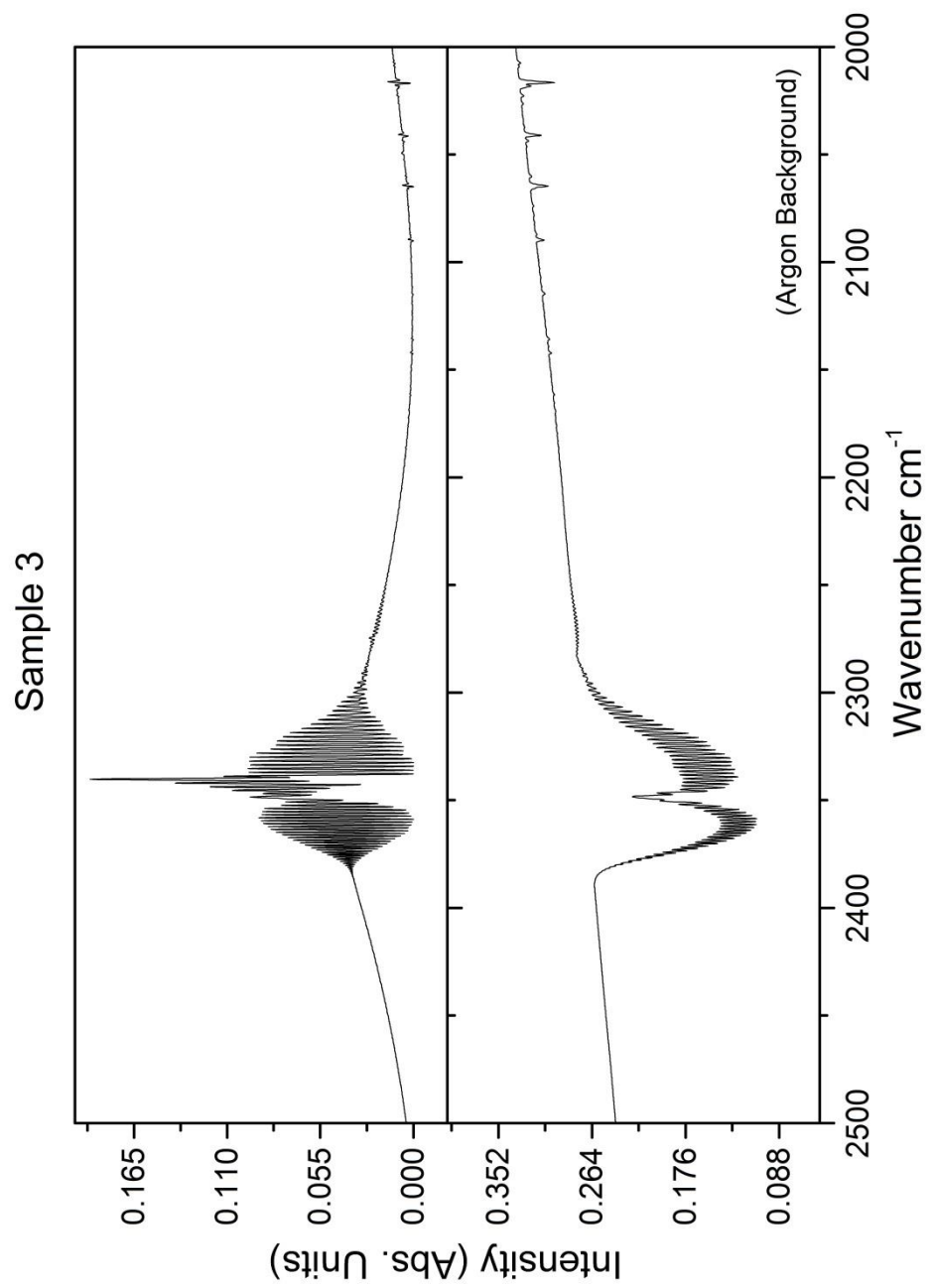


Figure 1-9e: Expanded view of Sample 3 IR spectrum,  $2500\text{-}2000 \text{ cm}^{-1}$ . Genuine signal peaks are marked to indicate position where present.

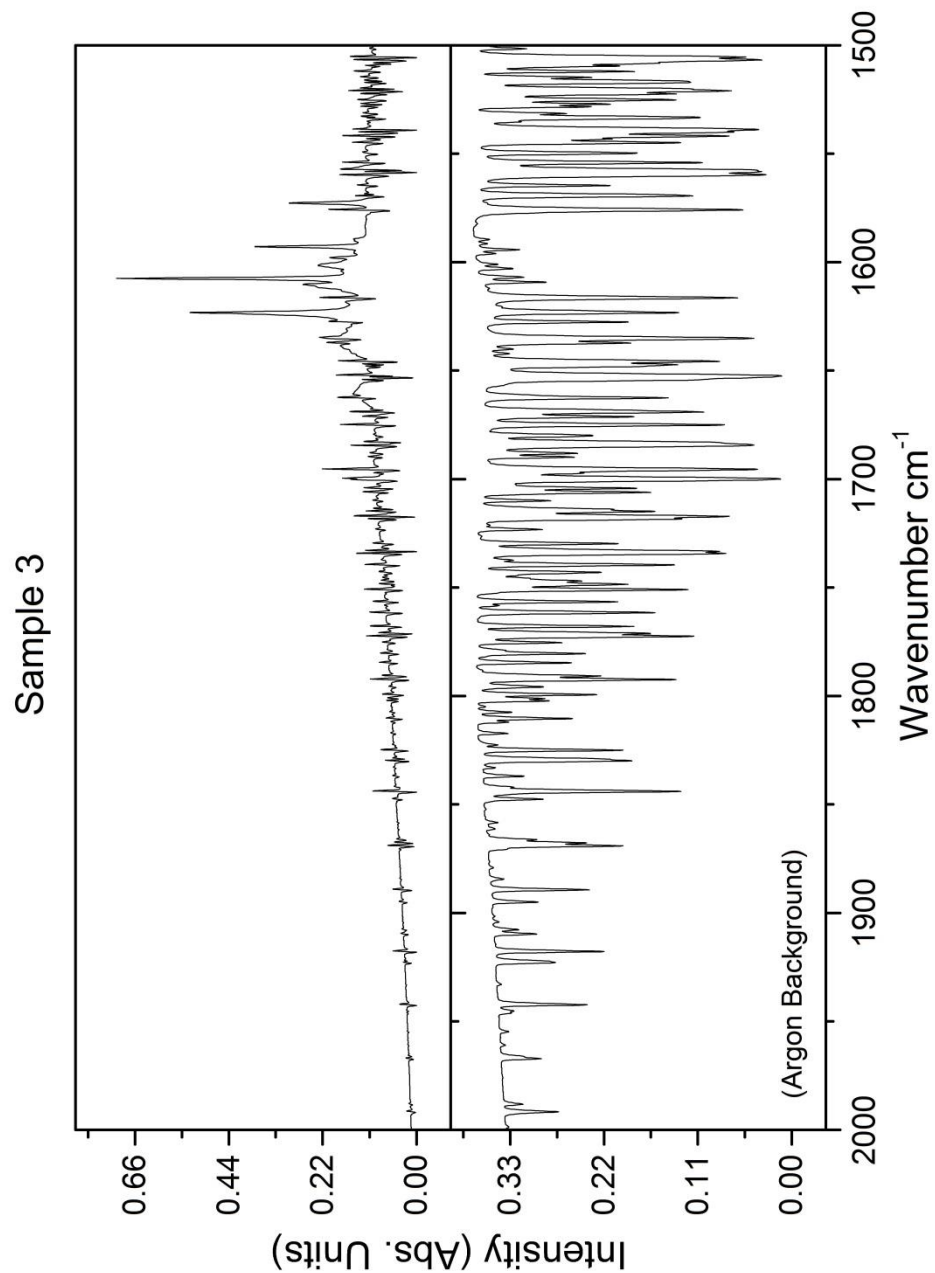
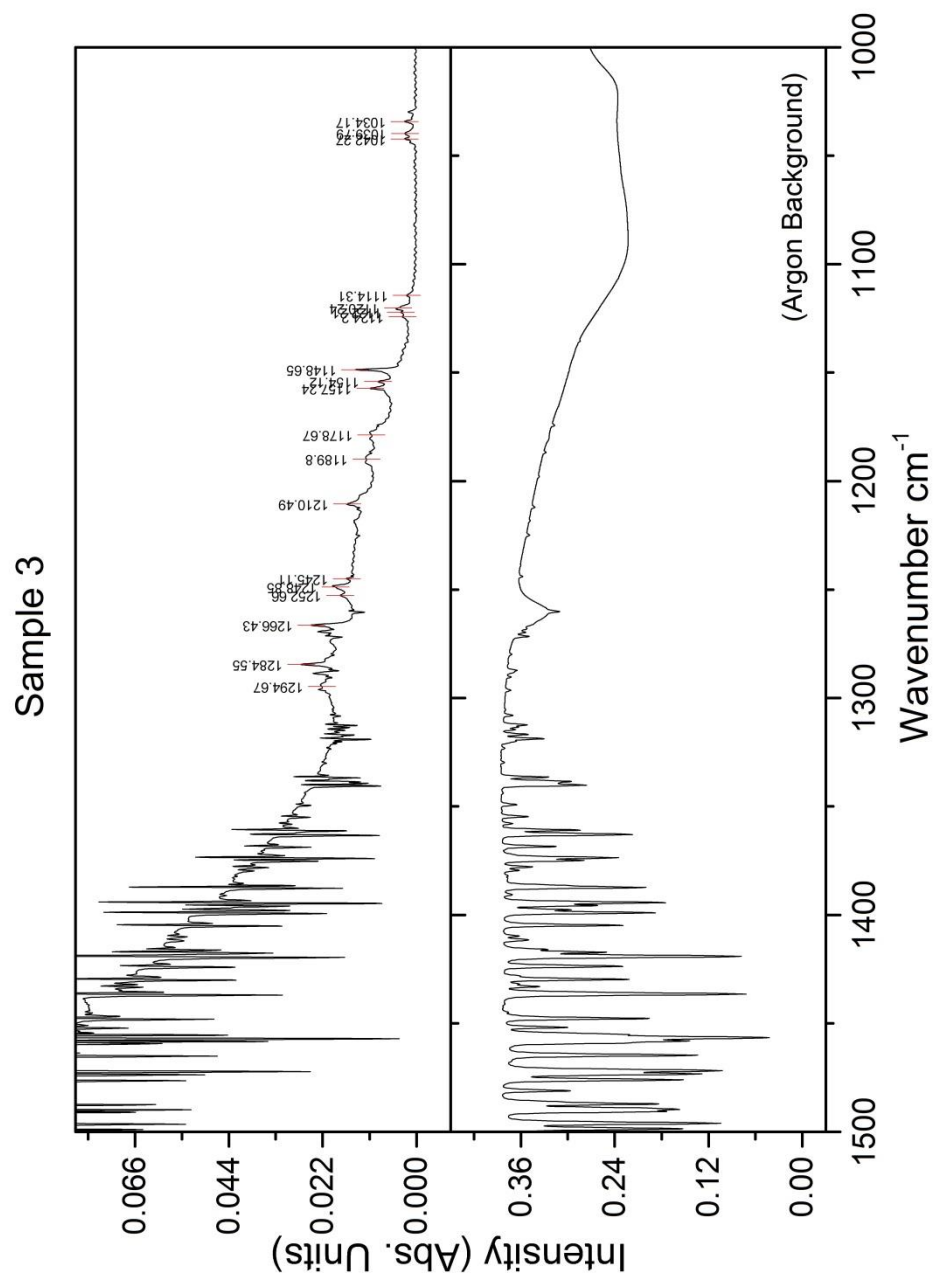


Figure 1-9f: Expanded view of Sample 3 IR spectrum,  $2000\text{-}1500 \text{ cm}^{-1}$ . Genuine signal peaks are marked to indicate position where present.



*Figure 1-9g: Expanded view of Sample 3 IR spectrum, 1500-1000 cm<sup>-1</sup>. Genuine signal peaks are marked to indicate position where present.*

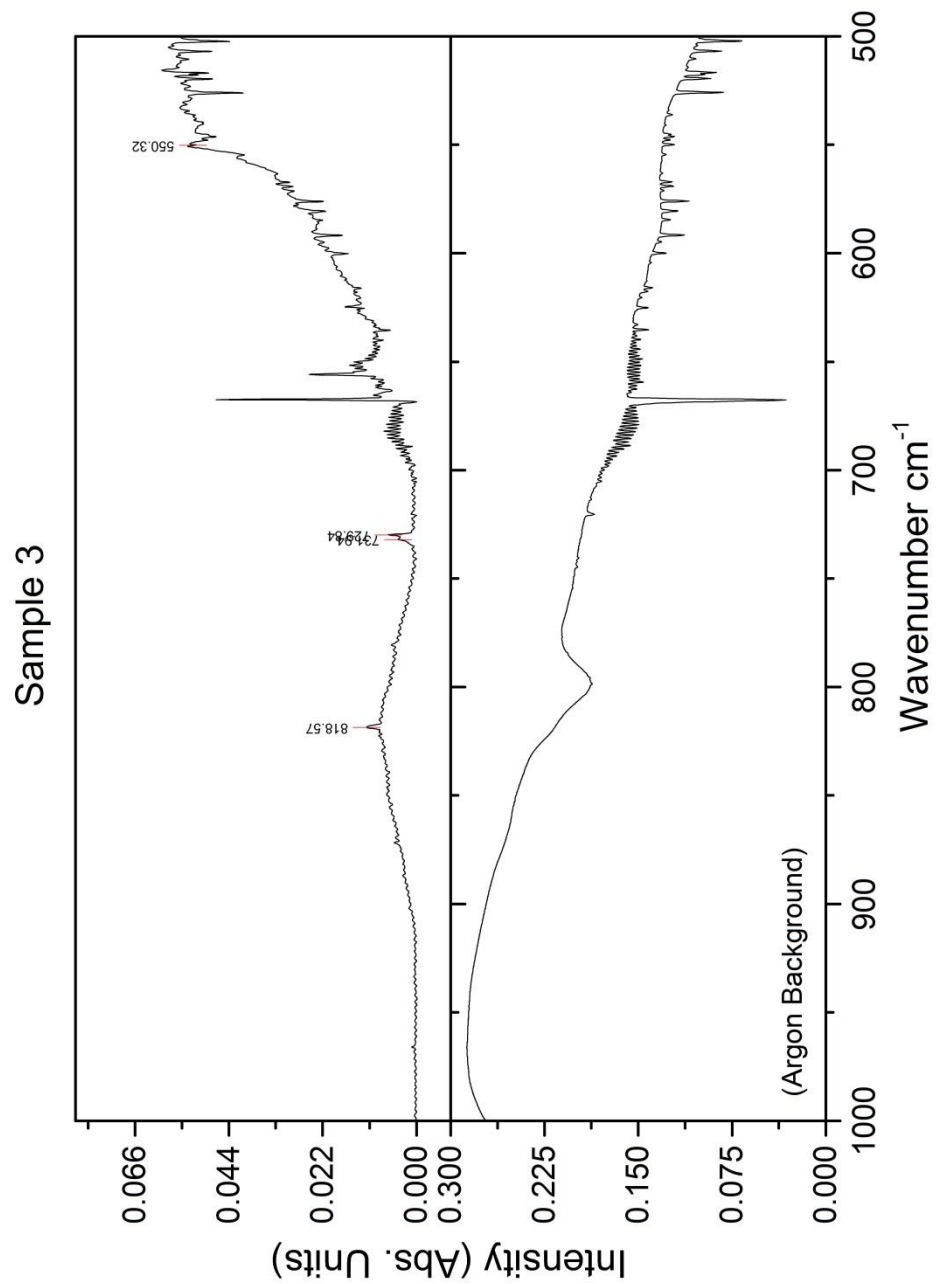


Figure 1-9h: Expanded view of Sample 3 IR spectrum,  $1000\text{-}500 \text{ cm}^{-1}$ . Genuine signal peaks are marked to indicate position where present.

<b>Position</b>	<b>FWHM (cm<sup>-1</sup>)</b>	<b>Intensity (Abs. Units)</b>
495.30	0.011	1.57
550.32	0.014	5.98
729.84	0.005	1.11
731.94	0.003	1.39
818.57	0.004	1.58
1034.17	0.003	1.40
1039.79	0.003	1.80
1042.27	0.002	1.26
1114.31	0.001	1.96
1120.24	0.003	1.98
1122.21	0.001	1.26
1124.20	0.001	2.76
1148.65	0.009	1.05
1154.12	0.003	1.25
1157.24	0.004	1.30
1178.67	0.003	8.90
1189.76	0.002	6.90
1210.49	0.005	2.75
1245.11	0.001	0.85
1248.85	0.004	2.40
1252.66	0.002	1.90
1266.43	0.007	1.15
1284.55	0.008	1.30
1294.67	0.003	5.45
3213.01	0.012	19.70
3323.62	0.040	12.30
3372.82	0.067	11.70
3514.37	0.108	9.30

*Table 1-5: Integrated Gaussian fitting parameters for signal peaks in Sample 3.*

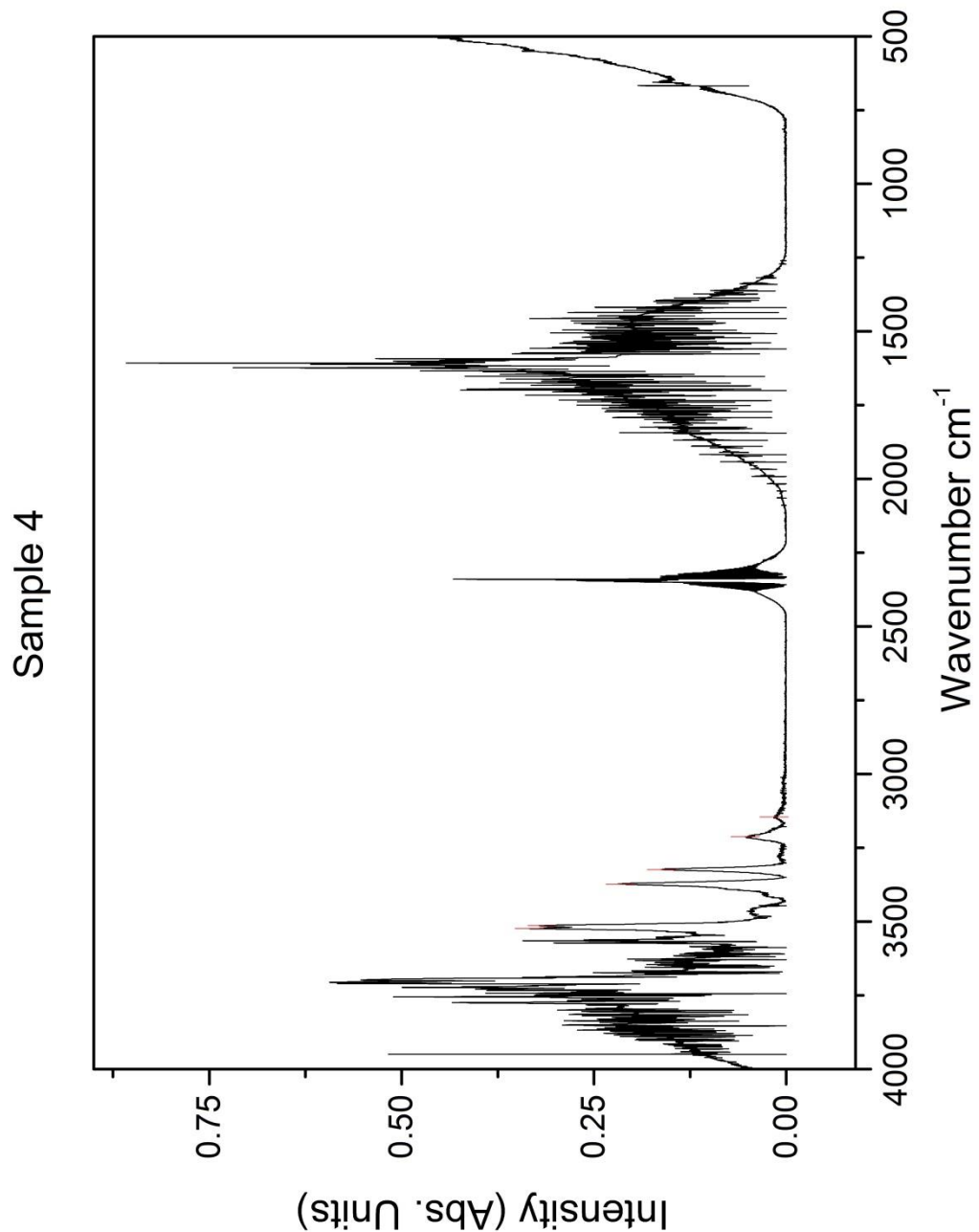


Figure 1-10a: Overview of Sample 4 IR spectrum, 4000-500  $\text{cm}^{-1}$ .

Sample 4

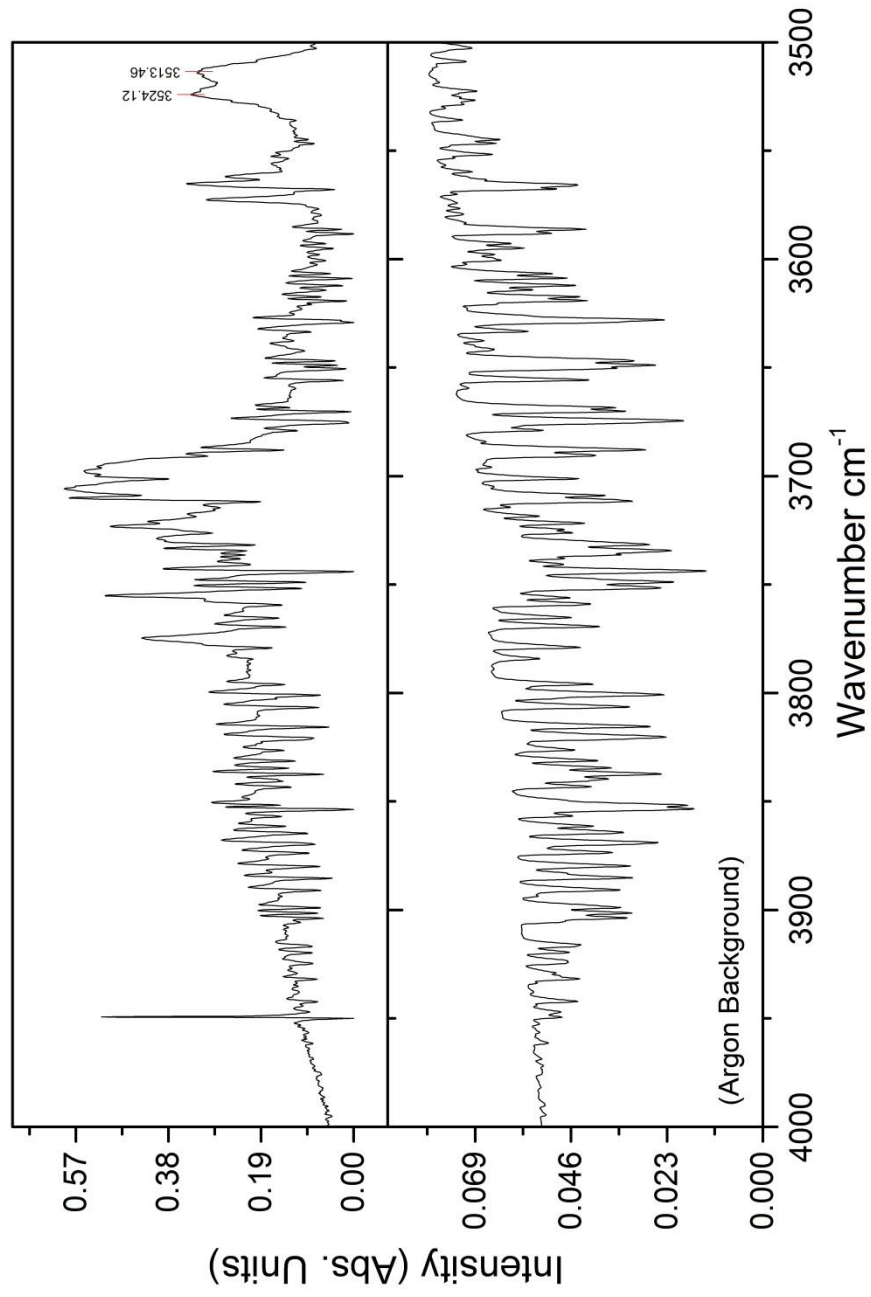


Figure 1-10b: Expanded view of Sample 4 IR spectrum,  $4000\text{-}3500 \text{ cm}^{-1}$ . Genuine signal peaks are marked to indicate position where present.

Sample 4

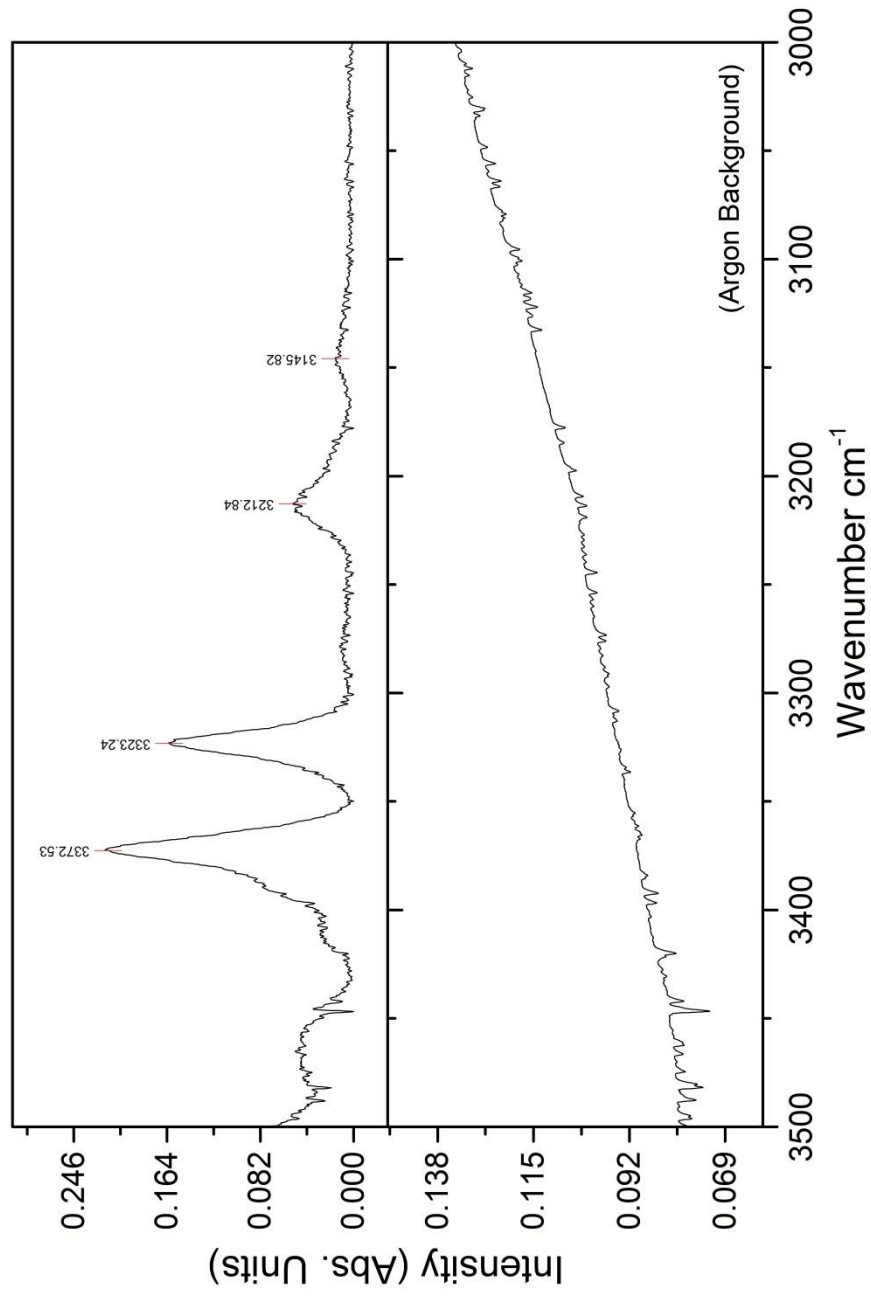
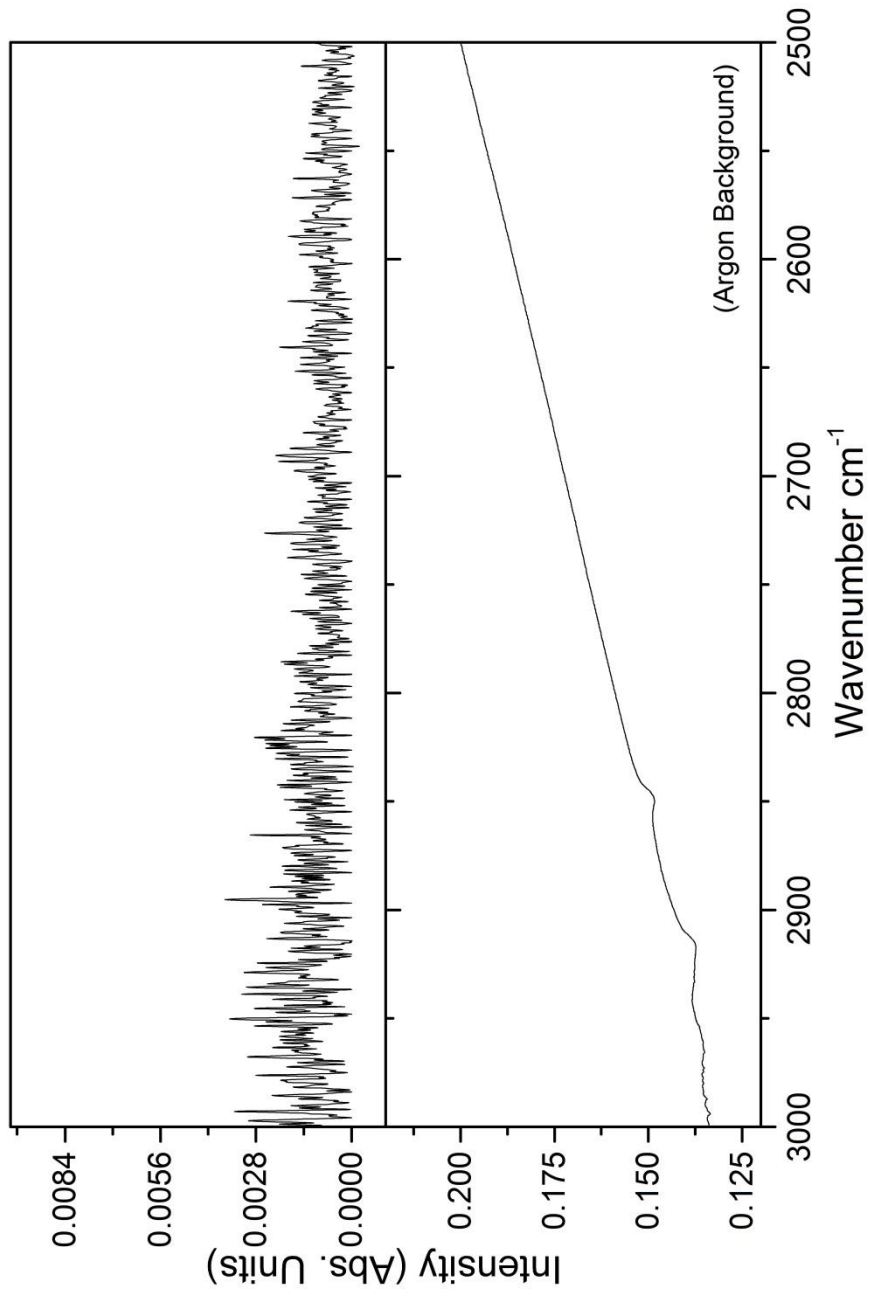


Figure 1-10c: Expanded view of Sample 4 IR spectrum,  $3500\text{-}3000 \text{ cm}^{-1}$ . Genuine signal peaks are marked to indicate position where present.

Sample 4



*Figure 1-10d: Expanded view of Sample 4 IR spectrum, 3000-2500 cm<sup>-1</sup>. Genuine signal peaks are marked to indicate position where present.*

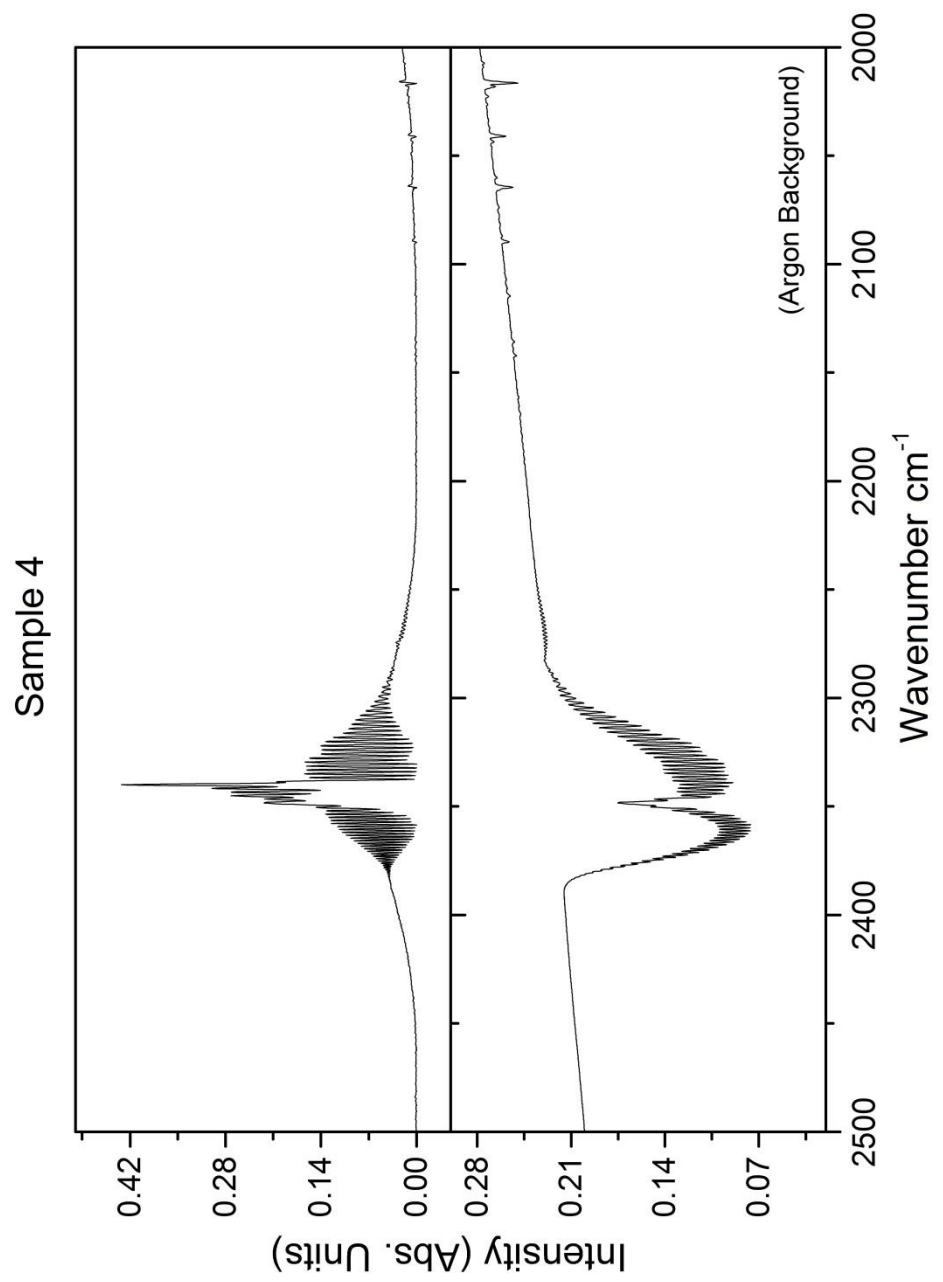
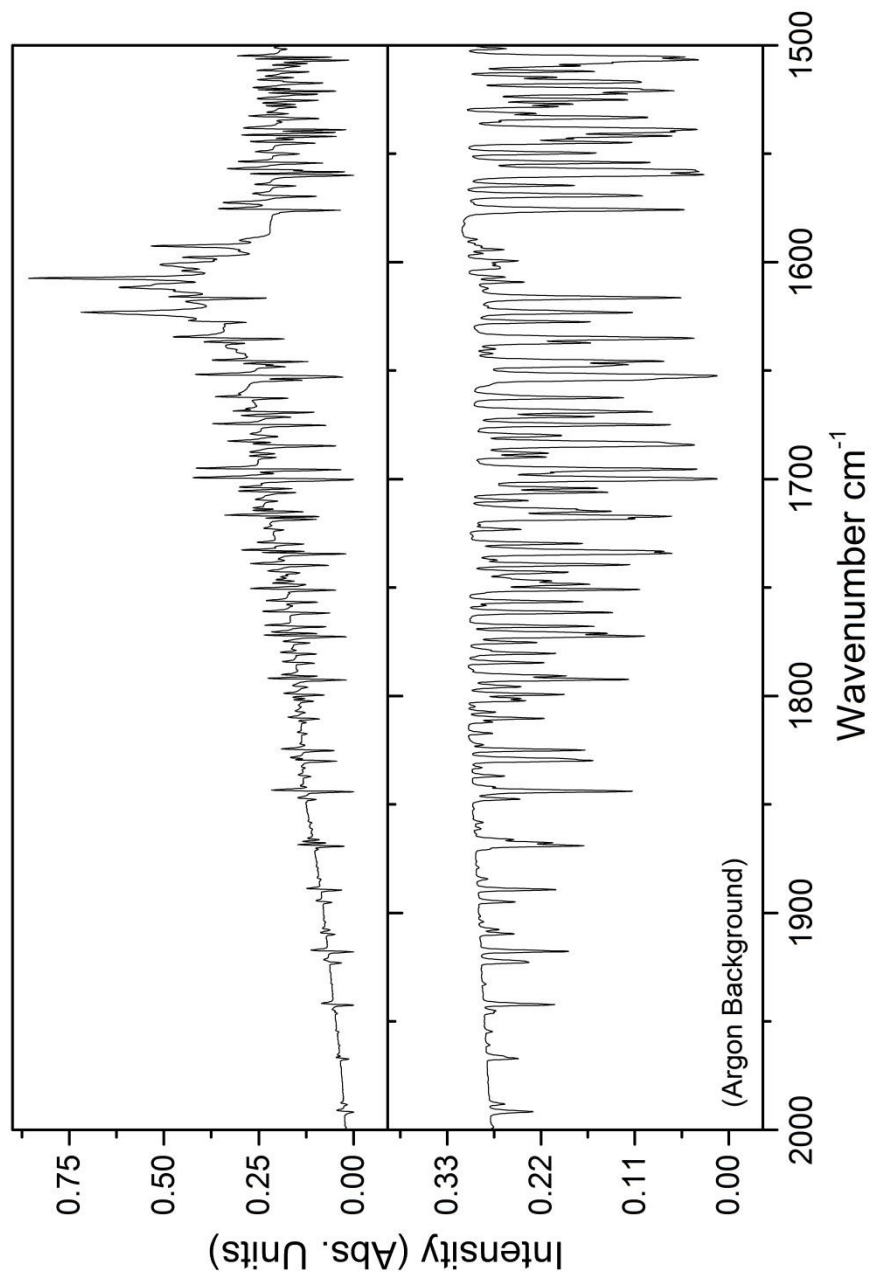


Figure 1-10e: Expanded view of Sample 4 IR spectrum, 2500-2000 cm<sup>-1</sup>. Genuine signal peaks are marked to indicate position where present.

Sample 4



*Figure 1-10f: Expanded view of Sample 4 IR spectrum, 2000-1500 cm<sup>-1</sup>. Genuine signal peaks are marked to indicate position where present.*

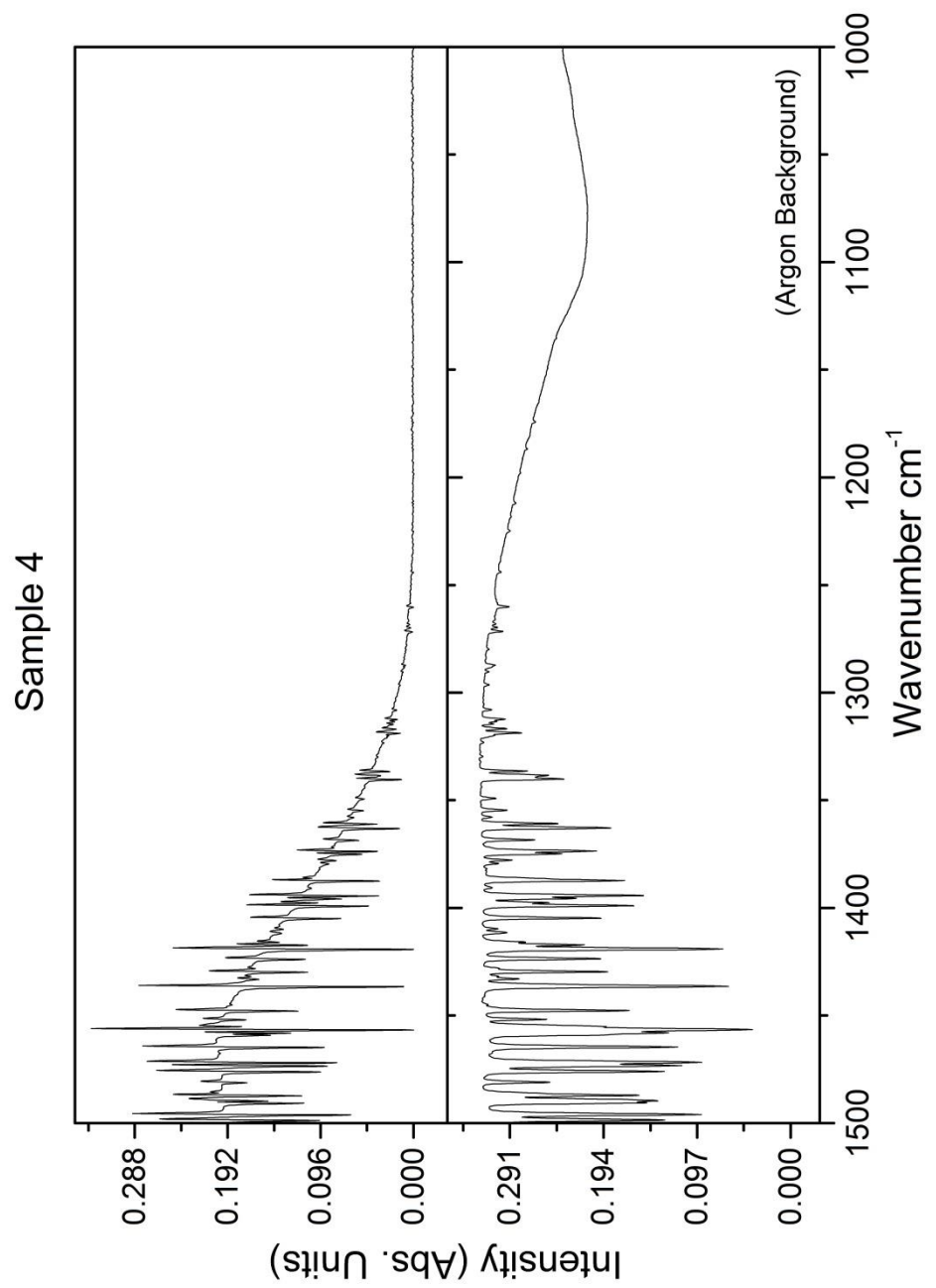


Figure 1-10g: Expanded view of Sample 4 IR spectrum,  $1500\text{-}1000 \text{ cm}^{-1}$ . Genuine signal peaks are marked to indicate position where present.

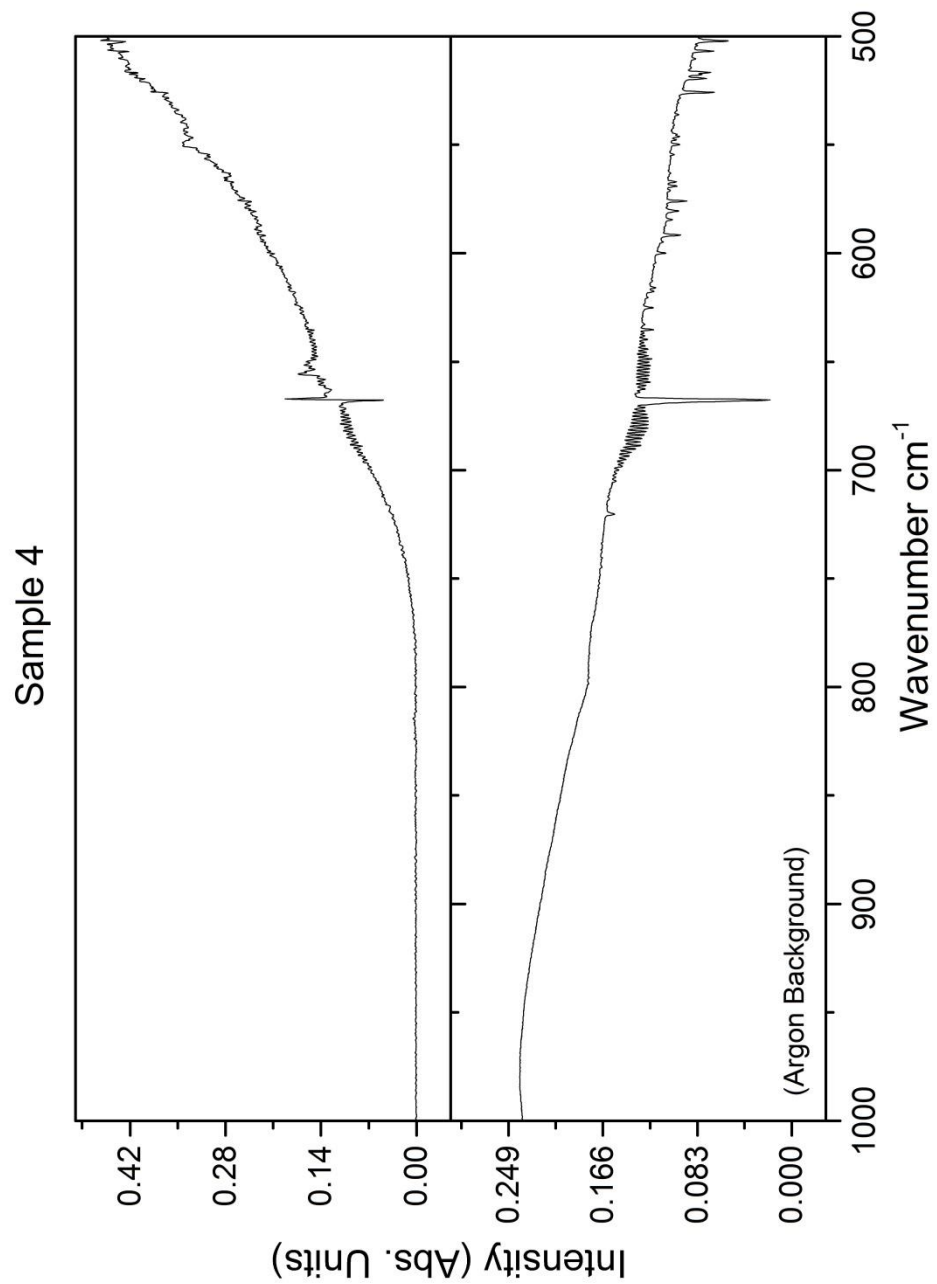


Figure 1-10h: Expanded view of Sample 4 IR spectrum, 1000-500 cm<sup>-1</sup>. Genuine signal peaks are marked to indicate position where present.

<b>Position</b>	<b>FWHM (cm<sup>-1</sup>)</b>	<b>Intensity (Abs. Units)</b>
3145.82	0.011	15.95
3212.84	0.047	23.81
3323.24	0.149	13.81
3372.53	0.202	15.31
3513.46	0.281	10.21
3524.12	0.286	9.61

*Table 1-6: Integrated Gaussian fitting parameters for signal peaks in Sample 4.*

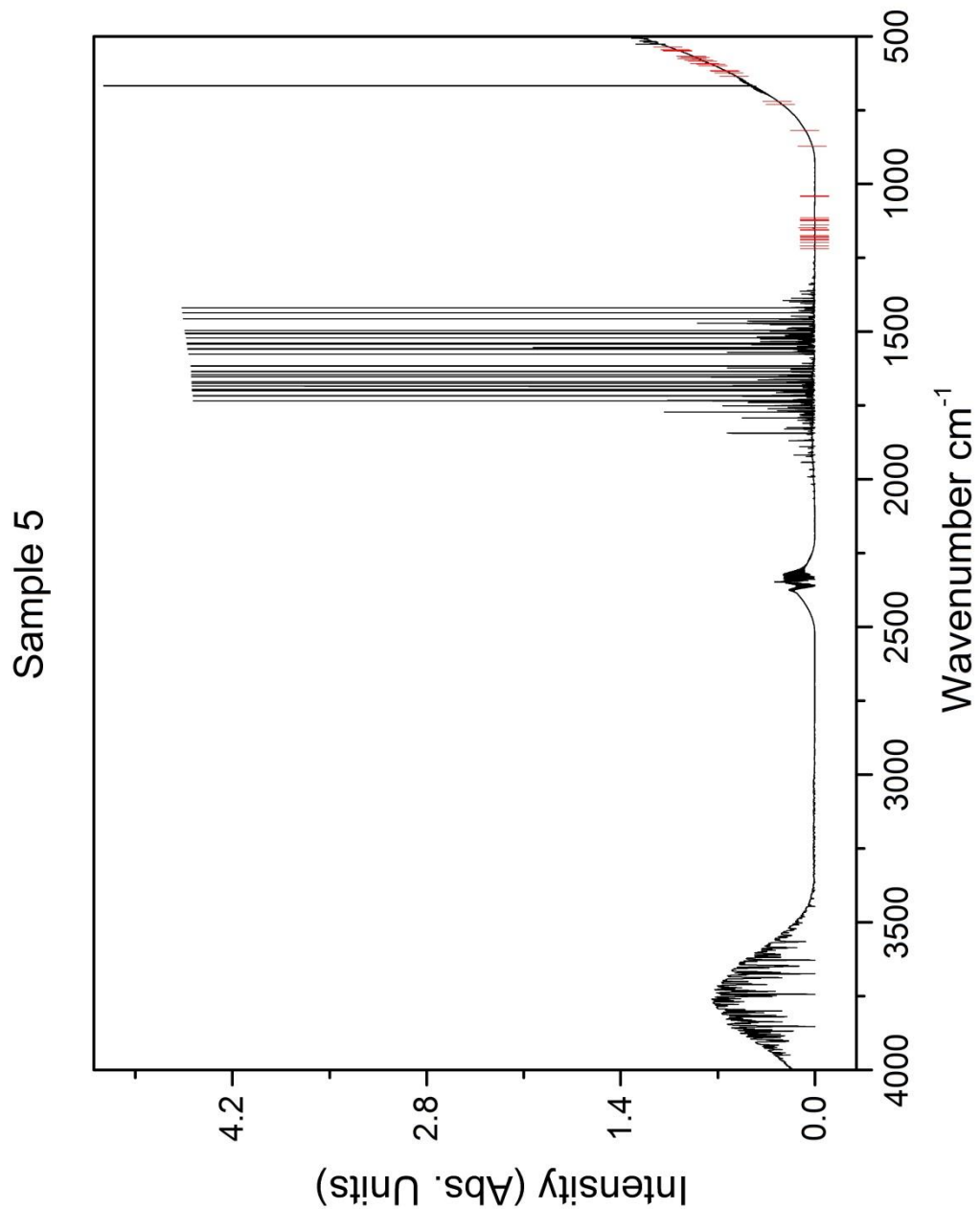


Figure 1-11a: Overview of Sample 5 IR spectrum, 4000-500 cm<sup>-1</sup>.

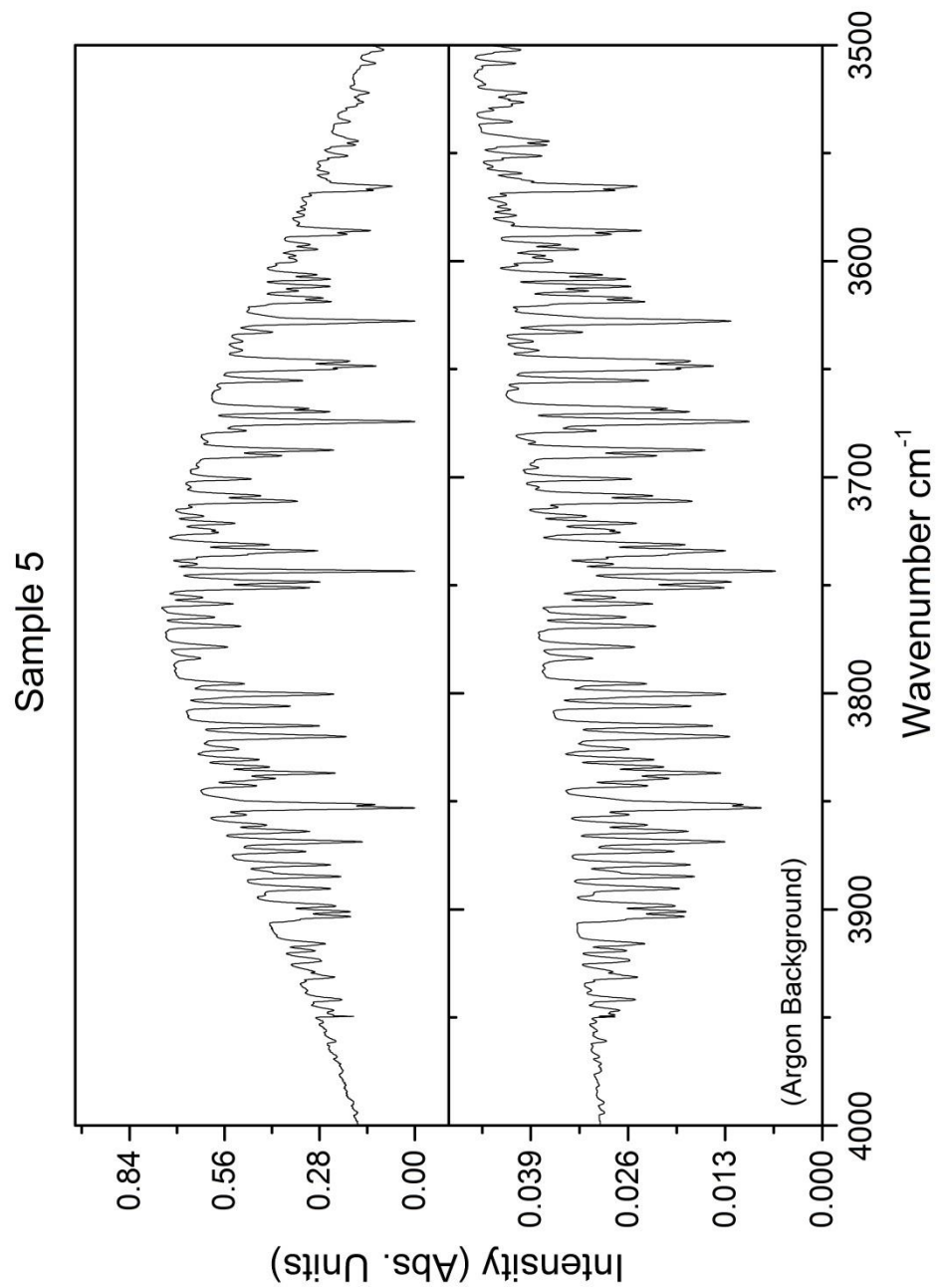


Figure 1-11b: Expanded view of Sample 5 IR spectrum,  $4000\text{-}3500 \text{ cm}^{-1}$ . Genuine signal peaks are marked to indicate position where present.

Sample 5

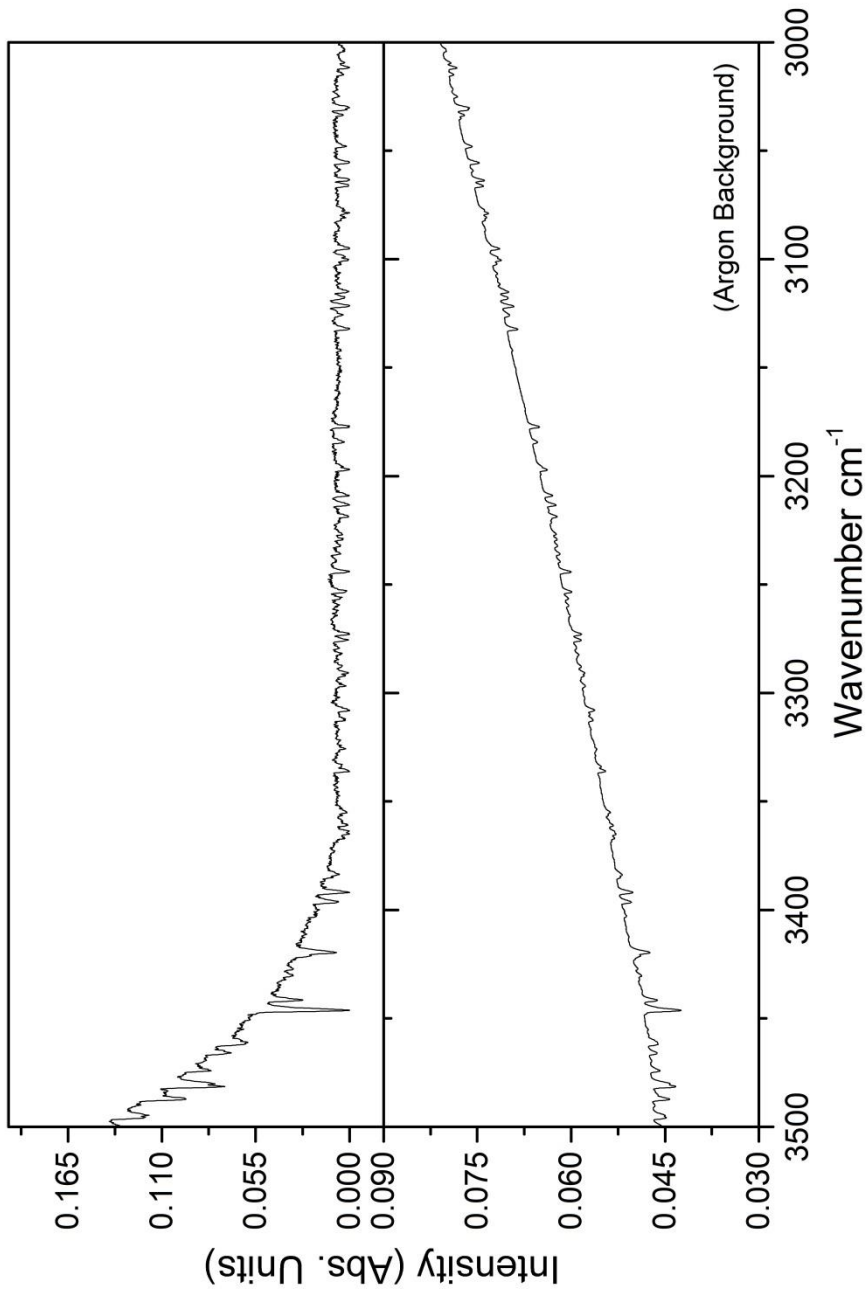


Figure 1-11c: Expanded view of Sample 5 IR spectrum,  $3500\text{-}3000 \text{ cm}^{-1}$ . Genuine signal peaks are marked to indicate position where present.

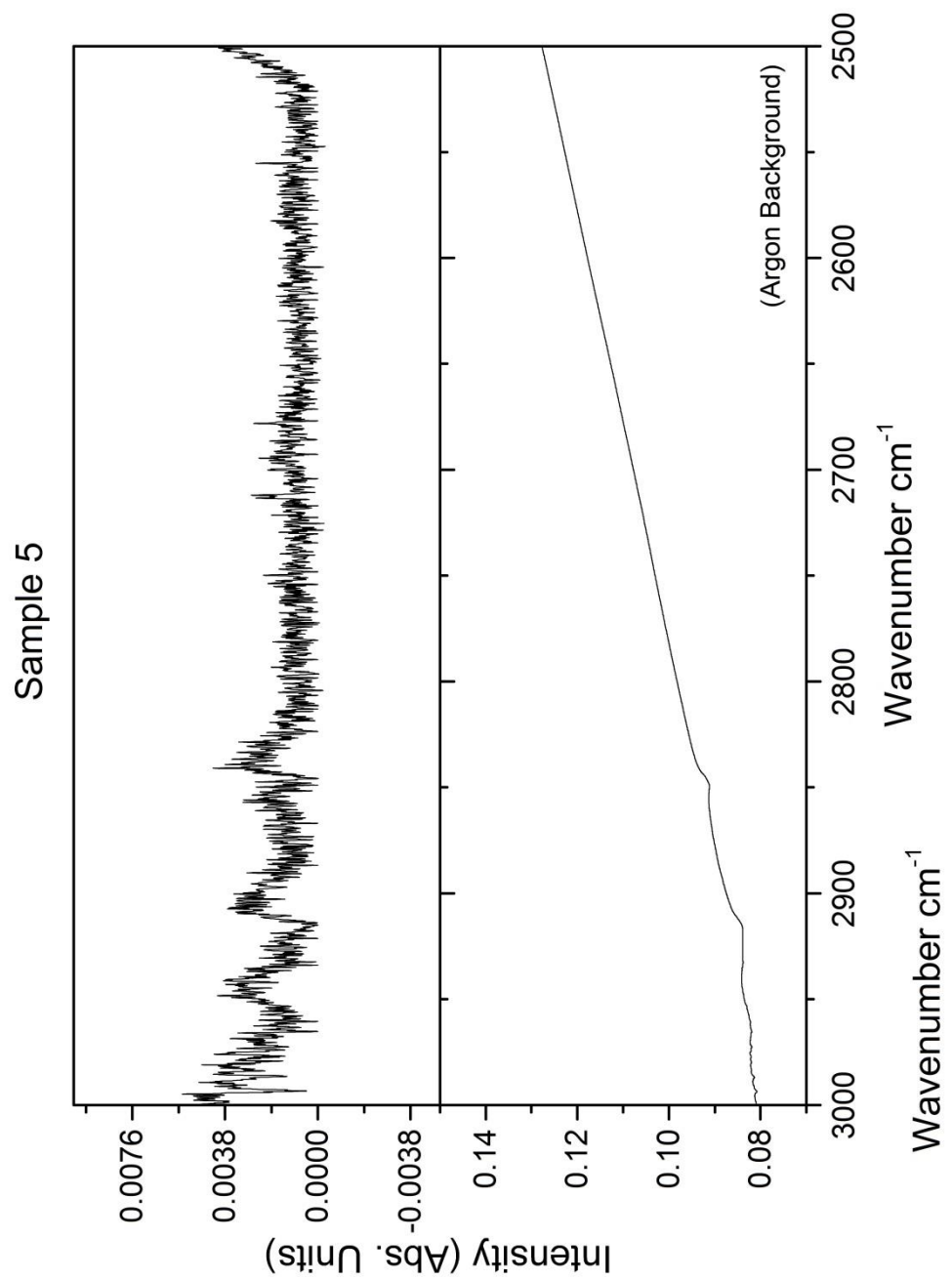


Figure 1-11d: Expanded view of Sample 5 IR spectrum,  $3000\text{-}2500\text{ cm}^{-1}$ . Genuine signal peaks are marked to indicate position where present.

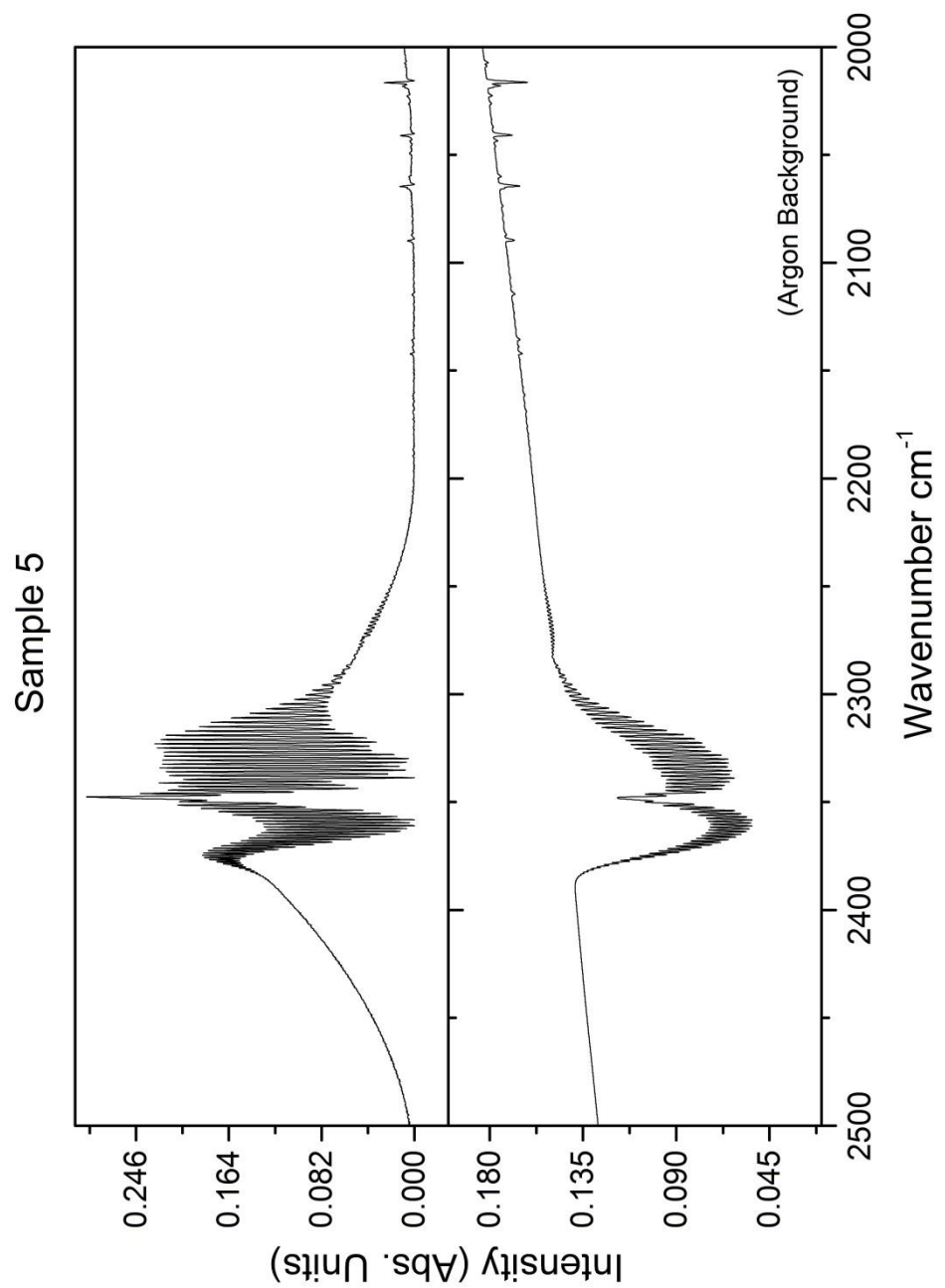


Figure 1-11e: Expanded view of Sample 5 IR spectrum,  $2500\text{-}2000\text{ cm}^{-1}$ . Genuine signal peaks are marked to indicate position where present.

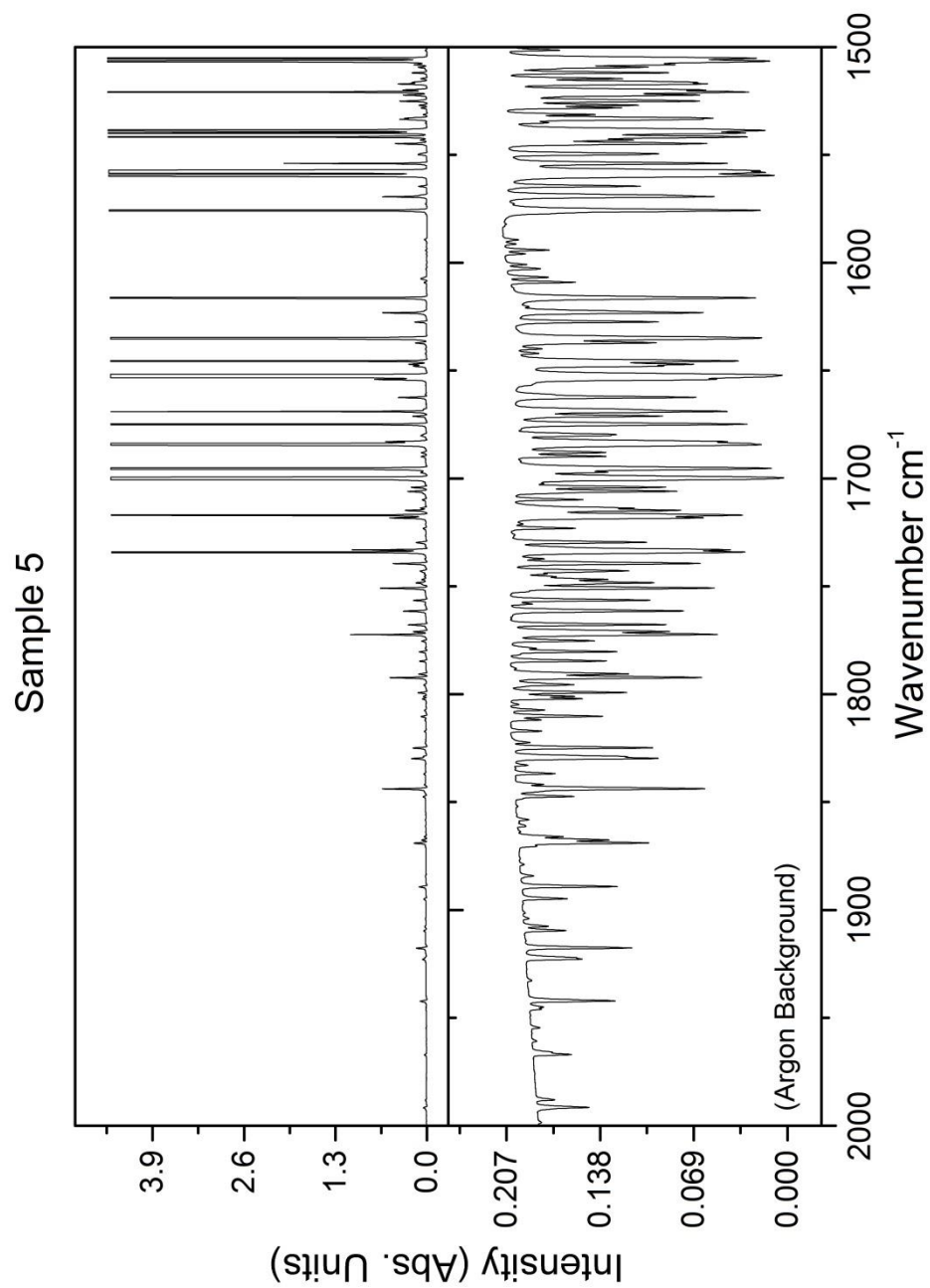
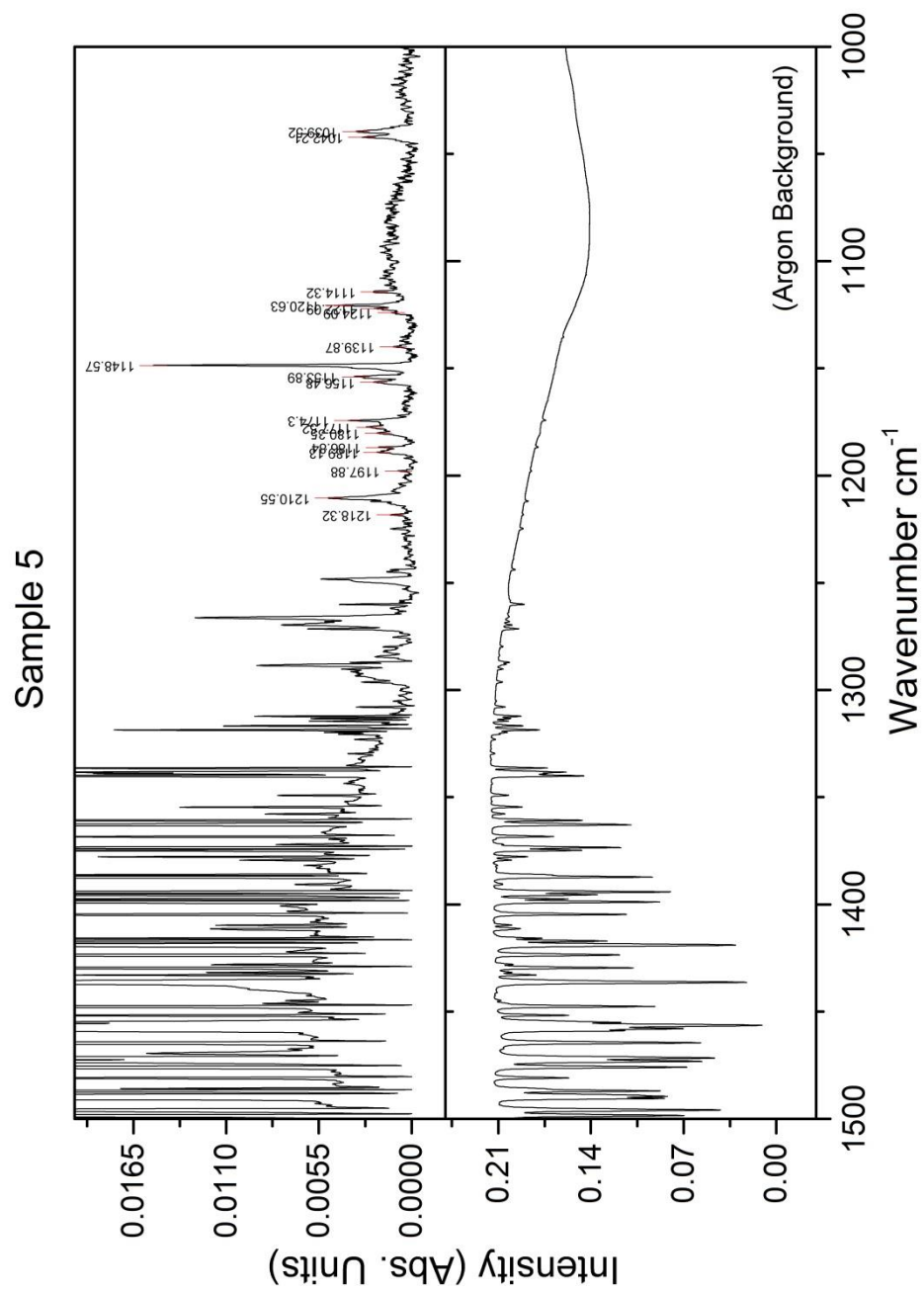


Figure 1-11f: Expanded view of Sample 5 IR spectrum,  $2000\text{-}1500\text{ cm}^{-1}$ . Genuine signal peaks are marked to indicate position where present.



*Figure 1-11g: Expanded view of Sample 5 IR spectrum, 1500-1000  $\text{cm}^{-1}$ . Genuine signal peaks are marked to indicate position where present.*

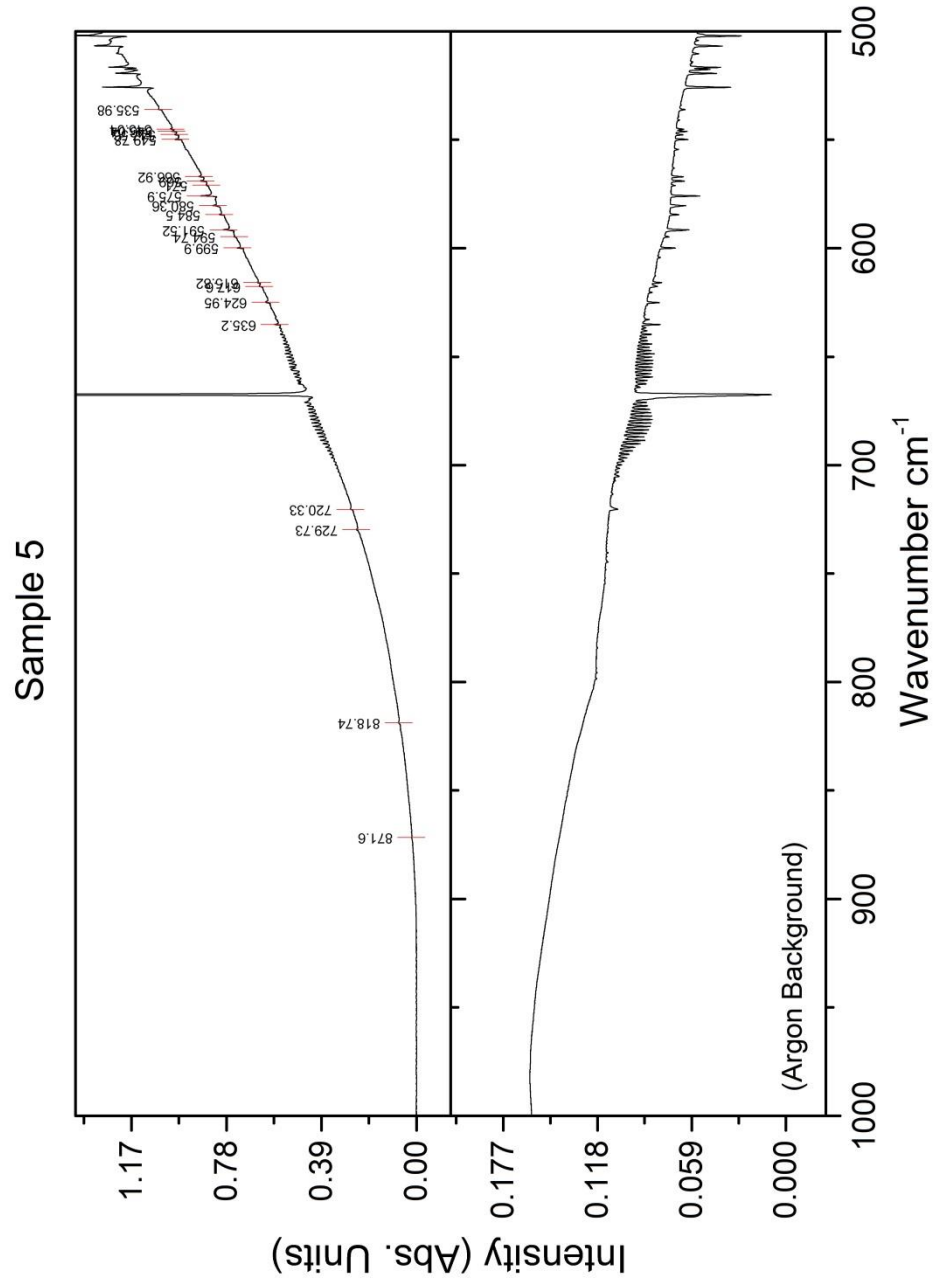


Figure 1-11h: Expanded view of Sample 5 IR spectrum,  $1000\text{-}500 \text{ cm}^{-1}$ . Genuine signal peaks are marked to indicate position where present.

<b>Position</b>	<b>FWHM (cm<sup>-1</sup>)</b>	<b>Intensity (Abs. Units)</b>
535.98	0.014	0.42
545.04	0.015	0.52
546.04	0.016	0.36
547.56	0.013	0.43
549.78	0.022	0.47
566.92	0.020	0.58
569.00	0.023	0.44
571.00	0.010	0.68
575.90	0.057	0.38
580.36	0.027	0.54
584.50	0.019	0.52
591.52	0.036	0.56
594.74	0.008	0.52
599.90	0.028	0.42
615.82	0.019	0.58
617.60	0.018	0.63
624.95	0.025	0.70
635.20	0.025	0.70
720.33	0.009	0.54
729.73	0.013	0.75
818.74	0.006	0.89
871.60	0.003	0.56
1039.52	0.003	1.97
1042.21	0.003	1.15
1114.32	0.002	1.04
1120.63	0.004	1.03
1122.09	0.002	0.95
1124.09	0.001	1.28
1139.87	0.001	1.18
1148.57	0.015	0.87
1153.89	0.003	1.73
1156.48	0.002	1.56
1174.30	0.003	0.98
1177.52	0.001	0.93
1180.35	0.001	1.32
1186.84	0.002	1.08
1189.13	0.002	1.42
1197.88	0.001	0.63
1210.55	0.004	1.40
1218.32	0.001	0.80

Table 1-7: Integrated Gaussian fitting parameters for signal peaks in Sample 5.

## 1-4: Discussion and Conclusions

### 1-4-1: Vanillin Intensity in Matrix Isolated IR Spectra

Vanillin has proven to be a more difficult material to isolate than was first envisioned: though it has a naturally strong odour, it only displays a vapour pressure of  $2.933 \times 10^{-5}$  bar at  $25^\circ\text{C}$ . Practical attempts to introduce the vapour into the free path of the bulk argon gas required moderate amounts of heating to avoid preferential deposition on the interior surfaces of the glassware. In contrast, it proved to be more effective to vary the pressure (i.e. rate) of Ar introduction to control the resulting concentration of 4-hydroxy-3-methoxy benzaldehyde in the final matrix.

It is difficult to conclusively state whether the vanillin molecules present in the matrix are in a truly isolated state: this judgement is based on the behaviour of observed peak distributions over a range of concentrations. Isolated species show a characteristic narrow peak distribution; consideration of the Gaussian fittings of the peaks observed around  $1000\text{ cm}^{-1}$  in each sample spectrum (typical of the vibrational peaks of vanillin, and seen in all of the experimental samples except Sample 4) shows a typical peak FWHM of  $2\text{-}2.5\text{ cm}^{-1}$  in Samples 1 and 2, dropping to a typical value of approximately  $1\text{-}1.5\text{ cm}^{-1}$  in Sample 3, then to  $0.8\text{ cm}^{-1}$  in Sample 5 (though Sample 5 was recorded at a resolution of  $0.25\text{ cm}^{-1}$ , while the others are of resolution  $0.5\text{ cm}^{-1}$ ). This change in peak character suggests that the vanillin molecules in Samples 3 and 5 are at least *more* isolated than in 1 and 2, though whether this is a true isolated state could only be confirmed by obtaining more spectra at lower deposition temperatures/ higher pressures to confirm there is no further change in the observed peak width.

Though the signal peaks observed in the final sample spectra above do show the characteristically narrow widths associated with isolated species, the actual

concentration of the matrix can only be calculated by use of the Beer-Lambert relationship between the absorption coefficient of the sample molecule and the path length. Taking the interference fringe pattern observed in Sample 1 as a representative value for a sample collected under these conditions we can calculate a typical thickness for these matrices:

$$l = \frac{n}{2r(\bar{v}_1 - \bar{v}_2)} = 0.00258146153 \dots$$

*Equation 1-1: Path length l (cm) from number of interference fringes observed n in wavenumber range  $\bar{v}_1$  to  $\bar{v}_2$ , with refractive index r. In this case n=11,  $\bar{v}_1=2270 \text{ cm}^{-1}$ ,  $\bar{v}_2=590 \text{ cm}^{-1}$  and the refractive index of the Ar matrix is 1.2682 (+/-0.00016).*

Later chapters in this thesis will show calculated intensity coefficients for vanillin produced by Density Functional Theory in the km/ Mole (the coefficient integrated over the entire absorption band); these may be used for the prediction of peak intensity at given matrix thicknesses and concentrations (and vice versa), and have been used to calculate simulated spectra of multiple components at relative intensity distributions.

$$\log \frac{I_0}{I_1} = \epsilon cl = A$$

Hence:

$$c = \frac{A}{\epsilon l}$$

*Equation 1-2a and b: The classic Beer-Lambert Law. Concentration c of material in matrix per unit path length (mol.  $\text{cm}^{-1}$ ), molar absorption coefficient  $\epsilon$  and path length l (calculated above to have a typical value of 0.00258 cm) give the resulting absorbance of the molecule A.*

### 1-4-2: Discussion of Splitting Effects in the Matrix Isolated Spectra

It is clear (even with the unexpected absences of certain peaks from some of the sample spectra) that there are more visible peaks attributable to signal from the matrix visible than would be expected for the normal modes of a molecule of this size; this is not unanticipated, since it was noted earlier that matrix isolated species are expected to be affected by environmental effects that give rise to splitting effects. In order to explain these additional peaks, there are four factors in this system to be considered: the concentration of the matrix mixture, the packing effects expected in the matrix and how they are affected by the temperature of deposition, the rotational stereochemistry of the molecule and the possible isotopic substitutions present in the species.

Concentration has the greatest role to play in the distribution of the peak intensity observed. The proportion of vanillin compared to argon in the matrix gas mixture is controlled by two factors: the temperature to which the vanillin was heated (higher temperatures naturally resulting in a higher vapour pressure), and the flow pressure of the argon gas that forms the bulk of the matrix. When the temperature is low and the Ar flow proportionately high, the resulting matrix would be expected to show narrower peaks of lower intensity, as the vanillin is found in an isolated state. When the temperature is *high* and the flow pressure *low*, however, it is more reasonable to expect to see larger aggregate structures in the matrix as the analyte molecules remain in close enough proximity/ high enough concentration to interact. Such aggregate structures are generally characterised by a sequence of several peaks shifted to slightly lower wavenumber values echoing the ‘main’ peak for each vibration, each of decreasing intensity and *increasing* width; the loose association of aggregate structures effectively adding to the mass of the vibrating molecule(s). At the higher concentrations these aggregate structures will dominate the spectrum and form the vibrational bands more familiar to solid state spectra, though at concentrations close to the isolated state (such as we have here) it can be very difficult to characterise these peaks properly. In all likelihood there are some peaks in Samples 3, 4 and 5 above that are in fact due to dimeric interactions

between vanillin molecules: this kind of interaction would be expected to be most expressed in the  $\sim 3550\text{ cm}^{-1}$  –OH stretching peak due to the strong hydrogen bonds that form between closely associated hydroxyl groups. Although absent from Sample 5 due to swamping of the signal by residual water structure, this peak can be seen in Samples 3 and 4 to begin to separate into two peaks of near-equivalent strength: this indicates that the broadening of the vOH band is in fact due to extended structures forming between aggregate groups.

The vanillin structure has a central 6-membered ring and three substituent side groups; as discussed in *Section 1-1-4* above, this arrangement occupies the equivalent volume of 3.071 argon atoms in the matrix lattice. It is important to remember that this value means that a number of situations may occur in order to *actually* accommodate the molecule, and that (given its large, ovoid shape) it may actually replace more argon sites than the 3.071 value would suggest- given the relative size and fcc packing arrangement in the matrix a minimum of *seven* sites would appear to be disrupted by the presence of the vanillin. The assumption can be made that the steric effects of the covalently bound atoms of vanillin will cause the argon (held together only by van der Waals forces) to arrange themselves around the vanillin; because of this, the most probable packing arrangement would have a slightly distorted Ar matrix surrounding the molecule as it occupies the minimum necessary space (closer to the calculated 3.071). Alternatively, a more relaxed configuration would have the molecule displace additional argon atoms (perhaps five, six or seven) in order to reduce stress on the volume occupied by the functional groups to varying degrees. Each of these different arrangements may be occupied by different molecules at the same time, their proportions dictated only by the energy available to the molecule at the time of deposition (i.e. the deposition temperature), and would be expected to give a minute shift in the resulting vibrational position for each transition.

The packing of vanillin into the matrix is not the only factor that is influenced by the conformation of the molecule in the vapour phase. For studies in the solid phase, such as a fine powder pressed into a KBr disc for an IR spectrum,

the crystal structure of vanillin is well known and documented by x-ray crystallographic techniques. Passing into the vapour phase, however, the molecular stereochemistry is free to rotate and distort. The exact structure that the molecule relaxes into would be expected to be a local energy minimum, but depending on the amount of energy available and the rate of cooling/ argon matrix formation it is entirely possible that the functional groups of vanillin may be promoted and fixed into a different geometry to the crystal structure. Changes as significant as rotating the aldehyde group would be expected to produce a significant difference in the resulting vibrational spectra for the matrix: the proportion of molecules promoted into each rotational isomer would be expected to be controlled only by the temperature of deposition, and a theoretical model of this mechanism is elaborated on in *Chapter 3b* later on.

As with the other effects discussed here, isotopic substitution in the vanillin population would be expected to produce changes in the resulting vibrational spectra. Indeed, the alterations to vibrational position due to changes in mass (particularly for vibrational modes involving hydrogen replaced with deuterium) would be expected to be quite drastic. A near-natural abundance of ‘secondary’ isotopes is expected in the vanillin IR system, though the synthetic procedure used to manufacture the sample would undoubtedly influence the isotopic distribution through some degree of gravimetric fractionation. However, with even the strongest of the secondary isotopes of each atomic species having only a *natural* abundance of ~1% it is apparent from the intensity and noise values seen in the latter samples that it is not reasonable to assume the visibility of isotopic peaks in the isolated state with the available instrumentation for this investigation.

### **1-4-3: Conclusions and Further Development**

As the system stands now contamination is a serious issue; traces of IR-active species such as H<sub>2</sub>O and CO<sub>2</sub> can be seen in all spectra and are a serious impediment in the lower concentration matrices. Removal of these traces is a priority, but will only be possible with rigorous treatment of the vacuum system itself- replacing aging parts and sealing all possible sources of leaks such as joints. The performance of the Leybold BMH70 turbopump has been quite satisfactory in these experiments, but the best possible vacuum is always preferred. Significant uncertainty is found in the apparatus used: pressure control in particular has largely been performed manually, and an automated system to regulate deposition flow rate is highly desirable as this is the principle control of matrix concentration in conjunction with vanillin sample temperature.

Assigning the complicated structure seen in these spectra is a difficult process and without further information it is problematic to assign the structures seen to particular sources, be they aggregation, conformational, site effects or isotopic substitutions. The greatest limiting factor in these spectra is the low intensity of signal in comparison to the undesirable peaks attributed to both contaminants and artefacts, and the simplest method of improving this would be to run a sufficient number of scans to reduce background noise further than has already been achieved. The issue of noise is compounded by working at high resolution: although the use of 0.25 cm<sup>-1</sup> resolution in Sample 5, rather than the 0.5 cm<sup>-1</sup> resolution used for the other spectra, allows for a more precise integration of the resulting peak (more data points naturally giving a more reliable peak measurement), the relative impact of noise is increased. The spectra presented in this chapter were each collected in an isolation procedure that required 9-12 hours to complete, most of which was taken up by infrared scan time. Extending sample collection time by a factor of 16 would produce a resulting spectrum with proportionately 75% less noise, but would require an entire week to collect equivalent data: with effects on the spectra from the outside environment noted over the period of just one day, the effect of changes in weather, temperature and air pressure, etc., become a serious concern, and the use of a

climate-controlled workspace would be recommended should such a long collection process be undertaken.

With improvements to the signal to noise ratio comes the ability to distinguish very low intensity components in the spectra from the background: in particular, the ability to observe repetition of structures in the IR would potentially allow these to be assigned as either matrix packing or isotopic effects (most likely a combination thereof) based on their width and behaviour with changes in matrix concentration. As well as observing changes with concentration, it is also practical to consider the deliberate doping of sample materials with isotopic markers, in order to aid in assignment between matrix and isotopic effects, deliberately increasing the intensity of isotopic bands to make them stand out.

Proper assignment of peak structure is largely a matter of performing multiple isolations while changing only one variable (temperature, pressure, isotopic ratio) and keeping the others the same, in order to gather sufficient information. Changes in pressure would vary the concentration of the matrix, while (at sufficiently high deposition flow pressure) conformational distribution would be expected to be largely temperature controlled; ‘spiking’ the material would of course increase the relative intensity of vibrational structure involving those atomic species. This level of comparison has not been possible in my time working on this project, but a future investigation may be able to use these methods to conclusively assign structures to one mechanism or the other.

## **Part Two:**

**Fundamentals of Density Functional Theory and the  
Simulation of Vanillin in both the Solid and Isolated Phase.**

# Chapter 2: Fundamentals of Density Functional Theory

## 2-1: Introduction

### 2-1-1: Isotopic Labelling in High Resolution Vibrational Spectra

As has been discussed in *Chapter 1*, high resolution vibrational spectra of isolated molecules can be obtained relatively easily for small molecular species; with an increase in detector sensitivity comes a lowering of the detection limit for the system. Using low-temperature deposition and small sample concentration in an inert matrix (i.e. the Matrix Isolation technique, detailed in the next chapter) it is possible to record the pseudo-isolated vibrational spectra of small species such as CO<sub>2</sub> and N<sub>2</sub>O, and *Chapter 1* details a series of experimental attempts to obtain matrix isolated vibrational spectra of vanillin in a conventional laboratory setting.

Each element in nature has a certain natural abundance of stable isotopes (for example the abundance of <sup>13</sup>C is typically quoted as 1.1% of the total carbon population). In an infrared spectrum, were there only the two possible isotopomers, intensity of the total population of any vibration involving a given carbon would be expected to be split 98.9/ 1.1% between the expected peak and an isotopomeric vibrational peak shifted a relatively small amount in the x-axis from it (for example, the CO<sub>2</sub> asymmetric stretch is seen in an argon matrix at ~2345 cm<sup>-1</sup>, but the <sup>13</sup>C isotopic vibration can clearly be seen, repeating the additional structure caused by matrix effects, at ~2280 cm<sup>-1</sup>). Asymmetry in the molecule allows isotopic shifts to be assigned to specific atoms where a plane of molecular symmetry would not, i.e. the equivalent stretching vibrations for <sup>18</sup>O in CO<sub>2</sub> could not be assigned to a specific oxygen position (symmetrical structure O=C=O), but it *would* be possible to distinguish between nitrogen atoms for positional labelling of <sup>15</sup>N in N<sub>2</sub>O (N=N=O).

Such positional information is difficult for other techniques to provide- SNIF-NMR and Mass Spectrometry both requiring modifications to the molecular structure such as protonation and fractionation. Use of common infra-red to achieve the same information would make for a much cheaper and more practical alternative.

Though in principle the probability any atom in the molecule would have of being such an isotope would be equal to its natural abundance, in practice due to the synthetic steps taken to produce the sample molecule these distributions are rarely as expected. Some reference data for small molecules with isotopic substitutions exists (for example  $^{13}\text{C}$  in small molecules such as  $\text{CO}_2$  has been studied by a number of authors through the decades), but this kind of information becomes rapidly more scarce the larger the molecule and more specific the isotopic labelling of the molecular species in question. One of the purposes of this investigation is to theoretically simulate the vibrational spectra of such species, and use such calculated vibrations to predict the possibility of experimentally observing the natural isotope abundances using vibrational spectroscopy within the achievable spectral resolutions and signal to noise ratios.

## **2-1-2: Density Functional Theory (DFT) Modelling of Vibrational Spectra**

Species where synthetic routes have been chosen to isotopically label specific sites are frequently expensive to purchase, making rigorous exploration of such molecules an expensive process. Reliable predicted data for isotopomeric vibrations, which can be manipulated to produce simulated spectra for arbitrary user-defined isotopic populations, is desirable to predict and characterise such species. These predictions could then be used to predict whether such compounds would be experimentally observable, in order to test the accuracy of such simulations.

With modern computer modelling techniques and processing power, it is possible to simulate the physical and energetic properties of molecules to a high degree of accuracy<sup>7</sup>. Although mathematical assumptions are required to model such systems<sup>6</sup>, choosing the correct Basis Set and level of theory (see later) can give a simulated array of vibrations that closely approach the observed experimental data. This chapter describes the application of such techniques to vanillin, chosen due to its modest size (19 main-group atoms) and three dissimilar functional groups.

The use of Density Functional Theory has a number of advantages over other methods<sup>54</sup>: unlike the Hartree-Fock method, the orbital theory applied by DFT necessitates a degree of correlation between multiple electrons localised to specific atoms, rather than assuming that the overall field effects are equally experienced by all of the particles in the system (an approximation, intended to reduce the calculation time required to solve the fully correlated Schröedinger Equation down to a manageable level). In Hartree-Fock calculations, electron density is not localised to any particular position and instead of interacting with each other the electrons all experience the same average field effect; thus the method (while very capable at calculating the total energy of a molecular system) has great difficulty in determining the thermochemical properties of *specific* bonding interactions (and tends to systematically overestimate the calculated energies for molecules). The system is, in effect, calculated as the sum of a large number of single-electron wavefunctions. Modifications to this procedure can produce more accurate results by incorporating the wavefunctions of excited states (for example the second-order Møller-Plesset model, generally referred to as MP2), but these methods are very computationally expensive.

Most modern Density Functional Theory methods also treat the electrons in the molecular system as functions of electronic density to the same effect as the Hartree-Fock method, summed together to find the total energy of the system; where DFT differs is that correlation between electrons is modelled as an additional approximation term (the Exchange-Correlation approximation) based on observed energy values in molecular systems. By taking a hybrid approach to the calculation

of electronic density in the molecule (ab-initio calculations corrected by an approximation based on empirical data), DFT methods achieve a significantly more accurate result than the Hartree-Fock method alone at an equivalent level of theory (though generally less so than methods such as MP2) but only require marginally more computational power.

DFT is fundamentally an approximation, and as a result the choice of an incorrect correlation term for the species being studied can have a significant effect on the accuracy of the final results. A number of alternatives are available, including the *Becke three-parameter hybrid method functional with the Perdew/Wang 91 non-local correlation correction term* (shorthanded to B3PW91), and its successor, the popular *Becke three-parameter hybrid method functional with the Lee, Yang and Parr local and non-local correlation correction term* (shorthand B3LYP)<sup>55-58</sup>. The behaviour of these correlation terms will be evaluated in *Chapters 3a* and *3b* later on in this text.

## 2-2: Density Functional Theory

### 2-2-1: Origins of Density Functional Theory

*Note: The description of the DFT process presented in this chapter draws on references <sup>5-7</sup> and <sup>55-58</sup> throughout the text.*

At the core of Density Functional Theory modelling is the many-body Schrödinger equation; solving this equation exactly is an extremely difficult task that requires huge amounts of computing power and time, and is only realistically possible for a very select few specific cases. As a result of this, a series of assumptions and approximations are made to reduce this equation to a more manageable form that *can* be solved to give a result close to (if not precisely correct for) the true case.

We start by assuming, as in the Schrödinger Equation, that the energy of a system can be described by a single operator, the Hamiltonian  $\hat{H}$ , including terms to describe all contributions to the energy such that:

$$\hat{H}\Psi = E\Psi$$

*Equation 2-1*

For an inhomogeneous system comprised of N interacting electrons we can split this equation into three sources of energy contributions:

$$E = \langle \Phi | \hat{T} + \hat{V} + \hat{U} | \Phi \rangle = \langle \Phi | \hat{T} | \Phi \rangle + \langle \Phi | \hat{V} | \Phi \rangle + \langle \Phi | \hat{U} | \Phi \rangle$$

*Equation 2-2*

Where  $|\Phi\rangle$  is the ground state wavefunction (in a different form to that seen in the Hartree/ Hartree-Fock methods),  $\hat{T}$  the kinetic energy of the system,  $\hat{V}$  its interaction with fields external to the molecule, and  $\hat{U}$  the electron interaction term (the internal energy of the system);  $\hat{T} + \hat{U}$  can be considered the total internal energy of the system,  $\hat{F}$ .

Atomic and molecular systems are considered in DFT (and indeed quantum mechanics in general) as a system of electrostatic forces interacting with one another. In a molecular system, this Hamiltonian must therefore include terms to describe every possible interaction, as described by the general form seen here:

$$\begin{aligned} \hat{H} = & - \sum_{I=1}^P \frac{\hbar^2}{2M_I} \nabla_I^2 - \sum_{i=1}^N \frac{\hbar^2}{2M_i} \nabla_i^2 + \frac{e^2}{2} \sum_{I=1}^P \sum_{J \neq I}^P \frac{Z_I Z_J}{|\mathbf{R}_I - \mathbf{R}_J|} + \frac{e^2}{2} \sum_{i=1}^N \sum_{j \neq i}^N \frac{1}{|r_i - r_j|} \\ & - e^2 \sum_{I=1}^P \sum_{i \neq 1}^N \frac{Z_I}{|\mathbf{R}_I - r_i|} \end{aligned}$$

*Equation 2-3*

Where  $R = \{\mathbf{R}_I\}$  and  $I = 1, \dots, P$ , are a set of  $P$  nuclear coordinates, and  $r = \{r_i\}$  and  $i = 1, \dots, N$ , are a set of  $N$  electronic coordinates;  $Z_I$  and  $M_I$  are the nuclear charges and masses respectively. This can, in principle, have all of the unknown terms derived by solving the classical form of the many-body Schrödinger Equation, but in practice, however, this is almost impossible to do because of the large number of degrees of freedom for both the electrons and the atom. The first

assumption made to simplify this calculation process is that the timescale of electron motion is so much faster, and the mass so much lower, than the motion of the nuclei they orbit that they can simply be considered a probability wavefunction of electron density about a stationary atom (the Born-Oppenheimer approximation). This approximation also assumes that there are no non-radiative transitions between different orbitals: electronic transitions can only occur with some form of external interaction.

The second assumption, the Classical Nuclei approximation states that the equivalent particle density in the nuclei of the atoms is highly localised (enough that the atoms can be treated classically as single objects, rather than quantum mechanical wavefunctions unto themselves). With these two approximations in place, the many-body Schrödinger Equation is left as a series of electronic wavefunctions about fixed nuclear positions, not an easy task, but far more accessible than the former case.

There are two basic approaches to the problem of combining wavefunctions to form the electronic probability distribution in a molecular system: Hartree-Fock (HF) calculations and Density Functional Theory. In practice many of the best calculated results possible today (and, indeed, the method used in this research) actually use a hybrid of the two methods, taking some of the components introduced in Hartree-Fock and converting them to a form that can be applied to modify the electron density calculations (hence the DFT that we commonly refer to is typically an extension of the earlier Density approximation method [see later]).

It is the final term in *Equation 2-2*,  $\hat{U}$ , where many-body effects come into play. As seen in *Equations 2-2 and 2-3*:

$$\hat{U} = \langle \Phi | U | \Phi \rangle = \left\langle \Phi \left| \frac{1}{2} \sum_{i=1}^N \sum_{j \neq i}^N \frac{1}{|r_i - r_j|} \right| \Phi \right\rangle = \int \frac{\rho_2(\mathbf{r}, \mathbf{r}')}{|\mathbf{r} - \mathbf{r}'|} d\mathbf{r} d\mathbf{r}'$$

*Equation 2-4*

Where

$$\rho_2(\mathbf{r}, \mathbf{r}') = \frac{1}{2} \sum_{\sigma, \sigma'} \langle \Phi | \Psi_\sigma^\dagger(\mathbf{r}) \Psi_{\sigma'}^\dagger(\mathbf{r}') \Psi_{\sigma'}(\mathbf{r}') \Psi_\sigma(\mathbf{r}) | \Phi \rangle$$

*Equation 2-5*

And  $\Psi$  and  $\Psi^\dagger$  are the creation and annihilation operators for the electrons, obeying the anti-commutation rule  $\{\Psi_\sigma(\mathbf{r}), \Psi_{\sigma'}^\dagger(\mathbf{r}')\} = \delta_{\sigma, \sigma'} \delta(\mathbf{r} - \mathbf{r}')$ .  $\rho(\mathbf{r}, \mathbf{r}')$  is the one-body density matrix, where the diagonal elements  $\rho(\mathbf{r}) = \rho(\mathbf{r}, \mathbf{r})$  correspond to electron density:

$$\rho_2(\mathbf{r}, \mathbf{r}') = \frac{1}{2} \rho(\mathbf{r}, \mathbf{r}) \rho(\mathbf{r}', \mathbf{r}') g(\mathbf{r}, \mathbf{r}')$$

*Equation 2-6*

In which:

$$\rho(\mathbf{r}, \mathbf{r}') = \sum_{\sigma} \rho_{\sigma}(\mathbf{r}, \mathbf{r}')$$

$$\rho_{\sigma}(\mathbf{r}, \mathbf{r}') = \langle \Phi | \Psi_{\sigma}^\dagger(\mathbf{r}) \Psi_{\sigma}(\mathbf{r}') | \Phi \rangle$$

*Equations 2-7 and 2-8*

Essentially, the interaction between the two particles is the sum of the calculated interaction in either direction, halved, then acted upon by a correlation function to define their true interaction potential (i.e. A acting on B, plus B acting on A, divided by two then multiplied by some unknown coefficient).

With these definitions,  $U$  can be rewritten as:

$$U = \frac{1}{2} \int \frac{\rho(\mathbf{r})\rho(\mathbf{r}')}{|\mathbf{r} - \mathbf{r}'|} d\mathbf{r}d\mathbf{r}' + \frac{1}{2} \int \frac{\rho(\mathbf{r})\rho(\mathbf{r}')}{|\mathbf{r} - \mathbf{r}'|} [g(\mathbf{r}, \mathbf{r}') - 1] d\mathbf{r}d\mathbf{r}'$$

*Equation 2-9*

In which the first term is the classical interaction of two electrostatic charges, while the second takes into account the exclusion of two similarly charged particles in similar loci.

This term can be split into two components: one for exchange ( $g_x$ ) and one for correlation ( $g_c$ ); the value of  $U$  is affected even further with the inclusion of an exchange term, which also adds the mutual exclusion of two particles with the same spin (the Pauli Exclusion Principle). There is, of course, no exclusion from this for electrons of the opposite spin at the same location, so we can say that  $g_x(\mathbf{r}, \mathbf{r}')$  approaches  $\frac{1}{2}$  as particle  $\mathbf{r}$  approaches  $\mathbf{r}'$ :

$$g_x(\mathbf{r}, \mathbf{r}') \rightarrow \frac{1}{2} \text{ for } \mathbf{r} \rightarrow \mathbf{r}'$$

*Equation 2-10*

$U$  from *Equation 2-9* can be rewritten in the form:

$$U_{HF} = \frac{1}{2} \int \frac{\rho^{HF}(\mathbf{r})\rho^{HF}(\mathbf{r}')}{|\mathbf{r} - \mathbf{r}'|} d\mathbf{r}d\mathbf{r}' + \frac{1}{2} \int \frac{\rho^{HF}(\mathbf{r})\rho^{HF}(\mathbf{r}')}{|\mathbf{r} - \mathbf{r}'|} \left[ -\frac{\sum_{\sigma} |\rho_{\sigma}^{HF}(\mathbf{r}, \mathbf{r}')|^2}{\rho^{HF}(\mathbf{r})\rho^{HF}(\mathbf{r}')} \right] d\mathbf{r}d\mathbf{r}'$$

*Equation 2-11*

And so the term that describes the depletion effect of the exchange (typically referred to as the *exchange hole*) is:

$$g_x(\mathbf{r}, \mathbf{r}') = 1 - \frac{\sum_{\sigma} |\rho_{\sigma}^{HF}(\mathbf{r}, \mathbf{r}')|^2}{\rho^{HF}(\mathbf{r})\rho^{HF}(\mathbf{r}')}$$

*Equation 2-12*

Unfortunately, the calculation of the equivalent term for correlation (the *correlation hole*) between the two electrons,  $g_c(\mathbf{r}, \mathbf{r}')$ , is not as easy to work out, and the two must still be included as a single term encompassing both contributions  $E_{XC}$  (the *exchange-correlation hole*):

$$E_{XC} = \frac{1}{2} \int \frac{\rho(\mathbf{r})\rho(\mathbf{r}')}{|\mathbf{r} - \mathbf{r}'|} [g(\mathbf{r}, \mathbf{r}') - 1] d\mathbf{r}d\mathbf{r}'$$

*Equation 1-13*

Hence, we can re-define:

$$E = T + V + U$$

*Equation 1-14*

With:

$$T = -\frac{\hbar^2}{2m} \int [\nabla_i^2 \rho(\mathbf{r}, \mathbf{r}')]_{\mathbf{r}'=\mathbf{r}} d\mathbf{r}$$

$$V = \sum_{I=1}^P \int \rho(\mathbf{r}) (\mathbf{r}_i - \mathbf{R}_I) d\mathbf{r}$$

$$U = \frac{1}{2} \int \frac{\rho(\mathbf{r}) \rho(\mathbf{r}')}{|\mathbf{r} - \mathbf{r}'|} d\mathbf{r} d\mathbf{r}' + E_{XC}$$

Where:

$$E_{XC} = \frac{1}{2} \int \frac{\rho(\mathbf{r}) \rho(\mathbf{r}')}{|\mathbf{r} - \mathbf{r}'|} [g(\mathbf{r}, \mathbf{r}') - 1] d\mathbf{r} d\mathbf{r}'$$

*Equations 2-15, 2-16, 2-17 and 2-13*

As:

$$\begin{aligned} E = & -\frac{\hbar^2}{2m} \int [\nabla_i^2 \rho(\mathbf{r}, \mathbf{r}')]_{\mathbf{r}'=\mathbf{r}} d\mathbf{r} + \sum_{I=1}^P \int \rho(\mathbf{r}) (\mathbf{r}_i - \mathbf{R}_I) d\mathbf{r} \\ & + \frac{1}{2} \int \frac{\rho(\mathbf{r}) \rho(\mathbf{r}')}{|\mathbf{r} - \mathbf{r}'|} d\mathbf{r} d\mathbf{r}' + \frac{1}{2} \int \frac{\rho(\mathbf{r}) \rho(\mathbf{r}')}{|\mathbf{r} - \mathbf{r}'|} [g(\mathbf{r}, \mathbf{r}') - 1] d\mathbf{r} d\mathbf{r}' \end{aligned}$$

*Equation 2-18*

## 2-2-2: The Kohn-Sham Approximation

In 1965 Kohn and Sham proposed replacing the kinetic energy term  $T$  for interacting electrons with the equivalent term from a non-interacting system  $T_R$ . This approximation would save considerable calculation time, making it highly desirable.

In this approximation,  $E_{XC}$  is redefined as:

$$E = T_R + J + V + E_{XC}$$

*Equation 2-19*

Where:

$$E = T + V + U = F + V$$

$J$  is an approximation of  $U$  from a repulsive gas model where there are no interactions between valence electrons, the equivalent of replacing  $T$  with  $T_R$ .

In effect, the energy contribution from the interaction between electrons is ‘moved’ and subsumed into the correlation term in  $E_{XC}$ ; this leaves the effective kinetic contribution as simply the ground-state kinetic energy level, and means that the exchange-correlation term can be far more easily calculated while the unknown from the correlation is approximated later on.

## 2-2-3: The Local Density Approximation and Modern DFT Methods

We can see from the classical equations shown above that the total energy of the system is dependent on three things: the kinetic energy of the system, its external interactions, and the internal energy of the system (including as it does a complicated series of interactions, particle exchanges and correlation effects between electrons). As described in *Section 2-2-1*, in Density Functional Theory the entire molecular system is treated as a collection of interacting electrostatic forces; as a result of this, the three contributions are written and displayed in a format that describes their energies in the form of electronic probability functions. We also know that the exchange and correlation term cannot be easily calculated for a complex system and must be approximated to save on computing power.

The simplest and still most widely used method of approximating the internal energy of the system is the Local Density Approximation (commonly referred to as the LDA). In this approximation the electron density for the inhomogeneous system (i.e. larger molecules, condensed phase systems, etc) is instead treated as being locally homogeneous since the simpler homogeneous systems (such as very simple gases) *do* have exact numerical solutions, or can at least be approximated very closely. The two approximations made in the LDA are that: one, the *exchange-correlation hole* is centred at the first electron  $\mathbf{r}$  when it is actually centred at the other  $\mathbf{r}'$ , and two, that it is approximated by the equivalent from the homogeneous electron gas, with a correction for the change in density to compensate for the incorrect position:

$$\tilde{g}(\mathbf{r}, \mathbf{r}') \approx \tilde{g}^h[|\mathbf{r} - \mathbf{r}'|, \rho(\mathbf{r})] \left( \frac{\rho(\mathbf{r})}{\rho(\mathbf{r}')} \right)$$

*Equation 2-20*

The Local Density approximation calculates the energy of the exchange-correlation term using the inverse radius (the exchange-correlation energy density  $\varepsilon_{XC}^{LDA}[\rho]$ ) of the *exchange-correlation hole*:

$$E_{XC}^{LDA}[\rho] = \int \rho(\mathbf{r}) \varepsilon_{XC}^{LDA}[\rho] d\mathbf{r}$$

*Equation 2-21*

Where:

$$\varepsilon_{XC}^{LDA}[\rho] = \frac{1}{2} \int \frac{\rho_{XC}^{LDA}(\mathbf{r} - \mathbf{r}')}{|\mathbf{r} - \mathbf{r}'|} d\mathbf{r}'$$

*Equation 2-22*

is the exchange-correlation energy density.

In the years since its publication, the LDA has been improved by a variety of correction factors for local density gradients, variations in decay with separation, etc. In many cases, the construction of one functional (be it correlation or exchange) has also led to the postulation of a term to describe its counterpart; a full description of these terms is inappropriate for this work, but a summary of those used here can be found below.

As noted earlier, the most frequently used Density Functional Theory equations use a hybrid approach to the calculation of molecular orbital properties. Starting from the LDA, further terms are added in a linear combination (i.e. of the form  $ax + by + \dots ij$ ) to build up an appropriate mixed term that describes the experimental system. The two methods used in the following investigation, B3LYP and its predecessor B3PW91 are examples of this type of hybrid method. It is

important to realise that the development of these exchange-correlation terms is an on-going process: these are simply some of the best functionalities available in the present day for the calculation of the properties of molecular systems<sup>55-59</sup>. Exact terms for the B3LYP and B3PW91 functions, together with their derivation, may be found in such publications as *DFT Basics, New Trends and Applications by Kohanoff and Gidopoulos, 2003*<sup>6</sup>.

## 2-3: Basis Set Construction

The choice of basis set is simple but not necessarily an easy one to make<sup>60, 61</sup>, since the basis set used determines the underlying shapes and construction of the orbital density wavefunctions used to build the molecular system (in particular the valence orbitals used for bonding interactions).

Wavefunctions are not typically built from simple functionalities (for example Gaussian distributions), but instead take the form of multiple overlaid functions that may be adjusted in varying proportions according to the surrounding molecular environment; the more complex the construction of a wavefunction, the better able it is to adjust under any given circumstances. For example, in a very simple one-component orbital, a bond through space to a given point may be calculated as having an unusually high energy value. That same bond, calculated instead with a composite wavefunction (with approximately the same overall intensity, but different local distributions along  $x$ ) may instead calculate a lower energy due to a local mixing of the underlying functions that comprise it. Changes in the linear combination of such functions also allow effects such as polarisation within orbitals to be accounted for, as the resulting changes in electronic density may be represented by altering the shape of the composite distribution.

Work in this investigation has been carried out using an array of additional valence orbitals, polarisation and diffusion functions to see if any combinations produce observably better fits to experimental data.

Basis sets have been constructed in considerable variety; typical Pople notation describes the basis set in terms of:

1. The number of Gaussian functions comprising the core atomic orbital basis function (followed by a hyphen).

- Two to four numbers, each indicating how many Gaussians are combined into that many sets of linear combinations to form the valence orbitals (the number of integers is referred to as zeta, from the notation originally used to describe the STO basis functions). These are referred to as ‘split valence’ basis sets.

All work in this chapter has been conducted using the 6-311+G (d) basis set which has six terms for the core orbitals, sets of three, one and one terms for the valence orbitals, and a combination of diffuse (+) and additional d-orbital contributions, representing an flexible basis set for a calculation of this nature. Initial experiments with vanillin showed no observable differences in the resulting vibrational or energetic calculations for either additional p-orbital contributions or doubly-diffuse orbitals, and thus these options have been omitted.

## **Chapter 3a: Gaussian Simulation Results Part I- Solid Phase Vanillin**

### **3a-1: Determination of the Optimised Molecular Structure for Vibrational Calculation**

This simulation process attempts to represent the solid phase infrared and Raman behaviour of the vanillin crystal. Some assumptions have been made in the construction of the initial model: although the crystal normally consists of multiple identical molecules in close proximity and a repeating three-dimensional pattern, the structure here represents only a single molecule. Though the angles and bond lengths in the molecular structure are manually fixed in the Gaussian input file to those observed in the crystal there is no attempt made to simulate the peak broadening effects normally present from intermolecular interactions, and the calculated molecule remains isolated in a vacuum. Simulations of vibrational spectra were performed using Gaussian 09 software package. The molecular structure of vanillin was first constructed by user defined input to agree with the structure determined from the single crystal x-ray diffraction data, with all atomic bond angles and lengths fixed other than for hydrogen atoms (the repeating asymmetric unit for solid phase vanillin can be found in *Figure 3a-1a and b* below as pictured using the ORTEP-3 program<sup>62</sup>, followed by the associated crystallographic data in *Table 3a-I*):

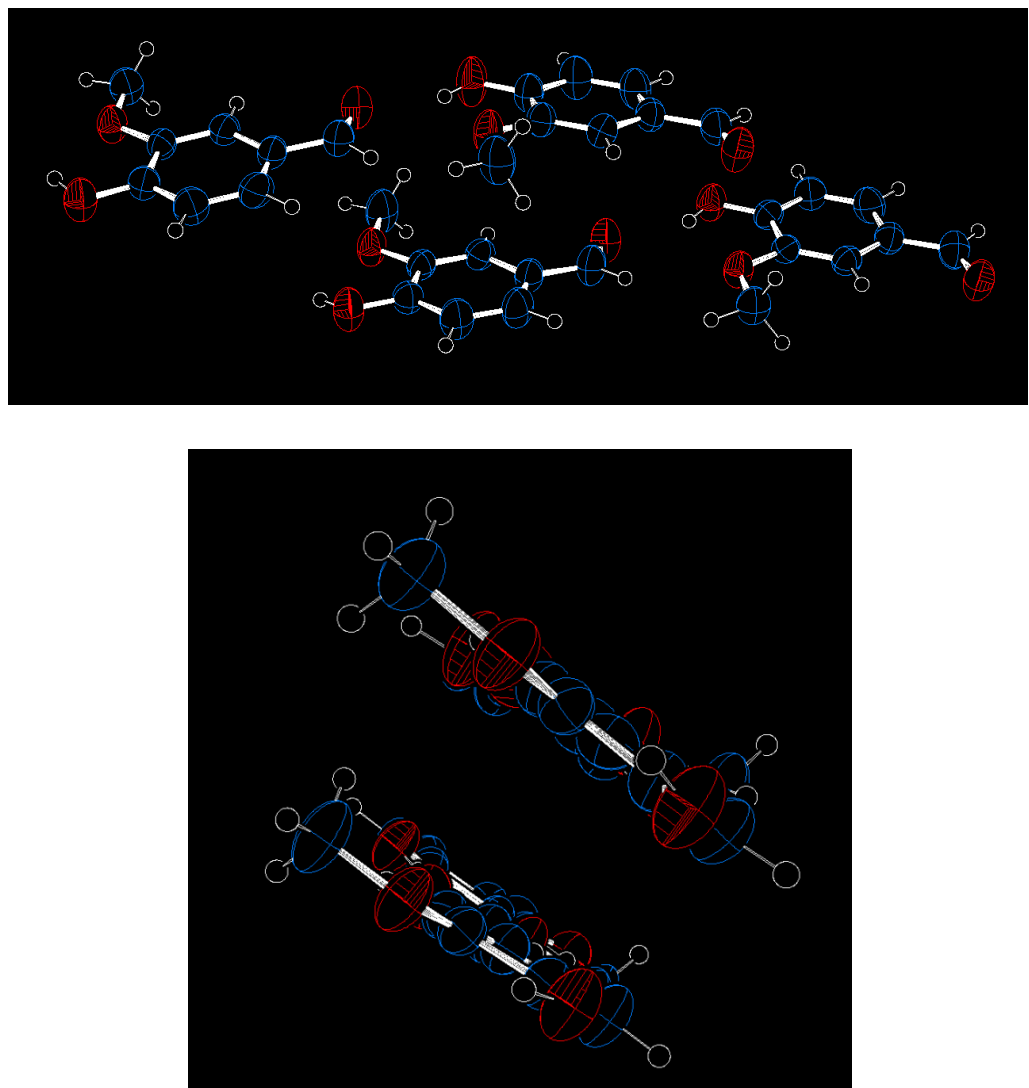


Figure 3a-1 and b: ORTEP display of the repeating four-molecule asymmetric unit of solid phase vanillin (lateral 'x/y' plane and end-on 'z/y' plane respectively); (Crystal data obtained from R. Velavan, et al, Acta Cryst (1995) C51, p1131).

<b>Unit Cell Lengths (Å):</b>	14.049	7.874	15.017
<b>Unit Cell Angles (Degrees °):</b>	90	115.45	90
<hr/>			
<b>Atomic Species:</b>	<b>C</b>	<b>H</b>	<b>O</b>
<b>No. in Assymmetric Unit:</b>	32	32	12
<b>No. in Unit Cell:</b>	256	256	96
<b>Covalent Radii (Å):</b>	0.77	0.37	0.66
<hr/>			
<b>Space Group Hall Symbol:</b>	P 2yb		
<b>Space Group H-M Symbol:</b>	P 1 21 1		
<b>Crystal Class:</b>	Monoclinic		
<b>International Tables Number:</b>	4		
<b>Space Group Multiplicity:</b>	2		

*Table 3a-1: Crystallographic data for the repeating asymmetric unit of solid phase vanillin.*

The hydrogen atoms were then optimised using the B3LYP function with the 6-311G Basis Set. This process normally produces a representation of the molecule optimised in space for minimal group overlap, bond angle stresses, etc., though in this case only the hydrogen atoms are permitted to move and all others are fixed in place. Naturally, this also modifies the Cartesian coordinates that the system records for the constituent atoms in the molecule , and it is this modified version that was then used for the further calculations detailed below.

Literature sources such as *Govindarajan, et al.*,<sup>59</sup> suggest the use of either the 6-31, 6-311 or 6-311G basis sets, using a variety of methods of calculation. It is suggested that the best results (i.e. most reliably close to the observed experimental values for a molecular species of similar size and functionality) are obtained for the 6-311G basis set using the B3LYP and B3PW91 methods. As a result, initial evaluations were performed using the B3LYP and B3PW91 Density Functional Theory methods, using the 6-311G basis set with varying levels of modification as listed in *Table 3a-2*:

Basis Set	Method	Modifications Used
6-311G	B3LYP	Unmodified
6-311G	B3LYP	Diffuse Molecular Orbitals ('+' notation)
6-311G	B3LYP	Additional Accessible d-orbitals ('d' notation)
6-311G	B3LYP	Both Diffuse Molecular Orbitals and Additional Accessible d-orbitals ('+d' notation)
6-311G	B3PW91	Unmodified
6-311G	B3PW91	Diffuse Molecular Orbitals ('+' notation)
6-311G	B3PW91	Additional Accessible d-orbitals ('d' notation)
6-311G	B3PW91	Both Diffuse Molecular Orbitals and Additional Accessible d-orbitals ('+d' notation)

*Table 3a-2: Basis set construction for initial solid phase vanillin calculations.*

Test example calculations were also performed using additional accessible p-orbitals in combination with other modifications, but these produced no difference in the calculated vibrational frequencies or energies from the originals as the molecule is not expected to make use of higher level p-orbitals, and have thus been omitted. The resulting absolute energy values for this structure were calculated using the eight methods described in *Table 3a-2*; the resulting values can be found in *Table 3a-3* below. Basis sets are described using the relevant exchange function and modification notation as described in *Table 3a-2* above:

Function/ Basis Set	Calculated Absolute Energy (kJmol <sup>-1</sup> )
B3LYP	-1405433.505
B3LYP +	-1405466.012
B3LYP d	-1405812.597
B3LYP +d	-1405848.545
B3PW91	-1404867.821
B3PW91 +	-1404897.099
B3PW91 d	-1405246.373
B3PW91 +d	-1405272.906

*Table 3a-3*

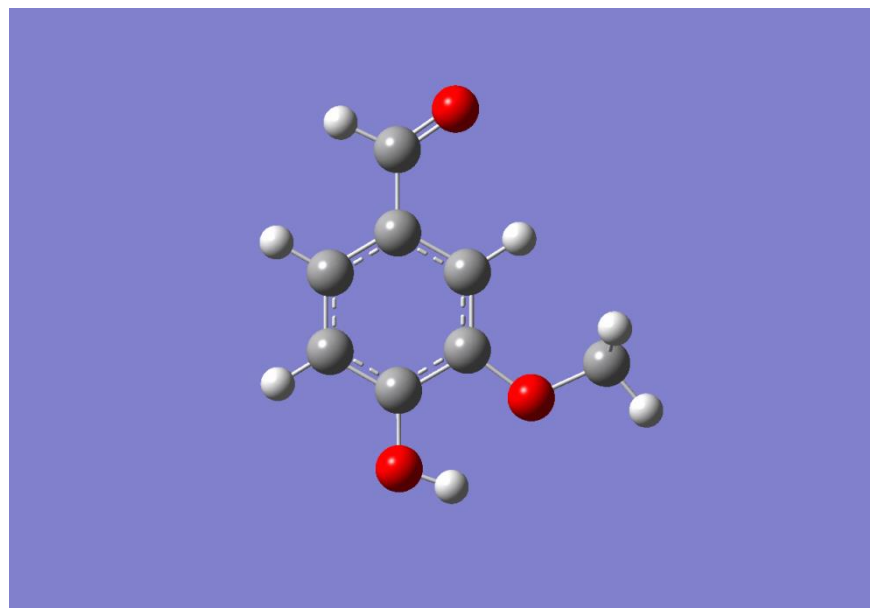


*Figure 3a-2: The configuration of the functional groups of vanillin in the solid phase crystal structure. Original picture in colour: the light coloured spheres represent hydrogen, the grey carbon and the red spheres represent oxygen atoms.*

### **3a-2 Vibrational Spectra Calculation and Evaluation for 4-Hydroxy-3-Methoxy Benzaldehyde**

With the solid-state configurations geometrically optimised, we can now use the Gaussian program to perform a simulation of the vibrational properties of the molecule using Density Functional Theory. *Tables 3a-5 to 3a-11* contain the relevant peak values for the simulated spectra including unscaled wavenumber values (see later), calculated infrared intensities and calculated Raman activities, and will be used for their evaluation shortly. In order to evaluate the quality of these simulated spectra, it is necessary to make a direct comparison to experimental data. Since the Raman data for the solid powder is the best resolved of the experimental data obtained, we will initially consider the solid phase Raman spectrum of vanillin then move on to the infrared spectrum of vanillin pressed in a KBr disc.

Experimentally obtained Raman data for vanillin is shown in *Figure 3a-3* (obtained using a Bruker IFS 66 with an FRA 106 Raman module attachment, a 1028 nm laser source at 658 mW intensity and a liquid nitrogen cooled PbS diode detector at a resolution of  $0.5\text{ cm}^{-1}$ ) with associated peak data listed in *Table 3a-4*.

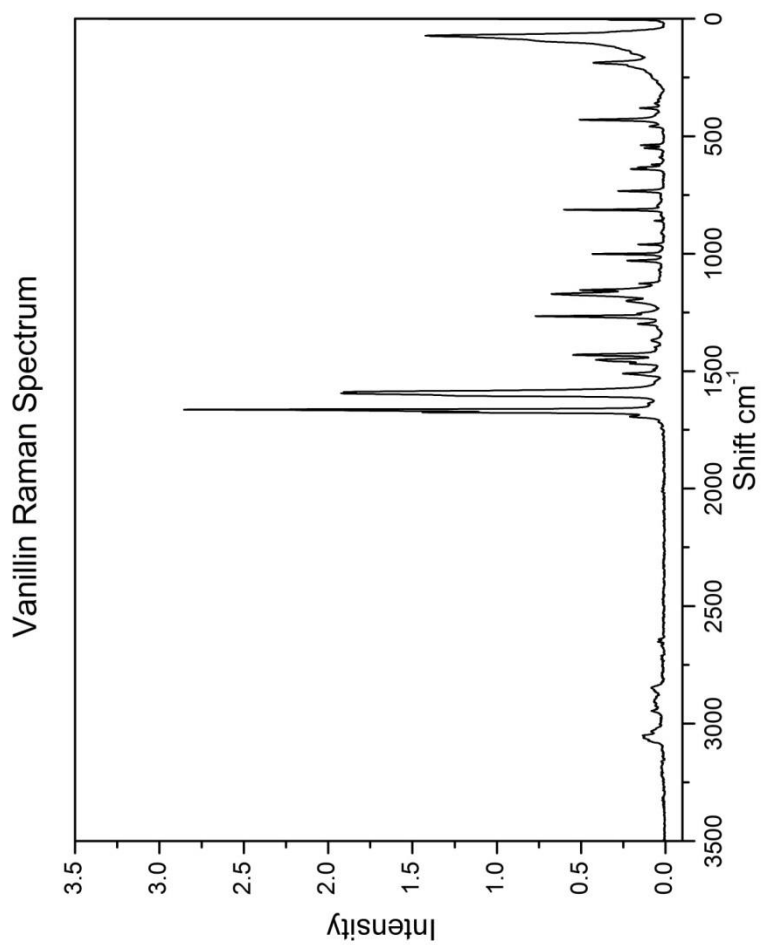


Figure 3a-3: Experimentally obtained Raman spectrum for reference data.

<b>Position (cm<sup>-1</sup>)</b>	<b>Raman Intensity</b>	<b>Full Width at Half Maximum (cm<sup>-1</sup>)</b>
327.83	0.012	14.31
344.33	0.020	9.05
360.17	0.032	10.21
379.83	0.113	5.92
429.75	0.423	7.08
458.09	0.072	7.17
538.07	0.124	6.09
550.67	0.105	5.90
590.76	0.023	7.83
620.60	0.051	3.65
632.39	0.122	4.57
639.59	0.174	5.78
733.21	0.247	7.04
796.00	0.020	13.68
813.09	0.565	5.20
859.87	0.050	3.54
909.86	0.022	13.51
960.90	0.150	4.88
1001.29	0.414	4.97
1029.71	0.209	7.48
1070.14	0.024	24.18
1126.58	0.080	4.02
1154.38	0.394	6.27
1171.80	0.619	17.03
1200.90	0.188	16.62
1254.95	0.131	14.22
1265.71	0.647	5.84
1271.36	0.257	8.03
1298.72	0.099	7.21
1369.28	0.076	16.29
1397.84	0.030	10.21
1430.25	0.462	9.01
1450.42	0.283	7.12
1456.66	0.228	7.39
1467.10	0.149	8.18
1509.98	0.201	7.44
1517.81	0.092	9.30
1588.48	1.328	11.55
1595.41	0.848	5.54
1603.91	0.978	6.75
1663.05	2.297	4.02
1667.93	1.202	4.99
1675.27	0.998	4.26
1693.66	0.204	10.74
2640.83	0.030	5.39
2651.39	0.030	6.09

2669.70	0.011	7.18
2846.60	0.079	20.35
2864.38	0.033	15.24
2903.22	0.054	49.76
2945.56	0.050	14.53
3033.54	0.060	21.00
3050.23	0.091	9.80
3060.80	0.109	11.98
3074.29	0.080	13.20

*Table 3a-4: Experimental Raman peak wavenumber values, intensities and widths; peak parameters determined by manual fitting with Gaussian functions.*

### **3a-2-1: Simulated Raman Spectra**

In order to evaluate how closely each of these eight simulations match the experimentally obtained data (see above for the Raman spectrum), the peak positions found in those spectra are plotted against the calculated results. In the case of a simulation that exactly replicates the experimental data a linear fit of the plot will show a correlation value of one; naturally this means that the closer the correlation is to unity for a given fit, the more closely those simulation results represent reality. This does not necessarily mean that that particular method is better for *all* molecules or structures- as a general rule the larger the basis set used, the more reliable the simulation is for all cases- but in the case of a single structure multiple calculation methods may be evaluated to find the ‘best’ fit of the available range.

It is known that a systematic error in vibrational spectra simulated by Density Functional Theory requires the application of a scaling factor to obtain correct wavenumber values<sup>61</sup>. Such scale factors are available in literature, but are only the averages of multiple calculations performed using each basis set and method- since each spectrum theoretically requires a unique scale factor, it is more practical in this case to calculate our own and avoid confusion. By plotting the wavenumber values obtained from the experimental data against the nearest equivalents found in the simulations, scatter plots can be produced and evaluated with simple linear best-fit lines; in such a fit the correlation between data sets can be assumed to be given by the  $R^2$  of the fitted line (which in a good relationship will approach unity), while the appropriate scale factor will be given by the slope of the line  $y = mx + c$  where the experimental point(s)  $y$  are given in terms of simulated points  $x$ ,  $m$  (the gradient) is the scale factor and  $c$  the extrapolated  $y$ -intercept. Simulated Raman spectral data is tabulated below in *Tables 3a-5 to 3a-12*, and plots for the eight sets of calculated data are shown in *Figures 3a-4 to 3a-11*, along with accompanying linear fits:

<b>Calculated Peak Wavenumber (cm<sup>-1</sup>)</b>	<b>IR Intensity I (KM/ Mole)</b>	<b>Raman Activity A (A<sup>4</sup>/AMU)</b>
77.76	11.57	1.90
111.92	0.18	0.38
150.38	9.70	1.80
185.61	0.08	2.05
208.96	7.52	0.95
236.65	4.09	0.64
251.19	0.04	0.93
328.83	3.15	2.30
381.42	3.06	0.51
420.88	0.69	9.15
466.07	3.41	0.66
538.21	3.61	3.63
544.20	9.28	3.43
544.63	151.38	2.73
599.58	17.97	0.18
635.62	57.37	7.60
710.18	0.28	0.02
739.38	41.42	12.33
818.74	1.92	13.61
854.41	36.41	0.59
924.62	25.30	1.16
954.21	3.76	2.74
974.95	3.76	0.45
1026.42	2.86	5.22
1034.90	58.76	7.84
1153.23	60.97	0.95
1163.19	0.52	5.36
1176.27	52.40	0.99
1204.32	89.83	11.15
1228.68	238.55	19.32
1262.72	38.25	6.69
1298.93	228.69	26.02
1337.46	24.77	1.14
1420.22	4.87	10.12
1448.10	44.23	3.86
1478.95	91.74	25.96
1500.92	4.38	9.68
1525.78	12.66	21.68
1534.67	135.44	4.95
1544.59	24.60	5.64
1635.30	135.64	109.11
1651.99	166.56	183.50
1677.05	62.60	24.12
2942.00	129.57	170.62
3018.88	36.50	117.42
3091.89	33.13	44.50

3157.72	18.35	107.40
3169.40	10.63	71.59
3207.73	4.76	10.53
3211.75	6.52	175.65
3631.87	114.13	109.84

*Table 3a-5: Unscaled simulated vibrational wavenumbers for B3LYP for the vanillin molecular structure fixed in the solid phase crystal structure, with associated infrared and Raman intensity values.*

<b>Calculated Peak Wavenumber (cm<sup>-1</sup>)</b>	<b>IR Intensity I (KM/ Mole)</b>	<b>Raman Activity A (Å<sup>4</sup>/AMU)</b>
70.86	12.93	1.45
106.57	0.46	0.32
149.31	10.26	1.99
183.02	0.11	1.65
202.65	7.43	0.88
234.94	4.22	0.62
245.69	0.01	0.66
327.51	2.83	2.45
376.01	3.11	0.69
420.14	0.96	10.06
462.21	3.49	0.44
514.28	144.36	1.33
536.28	2.99	4.16
542.36	6.99	3.14
590.30	18.64	0.12
633.76	60.42	7.06
721.62	0.10	0.14
736.73	41.06	13.63
816.79	2.47	13.53
857.03	39.07	0.49
922.06	23.99	0.35
950.60	3.66	4.33
983.56	3.80	0.18
1025.02	4.69	2.42
1032.14	56.04	8.53
1149.63	64.95	0.94
1162.69	0.51	3.42
1173.06	62.67	1.33
1198.44	131.20	17.45
1220.24	191.37	20.02
1255.72	26.50	8.04
1294.13	263.26	37.44
1334.10	22.76	1.25
1414.09	3.00	13.72
1442.79	41.22	2.91
1475.30	87.01	31.63
1495.57	9.08	12.18
1523.92	14.62	15.92
1528.54	129.78	4.88
1538.10	37.71	4.13
1626.15	235.10	193.20
1647.36	153.88	191.45
1667.72	39.25	23.99
2944.64	113.07	167.42
3016.43	37.12	131.96
3092.59	29.47	41.20

3153.79	16.32	106.35
3166.36	9.15	69.05
3204.36	4.47	2.54
3206.91	6.04	185.79
3624.90	117.51	114.89

*Table 3a-6: Unscaled simulated vibrational wavenumbers for B3LYP + for the vanillin molecular structure fixed in the solid phase crystal structure, with associated infrared and Raman intensity values.*

<b>Calculated Peak Wavenumber (cm<sup>-1</sup>)</b>	<b>IR Intensity I (KM/ Mole)</b>	<b>Raman Activity A (Å<sup>4</sup>/AMU)</b>
127.45	5.86	1.75
141.36	0.06	0.22
174.12	6.65	1.90
192.25	0.15	1.54
251.53	2.62	0.29
261.56	2.87	0.45
280.37	6.20	2.47
338.06	2.45	2.23
396.19	3.09	0.36
414.95	1.30	8.71
470.22	11.53	0.50
507.65	116.00	2.71
537.20	3.08	3.11
545.20	5.31	2.52
598.38	9.06	0.15
635.06	47.39	7.87
726.35	0.26	0.00
737.18	56.38	9.71
809.58	4.81	13.34
831.40	32.78	0.52
902.75	21.94	1.04
937.32	2.39	0.68
943.86	9.90	2.05
1008.20	88.73	8.14
1020.53	1.14	4.00
1123.01	113.09	1.03
1156.28	7.01	0.61
1160.52	0.46	3.92
1204.01	25.82	6.91
1216.72	144.79	17.50
1249.90	230.62	10.34
1270.25	212.50	30.12
1316.27	21.63	2.14
1397.31	8.75	7.62
1435.75	57.34	4.23
1468.82	102.03	18.31
1483.76	28.09	13.77
1503.89	9.68	16.28
1515.05	83.97	4.63
1527.22	59.92	2.19
1604.67	288.89	196.00
1653.54	82.38	67.98
1656.33	0.15	22.37
2929.08	134.34	177.10
3036.26	37.27	115.72
3108.27	31.41	45.28

3164.88	19.37	104.35
3167.84	8.91	76.68
3199.94	7.32	148.74
3210.26	3.76	47.67
3729.02	100.19	87.94

*Table 3a-7: Unscaled simulated vibrational wavenumbers for B3LYP d for the structure fixed in the solid phase crystal structure, with associated infrared and Raman intensity values.*

<b>Calculated Peak Wavenumber (cm<sup>-1</sup>)</b>	<b>IR Intensity I (KM/ Mole)</b>	<b>Raman Activity A (Å<sup>4</sup>/AMU)</b>
123.26	6.90	1.23
137.83	0.02	0.13
172.73	7.30	2.07
188.41	0.28	1.28
246.23	3.49	0.18
259.88	2.91	0.44
272.06	6.68	2.04
336.86	2.30	2.30
388.15	3.74	0.62
414.18	1.69	9.59
462.76	46.91	0.05
469.53	78.16	1.56
535.38	3.31	3.29
543.79	5.10	2.58
591.63	11.02	0.07
633.14	50.76	7.49
734.62	55.65	11.01
737.49	0.59	0.14
808.00	5.45	13.71
835.18	33.85	0.56
897.18	20.59	0.25
942.14	9.20	3.34
948.96	1.20	0.18
1007.39	88.04	9.67
1015.18	2.11	1.75
1119.54	122.76	0.84
1155.64	7.74	1.03
1160.33	0.61	2.34
1200.89	38.80	9.91
1213.07	151.66	21.39
1242.01	190.38	11.48
1266.68	270.87	42.74
1312.16	18.88	2.18
1396.61	5.98	11.64
1430.08	55.11	3.64
1464.57	83.75	19.91
1479.57	41.59	21.23
1502.91	10.91	12.00
1510.79	77.58	3.69
1524.02	72.89	2.14
1597.31	362.78	267.94
1649.62	69.27	55.87
1652.30	11.90	51.27
2939.82	112.51	163.71

3038.47	37.29	128.61
3112.83	26.67	40.60
3165.17	16.70	101.36
3168.28	7.26	71.18
3198.59	5.84	148.94
3209.84	3.70	44.94
3722.57	106.35	91.01

*Table 3a-8: Unscaled simulated vibrational wavenumbers for B3LYP +d for the vanillin molecular structure fixed in the solid phase crystal structure, with associated infrared and Raman intensity values.*

<b>Calculated Peak Wavenumber (cm<sup>-1</sup>)</b>	<b>IR Intensity I (KM/ Mole)</b>	<b>Raman Activity A (Å<sup>4</sup>/AMU)</b>
91.27	11.47	2.04
120.18	0.01	0.34
151.70	9.66	1.80
185.48	0.09	1.73
214.87	8.21	0.80
235.36	4.23	0.64
252.18	0.10	1.08
326.74	3.30	2.27
385.48	3.08	0.53
419.23	0.71	8.73
468.85	3.72	0.64
539.16	3.76	3.56
544.64	6.45	3.34
548.22	156.09	2.48
600.16	18.33	0.16
636.17	55.96	7.64
711.30	0.47	0.02
739.97	43.99	11.62
819.26	2.65	13.82
854.25	37.64	0.41
920.22	27.09	0.95
957.43	4.11	2.76
975.01	3.70	0.38
1027.51	3.03	4.71
1037.39	57.23	7.61
1154.32	64.64	0.80
1159.59	0.32	5.32
1176.73	43.49	0.67
1201.91	80.48	9.03
1227.85	239.65	18.56
1261.02	43.42	5.71
1303.56	193.69	29.08
1344.11	63.19	1.24
1420.19	4.92	8.76
1458.36	41.23	3.72
1480.50	70.59	17.69
1499.93	26.57	15.73
1521.77	13.60	21.01
1533.93	80.98	6.95
1549.46	74.96	2.72
1645.30	179.04	141.69
1664.61	154.36	163.75
1685.94	44.08	16.52
2958.57	125.03	164.83
3029.33	35.36	117.28
3111.98	29.94	41.94

3176.16	16.53	100.10
3181.81	9.35	69.93
3213.90	4.31	25.76
3225.89	5.67	153.10
3649.61	117.35	104.83

*Table 3a-9: Unscaled simulated vibrational wavenumbers for B3PW91 for the vanillin molecular structure fixed in the solid phase crystal structure, with associated infrared and Raman intensity values.*

<b>Calculated Peak Wavenumber (cm<sup>-1</sup>)</b>	<b>IR Intensity I (KM/ Mole)</b>	<b>Raman Activity A (Å<sup>4</sup>/AMU)</b>
86.67	12.48	1.55
116.14	0.16	0.25
151.14	10.03	1.99
182.95	0.14	1.43
210.27	8.15	0.77
234.07	4.36	0.63
247.00	0.05	0.85
325.58	2.94	2.41
380.21	2.88	0.67
418.43	0.97	9.50
465.22	4.06	0.41
518.77	142.98	1.29
537.31	3.34	4.06
542.99	6.58	3.00
589.37	19.14	0.13
634.53	57.86	7.14
720.56	0.18	0.13
737.47	43.65	12.71
817.45	3.18	13.67
855.42	38.91	0.41
918.35	25.11	0.34
953.78	4.14	4.20
981.88	3.59	0.16
1025.78	4.85	2.49
1034.41	54.58	8.18
1150.79	68.95	0.78
1158.63	0.33	3.51
1173.70	47.17	0.72
1196.59	112.15	13.00
1219.45	206.16	21.01
1254.21	30.89	6.38
1299.87	221.11	40.26
1339.26	64.87	1.05
1415.14	2.88	11.12
1453.61	39.35	3.21
1476.23	57.00	16.98
1495.19	37.88	22.00
1519.76	15.52	15.85
1527.38	76.00	5.36
1544.03	86.47	2.52
1636.32	270.77	223.37
1660.75	139.20	167.19
1678.17	23.21	16.89
2958.52	111.62	162.73
3026.24	36.24	131.54
3111.89	27.01	38.89

3170.98	14.90	99.34
3177.18	8.46	68.79
3210.09	4.25	24.54
3220.19	5.49	158.84
3641.72	117.59	110.41

*Table 3a-10: Unscaled simulated vibrational wavenumbers for B3PW91 + for the vanillin molecular structure fixed in the solid phase crystal structure, with associated infrared and Raman intensity values.*

<b>Calculated Peak Wavenumber (cm<sup>-1</sup>)</b>	<b>IR Intensity I (KM/ Mole)</b>	<b>Raman Activity A (A<sup>4</sup>/AMU)</b>
134.86	5.33	1.85
146.62	0.48	0.33
175.13	6.63	1.90
191.94	0.23	1.18
252.73	2.44	0.34
260.02	2.93	0.45
284.55	6.81	2.35
335.70	2.56	2.21
398.57	3.19	0.39
412.18	1.32	8.28
472.61	12.97	0.47
510.88	116.41	2.49
537.06	3.32	3.02
544.71	5.21	2.48
597.64	9.20	0.13
634.25	45.13	7.92
726.50	0.36	0.00
736.68	59.46	8.94
808.94	6.24	13.62
830.46	34.32	0.36
897.96	23.71	0.86
937.93	2.41	0.54
945.72	10.70	2.02
1009.57	85.77	7.92
1020.44	1.24	3.62
1121.35	114.07	0.81
1155.16	5.19	0.59
1155.77	0.27	3.85
1200.04	20.26	4.89
1212.93	128.99	15.42
1248.74	196.03	8.54
1273.75	243.53	35.58
1320.56	44.69	1.46
1394.30	12.84	6.32
1447.27	43.85	3.80
1465.71	68.21	8.64
1485.51	68.05	20.47
1498.32	10.48	15.80
1510.71	62.77	4.98
1532.35	76.89	1.18
1611.94	301.23	198.42
1666.90	79.78	82.68
1667.88	3.27	8.42
2942.37	128.72	172.22
3044.32	35.85	115.97
3125.02	27.83	42.87

3178.19	9.40	63.43
3180.37	15.22	110.03
3211.87	5.65	113.89
3214.60	3.86	75.32
3749.46	104.03	83.64

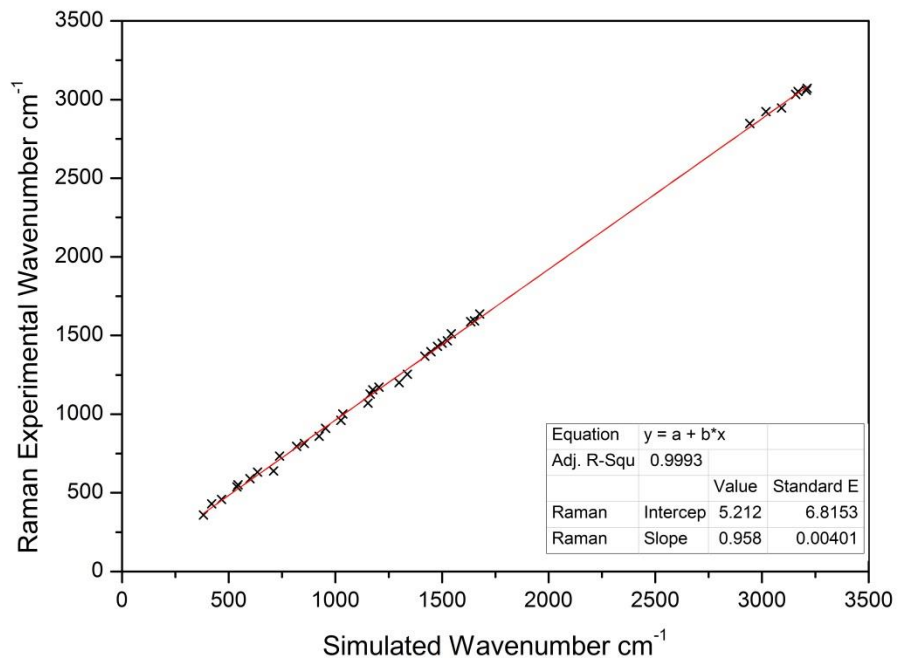
*Table 3a-11: Unscaled simulated vibrational wavenumbers for B3PW91 d for the vanillin molecular structure fixed in the solid phase crystal structure, with associated infrared and Raman intensity values.*

<b>Calculated Peak Wavenumber (cm<sup>-1</sup>)</b>	<b>IR Intensity I (KM/ Mole)</b>	<b>Raman Activity A (A<sup>4</sup>/AMU)</b>
129.17	3.57	1.35
145.21	0.29	0.12
185.71	3.10	1.60
191.41	2.39	1.38
239.17	6.46	0.76
252.40	1.88	1.16
311.14	7.73	0.83
339.06	6.86	4.45
353.62	0.52	0.72
396.69	1.46	6.84
464.75	86.32	0.17
475.63	36.25	1.13
513.35	10.95	2.46
544.60	22.56	5.07
585.76	8.72	0.07
643.80	12.38	3.57
734.61	0.05	0.16
784.12	78.96	14.33
794.49	1.11	5.78
846.96	31.37	0.08
861.67	24.67	0.16
917.90	2.21	8.53
971.56	0.20	0.03
1006.79	108.11	8.42
1016.78	1.72	2.19
1114.61	104.12	2.10
1155.64	0.40	2.55
1160.29	22.30	2.79
1194.86	23.67	3.30
1213.66	168.82	32.82
1235.82	148.36	6.69
1279.81	309.60	39.13
1321.66	61.41	5.08
1396.62	0.14	4.18
1432.17	23.87	20.39
1458.85	1.56	10.98
1470.66	12.45	9.10
1497.56	11.50	12.38
1507.24	43.32	4.78
1535.93	94.07	1.48
1607.30	481.04	296.93
1652.70	34.59	83.80
1667.35	24.26	10.19
2932.37	111.37	131.39
3040.61	40.33	133.29
3121.16	27.24	42.47

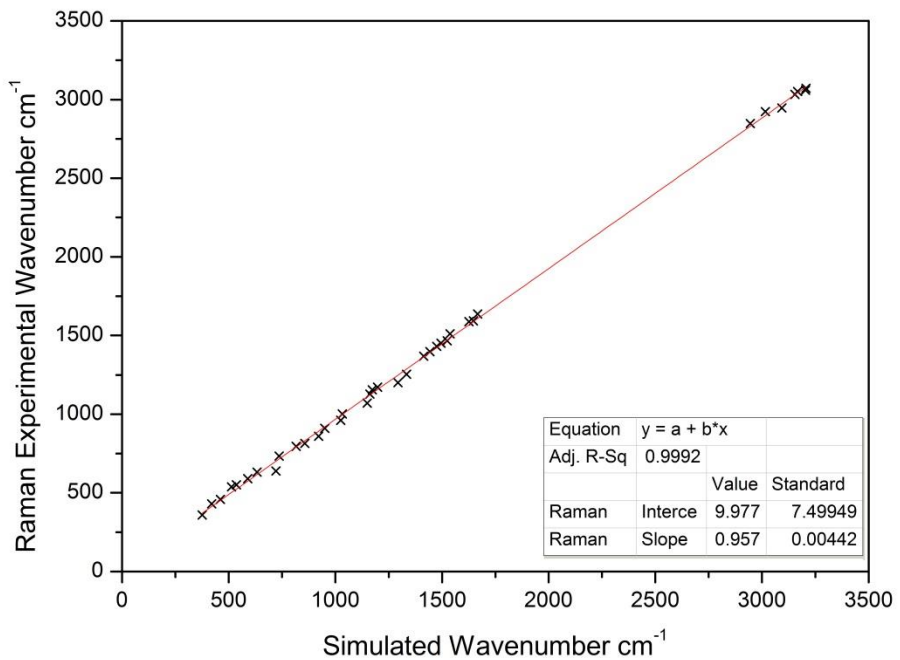
3177.22	14.83	108.40
3188.75	5.20	42.95
3201.27	0.85	57.01
3214.98	3.44	141.55
3745.52	108.73	92.12

*Table 3a-12: Unscaled simulated vibrational wavenumbers for B3PW91 +d for the vanillin molecular structure fixed in the solid phase crystal structure, with associated infrared and Raman intensity values.*

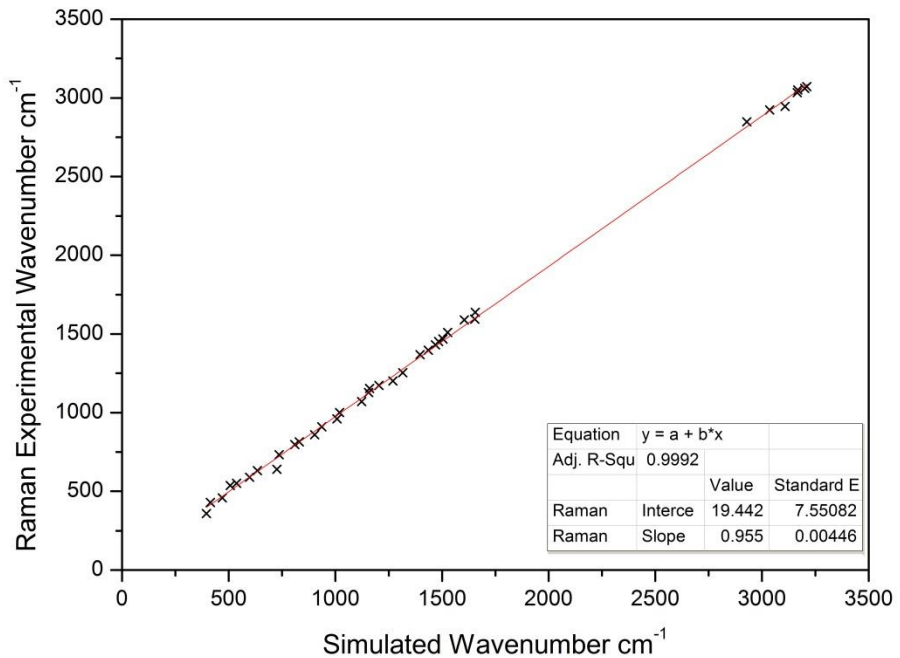
Experimental Raman vs B3LYP



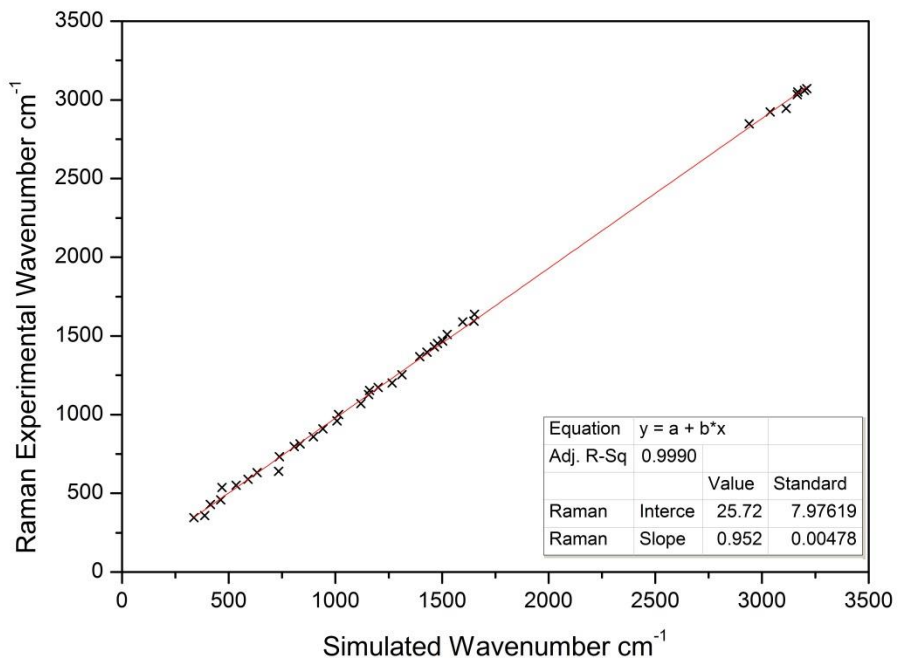
Experimental Raman vs B3LYP +

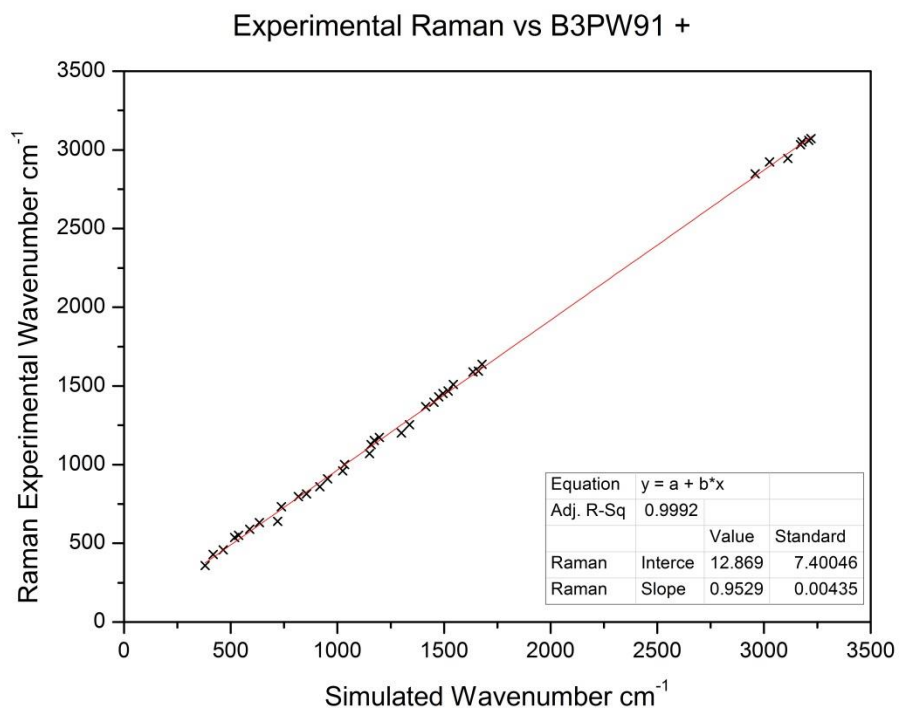
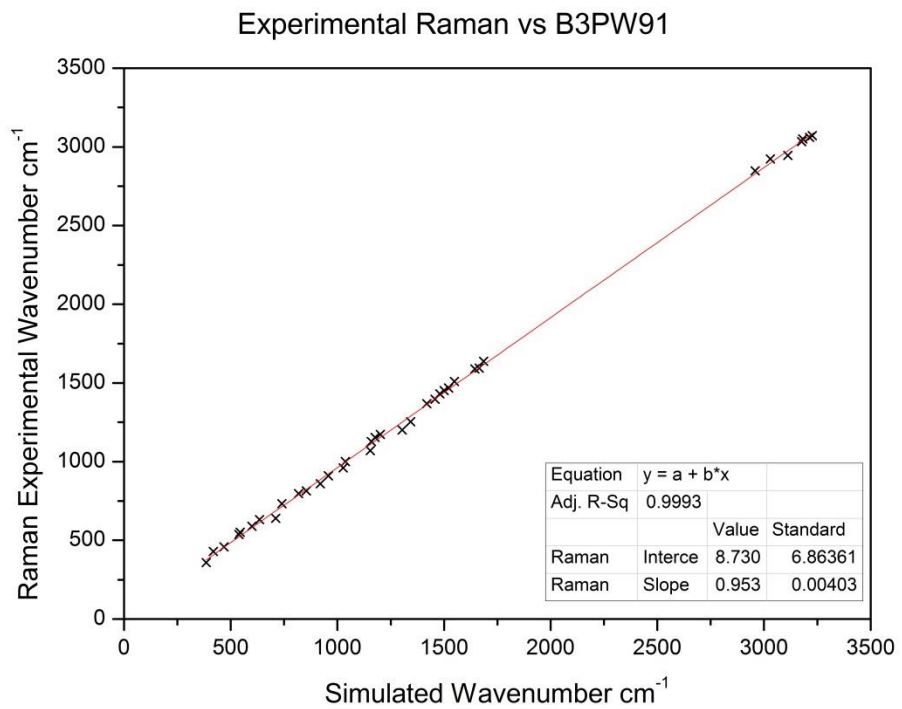


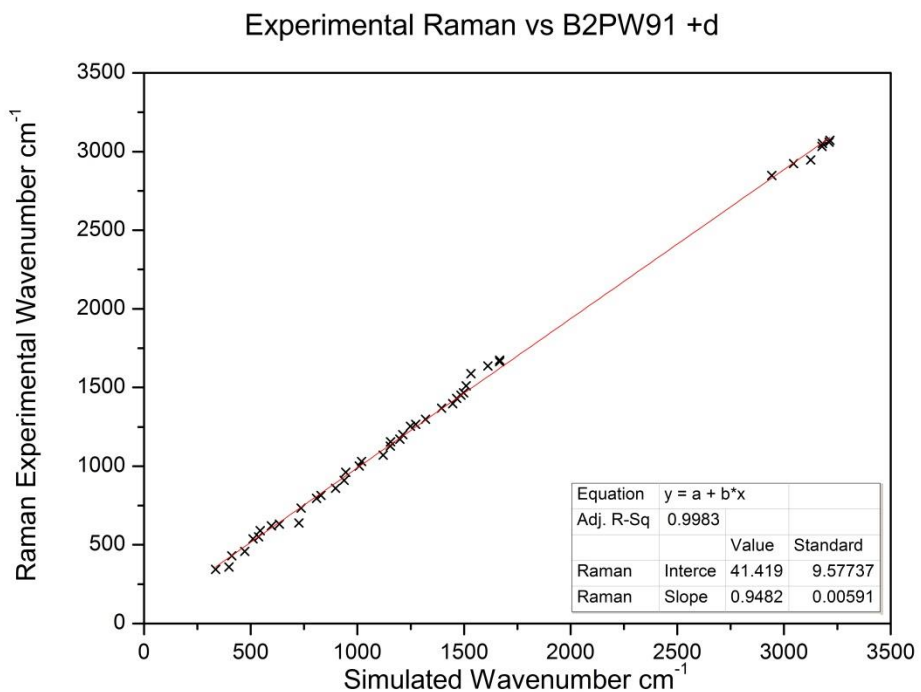
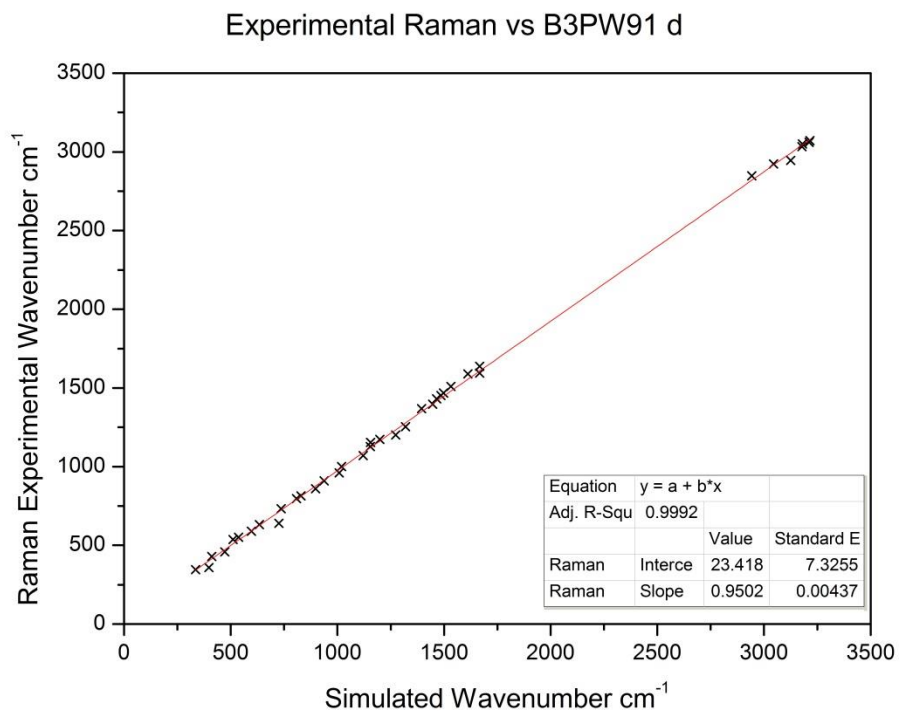
Experimental Raman vs B3LYP d



Experimental Raman vs B3LYP +d







*Figures 3a-4 to 3a-11: Plot of the (approximately) linear relationship between simulated data sets (B3LYP, B3LYP +, B3LYP d, B3LYP +d, B3PW91, B3PW91 +, B3PW91 d and B3PW91 +d) and the experimentally obtained Raman data points.*

<b>Method</b>	<b>R<sup>2</sup> Value</b>	<b>Gradient (Calculated Scale Factor)</b>
B3LYP	0.99937	0.95852
B3LYP +	0.99923	0.95776
B3LYP d	0.99921	0.955
B3LYP +d	0.99907	0.95228
B3PW91	0.99936	0.95325
B3PW91 +	0.99925	0.95297
B3PW91 d	0.99922	0.95025
B3PW91 +d	0.99837	0.94821

*Table 3a-13: Summary of linear fit data.*

As can be seen from the linear fit data summarised in *Table 3a-13* although the resulting R<sup>2</sup> residuals are very similar in all cases, the two closest matches are actually found in the unmodified B3LYP and B3PW91, though the values are very closely comparable overall (there is only a difference of 0.001 in the R<sup>2</sup> values of the best and worst fits).

Gaussian offers a number of formats for data output, including the option to simulate infrared and Raman spectra on a wavenumber (cm<sup>-1</sup>) scale with a user-defined half-width at half-maximum. Because the width of vibrational bands in the solid phase is generally broad the calculated peaks have been represented here in the form of Gaussian curve functions with a uniform full width at half height of 10 cm<sup>-1</sup>. Scaled wavenumber values for the peaks found in the B3LYP and B3PW91 calculations are shown immediately below in *Tables 3a-14* and *3a-15* (reproducing the calculated Raman activity values seen above in *Tables 3a-5* and *3a-9* respectively), while the resulting simulated Raman spectra for the two calculation methods are shown in *Figures 3a-12* and *3a-13*.

<b>Calculated Peak Wavenumber (cm<sup>-1</sup>)</b>	<b>Raman Activity A (A<sup>4</sup>/AMU)</b>
74.53	1.90
107.28	0.38
144.14	1.80
177.91	2.05
200.30	0.95
226.83	0.64
240.77	0.93
315.19	2.30
365.60	0.51
403.42	9.15
446.73	0.66
515.88	3.63
521.63	3.43
522.04	2.73
574.71	0.18
609.25	7.60
680.72	0.02
708.71	12.33
784.78	13.61
818.97	0.59
886.26	1.16
914.63	2.74
934.51	0.45
983.84	5.22
991.97	7.84
1105.39	0.95
1114.94	5.36
1127.48	0.99
1154.37	11.15
1177.71	19.32
1210.35	6.69
1245.05	26.02
1281.99	1.14
1361.31	10.12
1388.03	3.86
1417.60	25.96
1438.66	9.68
1462.49	21.68
1471.01	4.95
1480.52	5.64
1567.47	109.11
1583.46	183.50
1607.49	24.12
2819.97	170.62
2893.65	117.42
2963.64	44.50

3026.74	107.40
3037.93	71.59
3074.67	10.53
3078.53	175.65
3481.22	109.84

*Table 3a-14: Scaled simulated vibrational wavenumbers for B3LYP for the vanillin molecule fixed in the solid phase crystal structure, with associated Raman activity values (wavenumber values scaled by 0.95852)*

<b>Calculated Peak Wavenumber (cm<sup>-1</sup>)</b>	<b>Raman Activity A (A<sup>4</sup>/AMU)</b>
87.00	2.04
114.56	0.34
144.61	1.80
176.81	1.73
204.83	0.80
224.36	0.64
240.39	1.08
311.46	2.27
367.46	0.53
399.63	8.73
446.93	0.64
513.96	3.56
519.18	3.34
522.59	2.48
572.10	0.16
606.43	7.64
678.05	0.02
705.37	11.62
780.96	13.82
814.31	0.41
877.20	0.95
912.67	2.76
929.43	0.38
979.48	4.71
988.89	7.61
1100.36	0.80
1105.38	5.32
1121.72	0.67
1145.72	9.03
1170.44	18.56
1202.07	5.71
1242.62	29.08
1281.27	1.24
1353.79	8.76
1390.18	3.72
1411.29	17.69
1429.80	15.73
1450.63	21.01
1462.22	6.95
1477.02	2.72
1568.38	141.69
1586.79	163.75
1607.12	16.52
2820.26	164.83
2887.71	117.28
2966.50	41.94

3027.68	100.10
3033.06	69.93
3063.65	25.76
3075.08	153.10
3478.99	104.83

*Table 3a-15: Scaled simulated vibrational wavenumbers for B3PW91 for the vanillin molecule fixed in the solid phase crystal structure, with associated Raman activity values (wavenumber values scaled by 0.95325).*

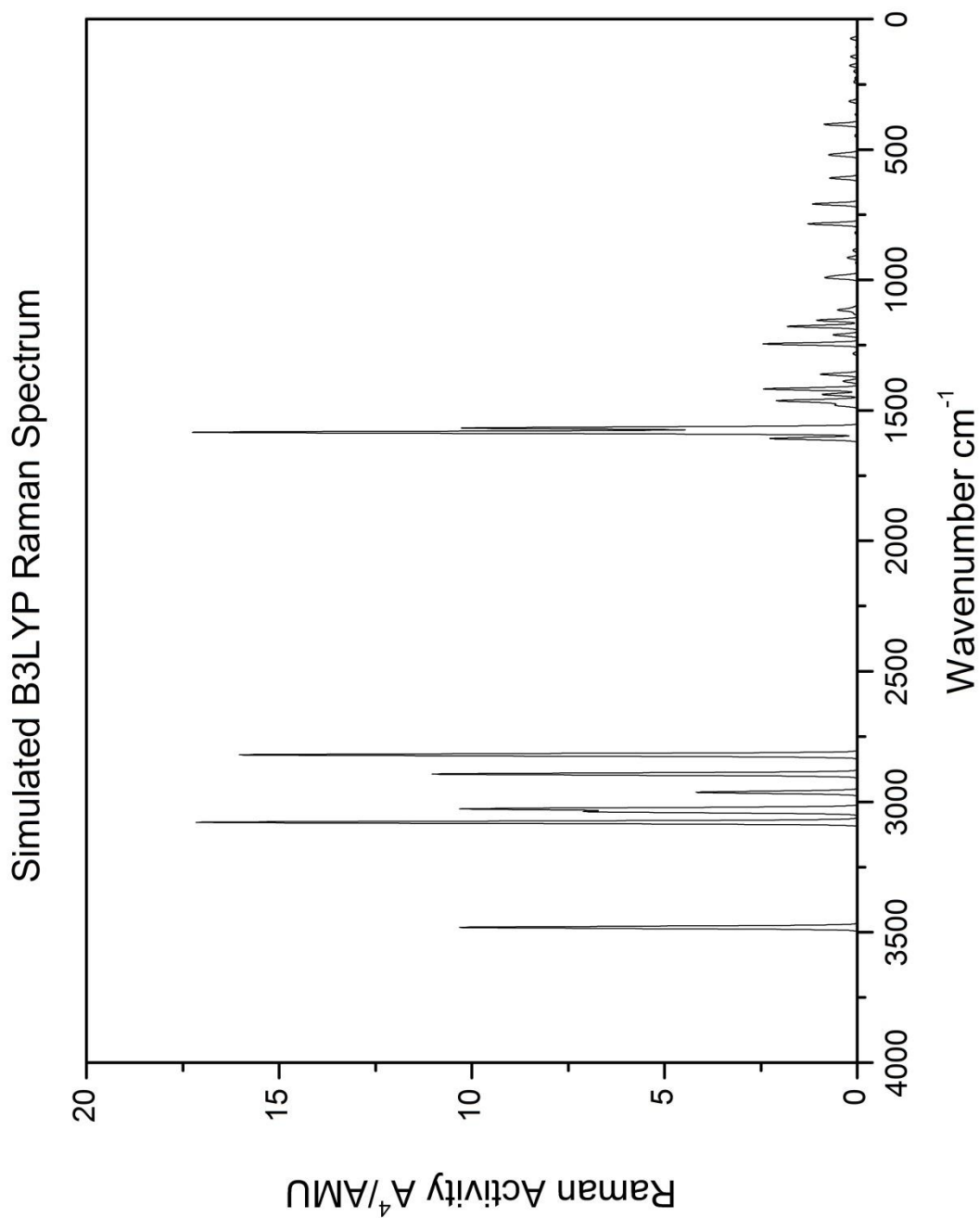


Figure 3a-12: Simulation of vanillin Raman spectrum from the molecule fixed in the solid phase crystal structure; simulation uses the B3LYP method (scale factor 0.95852, peaks set to uniform  $10 \text{ cm}^{-1}$  FWHM).

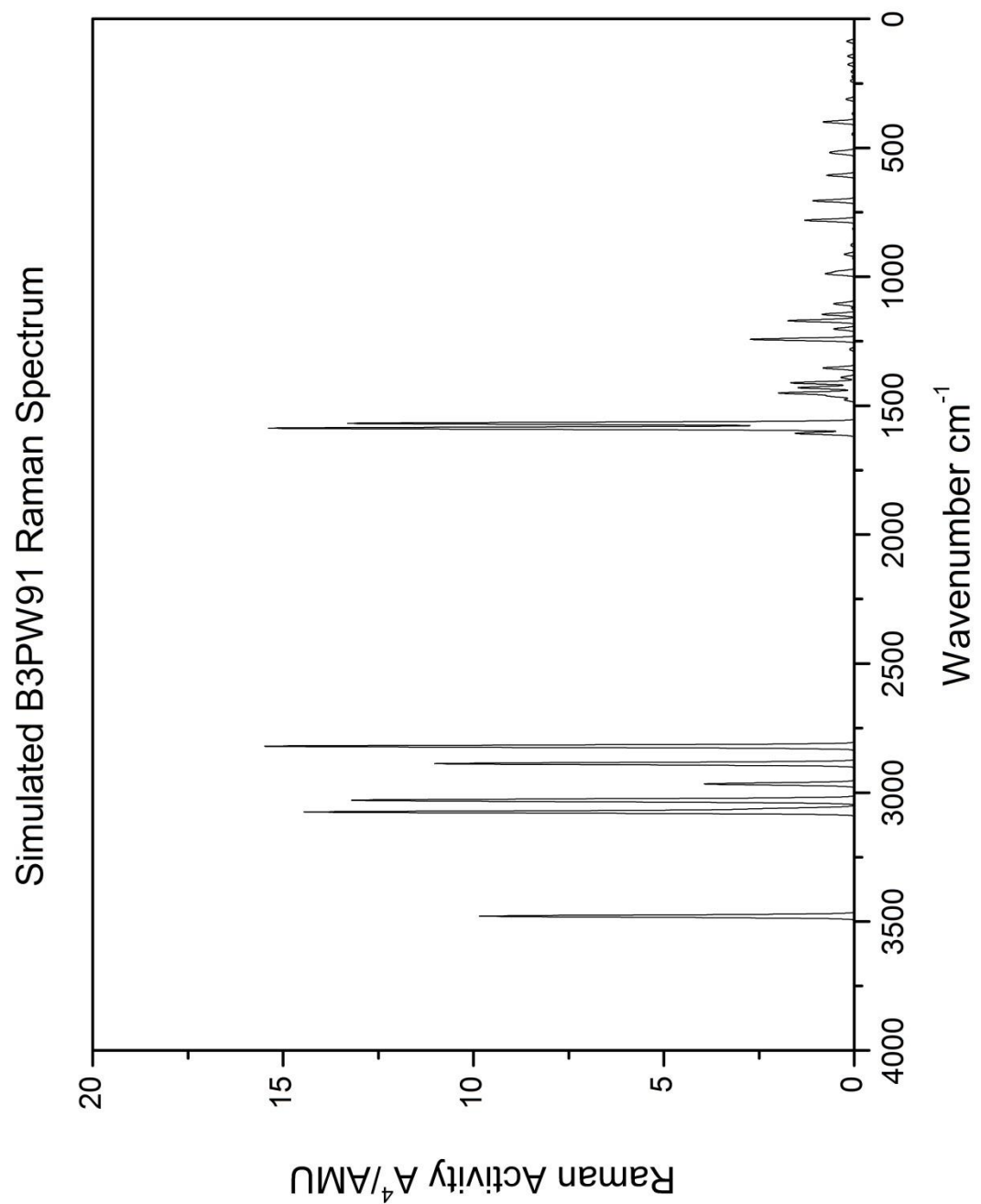
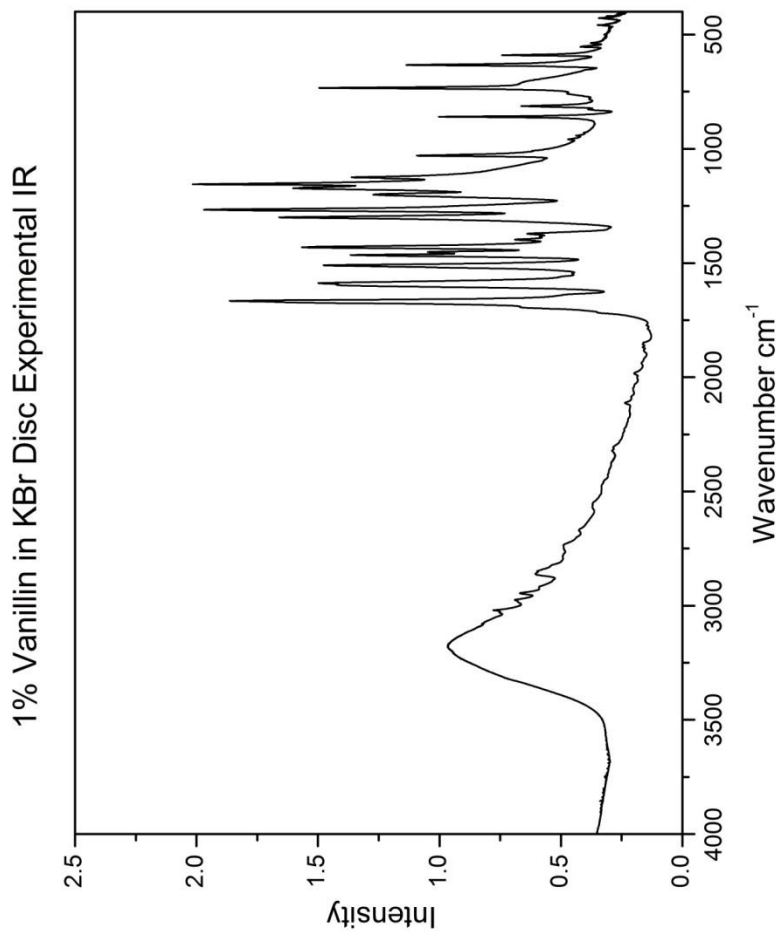


Figure 3a-13: Simulation of vanillin Raman spectrum from the molecule fixed in the solid phase crystal structure; simulation uses the B3PW91 method (scale factor 0.95325, peaks set to uniform  $10 \text{ cm}^{-1}$  FWHM).

### 3a-2-2 Simulated Infrared Spectra

Experimental data was obtained for vanillin from the dry powder sample, ground in a pestle and mortar, dried in a 60° oven for 24 hours, mixed with powdered KBr and pressed into a 10mm diameter, ~1mm thickness disc. Vanillin concentration was calculated at a mole fraction of  $x_V = 0.0102$  (c.a. 1%); the experimental infrared transmission is plotted here in *Figure 3a-14* at a resolution of 0.5  $\text{cm}^{-1}$ , with the labelled significant peaks tabulated in *Table 3a-16*:



*Figure 3a-14: Experimentally obtained infrared reference spectrum of vanillin powder, pressed in a KBr disc.*

<b>Position (cm<sup>-1</sup>)</b>	<b>Intensity (Abs Units<sup>2</sup>)</b>	<b>Full Width at Half Maximum (cm<sup>-1</sup>)</b>
589.55	0.370	6.01
632.90	0.756	9.20
733.62	0.845	8.19
813.30	0.290	9.21
859.87	0.627	6.00
1023.10	0.271	19.19
1030.17	0.385	6.02
1124.29	0.412	5.59
1130.22	0.227	5.99
1154.17	0.982	7.60
1172.62	0.782	17.60
1201.42	0.653	17.23
1266.93	1.154	14.02
1300.08	0.925	15.40
1371.08	0.330	14.99
1386.17	0.253	14.81
1397.73	0.236	9.51
1413.07	0.298	24.31
1430.77	1.130	16.03
1452.10	0.634	10.50
1466.33	0.932	12.00
1510.77	1.023	16.51
1587.51	1.069	20.46
1601.66	0.628	12.52
1642.86	0.149	13.81
1665.51	1.392	15.03
1676.37	0.529	8.50
1689.45	0.416	33.01
1852.75	0.033	19.65
1868.97	0.019	8.21
1882.69	0.018	16.08
1937.02	0.012	12.94
1982.63	0.027	16.29
2112.04	0.027	12.41
2861.94	0.110	18.80
2944.82	0.098	16.40
2974.97	0.086	18.40
3019.21	0.100	9.41

*Table 3a-16: Experimental IR peak wavenumber values, intensities and widths; peak parameters determined by manual fitting with Gaussian functions.*

We can see that although there are fewer clear peaks visible in the powder/KBr disc, they show good agreement with the nearest equivalent observed wavenumbers seen in the Raman (while a strong signal in one is generally associated with a weak one in the other, the two techniques are not expected to be mutually exclusive for a molecule without a centre of symmetry):

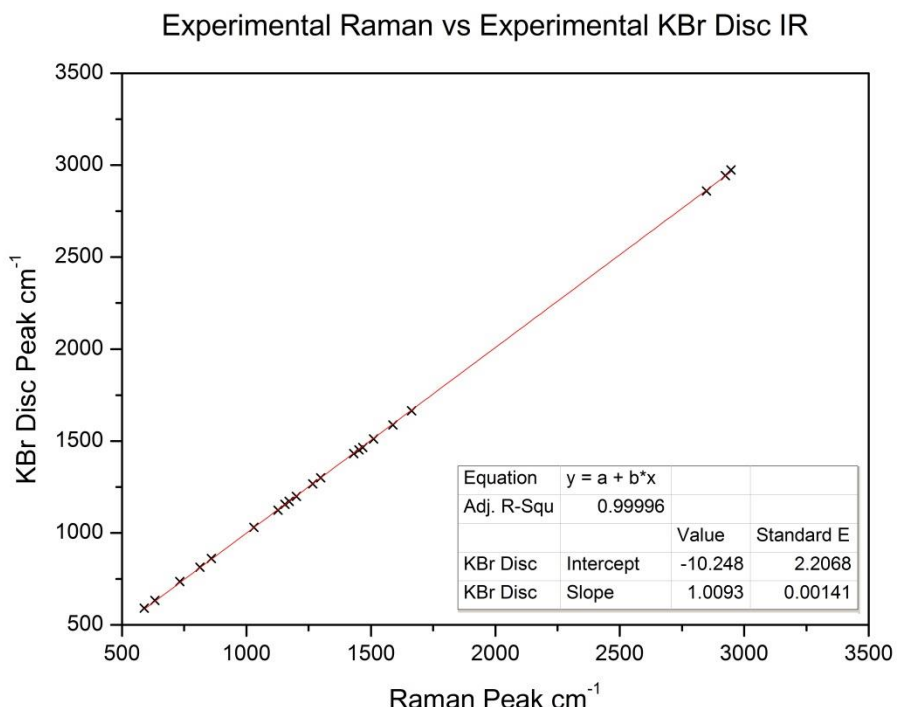


*Figure 3a-15: Linear relationship between Raman and infrared experimental data for vanillin powder.*

The large, broad peak at  $\sim 3200\text{ cm}^{-1}$  has been omitted from this plot; this signal is assigned to a strongly hydrogen-bonding population of residual water atoms in the sample. This signal remains strong despite the powdered vanillin sample spending a 48 hour drying period in a  $60^\circ\text{C}$  oven.

Again, for this type of plot the accuracy of the linear fit is given by the  $R^2$  residual, and the scalar relationship by the gradient of the line. As would be

expected for the two complementary techniques, with an  $R^2$  of 0.99996 and a slope of 1.0093 the two sets of data points are in very good agreement.

Because of this good relationship (and due to the comparatively small number of peaks) the same scale factor(s) calculated for the Raman will be used for the IR spectra wavenumber values. Using the same method as for the Raman spectra above equivalent plots can be produced for the infrared in *Figures 3a-16 and 3a-17* below; data for scaled wavenumber values and relative IR intensities can be found in *Tables 3a-17 and 3a-18* (again, reproducing intensity data first found in *Tables 3a-5 and 3a-9*):

<b>Calculated Peak Wavenumber (<math>\text{cm}^{-1}</math>)</b>	<b>IR Intensity I (KM/ Mole)</b>
74.53	11.57
107.28	0.18
144.14	9.70
177.91	0.08
200.30	7.52
226.83	4.09
240.77	0.04
315.19	3.15
365.60	3.06
403.42	0.69
446.73	3.41
515.88	3.61
521.63	9.28
522.04	151.38
574.71	17.97
609.25	57.37
680.72	0.28
708.71	41.42
784.78	1.92
818.97	36.41
886.26	25.30
914.63	3.76
934.51	3.76
983.84	2.86
991.97	58.76
1105.39	60.97
1114.94	0.52

1127.48	52.40
1154.37	89.83
1177.71	238.55
1210.35	38.25
1245.05	228.69
1281.99	24.77
1361.31	4.87
1388.03	44.23
1417.60	91.74
1438.66	4.38
1462.49	12.66
1471.01	135.44
1480.52	24.60
1567.47	135.64
1583.46	166.56
1607.49	62.60
2819.97	129.57
2893.65	36.50
2963.64	33.13
3026.74	18.35
3037.93	10.63
3074.67	4.76
3078.53	6.52
3481.22	114.13

*Table 3a-17: Scaled simulated vibrational wavenumbers for B3LYP for the vanillin molecule fixed in the solid phase crystal structure, with associated infrared intensity values (wavenumber values scaled by 0.95852)*

<b>Calculated Peak Wavenumber (cm<sup>-1</sup>)</b>	<b>IR Intensity I (KM/ Mole)</b>
87.00	11.47
114.56	0.01
144.61	9.66
176.81	0.09
204.83	8.21
224.36	4.23
240.39	0.10
311.46	3.30
367.46	3.08
399.63	0.71
446.93	3.72
513.96	3.76
519.18	6.45
522.59	156.09
572.10	18.33
606.43	55.96
678.05	0.47
705.37	43.99
780.96	2.65
814.31	37.64
877.20	27.09
912.67	4.11
929.43	3.70
979.48	3.03
988.89	57.23
1100.36	64.64
1105.38	0.32
1121.72	43.49
1145.72	80.48
1170.44	239.65
1202.07	43.42
1242.62	193.69
1281.27	63.19
1353.79	4.92
1390.18	41.23
1411.29	70.59
1429.80	26.57
1450.63	13.60
1462.22	80.98
1477.02	74.96
1568.38	179.04
1586.79	154.36
1607.12	44.08
2820.26	125.03
2887.71	35.36
2966.50	29.94

3027.68	16.53
3033.06	9.35
3063.65	4.31
3075.08	5.67
3478.99	117.35

*Table 3a-18: Scaled simulated vibrational wavenumbers for B3PW91 for the vanillin molecule fixed in the solid phase crystal structure, with associated infrared intensity values (wavenumber values scaled by 0.95325).*

Simulated B3LYP IR Spectrum

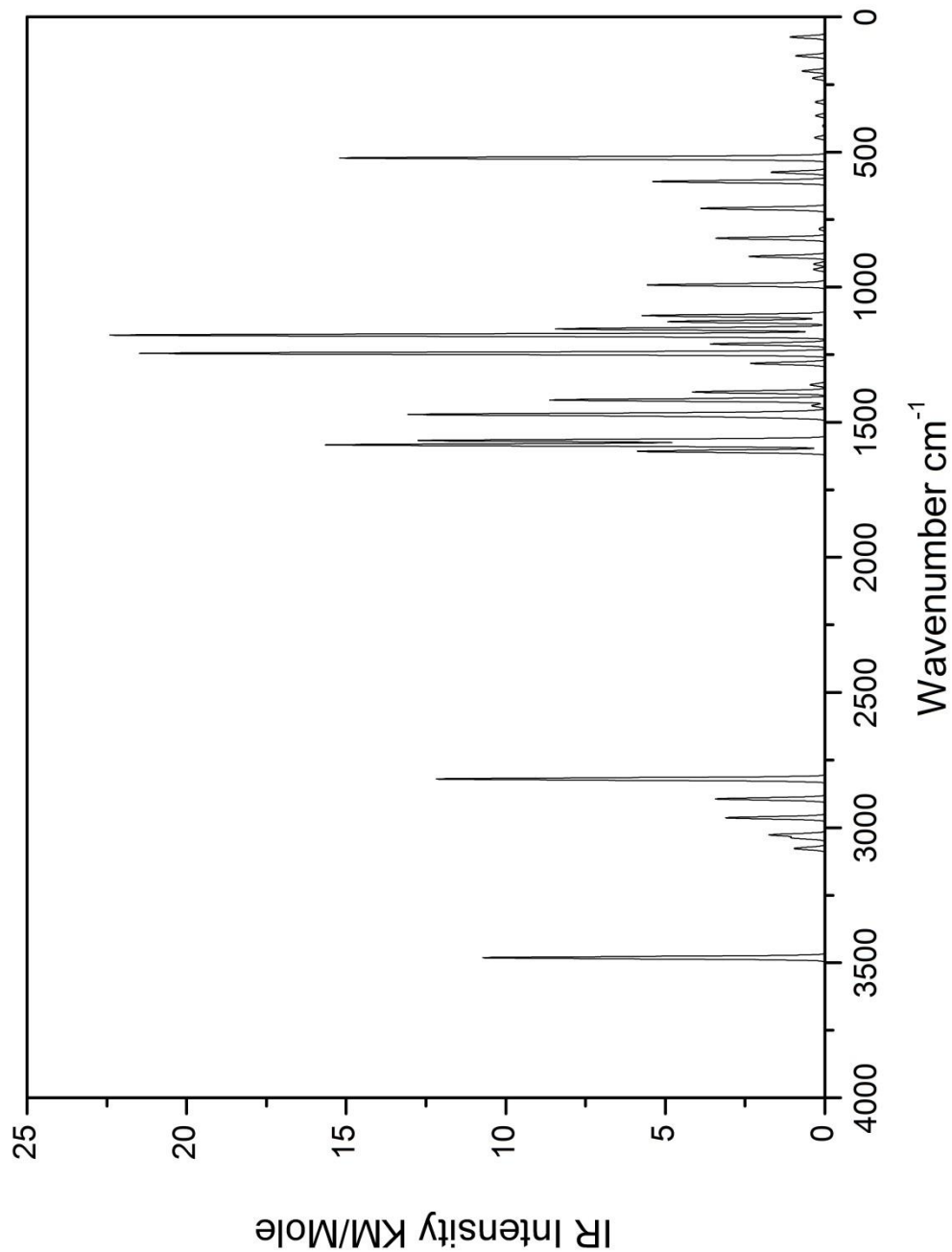


Figure 3a-16: Simulation of vanillin IR spectrum from the molecule fixed in the solid phase crystal structure; simulation uses the B3LYP method (scale factor 0.95852, peaks set to uniform 10 cm<sup>-1</sup> FWHM).

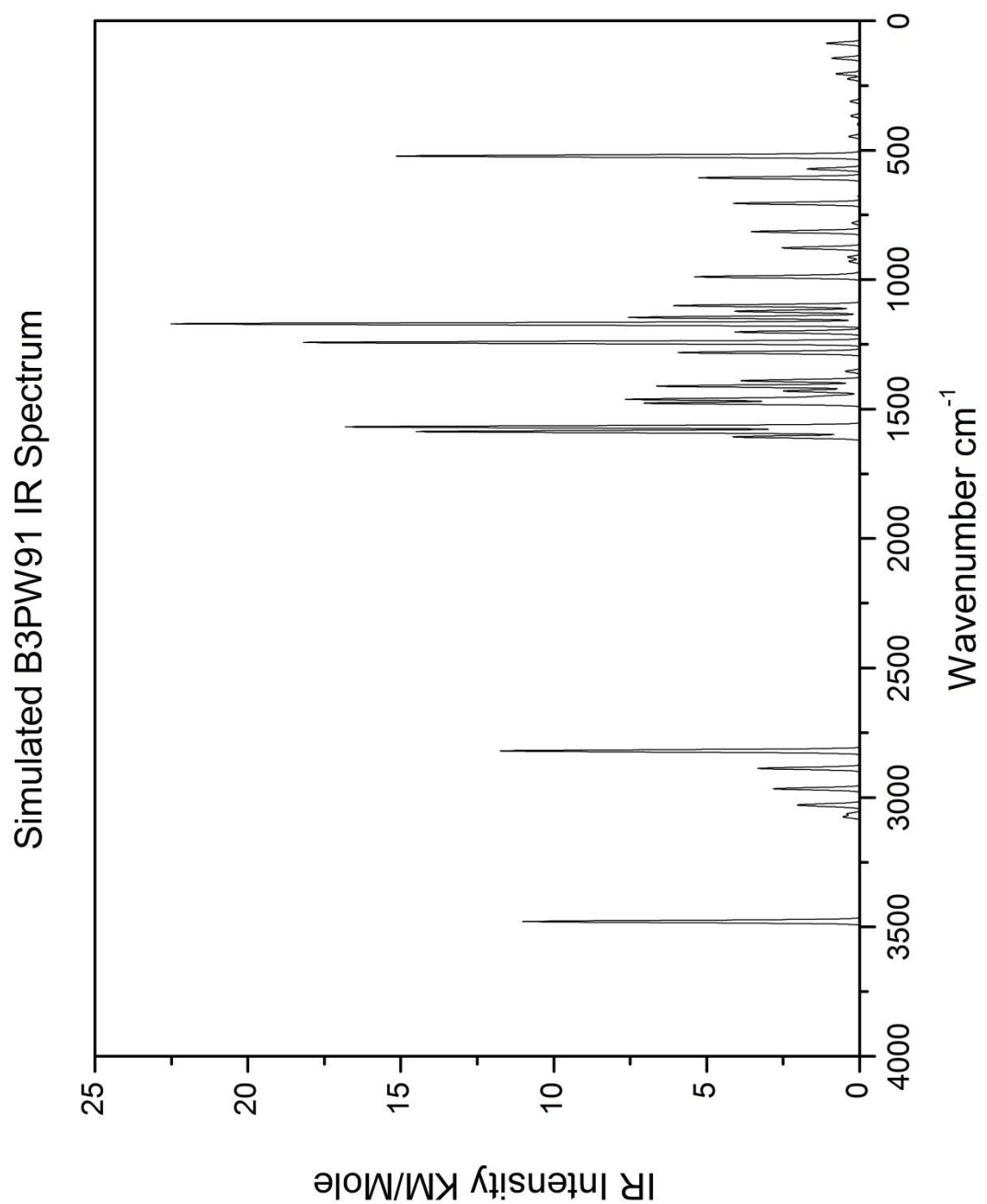
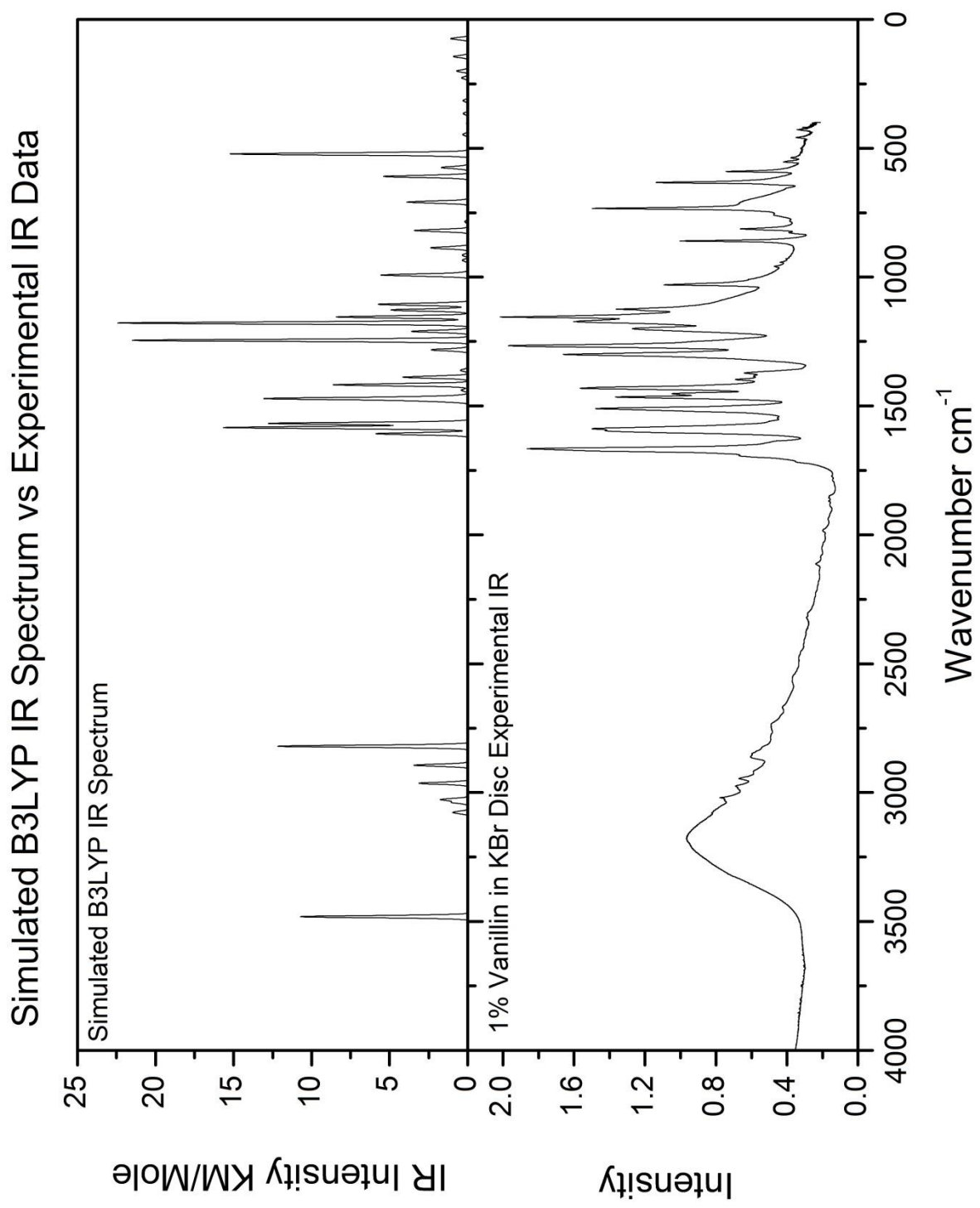


Figure 3a-17: Simulation of vanillin IR spectrum from the molecule fixed in the solid phase crystal structure; simulation uses the B3PW91 method (scale factor 0.95325, peaks set to uniform 10  $\text{cm}^{-1}$  FWHM).

### **3a-3: Conclusions and Application to Experimental Systems**

Solid phase simulations using Density Functional Theory methods produce interesting results whose patterns of intensity distribution bear a close similarity to the experimentally observed spectra. The practical application of these simulations however appears of limited use in making *accurate* predictions for the solid phase spectra of molecules such as vanillin, due to what appear to be calculation artefacts present in vibrations involving strongly electronegative atoms, or in regions of high electron density.



*Figure 3a-18: B3LYP simulated IR spectrum (top) versus KBr Disc infrared Reference Sample of solid-state vanillin (bottom) over the 4000-0  $\text{cm}^{-1}$  range.*

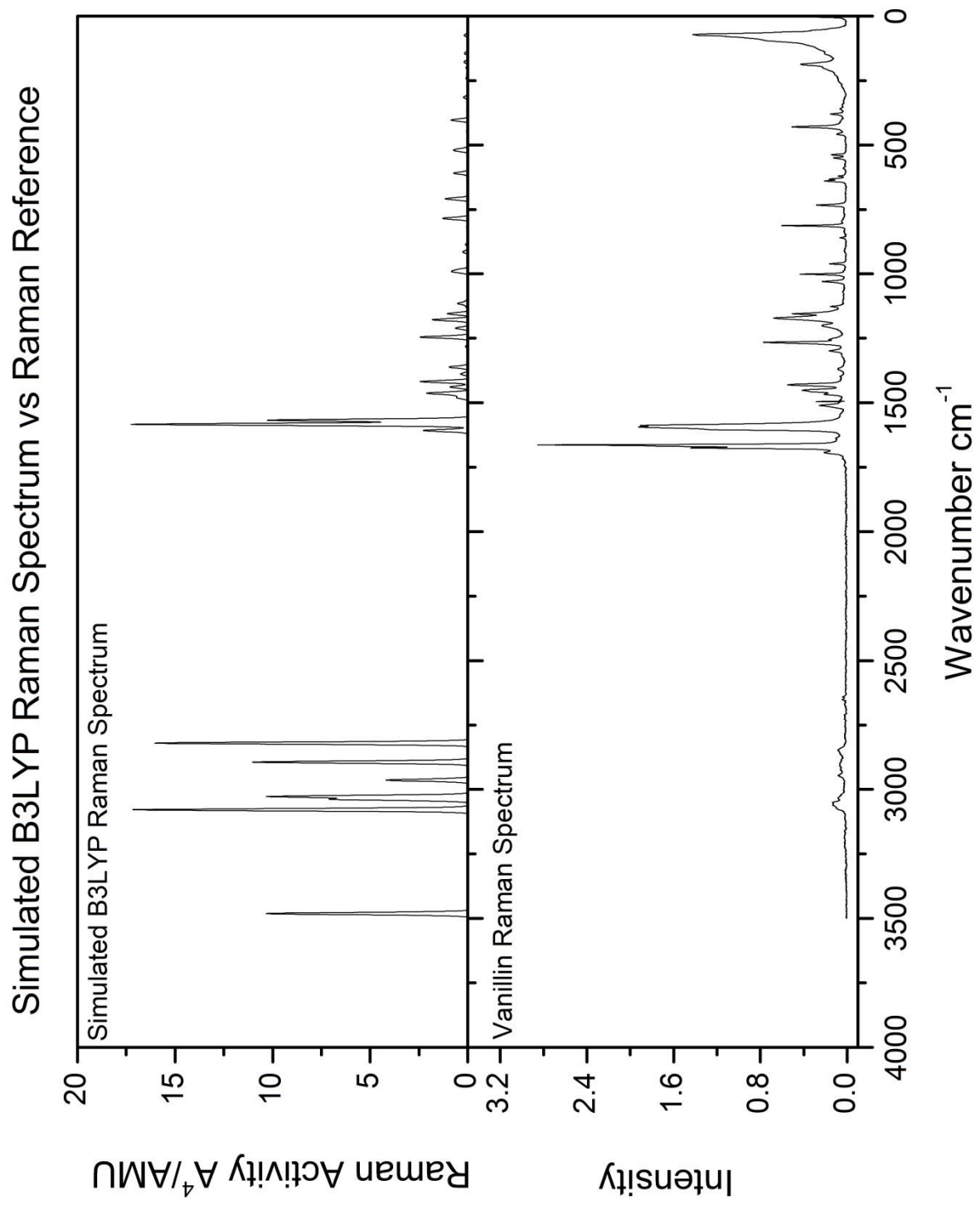


*Figure 3a-19: B3LYP simulated Raman spectrum (top) verses Raman Reference Sample of solid-state vanillin (bottom) over the 4000-0  $\text{cm}^{-1}$  range.*

Simulated B3PW91 IR Spectrum vs Experimental IR Data

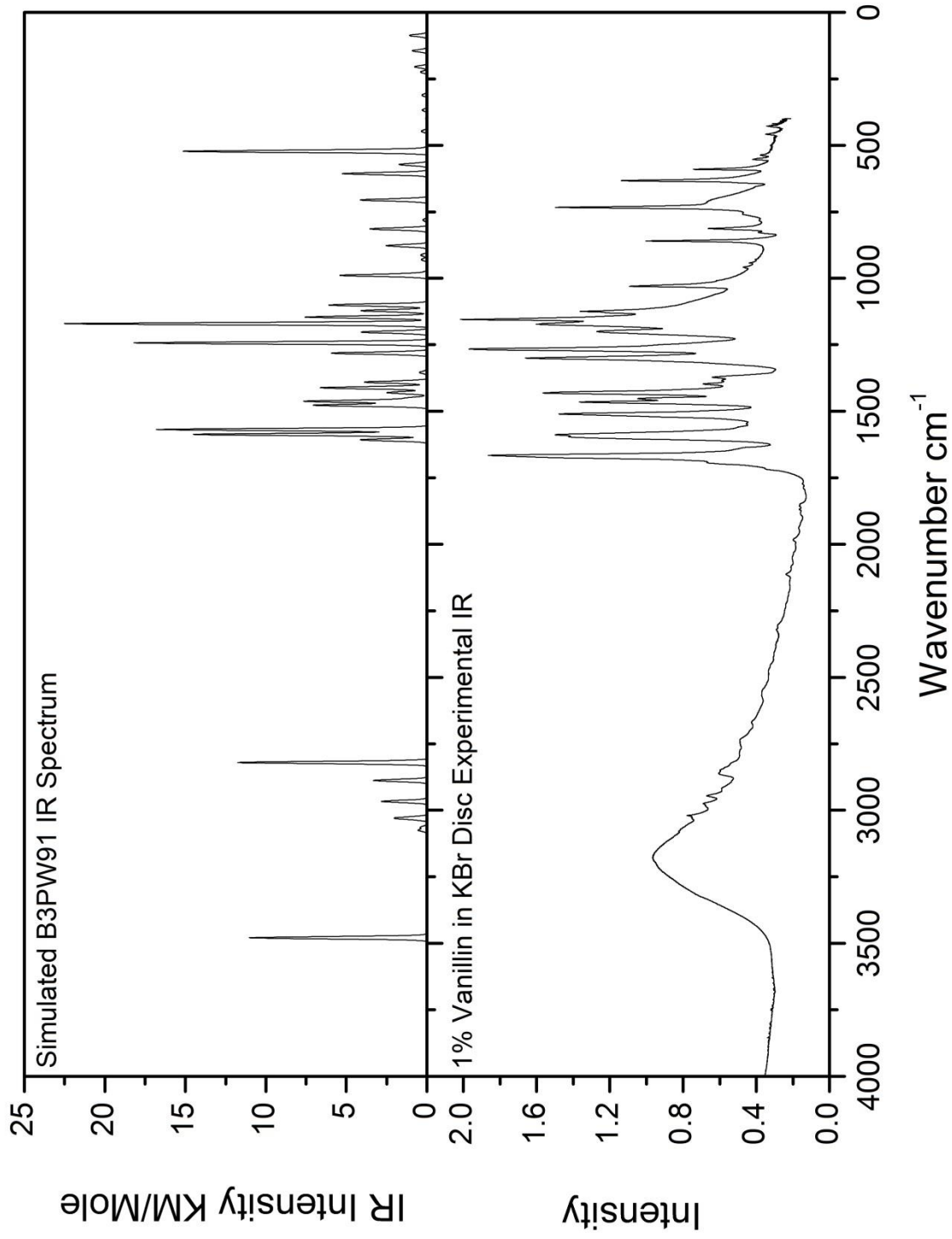


Figure 3a-20: B3PW91 simulated IR spectrum (top) versus KBr Disc infrared Reference Sample of solid-state vanillin (bottom) over the 4000-0 cm<sup>-1</sup> range.

Simulated B3PW91 Raman Spectrum vs Raman Reference

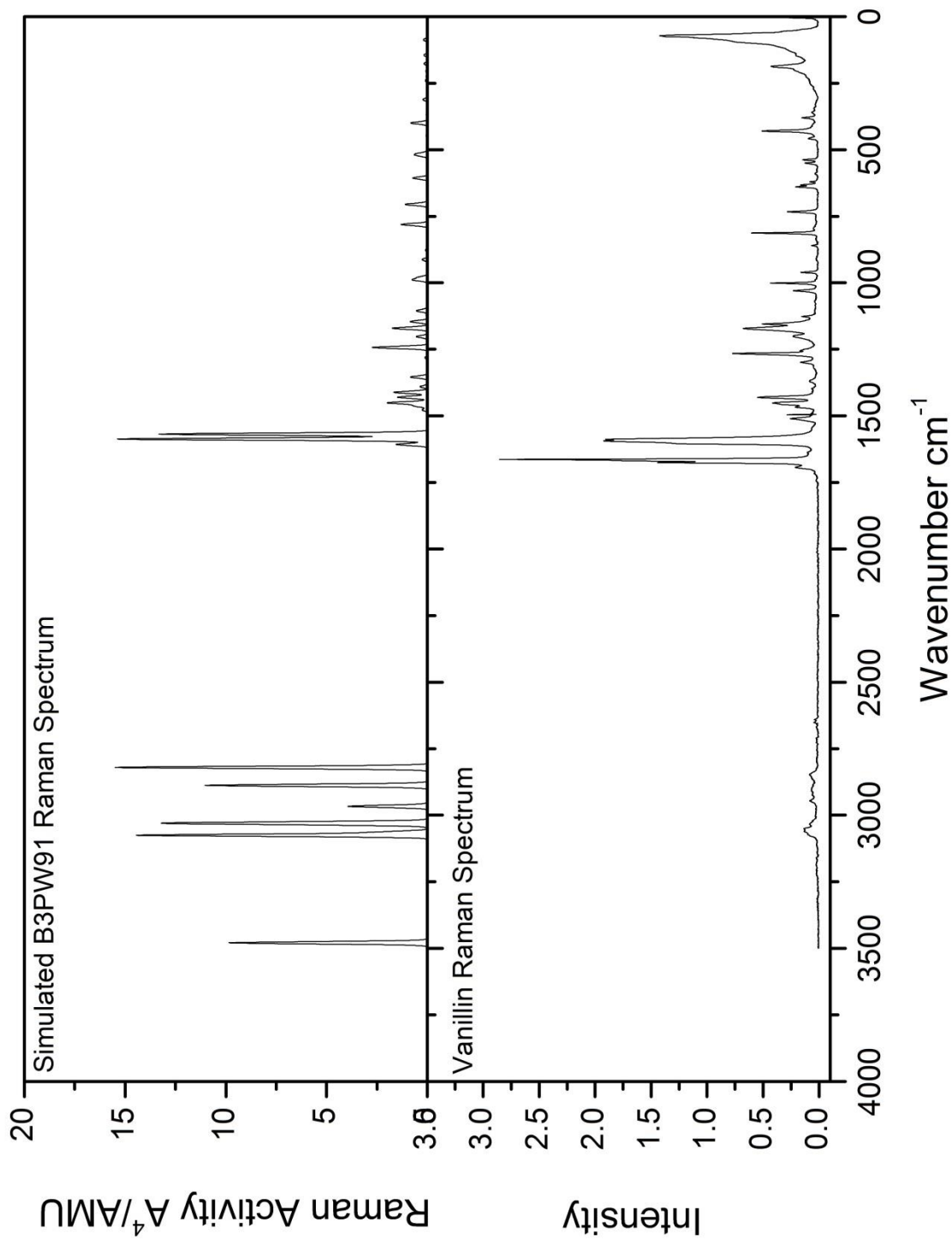


Figure 3a-21 B3PW91 simulated Raman spectrum (top) verses Raman Reference  
Sample of solid-state vanillin (bottom) over the  $4000-0\text{ }cm^{-1}$  range.

Some significant differences can be seen between the simulated and experimental Raman data; this is likely due to the restrictions imposed on the molecule in the original crystal form. While the molecule is fixed in both atomic bond length and angle during the optimisation process, it is still treated as if it exists in a vacuum with no other nearby atoms with which to interact. Although it is possible to simulate the effect of other molecules in close proximity by repeating the structure of the molecule in the input for the Gaussian program, introducing a greater number of particles would increase the necessary processing time geometrically. Fixing the molecular bond lengths and angles rather than optimising freely acts as a serviceable approximation of the steric effects present in the crystal state, and which have the greatest effect on the vibrations of the molecule.

Of particular note is the wide band of vibrations that are calculated in both methods between  $\sim 2700$  and  $3600\text{ cm}^{-1}$ : these bands are calculated as having a strong intensity in the Raman simulations, but show small signal intensity relative to other structure observed in the experimental data. Given that these signals arise from ring and oxygen hydrogen stretching transitions, it is reasonable to assume that this reduction in absorption intensity indicates that they are constrained to some extent by the real intermolecular packing structure. It should not be forgotten, however, that this model lacks intermolecular effects that may have a significant effect on the system, particularly dipole interactions from the functional groups of neighbouring molecules- such interactions can be seen in the strong band of hydrogen bonding effects between  $3500\text{-}2500\text{ cm}^{-1}$  in the experimental data. Instead, vibrations each appear as distinct absorption peaks of *user-defined* width, and will not show any of the small wavenumber shifts that would be influenced by such polar interactions.

Vibrational wavenumbers observed in *Figures 3a-18* and *3a-21* between  $1750$  and  $1200\text{ cm}^{-1}$  appear to underestimate the positions of bands that are typically associated with symmetric stretching modes involving carbon-bound oxygen. By far the single most significant difference is seen between the predicted wavenumber values of the double peak structure at  $1567.47$  and  $1583.46\text{ cm}^{-1}$  in the B3LYP and  $1568.38$  and  $1586.79\text{ cm}^{-1}$  in the B3PW91, and the experimental equivalents seen at

1593.85 and 1663.53  $\text{cm}^{-1}$ ; these peaks are attributed in literature to the  $\nu(C = O)$  and  $\nu_{as}(CC)$  vibrations though the Density Functional Theory calculation process calculates these as highly mixed modes, *both* involving heavy deformation of the carbon ring and out-of-plane asymmetric stretching of carbon-hydrogen bonds. Both simulations show a smaller side peak at 1607.49 and 1607.12 in B3LYP/ B3PW91 respectively that could be an expression of the peak seen in the experimental at 1693.39  $\text{cm}^{-1}$ . A similar set of phenomena are observed in the results of the infrared calculations shown in *Figures 3a-18* and *3a-21*: visible peaks above 200  $\text{cm}^{-1}$  and below 1200  $\text{cm}^{-1}$  show close agreement in both the B3LYP and B3PW91 methods. Between these ranges, however, equivalent simulated vibrations are shifted to lower wavenumber values by a varying margin of up to 10% of the experimental value. A full description of the calculated vibrational modes can be found in *Table 3a-19*:

	Calculated Vibrational Wavenumber (cm <sup>-1</sup> )	
Vibrational Mode	B3LYP	B3PW91
$\tau\text{CH}_3$	74.5341	86.9993
$\tau\text{CH}_3 + \tau\text{Ph}^1$	107.2752	114.5582
$(\delta\text{HC=O} + \delta\text{OCH}_3)^1$	144.1381	144.6120
$\tau\text{O-CH}_3 + \tau\text{Ph}$	177.9077	176.8059
$\gamma\text{HC=O} + \tau\text{Ph}$	200.2964	204.8295
$(\delta\text{HC=O} + \delta\text{OCH}_3)^2$	226.8315	224.3599
$\tau\text{O-CH}_3 + \tau\text{HC=O}$	240.7744	240.3914
$(\delta\text{C-OCH}_3 + \delta\text{C-CHO} + \delta\text{C-OH})^1$	315.1861	311.4612
$\tau\text{Ph}$	365.5984	367.4602
$(v^{\text{as}}\text{Ph}^1 + v\text{C-CHO})$	403.4220	399.6339
$\gamma\text{Ph}^1$	446.7339	446.9322
$\gamma\text{C-OH} + v\text{O-H}$	522.0400	522.5861
$(\delta\text{C-OCH}_3 + \delta\text{C-CHO} + \delta\text{C-OH})^2$	521.6311	519.1789
$\delta\text{Ph} + \delta\text{C-O-CH}_3$	515.8818	513.9588
$\gamma\text{Ph}^2$	574.7076	572.0978
$\delta\text{Ph}$	609.2510	606.4272
$\gamma\text{Ph}^3$	680.7195	678.0497
$[\delta\text{Ph} + (\delta\text{C-O-CH}_3 + \tau\text{C-CHO})]^1$	708.7107	705.3735
$[\delta\text{Ph} + (\delta\text{C-O-CH}_3 + \tau\text{C-CHO})]^2$	784.7819	780.9600
$(v^{\text{Hydrogen}}\text{Ph} + \delta^{\text{Hydrogen}}\text{Ph})^1$	818.9678	814.3123
$(v^{\text{Hydrogen}}\text{Ph} + \delta^{\text{Hydrogen}}\text{Ph})^2$	886.2637	877.1981
$(v^{\text{Hydrogen}}\text{Ph} + \gamma^{\text{Hydrogen}}\text{Ph})$	934.5058	929.4265
$(v^{\text{as}}\text{Ph} + \delta\text{Ph})$	914.6277	912.6729
$\gamma\text{O-C-H}$	983.8398	979.4765
$(v^{\text{as}}\text{Ph} + \delta\text{Ph}) + v\text{O-CH}_3$	991.9731	988.8927
$(\delta^{\text{Hydrogen}}\text{Ph} + \delta\text{Ph}) + \tau\text{C-OH}$	1105.3911	1100.3573
$(\tau\text{C-OCH}_3 + \tau\text{C-CHO} + \tau\text{C-OH})$	1127.4821	1121.7185
$(\tau\text{C-CH}_3 + v^{\text{as}}\text{C-H}_3)$	1114.9400	1105.3776
$[(\tau\text{C-CH}_3 + \tau\text{C-OH}) + \delta^{\text{Hydrogen}}\text{Ph}]^1$	1177.7146	1170.4449
$[(\tau\text{C-CH}_3 + \tau\text{C-OH}) + \delta^{\text{Hydrogen}}\text{Ph}]^2$	1154.3693	1145.7194
$\delta\text{Ph} + \delta\text{C-O-H} + \delta^{\text{Hydrogen}}\text{Ph}$	1210.3465	1202.0683
$v^{\text{Sym}}\text{Ph} + \delta^{\text{Hydrogen}}\text{Ph}$	1245.0521	1242.6216
$v\text{Ph} + \delta\text{C-O-H}$	1281.9868	1281.2695
$\delta\text{C-O-H} + \delta^{\text{Hydrogen}}\text{Ph}$	1361.3062	1353.7939
$(\delta\text{C-O-H} + \delta^{\text{Hydrogen}}\text{Ph} + v^{\text{as}}\text{Ph})^1$	1388.0295	1390.1781
$(\delta\text{C-O-H} + \delta^{\text{Hydrogen}}\text{Ph} + v^{\text{as}}\text{Ph})^2$	1417.6043	1411.2901
$(v\text{O-CH}_3 + \delta\text{C-O-CH}_3 + v^{\text{sym}}\text{C-H}_3)$	1438.6595	1429.8041
$v^{\text{as}}\text{CH}_3^1$	1462.4912	1450.6275
$v^{\text{as}}\text{CH}_3^2$	1471.0120	1462.2175
$(v^{\text{as}}\text{Ph} + \delta\text{Ph} + v\text{C-OH} + \delta\text{C-O-H} + v\text{O-CH}_3 + \delta\text{C-O-})$	1480.5240	1477.0202
$[v^{\text{as}}\text{Ph} + (\delta\text{C-OH} + \delta\text{C-CHO} + \delta^{\text{Hydrogen}}\text{Ph})]^1$	1567.4686	1568.3819
$\delta\text{C-O-H} + v^{\text{as}}\text{H-C=O} + v^{\text{as}}\text{Ph}$	1583.4611	1586.7859

$[v^{as}Ph + (\delta C-OH + \delta C-CHO + \delta^{Hydrogen}Ph)^2]$	1607.4859	1607.1182
$vH-CO$	2819.9661	2820.2603
$v^{sym}CH_3$	2893.6533	2887.7054
$v^{as}CH_3^3$	2963.6362	2966.4987
$v^{as}CH_3^4$	3026.7388	3027.6774
$v^{Hydrogen}Ph^1$	3037.9331	3033.0630
$v^{Hydrogen}Ph^2$	3078.5285	3075.0758
$v^{Hydrogen}Ph^3$	3074.6733	3063.6543
$vO-H$	3481.2236	3478.9906

*Table 3a-19: Vibrational modes and their equivalent calculated wavenumber values (scaled by factors of 0.95852 and 0.95325) in B3LYP and B3PW91 respectively.*

*Descriptions of modes show the principle components in order of descending magnitude; stretching components of normal modes are designated by  $v$  (symmetric by  $v^{sym}$  and asymmetric by  $v^{as}$  where appropriate), deformation components by  $\delta$  and torsional components by  $\tau$ .*

Although a high degree of electronic delocalisation is seen between the ring and the functional substituents, the presence of electron-withdrawing oxygen groups in all three of the functional groups leaves the carbons in the 3 and 4 positions with a comparatively electropositive charge. While the bond lengths and angles in the solid crystal are fairly typical for aromatic bonding a relatively high electron density is seen on those ring carbons that are not directly bound to electron-withdrawing oxygen atoms, leading to a degree of polarisation across the central aromatic ring. The calculated normal modes of vibration for vanillin also suggest a great deal of interdependency between the vibrations of atoms that are well separated across both the ring and the side groups ( $\delta HC=O + \delta OCH_3$  in the third vibration quoted in *Table 3a-20*, for example), which can be well explained by the delocalisation of charge across the molecule. *Figures 3a-22a and b* show the charge separation over the molecule as calculated by the unmodified B3LYP and B3PW91 methods respectively.

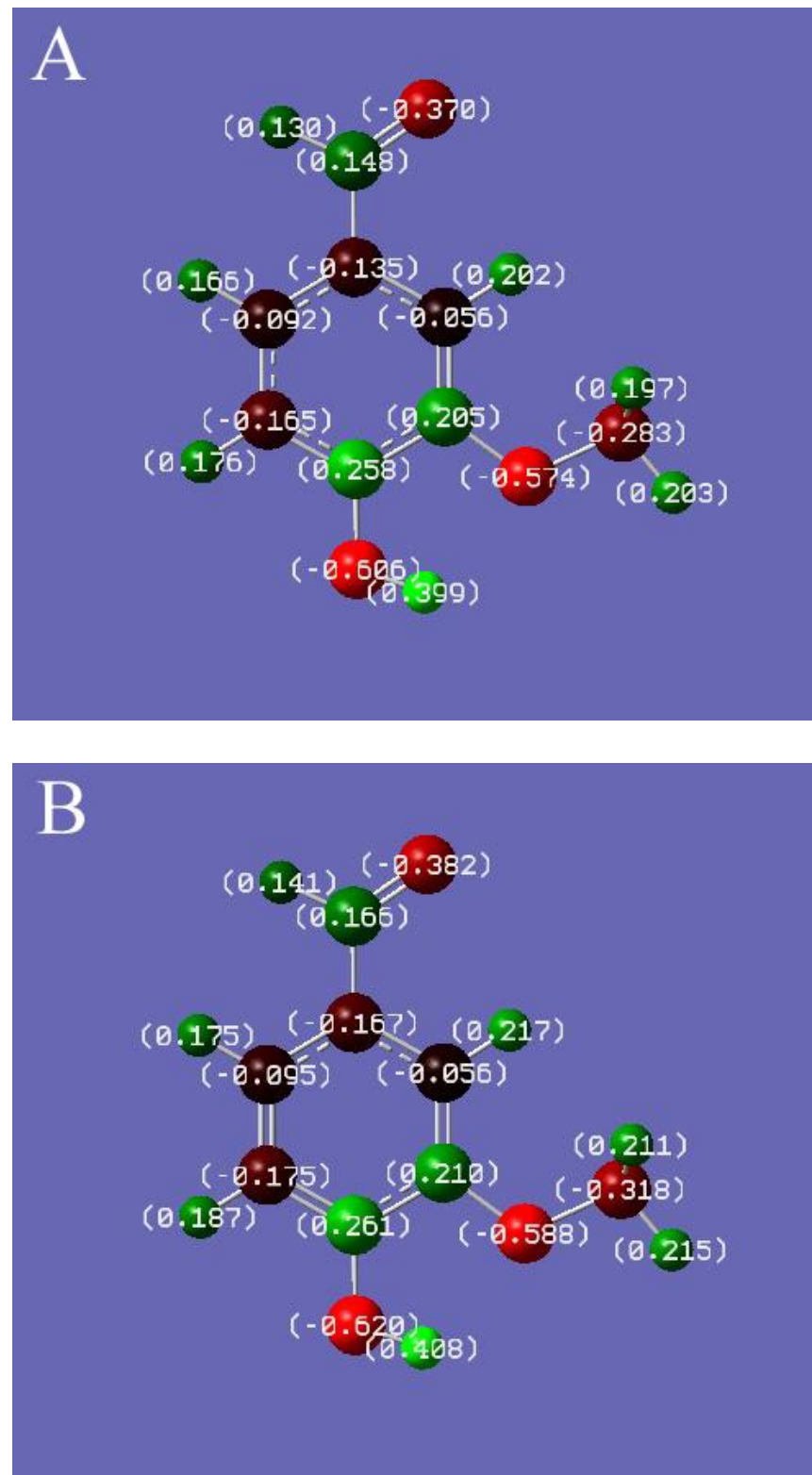


*Figure 3a-22a: Charge separation diagram of vanillin calculated using the B3LYP method; and b: Charge separation diagram of vanillin calculated using the B3PW91 method; original diagrams in colour with positive charges shown in shades of green and negative charges shown in shades of red, lighter shades indicating greater magnitude.*

It is known that the B3LYP and B3PW91 Correlation Functions tend to overestimate the energies of molecular bonds with strong dipole moments<sup>6,7</sup>, and is this polarisation that may have led to the unexpected degree of mixing of the calculated vibrational modes of vanillin- nonetheless, clear similarities in structure can be seen between the simulated and the experimentally obtained data compared in *Figures 3a-18 to 3a-21* above. These observed variations in vibrational position in the middle of the wavenumber range do not necessarily prevent the use of this technique for the prediction of structure in experimental spectra; though the resulting positions may be inaccurate when compared to the experimental ones, the *overall* distribution of intensity in the simulations follows a very similar pattern. With the application of this technique it may prove possible (see *Part II*) to predict the relative peak distributions in a molecule to a degree that isotopic splitting effects may be predicted (and thus compared to experimental data of sufficiently high resolution), even if the absolute wavenumber values of the bands are under- or overestimated.

## Chapter 3b: Gaussian Simulation Results Part II - Isolated Vanillin

### 3b-1: Determination of the Optimised Molecular Structure for Vibrational Calculation

The same initial optimisation method was used for the isolated phase vanillin structure determination as was for the solid, beginning with the molecular structure optimised to the global minimum. In the isolated phase we consider vanillin to be freely able to rotate and bend to occupy the most energetically favourable conformations possible, thus in the isolated case the atomic positions were *not* defined from the crystal structure and the molecule was instead geometrically optimised in its entirety using the B3LYP/ 6-311G calculation method. This produced the initial ‘optimised’ structure to be used in further simulation; as with the solid case, all further simulation for 4-hydroxy-3-methoxybenzaldehyde used the 6-311G basis set and modified versions of the B3LYP and B3PW91 functionals as listed in *Table 3b-1*:

Basis Set	Method	Modifications Used
6-311G	B3LYP	Diffuse Molecular Orbitals and Additional Accessible d-orbitals ('+d' notation)
6-311G	B3PW91	Diffuse Molecular Orbitals and Additional Accessible d-orbitals ('+d' notation)

*Table 3b-1: Methods and notation.*

Again, as with the solid state additional p-orbital modifications were omitted on the grounds that test calculations produced no visible differences in calculated frequencies or intensities for vibrations. In the previous chapter (*Chapter 3a*:

*Gaussian Simulation Results Part I - Solid Phase Vanillin*) a sequential evaluation of eight possible versions of B3LYP and B3PW91 was performed to find the method that generated the closest approximation to the well described experimental data; since in this case the experimental data is not as well described (please see *Chapter 1* for the full details of the Matrix Isolation process and the sample data obtained) and because a much larger number of simulations were necessary to describe the possible conformers and isotopic substitutions expected to be visible in this system, this investigation was limited to the use of only the two methods listed above.

For the sake of this text, all references to the above two functions/ basis set combinations will be written as B3LYP +d and B3PW91 +d respectively. These methods were chosen as the best available balance between computation time and efficiency, and the decision was made to produce both data sets (rather than simply one) as a comparative exercise between the results of using two popular exchange-correlation terms on the same target molecule.

The most probable changes in structure for the isolated molecule are rotations of its functional groups about single bonds; hence, after the initial optimisation of the structure the Gaussian program was used to calculate the ground-state energy levels for each rotational conformer of the molecule (in each method used)<sup>63</sup>. By scanning the functional groups of the simulated molecule through 360° rotation in 90 steps of 4°, the energy distributions were found to follow a sinusoidal distribution between maxima and minima over multiples of 90°. The most stable conformation (i.e. the rotational conformer of lowest energy) was thus found for each functional group:

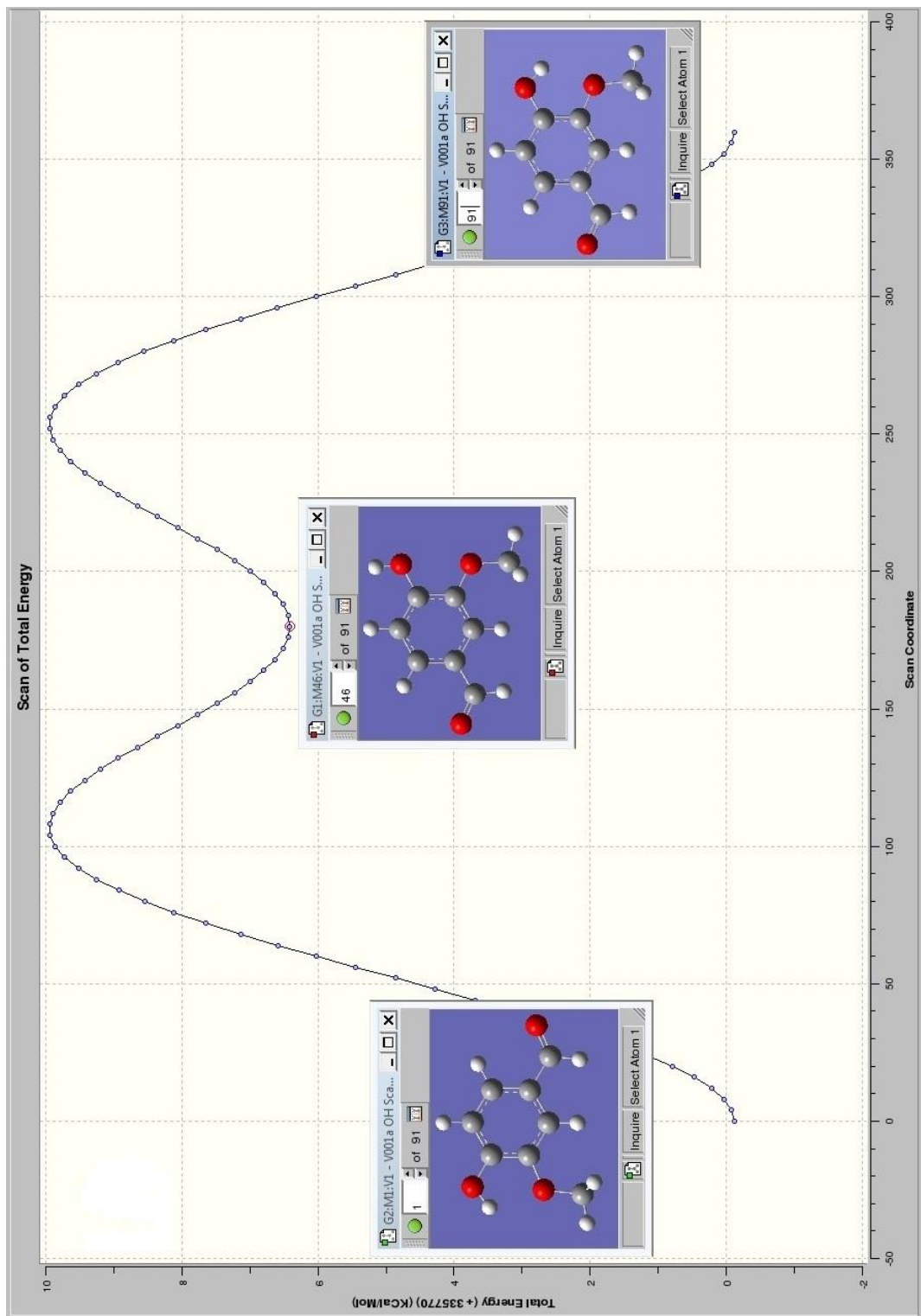


*Figure 3b-1a: Change in absolute energy of vanillin molecule with rotation of the OH group about the C-O bond axis. Sample structures are shown to indicate the orientation of the functional group at each stage.*

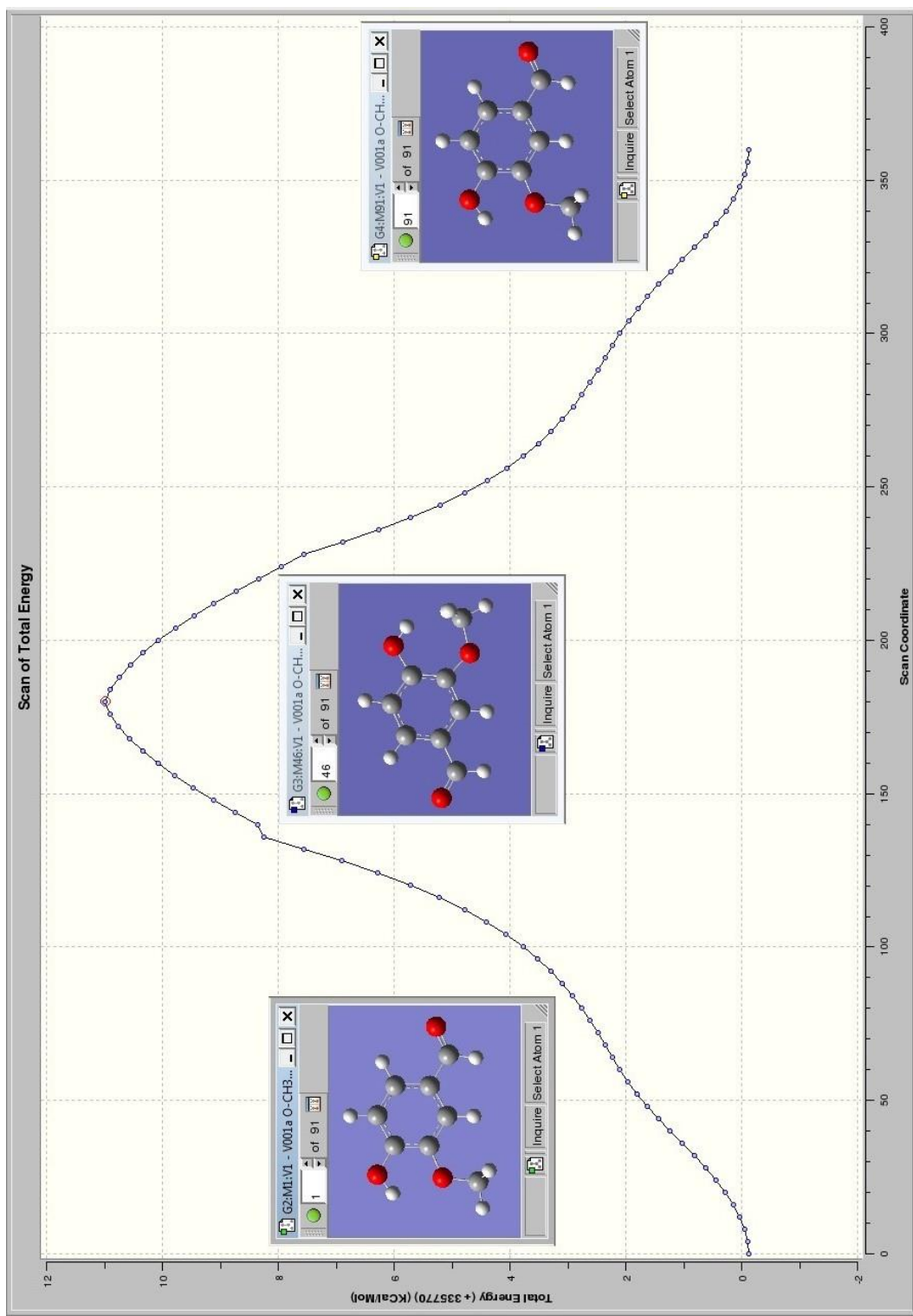


*Figure 3b-1b: Change in absolute energy of vanillin molecule with rotation of the O-CH<sub>3</sub> group about the C-O bond axis. Sample structures are shown to indicate the orientation of the functional group at each stage.*

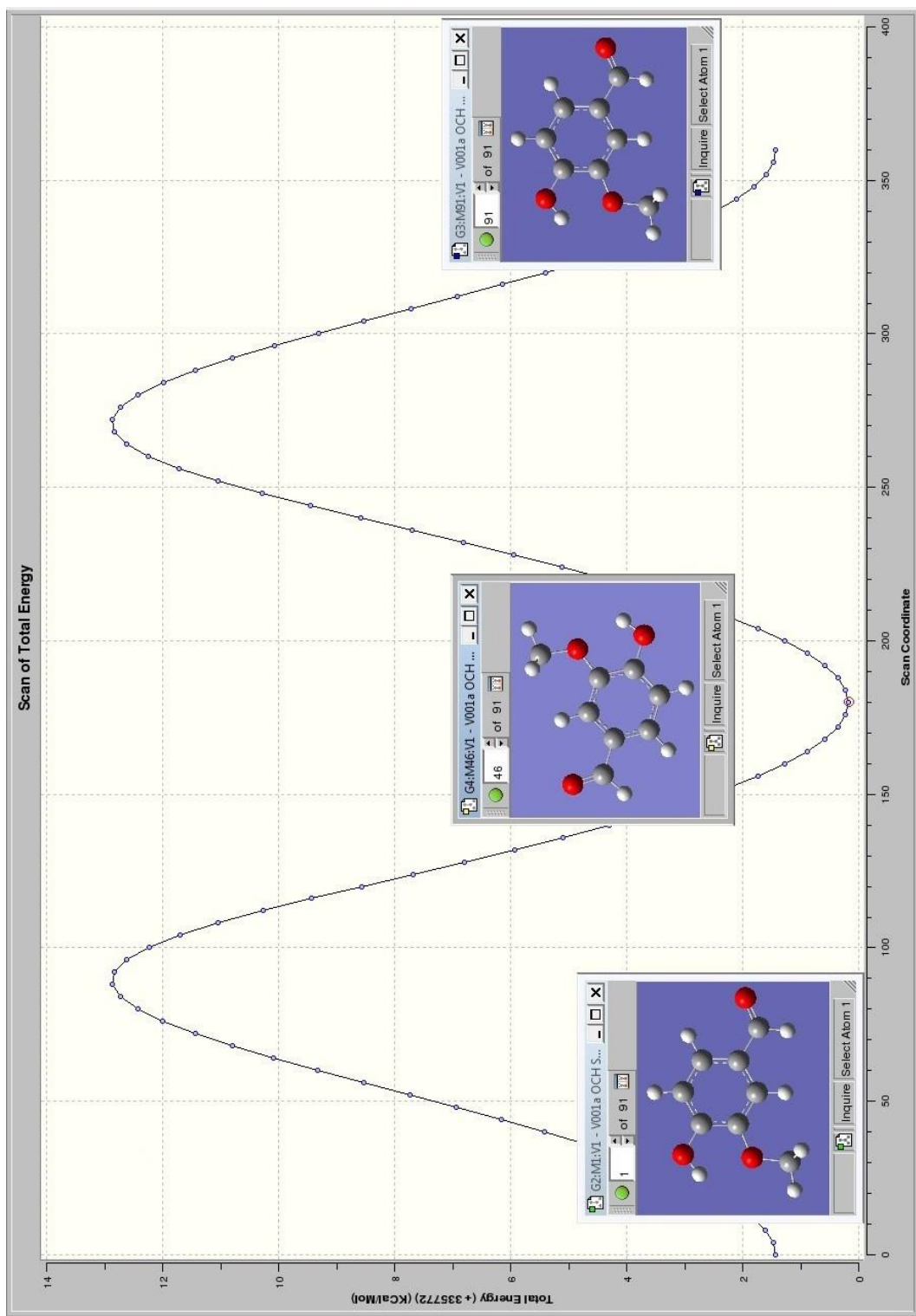


*Figure 3b-1c: Change in absolute energy of vanillin molecule with rotation of the CHO group about the C-C bond axis. Sample structures are shown to indicate the orientation of the functional group at each stage.*

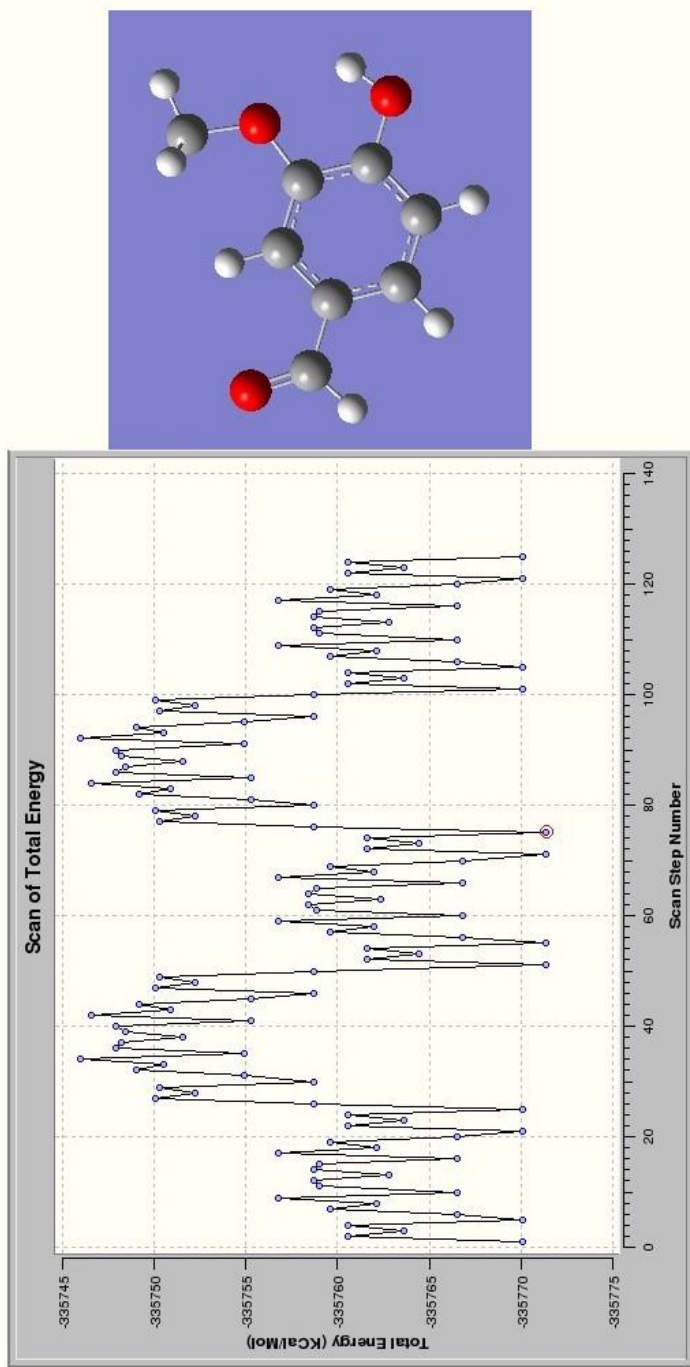


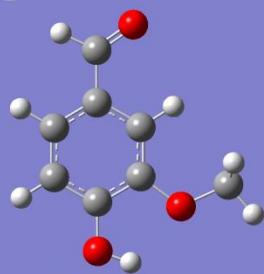
*Figure 3b-1d: Change in absolute energy of vanillin molecule with rotation of the OH group, the O-CH<sub>3</sub> group and the CHO group concurrently to find the global energy minimum. Sample structures are shown to indicate the orientation of the functional group(s) at each stage; the image indicated is the global energy minimum. This example is taken from the B3LYP process, but in diagrams of this resolution B3LYP and B3PW91 would be indistinguishable without data values.*

Using this data as a guide, the three functional groups were then rotated concurrently in each case to find the lowest *overall* energy state for the molecule (starting position plus four steps of  $90^\circ$  for each functional group, resulting in  $(n + 1)^x$  rotational structures where  $n$  is the number of steps and  $x$  is the number of rotating functional groups, for a total of 125 rotational structures; 23 of these structures are non-identical, and seven are either local or global minima). This process is very similar in principle to the method reported by *Cocinero, et al*<sup>63</sup>, in their 2010 publication, and shows good agreement in that the lowest overall energy state is indeed calculated as being the *s-cis* conformation, followed by the *s-trans* conformer. The slight ‘kink’ in the energy plot seen in Figure 3b-1b is due to a minor loss of symmetry in the molecule as a result of the optimisation process: this is unavoidable due to the optimisation method used, and for all practical purposes this loss has been disregarded as it constitutes an energy difference less than 1% of the magnitude of that generated by a full rotation of the C-O-CH<sub>3</sub> group. The calculated energy values for each conformer are shown below in *Table 3b-2* along with the basis set and method used; a graphical representation of the structures can be found in *Figure 3b-2*.

	<b>Calculated Absolute Energy Value (Hartree Units)</b>	
<b>Number</b>	<b>B3LYP +d</b>	<b>B3PW91 +d</b>
001	-535.462	-535.234
011	-535.460	-535.244
030	-535.449	-535.232
036	-535.447	-535.230
051	-535.454	-535.238
061	-535.453	-535.236
080	-535.448	-535.232
086	-535.302	-535.085

*Table 3b-2: Calculated energy levels for the rotational conformers of Vanillin.*

Structure 001



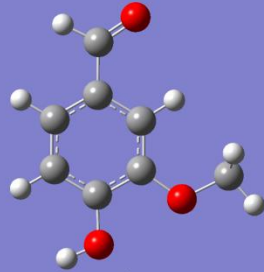
OH Hydrogen and CHO Oxygen oriented towards O-CH<sub>3</sub> group; all in plane.

Structure 030



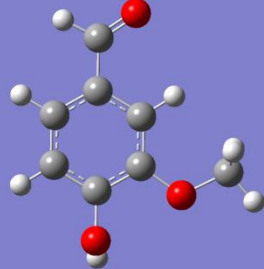
CHO Oxygen oriented towards O-CH<sub>3</sub> group; OH Hydrogen 90 degrees out of plane.

Structure 051



CHO Oxygen oriented towards O-CH<sub>3</sub> group, OH Hydrogen oriented away; all in plane.

Structure 080



CHO Oxygen oriented towards O-CH<sub>3</sub> group; OH Hydrogen directed 90 degrees into plane.

Structure 011



OH Hydrogen oriented towards O-CH<sub>3</sub> group, CHO Oxygen oriented away; all in plane.

Structure 036



CHO Oxygen oriented away from O-CH<sub>3</sub> group; OH Hydrogen 90 degrees out of plane.

Structure 061



OH Hydrogen and CHO Oxygen oriented away from O-CH<sub>3</sub> group; all in plane.

Structure 086



CHO Oxygen oriented away from O-CH<sub>3</sub> group; OH Hydrogen directed 90 degrees into plane.

*Figure 3b-2a to h: The eight lowest-energy rotational configurations of the functional groups of vanillin. Original pictures in colour: the light coloured spheres represent hydrogen, the grey carbon and the dark spheres represent oxygen atoms.*

Structure 001

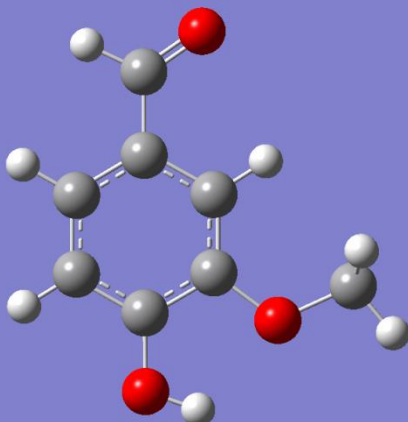


*Figure 3b-2i: The overall lowest-energy rotational configuration of vanillin. Again, original picture in colour: the light coloured spheres represent hydrogen, the grey carbon and the dark spheres represent oxygen atoms. This structure is properly labelled as the s-cis conformation, while structure 011 is more properly referred to as s-trans; for the sake of this text, however, they shall be labelled respectively by number to avoid confusion.*

## **3b-2 Vibrational Spectra Calculation and Evaluation for 4-Hydroxy-3-Methoxy Benzaldehyde**

### **3b-2-1: Energy Level Distribution for Rotational Conformers**

Now that the seven lowest energy conformations have been determined it becomes possible to not only determine their infrared vibrational spectra, but also to use their relative energy level values in conjunction with the Boltzmann Distribution to calculate their relative populations assuming conditions of equilibrium. Given that each rotational conformer is expected to give a slightly different vibrational spectrum, this means that a composite of these spectra weighted for predicted population should bear close resemblance to the experimental spectra. During the present investigation experimental data was not obtained for matrix isolated Raman spectra of this molecule, but the simulated spectra are presented here for future reference.

The calculated population fractions for each of the rotational states at a temperature of 298K are tabulated here in *Table 3b-3*. This temperature was used because of its accepted value as ‘room temperature’, and because this was the working deposition temperature at which vanillin was introduced into the matrix isolation system to produce experimental Samples 3 and 5 as seen in *Chapter 1* (the two samples that show the best evidence of vanillin in the isolated state).

B3LYP +d					
Rotational Structure	Calculated Energy (Hartree Units)	Calculated Energy Difference from Minimum (Hartree Units)	Calculated Energy Difference from Minimum (kJ/mol)	Population Fraction at 298K	Normalised Population Fraction
1	-535.316	0	0	0.875736534	0.876
11	-535.314	0.001845	4.844	0.123953494	0.124
30	-535.303	0.012303	32.302	1.907x10 <sup>-6</sup>	
36	-535.302	0.013733	36.056	4.189x10 <sup>-7</sup>	
51	-535.308	0.007713	20.251	2.470x10 <sup>-4</sup>	
61	-535.307	0.009071	23.816	5.857x10 <sup>-5</sup>	
80	-535.303	0.0124	32.556	1.720x10 <sup>-6</sup>	
86	-535.302	0.01383	36.311	3.778x10 <sup>-7</sup>	
B3PW91 +d					
Rotational Structure	Calculated Energy (Hartree Units)	Calculated Energy Difference from Minimum (Hartree Units)	Calculated Energy Difference from Minimum (kJ/mol)	Population Fraction at 298K	Normalised Population Fraction
1	-535.099	0	0	0.876756024	0.877
11	-535.097	0.001854	4.868	0.122919855	0.123
30	-535.086	0.012599	33.079	1.395x10 <sup>-6</sup>	
36	-535.085	0.014018	36.804	3.101x10 <sup>-7</sup>	
51	-535.091	0.007671	20.14	2.585x10 <sup>-4</sup>	
61	-535.09	0.009013	23.664	6.236x10 <sup>-5</sup>	
80	-535.086	0.012695	33.331	1.260x10 <sup>-6</sup>	
86	-535.085	0.014111	37.048	2.810x10 <sup>-7</sup>	

Table 3b-3: Calculated relative populations of rotational structures at 298K.

With the identification of the rotational conformations of lowest energy (and thus greatest stability and interest) we can use Gaussian to calculate a simulated spectrum from each geometry-optimised structure. Tables 3b-4 to 3b-7 contain the relevant peak values for these simulated spectra (including scaled wavenumber values, calculated infrared intensities and calculated Raman activities) and will be used for their evaluation shortly.

IMPORTANT NOTE: Conformers 001 and 011 are shown in Table 3b-3 to be expected to constitute <99.95% of the total population of the vanillin vapour at a temperature of 298K, calculated from the Boltzmann Distribution population ratios

in the form  $\frac{N_1}{N_0} = \exp^{\frac{-(E_1 - E_0)}{k_B T}}$  where  $E_1$  and  $E_0$  are the relative energy values

calculated for any two ‘neighbouring’ minima structures in Table 3b-3,  $k_B$  is the

Boltzmann coefficient and  $T$  the temperature (K); these population ratios were used to calculate the overall (normalised) distribution of population between the eight most stable structures in each case. As the primary contributors to the total intensity of the spectra, these two structures could then be used for the calculation of the principle isotopic contributions to the system.

Experimentally obtained data for vanillin isolated in argon matrices can be found in *Chapter 1* of this thesis. However, as has been discussed, the Matrix Isolation technique (in conjunction with high resolution infrared spectroscopy) is very strongly influenced by small variations in experimental temperature, gas pressure and deposition time. It is also apparent from both literature and our own experimental data that the formation of the close-packed argon lattice during deposition has a steric effect on the vanillin molecule, causing small shifts in wavenumber value (potentially up to  $\sim 50\text{ cm}^{-1}$  but more probably within  $\sim 5\text{ cm}^{-1}$ ); for example, in previous Matrix Isolation experiments (*Lee Iverson, MSc thesis 2009*) stretching and bending modes in CO<sub>2</sub> and N<sub>2</sub>O were observed to be shifted by up to  $7\text{ cm}^{-1}$ . Splitting of intensity from single peaks into multiples, correlating with different possible conformations within the matrix is also common and anticipated.

### 3b-2-2: Vibrational Frequency Scaling

As has been remarked upon, Density Functional Theory is fundamentally a collection of terms that approximate the behaviour of atoms in a molecule- as a result, there is a systematic overestimation of vibrational frequency that is (in principle) unique for each possible combination of basis set, function and target molecule. In a ‘normal’ simulation, the typical approach would be to scale the calculated values against the experimentally obtained ones, as exemplified in *Part I* of these results for the solid phase data. Since, however, the isolated phase we are trying to simulate here does not have all of its vibrational peaks properly described (i.e. uncertainty still exists in some of the peak assignments, and over the degree of isolation in the results of *Chapter 1*), this method is not appropriate to this situation. Instead, based on a range of literature sources<sup>61,64</sup> appropriate scaling values have

been chosen for each of the two methods: 0.967 for B3LYP +d and 0.963 for B3PW91 +d respectively. Where wavenumber values are quoted below they have already been scaled by these factors.

### 3b-2-3: Simulation Results

Initially we will look at the calculated vibrational spectra for the two most populous conformers of vanillin in each method, without consideration of isotopic effects, and combine the two pairs of results to simulate the most naturally abundant isotopic combination in both the infrared and Raman:

<b>Calculated Peak Wavenumber (cm<sup>-1</sup>)</b>	<b>IR Intensity I (KM/Mole)</b>	<b>Raman Activity A (A<sup>4</sup>/AMU)</b>			
71.87	9.51	1.19	984.46	1.58	2.02
98.97	0.37	0.39	1020.97	46.93	4.60
147.60	9.30	1.74	1106.26	44.51	1.00
182.28	0.22	1.85	1133.55	113.42	4.40
196.35	7.14	1.40	1143.34	0.64	1.91
238.18	2.95	0.49	1168.14	113.65	25.73
248.94	0.03	0.34	1191.15	51.87	4.00
327.11	2.74	1.94	1232.64	74.93	10.40
364.94	2.82	0.72	1258.30	278.87	31.97
401.76	1.27	9.24	1273.98	122.98	1.94
445.63	8.87	0.38	1365.52	26.81	8.94
452.84	116.08	1.14	1389.27	51.13	7.78
526.94	2.25	2.87	1423.67	87.63	15.18
529.44	4.99	2.77	1446.87	6.27	8.95
572.32	11.43	0.07	1458.65	11.17	12.51
613.86	43.02	6.99	1468.21	63.26	3.97
711.61	0.63	0.17	1492.38	153.74	3.93
717.69	51.41	10.92	1583.28	179.27	176.00
795.45	2.42	16.52	1586.95	25.25	22.78
805.30	34.27	0.66	1695.25	329.89	173.43
864.94	21.28	0.31	2800.87	132.90	167.40
914.20	1.08	0.18	2927.96	42.06	129.24
936.91	1.05	6.22	2992.05	30.41	42.56
			3048.36	20.11	109.95
			3065.71	7.32	64.87
			3092.21	6.98	147.82
			3101.60	3.91	48.21

Table 3b-4: Simulated vibrational wavenumbers for B3LYP +d for Structure 001 with associated infrared and Raman intensity values, scaled by a factor of 0.967.

<b>Calculated Peak Wavenumber (cm<sup>-1</sup>)</b>	<b>IR Intensity I (KM/ Mole)</b>	<b>Raman Activity A (A<sup>4</sup>/AMU)</b>			
69.04	2.45	1.14	986.27	1.08	2.53
95.91	4.84	0.13	1023.94	48.68	4.09
153.07	5.88	3.06	1100.82	62.79	3.08
158.56	3.60	0.92	1143.11	76.77	3.75
216.21	3.23	0.23	1143.42	1.15	2.03
230.43	2.15	1.34	1169.55	136.04	28.94
271.61	1.75	0.18	1190.73	86.14	9.42
329.63	9.22	4.68	1227.74	94.10	4.44
333.81	0.77	1.05	1269.02	375.98	32.38
386.60	1.82	6.33	1279.21	30.28	6.28
442.90	101.30	0.35	1366.89	25.15	9.44
448.44	22.53	0.90	1377.31	24.87	13.14
498.69	9.76	2.63	1422.48	6.30	4.47
537.63	20.78	4.79	1445.85	4.00	1.92
568.48	9.63	0.11	1459.44	10.86	12.98
628.92	10.51	3.38	1468.70	51.75	4.48
707.82	0.02	0.17	1497.41	141.71	2.91
761.14	48.00	9.60	1575.05	230.18	151.79
781.90	17.40	15.38	1591.40	27.79	63.86
818.82	31.92	0.09	1702.61	347.06	178.80
836.89	23.95	0.25	2780.95	135.12	139.44
907.71	2.88	9.66	2922.62	46.17	132.84
937.44	0.21	0.04	2984.45	34.30	46.45
			3046.73	20.36	116.96
			3078.17	7.44	39.09
			3085.81	2.32	82.16
			3100.05	3.59	129.21

Table 3b-5: Simulated vibrational wavenumbers for B3LYP +d for Structure 011 with associated infrared and Raman intensity values, scaled by a factor of 0.967.

<b>Calculated Peak Wavenumber (cm<sup>-1</sup>)</b>	<b>IR Intensity I (KM/ Mole)</b>	<b>Raman Activity A (A<sup>4</sup>/AMU)</b>	980.67	1.62	2.09
72.35	9.38	1.24	1029.83	34.65	3.63
98.77	0.24	0.37	1103.15	34.13	0.67
145.51	9.44	1.70	1137.29	122.85	5.08
182.65	0.36	1.74	1138.91	0.43	1.84
196.01	7.11	1.45	1164.90	97.56	19.94
235.47	3.14	0.47	1187.74	46.13	3.60
249.77	0.05	0.32	1236.15	72.79	12.02
324.86	2.87	1.86	1257.49	160.71	18.61
364.44	2.51	0.68	1284.69	250.64	12.64
398.96	1.10	8.69	1362.26	30.43	5.19
443.67	4.77	0.49	1395.22	33.64	9.51
457.72	120.05	0.99	1421.19	70.81	10.28
526.00	2.93	2.74	1442.77	21.70	16.05
528.79	3.87	2.73	1448.55	12.09	12.57
568.41	11.35	0.08	1459.69	72.51	4.02
611.92	39.89	7.14	1497.80	182.01	4.61
709.14	0.83	0.14	1592.54	113.04	98.60
716.88	52.34	10.03	1595.83	94.93	90.98
795.23	2.87	17.17	1708.23	333.59	173.26
800.84	34.53	0.56	2795.62	133.35	165.73
857.77	22.17	0.32	2920.02	42.09	129.34
908.70	1.16	0.17	2989.78	28.38	40.73
941.05	1.08	6.57	3046.03	18.89	105.93
			3060.84	6.84	64.95
			3089.14	6.13	128.28
			3092.81	4.19	63.93

*Table 3b-6: Simulated vibrational wavenumbers for B3PW91 +d for Structure 001 with associated infrared and Raman intensity values, scaled by a factor of 0.963.*

<b>Calculated Peak Wavenumber (cm<sup>-1</sup>)</b>	<b>IR Intensity I (KM/ Mole)</b>	<b>Raman Activity A (A<sup>4</sup>/AMU)</b>	982.07	1.13	2.60
69.39	2.39	1.20	1032.12	33.32	3.29
96.02	4.60	0.12	1098.54	52.10	2.60
152.14	6.17	2.98	1138.84	0.42	1.95
155.96	3.78	0.86	1144.17	87.39	4.92
217.49	3.07	0.23	1166.00	108.16	22.05
227.64	2.08	1.33	1186.92	77.42	7.13
271.45	1.85	0.17	1235.13	98.88	4.80
327.47	9.51	4.33	1270.89	223.27	25.09
333.08	0.57	0.94	1283.84	208.15	14.43
384.08	1.54	6.38	1364.89	8.09	1.76
444.23	22.36	0.03	1383.80	29.12	22.98
451.54	101.42	1.18	1419.74	5.78	3.79
497.06	9.30	2.56	1440.17	7.22	1.66
537.48	20.90	4.46	1449.21	11.79	13.02
564.64	9.34	0.09	1459.78	53.45	4.26
624.62	9.31	3.49	1501.77	167.94	3.20
705.11	0.08	0.14	1583.63	225.09	135.50
760.47	43.56	8.16	1600.39	35.97	70.87
783.27	20.66	16.80	1715.60	350.33	178.74
813.88	32.07	0.09	2775.51	135.41	137.67
829.46	25.23	0.21	2914.77	46.42	133.22
911.52	3.93	9.54	2982.31	32.05	44.50
931.08	0.20	0.03	3044.47	19.13	112.97
			3070.35	6.68	42.74
			3081.65	1.82	68.85
			3095.37	3.71	134.68

*Table 3b-7: Simulated vibrational wavenumbers for B3PW91 +d for Structure 011 with associated infrared and Raman intensity values, scaled by a factor of 0.963.*

Treating each peak as a Gaussian function of area I (IR intensity) or A (Raman activity), and adding the sum of each conformer weighted by the energy population distributions found in *Table 3b-3* above, the resulting simulated spectra can be plotted as the following Figures *3b-3*, *3b-4*, *3b-5* and *3b-6*.

It should be noted that, unlike the solid phase, many of the peaks found in the experimental data show very narrow band widths. Assuming that these peaks represent vibrational modes of the molecule in the true isolated state only this means that there is a typically observed band width of between  $0.6$  and  $1.5\text{ cm}^{-1}$ , with variances due to noise and convolution of closely related modes. Because of this, the simulated vibrational peaks here in *Part II* have all been plotted as Gaussian curve functions with a full width at half-maximum (FWHM) of  $1\text{ cm}^{-1}$  to better simulate the ideal expected data, as opposed to the width of  $10\text{ cm}^{-1}$  used in *Part I*.

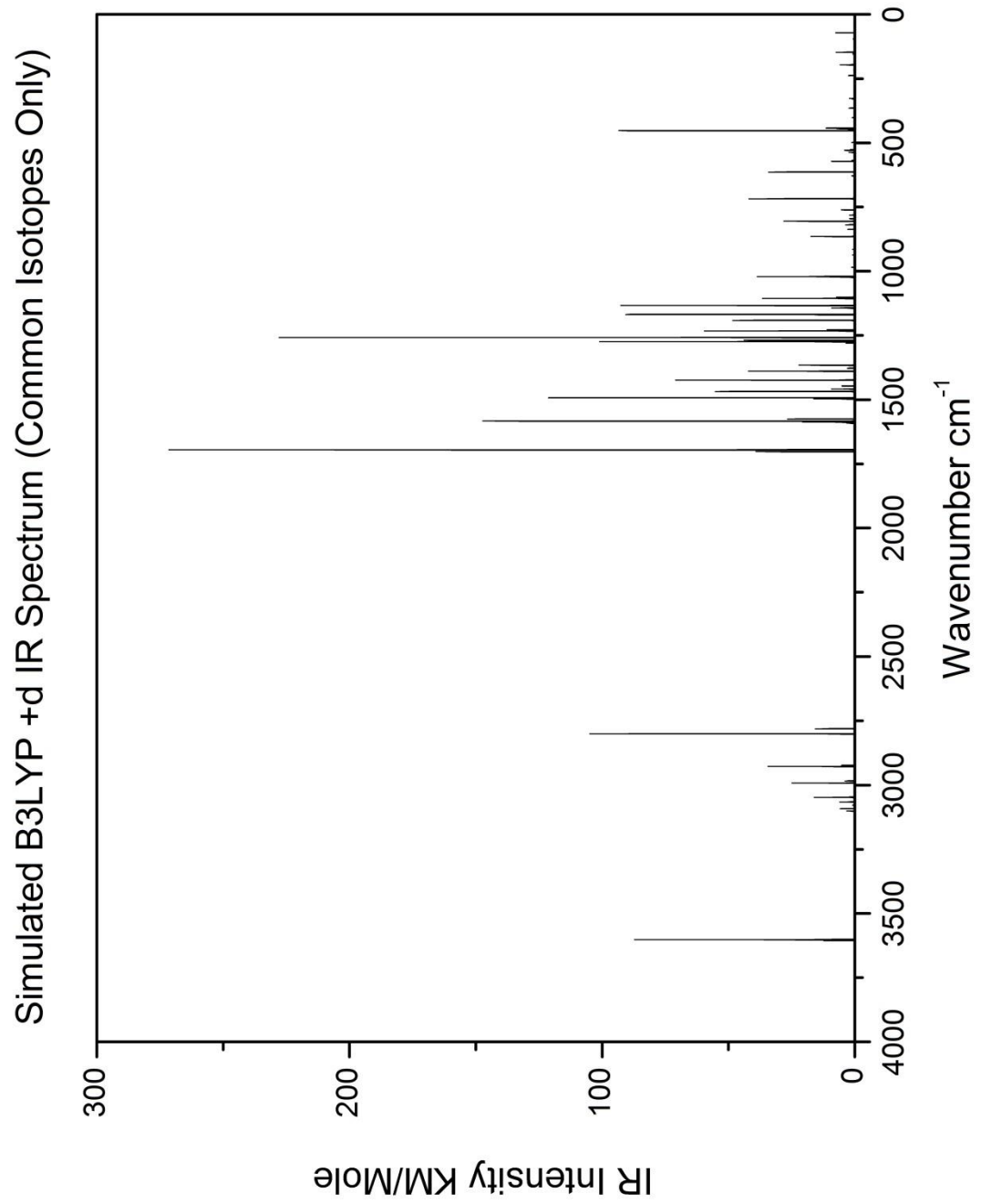
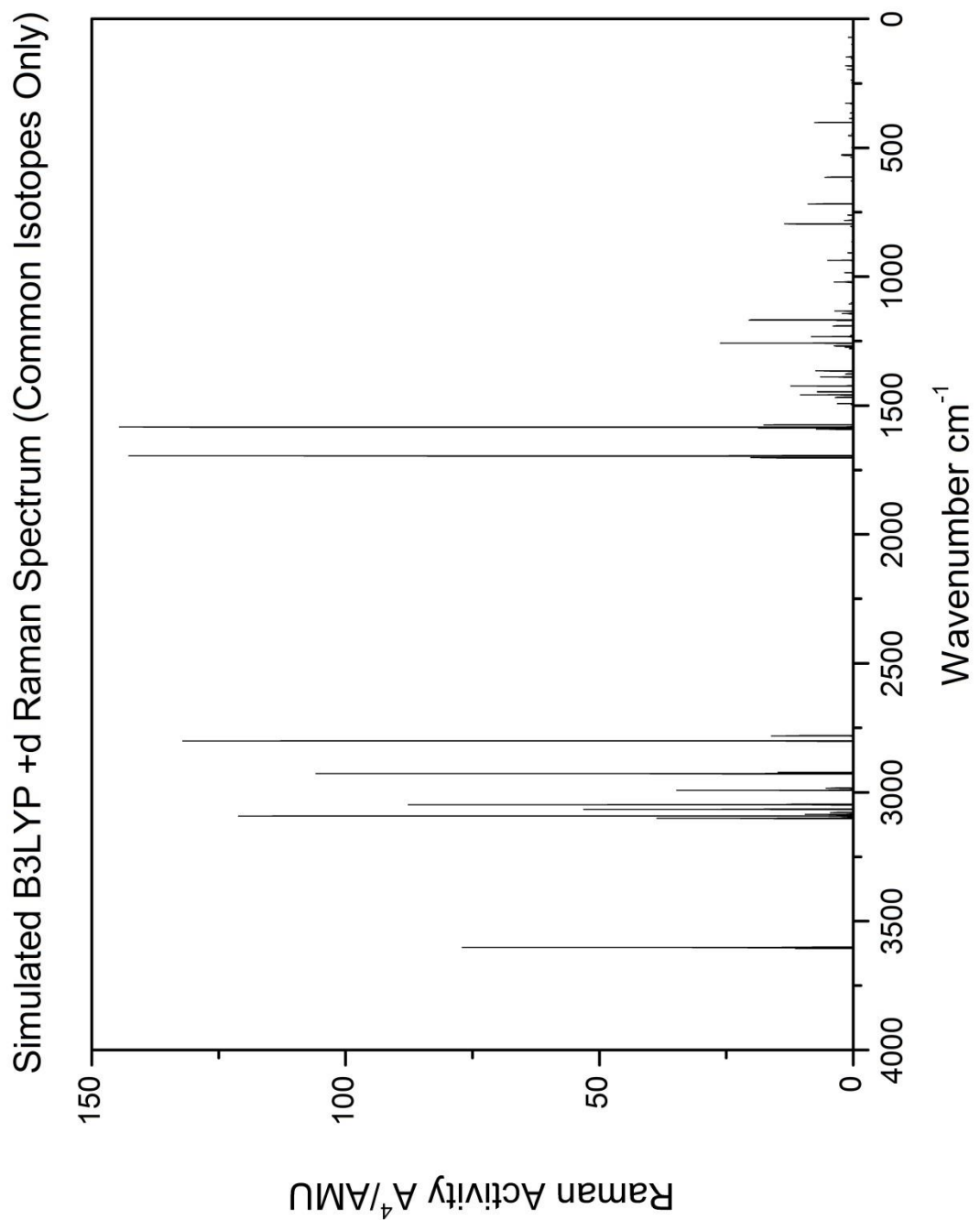
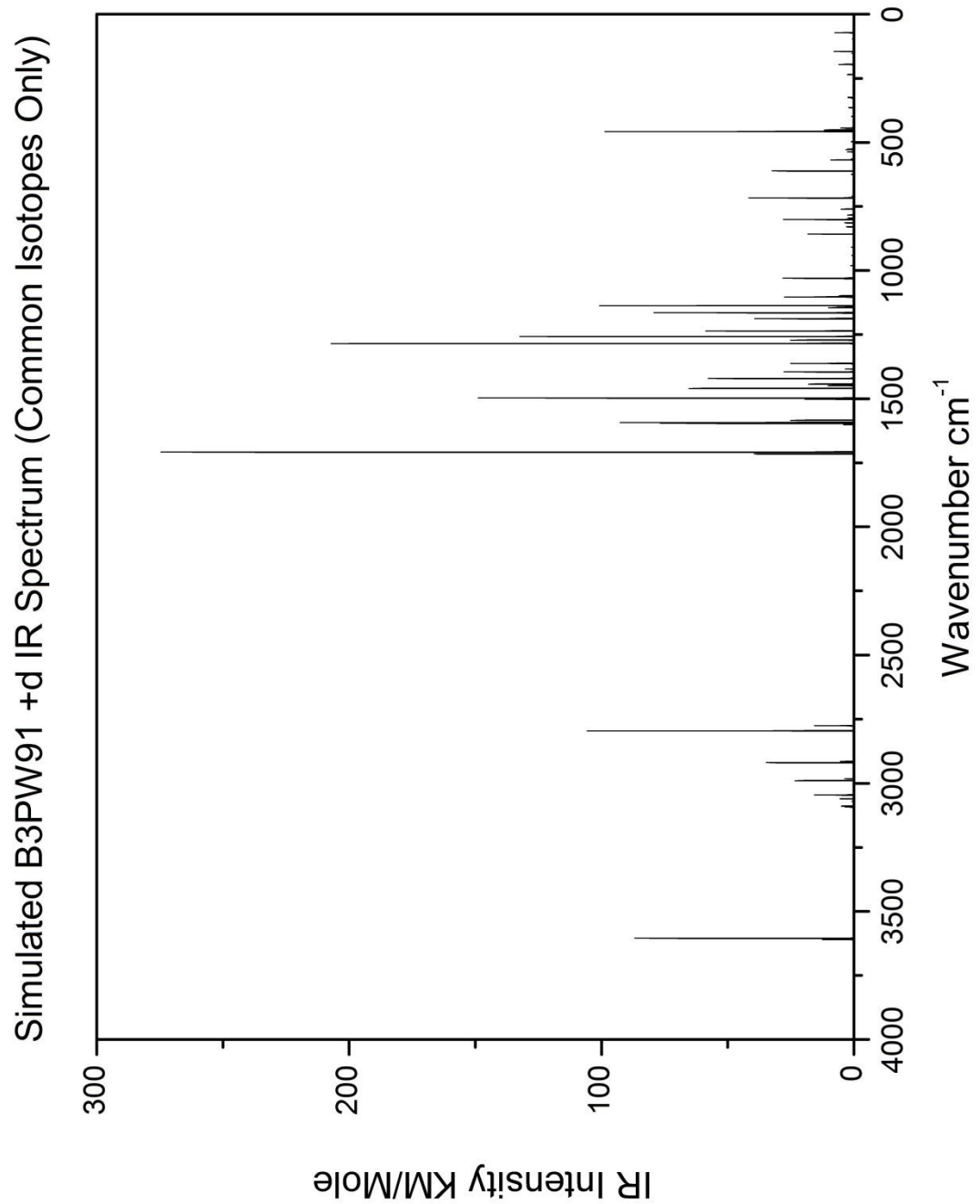


Figure 3b-3: Initial simulation of isolated phase vanillin IR spectrum, using B3LYP +d method (peaks set to uniform  $1\text{ cm}^{-1}$  FWHM, calculated area scaled to energy level population).



*Figure 3b-4: Initial simulation of isolated phase vanillin Raman spectrum, using B3LYP +d method (peaks set to uniform 1 cm<sup>-1</sup> FWHM, calculated area scaled to energy level population).*



*Figure 3b-5: Initial simulation of isolated phase vanillin IR spectrum, using B3PW91 +d method (peaks set to uniform 1 cm<sup>-1</sup> FWHM, calculated area scaled to energy level population).*

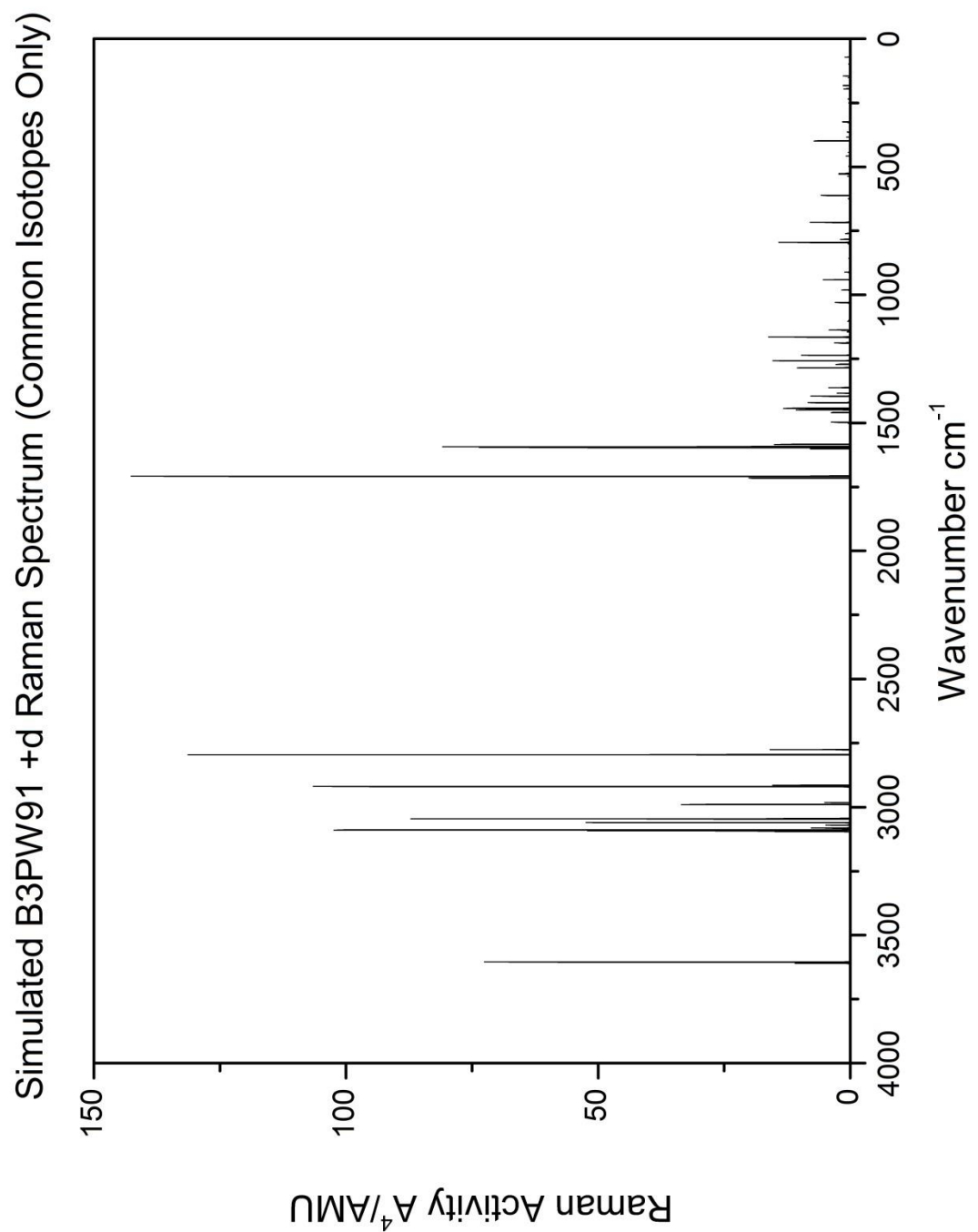


*Figure 3b-6: Initial simulation of isolated phase vanillin Raman spectrum, using B3PW91 +d method (peaks set to uniform 1 cm<sup>-1</sup> FWHM, calculated area scaled to energy level population).*

As they only account for the most common isotopes of carbon, oxygen and hydrogen, these spectra only represent approximately 91.12% of the total vanillin population (assuming each atom has a chance of isotopic substitution determined only by typical natural abundance). Given that there are 19 atoms in vanillin, equivalent calculations are therefore necessary for each possible substitution of  $^{13}\text{C}$ ,  $^2\text{D}$ ,  $^{17}\text{O}$  and  $^{18}\text{O}$ . We will assume that the probability of multiple isotopic substitutions is negligible; similarly, we will disregard the possibility of other isotopes such as  $^3\text{T}$  (indeed, assuming natural abundance, multiple substitutions and minority isotopes account for only 0.39% of the total vanillin population combined) and that isotopomers are mono-substituted only. Typical natural abundances for these isotopes are found in *Table 3b-8* below; the resulting calculated populations for the weighting of each isotopic substitution can be found in *Table 3b-9*.

Tables presenting the calculated wavenumber values, IR intensity I and Raman activity A before scaling to population can be found in *Appendix II* accompanying this text (labelled as *Tables A2-1, 2, 3 and 4, parts a to f*), though they also include the data previously presented as the ‘00’ structures (i.e. the zeroth iteration of isotopomeric substitutions, using the most naturally abundant isotopes of the species) of vanillin conformers 001 and 011 calculated using the B3LYP +d and B3PW91 +d methods.

<b>Naturally Occurring Isotope</b>	<b>Typical Natural Abundance</b>
$^1\text{H}$	0.99985
$^2\text{H}$	0.00015
$^{12}\text{C}$	0.989
$^{13}\text{C}$	0.011
$^{16}\text{O}$	0.9976
$^{17}\text{O}$	0.00039
$^{18}\text{O}$	0.00201

*Table 3b-8: Typical natural isotopic abundances.*

<b>Isotopomer Number</b>	<b>Natural Probability</b>	<b>Normalised Probability (for Weighting)</b>
00	0.907650104	0.911247859
01	0.010095198	0.010135214
02	0.010095198	0.010135214
03	0.010095198	0.010135214
04	0.010095198	0.010135214
05	0.010095198	0.010135214
06	0.010095198	0.010135214
07	0.010095198	0.010135214
08	0.010095198	0.010135214
09	0.000136168	0.000136708
10	0.000136168	0.000136708
11	0.000136168	0.000136708
12	0.000136168	0.000136708
13	0.000136168	0.000136708
14	0.000136168	0.000136708
15	0.000136168	0.000136708
16	0.000136168	0.000136708
17	0.000354835	0.000356242
18	0.000354835	0.000356242
19	0.000354835	0.000356242
20	0.001828766	0.001836015
21	0.001828766	0.001836015
22	0.001828766	0.001836015

*Table 3b-9: Total (normalised) population weights for the isotopically substituted variants of each structure 001 and 011.*

For the purposes of weighting, the structures described in *Tables 3b-4* to *3b-7* can be considered the ‘zeroth’ isotopomers for structures 001 and 011 respectively; the numbers of each of the other isotopomers refer to the position of the isotopically substituted atom, as seen in *Figure 3b-7* and *Table 3b-10* below. The final weighting of each vibrational calculation for the simulated IR and Raman spectra using each of the two methods, weighted for both conformer population and natural isotopomers abundance can therefore be found in *Table 3b-11* below (and extending over the following three pages). The resulting (final) simulated spectra for infrared

and Raman vibrations using these weightings are found at last in *Figures 3b-8, 3b-9, 3b-10 and 3b-11.*

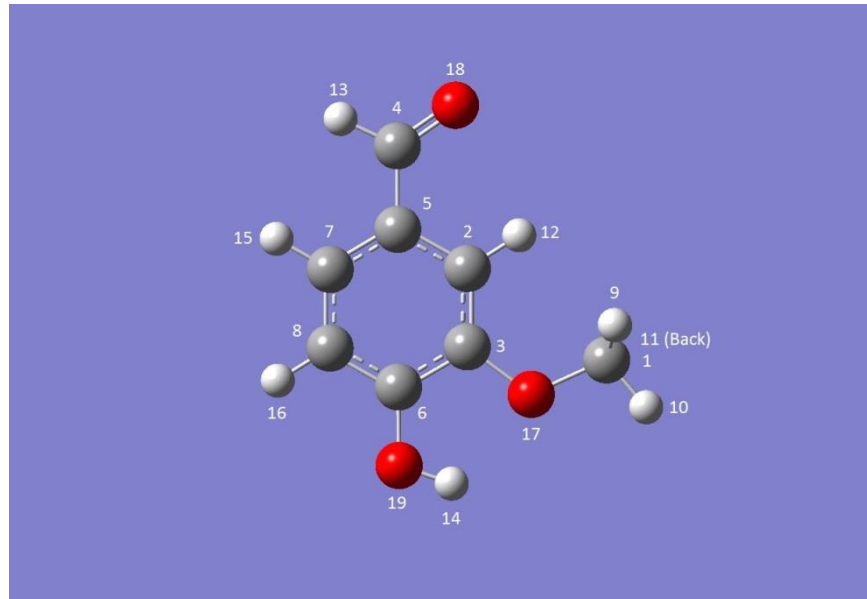


*Figure 3b-7: Atomic number assignment in simulations.*

<b>Isotopomer Number</b>	<b>Description of Substitution</b>
00	No substitutions: atomic species used are those of highest natural abundance
01	Atom 1 (carbon) substituted for $^{13}\text{C}$
02	Atom 2 (carbon) substituted for $^{13}\text{C}$
03	Atom 3 (carbon) substituted for $^{13}\text{C}$
04	Atom 4 (carbon) substituted for $^{13}\text{C}$
05	Atom 5 (carbon) substituted for $^{13}\text{C}$
06	Atom 6 (carbon) substituted for $^{13}\text{C}$
07	Atom 7 (carbon) substituted for $^{13}\text{C}$
08	Atom 8 (carbon) substituted for $^{13}\text{C}$
09	Atom 9 (hydrogen) substituted for $^2\text{D}$
10	Atom 10 (hydrogen) substituted for $^2\text{D}$
11	Atom 11 (hydrogen) substituted for $^2\text{D}$
12	Atom 12 (hydrogen) substituted for $^2\text{D}$
13	Atom 13 (hydrogen) substituted for $^2\text{D}$
14	Atom 14 (hydrogen) substituted for $^2\text{D}$
15	Atom 15 (hydrogen) substituted for $^2\text{D}$
16	Atom 16 (hydrogen) substituted for $^2\text{D}$
17	Atom 17 (oxygen) substituted for $^{17}\text{O}$
18	Atom 18 (oxygen) substituted for $^{17}\text{O}$
19	Atom 19 (oxygen) substituted for $^{17}\text{O}$
20	Atom 17 (oxygen) substituted for $^{18}\text{O}$
21	Atom 18 (oxygen) substituted for $^{18}\text{O}$
22	Atom 19 (oxygen) substituted for $^{18}\text{O}$

*Table 3b-10: Isotopic substitutions by position.*

<b>Simulation</b>	<b>Normalised Conformer Weight</b>	<b>Normalised Isotopomer Weight</b>	<b>Final Weighting</b>
B3LYP +d Conformer 001, Isotopomer 00	0.876008	0.911248	0.79826
B3LYP +d Conformer 001, Isotopomer 01	0.876008	0.010135	0.008879
B3LYP +d Conformer 001, Isotopomer 02	0.876008	0.010135	0.008879
B3LYP +d Conformer 001, Isotopomer 03	0.876008	0.010135	0.008879
B3LYP +d Conformer 001, Isotopomer 04	0.876008	0.010135	0.008879
B3LYP +d Conformer 001, Isotopomer 05	0.876008	0.010135	0.008879
B3LYP +d Conformer 001, Isotopomer 06	0.876008	0.010135	0.008879
B3LYP +d Conformer 001, Isotopomer 07	0.876008	0.010135	0.008879
B3LYP +d Conformer 001, Isotopomer 08	0.876008	0.010135	0.008879
B3LYP +d Conformer 001, Isotopomer 09	0.876008	0.000137	0.00012
B3LYP +d Conformer 001, Isotopomer 10	0.876008	0.000137	0.00012
B3LYP +d Conformer 001, Isotopomer 11	0.876008	0.000137	0.00012
B3LYP +d Conformer 001, Isotopomer 12	0.876008	0.000137	0.00012
B3LYP +d Conformer 001, Isotopomer 13	0.876008	0.000137	0.00012
B3LYP +d Conformer 001, Isotopomer 14	0.876008	0.000137	0.00012
B3LYP +d Conformer 001, Isotopomer 15	0.876008	0.000137	0.00012
B3LYP +d Conformer 001, Isotopomer 16	0.876008	0.000137	0.00012
B3LYP +d Conformer 001, Isotopomer 17	0.876008	0.000356	0.000312

B3LYP +d Conformer 001, Isotopomer 18	0.876008	0.000356	0.000312
B3LYP +d Conformer 001, Isotopomer 19	0.876008	0.000356	0.000312
B3LYP +d Conformer 001, Isotopomer 20	0.876008	0.001836	0.001608
B3LYP +d Conformer 001, Isotopomer 21	0.876008	0.001836	0.001608
B3LYP +d Conformer 001, Isotopomer 22	0.876008	0.001836	0.001608
B3LYP +d Conformer 011, Isotopomer 00	0.123992	0.911248	0.112987
B3LYP +d Conformer 011, Isotopomer 01	0.123992	0.010135	0.001257
B3LYP +d Conformer 011, Isotopomer 02	0.123992	0.010135	0.001257
B3LYP +d Conformer 011, Isotopomer 03	0.123992	0.010135	0.001257
B3LYP +d Conformer 011, Isotopomer 04	0.123992	0.010135	0.001257
B3LYP +d Conformer 011, Isotopomer 05	0.123992	0.010135	0.001257
B3LYP +d Conformer 011, Isotopomer 06	0.123992	0.010135	0.001257
B3LYP +d Conformer 011, Isotopomer 07	0.123992	0.010135	0.001257
B3LYP +d Conformer 011, Isotopomer 08	0.123992	0.010135	0.001257
B3LYP +d Conformer 011, Isotopomer 09	0.123992	0.000137	1.7E-05
B3LYP +d Conformer 011, Isotopomer 10	0.123992	0.000137	1.7E-05
B3LYP +d Conformer 011, Isotopomer 11	0.123992	0.000137	1.7E-05
B3LYP +d Conformer 011, Isotopomer 12	0.123992	0.000137	1.7E-05
B3LYP +d Conformer 011, Isotopomer 13	0.123992	0.000137	1.7E-05

B3LYP +d Conformer 011, Isotopomer 14	0.123992	0.000137	1.7E-05
B3LYP +d Conformer 011, Isotopomer 15	0.123992	0.000137	1.7E-05
B3LYP +d Conformer 011, Isotopomer 16	0.123992	0.000137	1.7E-05
B3LYP +d Conformer 011, Isotopomer 17	0.123992	0.000356	4.42E-05
B3LYP +d Conformer 011, Isotopomer 18	0.123992	0.000356	4.42E-05
B3LYP +d Conformer 011, Isotopomer 19	0.123992	0.000356	4.42E-05
B3LYP +d Conformer 011, Isotopomer 20	0.123992	0.001836	0.000228
B3LYP +d Conformer 011, Isotopomer 21	0.123992	0.001836	0.000228
B3LYP +d Conformer 011, Isotopomer 22	0.123992	0.001836	0.000228
B3PW91 +d Conformer 001, Isotopomer 00	0.87704	0.911248	0.799201
B3PW91 +d Conformer 001, Isotopomer 01	0.87704	0.010135	0.008889
B3PW91 +d Conformer 001, Isotopomer 02	0.87704	0.010135	0.008889
B3PW91 +d Conformer 001, Isotopomer 03	0.87704	0.010135	0.008889
B3PW91 +d Conformer 001, Isotopomer 04	0.87704	0.010135	0.008889
B3PW91 +d Conformer 001, Isotopomer 05	0.87704	0.010135	0.008889
B3PW91 +d Conformer 001, Isotopomer 06	0.87704	0.010135	0.008889
B3PW91 +d Conformer 001, Isotopomer 07	0.87704	0.010135	0.008889
B3PW91 +d Conformer 001, Isotopomer 08	0.87704	0.010135	0.008889
B3PW91 +d Conformer 001, Isotopomer 09	0.87704	0.000137	0.00012

B3PW91 +d Conformer 001, Isotopomer 10	0.87704	0.000137	0.00012
B3PW91 +d Conformer 001, Isotopomer 11	0.87704	0.000137	0.00012
B3PW91 +d Conformer 001, Isotopomer 12	0.87704	0.000137	0.00012
B3PW91 +d Conformer 001, Isotopomer 13	0.87704	0.000137	0.00012
B3PW91 +d Conformer 001, Isotopomer 14	0.87704	0.000137	0.00012
B3PW91 +d Conformer 001, Isotopomer 15	0.87704	0.000137	0.00012
B3PW91 +d Conformer 001, Isotopomer 16	0.87704	0.000137	0.00012
B3PW91 +d Conformer 001, Isotopomer 17	0.87704	0.000356	0.000312
B3PW91 +d Conformer 001, Isotopomer 18	0.87704	0.000356	0.000312
B3PW91 +d Conformer 001, Isotopomer 19	0.87704	0.000356	0.000312
B3PW91 +d Conformer 001, Isotopomer 20	0.87704	0.001836	0.00161
B3PW91 +d Conformer 001, Isotopomer 21	0.87704	0.001836	0.00161
B3PW91 +d Conformer 001, Isotopomer 22	0.87704	0.001836	0.00161
B3PW91 +d Conformer 011, Isotopomer 00	0.12296	0.911248	0.112047
B3PW91 +d Conformer 011, Isotopomer 01	0.12296	0.010135	0.001246
B3PW91 +d Conformer 011, Isotopomer 02	0.12296	0.010135	0.001246
B3PW91 +d Conformer 011, Isotopomer 03	0.12296	0.010135	0.001246
B3PW91 +d Conformer 011, Isotopomer 04	0.12296	0.010135	0.001246
B3PW91 +d Conformer 011, Isotopomer 05	0.12296	0.010135	0.001246

B3PW91 +d Conformer 011, Isotopomer 06	0.12296	0.010135	0.001246
B3PW91 +d Conformer 011, Isotopomer 07	0.12296	0.010135	0.001246
B3PW91 +d Conformer 011, Isotopomer 08	0.12296	0.010135	0.001246
B3PW91 +d Conformer 011, Isotopomer 09	0.12296	0.000137	1.68E-05
B3PW91 +d Conformer 011, Isotopomer 10	0.12296	0.000137	1.68E-05
B3PW91 +d Conformer 011, Isotopomer 11	0.12296	0.000137	1.68E-05
B3PW91 +d Conformer 011, Isotopomer 12	0.12296	0.000137	1.68E-05
B3PW91 +d Conformer 011, Isotopomer 13	0.12296	0.000137	1.68E-05
B3PW91 +d Conformer 011, Isotopomer 14	0.12296	0.000137	1.68E-05
B3PW91 +d Conformer 011, Isotopomer 15	0.12296	0.000137	1.68E-05
B3PW91 +d Conformer 011, Isotopomer 16	0.12296	0.000137	1.68E-05
B3PW91 +d Conformer 011, Isotopomer 17	0.12296	0.000356	4.38E-05
B3PW91 +d Conformer 011, Isotopomer 18	0.12296	0.000356	4.38E-05
B3PW91 +d Conformer 011, Isotopomer 19	0.12296	0.000356	4.38E-05
B3PW91 +d Conformer 011, Isotopomer 20	0.12296	0.001836	0.000226
B3PW91 +d Conformer 011, Isotopomer 21	0.12296	0.001836	0.000226
B3PW91 +d Conformer 011, Isotopomer 22	0.12296	0.001836	0.000226

Table 3b-11: Final weighting of all simulated components, inclusive of conformer population and natural isotopic abundance of atomic species.

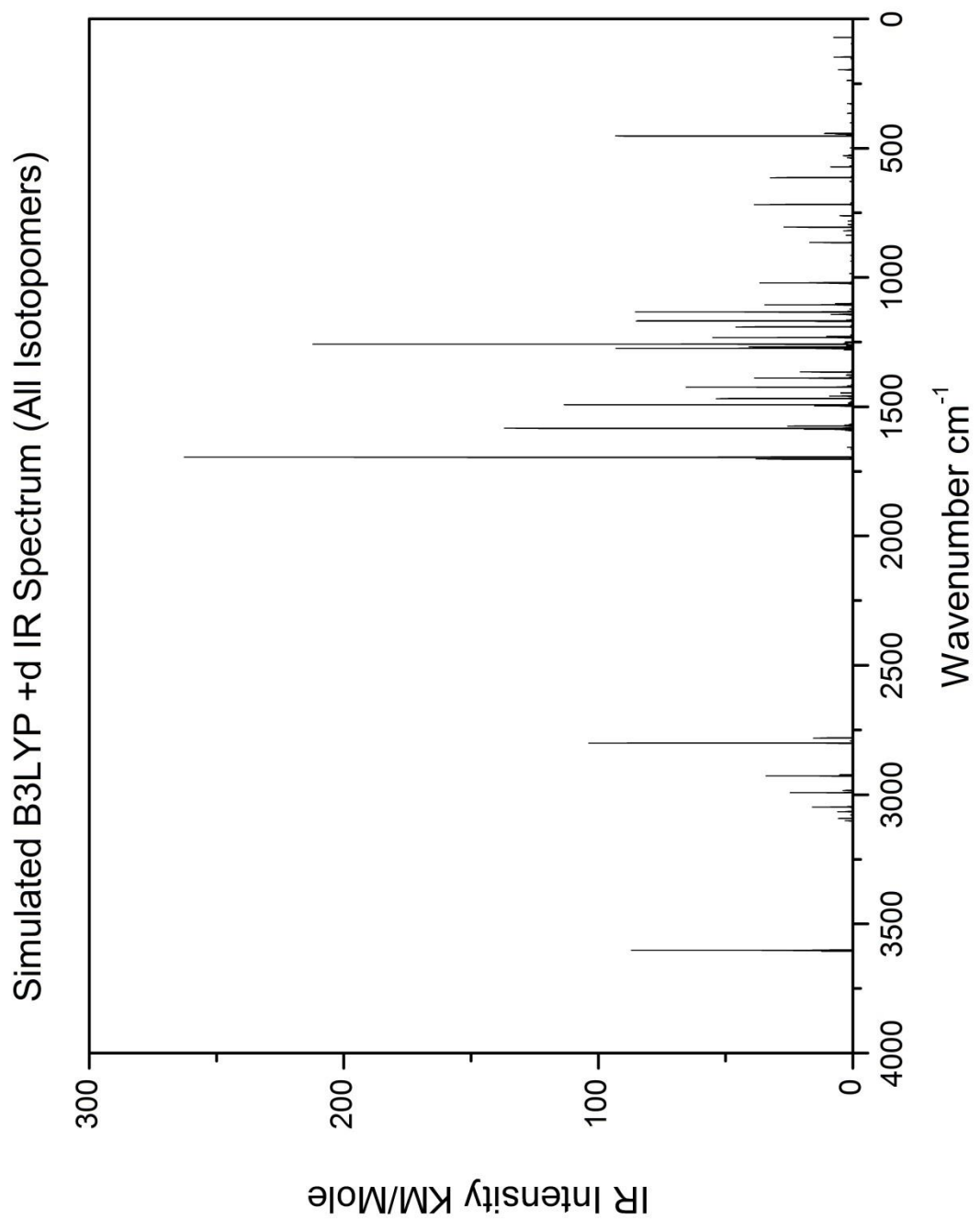


Figure 3b-8: Final simulation of isolated phase vanillin IR spectrum, using B3LYP +d method (peaks set to uniform  $1 \text{ cm}^{-1}$  FWHM, calculated area scaled to total population of each component).

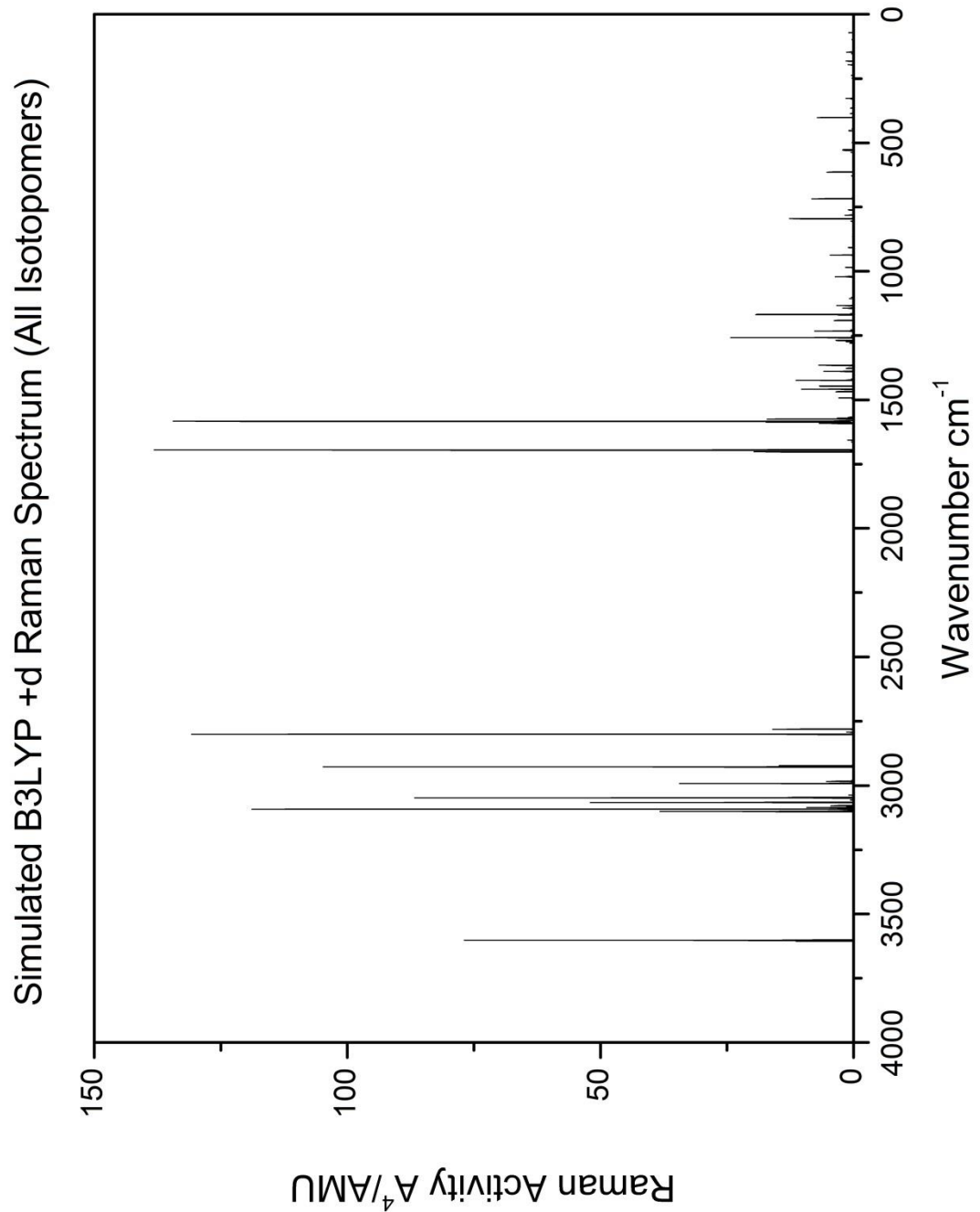


Figure 3b-9: Final simulation of isolated phase vanillin Raman spectrum, using B3LYP +d method (peaks set to uniform 1 cm<sup>-1</sup> FWHM, calculated area scaled to population of each component).

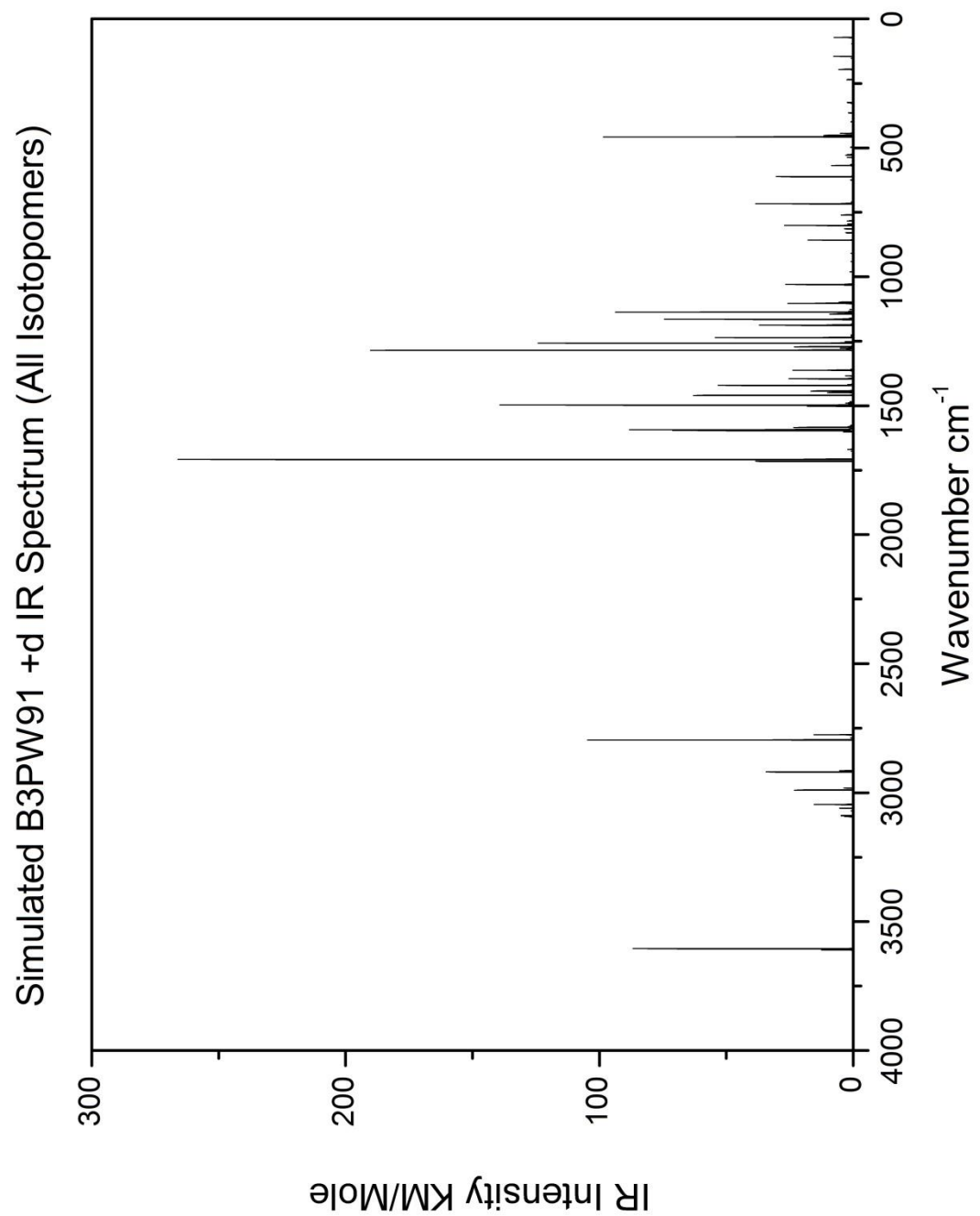


Figure 3b-10: Final simulation of isolated phase vanillin IR spectrum, using B3PW91 +d method (peaks set to uniform 1  $\text{cm}^{-1}$  FWHM, calculated area scaled to total population of each component).

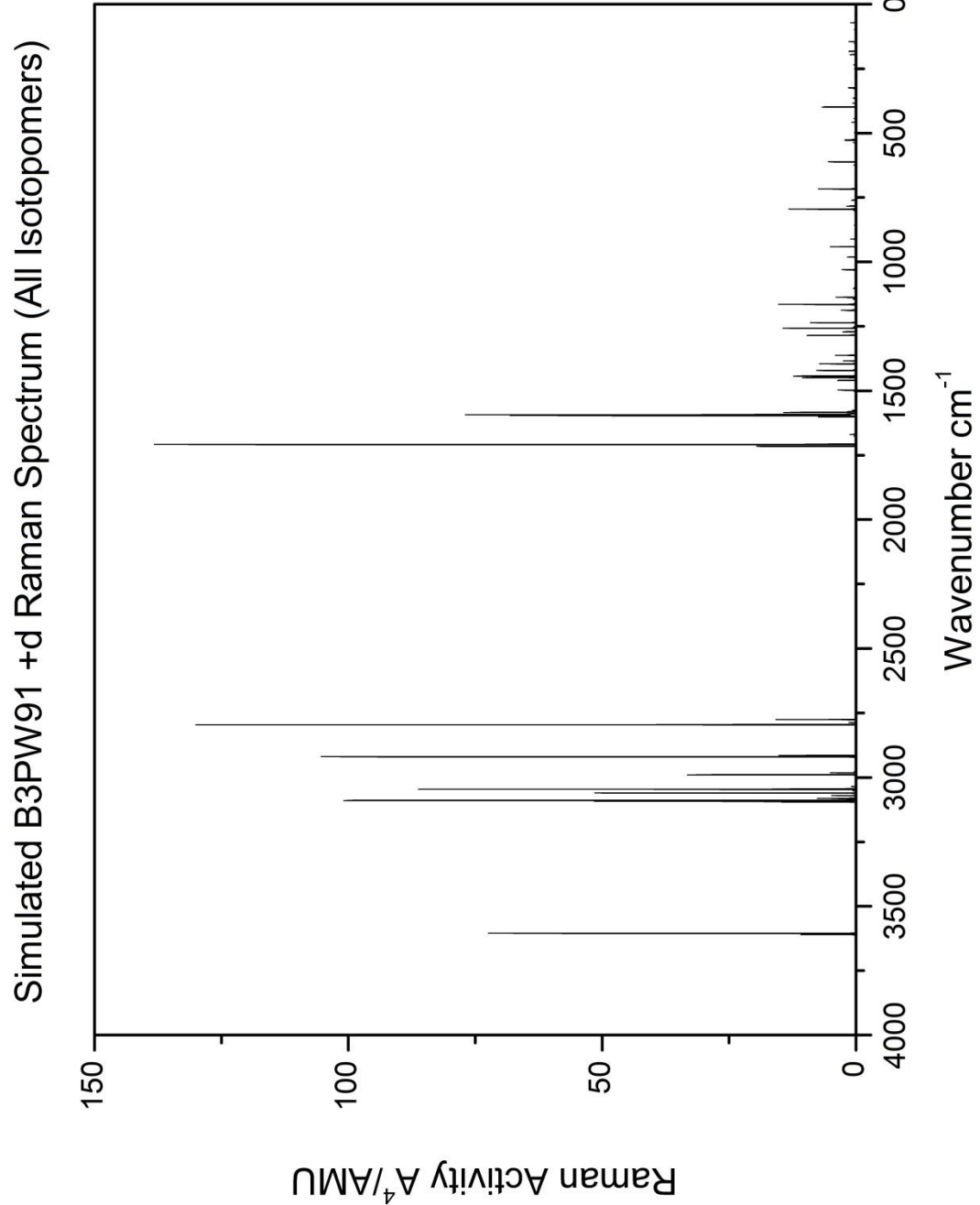


Figure 3b-11: Final simulation of isolated phase vanillin Raman spectrum, using B3PW91 +d method (peaks set to uniform  $1 \text{ cm}^{-1}$  FWHM, calculated area scaled to population of each component).

### 3b-2-4: Examination of Calculated Vibrational Modes

Fifty-one vibrational normal modes are calculated for each of the ninety-two simulated spectra discussed above, and the bends, stretches and deformation transitions of these modes are found to be virtually identical in each case. As with any normal mode of vibration, all of the vibrating bonds in the molecule do so at the same frequency and pass through their equilibria at the same instant: what is significant is that the vibrational modes described show a great deal of interdependence between the relative translations that seemingly unrelated atoms undergo. As was noted in *Part I*, the DFT process calculates a strong  $\pi$ -delocalisation over the molecule, and it is not unexpected that the association is strongest between the benzene ring and the electron withdrawing oxygen in the molecule's functional groups. Although the majority of the calculated vibrations are seen to have near-indistinguishable behaviour in their heavier carbon and oxygen atoms in each case (regardless of isotopic substitution), it is common for the ring hydrogens to show a change in their behaviour compared to the unsubstituted spectrum calculation. Similar changes are also seen between the two structures 001 and 011 (*s-cis* and *s-trans*), in which the carbonyl group is rotated through  $180^\circ$ , again affecting the electronic delocalisation through the molecule. A clear pattern cannot be distinguished from the results of these simulations alone, but further study with a molecule of simpler structure (for example another benzaldehyde lacking the additional functional to simplify the mechanism at work, or even an isomer of vanillin to compare their properties) may yield further information. One possible explanation is that inductive effects generate a partial positive charge at Carbon 2 (see *Figure 3b-5*) that the electronegative oxygen in *s-cis* vanillin (001) is better able to take advantage of than the *s-trans* (011), and the additional torsion in the ring has a small but significant effect on the magnitude and direction of the ring hydrogen vibrations. This effect is further compounded with each isotopic substitution, such that a great deal of variety is seen in the resulting vibrational magnitudes of the ring hydrogen over all simulated cases.

Data on the vibrational modes calculated in these vanillin simulations is presented below in *Tables 3b-16, 3b-17, 3b-18* and *3b-19* parts *a, b* and *c*. These are the same wavenumber values first presented in ascending order in *Tables 3b-10* to *13*, but re-structured such that the same mode (or the nearest possible match) is found in each row. These modes are described in the first column of each table, and reference should be made back to *Tables 3b-10* to *13* for the relevant IR intensities and Raman activities. In the descriptions given, once again  $\nu$  = stretching,  $\delta$  = in-plane deformation,  $\gamma$  = out-of-plane deformation and  $\tau$  = torsion transitions, and additional superscripts are added where necessary to differentiate alternate modes of similar vibrations; components are listed in descending order of contribution to mode- brackets around some components indicate a mixed contribution of approximately equal strength.

	B3LYP +d Structure 001 Vibrational Mode and Calculated Vibrational Wavenumber (W, cm <sup>-1</sup> ) for each Isotopic Substitution							
Vibrational Mode	00	01	02	03	04	05	06	07
$\tau\text{CH}_3$	71.87	71.12	71.82	71.77	71.86	71.84	71.86	71.62
$\tau\text{CH}_3 + \tau\text{Ph}^1$	98.97	98.91	98.49	98.77	98.97	98.65	98.95	98.82
$(\delta\text{HC=O} + \delta\text{OCH}_3)^1$	147.60	145.95	147.47	147.56	147.38	147.49	147.57	147.49
$\tau\text{O-CH}_3 + \tau\text{Ph}$	182.28	182.27	181.10	182.19	182.27	182.02	182.24	182.02
$\gamma\text{HC=O} + \tau\text{Ph}$	196.35	196.35	196.29	196.22	194.01	196.26	196.23	196.26
$(\delta\text{HC=O} + \delta\text{OCH}_3)^2$	238.18	236.70	237.59	237.66	238.15	237.56	238.03	237.76
$\tau\text{O-CH}_3 + \tau\text{HC=O}$	248.94	248.93	247.56	248.92	248.74	248.25	248.92	248.90
$(\delta\text{C-OCH}_3 + \delta\text{C-CHO} + \delta\text{C-OH})^1$	327.11	324.08	327.01	326.71	326.79	326.80	326.86	326.78
$\tau\text{Ph}$	364.94	364.93	364.85	363.54	364.22	362.94	362.56	362.35
$(\nu^{\text{as}}\text{Ph}^1 + \nu\text{C-CHO})$	401.76	401.08	400.36	401.47	398.99	400.55	400.30	401.54
$\gamma\text{Ph}^1$	445.63	445.63	443.22	441.81	445.62	445.15	442.41	445.14
$\gamma\text{C-OH} + \nu\text{O-H}$	452.84	452.84	452.81	452.84	452.84	452.78	452.75	452.84
$(\delta\text{C-OCH}_3 + \delta\text{C-CHO} + \delta\text{C-OH})^2 + \delta\text{Ph}$	526.94	525.44	524.19	528.05	528.29	528.27	525.79	528.86
$\delta\text{Ph} + \delta\text{C-O-CH}_3$	529.44	528.48	528.92	525.10	526.69	526.31	527.14	523.62
$\gamma\text{Ph}^2$	572.32	572.32	571.15	569.09	572.21	564.21	571.25	569.29
$\delta\text{Ph}$	613.86	613.86	613.59	613.56	610.45	612.06	613.24	609.36
$\gamma\text{Ph}^3$	711.61	711.61	710.86	703.49	711.54	709.99	702.63	709.58
$[\delta\text{Ph} + (\delta\text{C-O-CH}_3 + \tau\text{C-CHO})]^1$	717.69	716.76	713.74	717.53	712.18	716.83	715.87	715.51
$[\delta\text{Ph} + (\delta\text{C-O-CH}_3 + \tau\text{C-CHO})]^2$	795.45	795.39	788.70	792.70	793.11	794.90	795.37	789.95
$(\nu^{\text{Hydrogen}}\text{Ph} + \delta^{\text{Hydrogen}}\text{Ph})^1$	805.30	805.30	805.24	805.02	805.16	805.09	802.15	802.84
$(\nu^{\text{Hydrogen}}\text{Ph} + \delta^{\text{Hydrogen}}\text{Ph})^2$	864.94	864.94	857.32	863.79	864.66	864.66	864.94	864.91

$(\nu^{\text{Hydrogen}}\text{Ph} + \gamma^{\text{Hydrogen}}\text{Ph})$	914.20	914.20	913.95	914.12	913.86	914.19	914.04	910.27
$(\nu^{\text{as}}\text{Ph} + \delta\text{Ph})$	936.91	933.97	927.23	933.89	932.07	936.38	936.47	931.36
$\gamma\text{O-C-H}$	984.46	984.46	984.32	984.46	971.01	981.67	984.45	984.03
$(\nu^{\text{as}}\text{Ph} + \delta\text{Ph}) + \nu\text{O-CH}_3$	1020.97	1011.45	1017.74	1016.86	1020.96	1020.95	1020.85	1018.28
$(\delta^{\text{Hydrogen}}\text{Ph} + \delta\text{Ph}) + \tau\text{C-OH}$	1106.26	1105.10	1103.40	1106.04	1106.15	1105.81	1103.54	1103.71
$(\tau\text{C-OCH}_3 + \tau\text{C-CHO} + \tau\text{C-OH})$	1133.55	1131.01	1132.73	1130.18	1130.81	1121.91	1133.03	1132.41
$(\tau\text{C-CH}_3 + \nu^{\text{as}}\text{C-H}_3)$	1143.34	1135.38	1143.34	1143.34	1143.34	1143.34	1143.34	1143.34
$[(\tau\text{C-CH}_3 + \tau\text{C-OH}) + \delta^{\text{Hydrogen}}\text{Ph}]^1$	1168.14	1164.81	1167.95	1167.75	1167.59	1164.82	1163.64	1167.86
$[(\tau\text{C-CH}_3 + \tau\text{C-OH}) + \delta^{\text{Hydrogen}}\text{Ph}]^2$	1191.15	1186.09	1190.09	1189.61	1191.06	1190.93	1189.53	1190.99
$\delta\text{Ph} + \delta\text{C-O-H} + \delta^{\text{Hydrogen}}\text{Ph}$	1232.64	1232.16	1230.65	1221.62	1232.23	1226.83	1223.27	1231.74
$\nu^{\text{Sym}}\text{Ph} + \delta^{\text{Hydrogen}}\text{Ph}$	1258.30	1257.83	1257.19	1253.65	1258.26	1253.97	1249.14	1254.96
$\nu\text{Ph} + \delta\text{C-O-H}$	1273.98	1273.59	1273.07	1267.90	1272.84	1263.53	1270.85	1272.72
$\delta\text{C-O-H} + \delta^{\text{Hydrogen}}\text{Ph}$	1365.52	1365.43	1363.27	1364.67	1362.79	1361.07	1359.16	1359.65
$(\delta\text{C-O-H} + \delta^{\text{Hydrogen}}\text{Ph} + \nu^{\text{as}}\text{Ph})^1$	1389.27	1388.67	1385.67	1379.24	1386.93	1386.13	1386.62	1385.83
$(\delta\text{C-O-H} + \delta^{\text{Hydrogen}}\text{Ph} + \nu^{\text{as}}\text{Ph})^2$	1423.67	1422.53	1420.76	1418.65	1423.58	1413.93	1421.12	1419.40
$(\nu\text{O-CH}_3 + \delta\text{C-O-CH}_3 + \nu^{\text{sym}}\text{C-H}_3 + \delta\text{C-CH}_3)$	1446.87	1442.95	1446.01	1444.08	1446.63	1443.74	1446.60	1445.42
$\nu^{\text{as}}\text{CH}_3^1$	1458.65	1456.70	1458.65	1458.65	1458.65	1458.65	1458.65	1458.65
$\nu^{\text{as}}\text{CH}_3^2$	1468.21	1466.59	1468.03	1467.59	1468.20	1468.17	1467.62	1468.11
$(\nu^{\text{as}}\text{Ph} + \delta\text{Ph} + \nu\text{C-OH} + \delta\text{C-O-H} + \nu\text{O-CH}_3 + \delta\text{C-O-CH}_3 + \nu^{\text{as}}\text{C-H}_3 + \delta\text{C-CH}_3)$	1492.38	1492.29	1485.57	1485.00	1492.10	1488.09	1480.84	1491.32
$[\nu^{\text{as}}\text{Ph} + (\delta\text{C-OH} + \delta\text{C-CHO} + \delta^{\text{Hydrogen}}\text{Ph})]^1$	1583.28	1583.25	1571.29	1571.35	1582.18	1582.10	1582.10	1567.93

$\delta\text{C-O-H} +$ $\nu^{\text{as}}\text{H-C=O} +$ $\nu^{\text{as}}\text{Ph}$	1586.95	1586.92	1584.13	1582.76	1586.22	1575.12	1575.12	1584.92
$[\nu^{\text{as}}\text{Ph} +$ $(\delta\text{C-OH} + \delta\text{C-CHO}$ $+ \delta^{\text{HydrogenPh}})^2]$	1695.25	1695.25	1694.85	1695.13	1656.73	1694.51	1695.00	1694.93
$\nu\text{H-CO}$	2800.87	2800.87	2800.87	2800.87	2792.79	2800.86	2800.87	2800.87
$\nu^{\text{sym}}\text{CH}_3$	2927.96	2924.95	2927.95	2927.95	2927.96	2927.96	2927.96	2927.96
$\nu^{\text{as}}\text{CH}_3^3$	2992.05	2980.68	2992.05	2992.05	2992.05	2992.05	2992.05	2992.05
$\nu^{\text{as}}\text{CH}_3^4$	3048.36	3037.45	3048.35	3048.36	3048.36	3048.36	3048.36	3048.36
$\nu^{\text{Hydrogen}}\text{Ph}^1$	3065.71	3065.71	3065.70	3065.71	3065.70	3065.70	3065.71	3056.60
$\nu^{\text{Hydrogen}}\text{Ph}^2$	3092.21	3101.59	3092.21	3092.21	3092.21	3092.21	3092.19	3091.58
$\nu^{\text{Hydrogen}}\text{Ph}^3$	3101.60	3092.21	3101.59	3101.58	3101.60	3101.60	3101.60	3101.60
$\nu\text{O-H}$	3601.99	3601.99	3601.99	3601.99	3601.99	3601.99	3601.98	3601.99

Table 3b-12a: Simulated vibrational wavenumbers for all isotopically substituted variants of B3LYP +d for Structure 001, with associated description of the matching vibrational mode. Wavenumber values are scaled by a factor of 0.967.

	B3LYP +d Structure 001 Vibrational Mode and Calculated Vibrational Wavenumber (W, cm <sup>-1</sup> ) for each Isotopic Substitution							
Vibrational Mode	08	09	10	11	12	13	14	15
$\tau\text{CH}_3$	71.73	69.21	70.77	69.21	71.65	71.59	71.73	71.17
$\tau\text{CH}_3 + \tau\text{Ph}^1$	98.97	98.57	98.74	98.57	98.25	98.76	98.09	98.85
$(\delta\text{HC=O} + \delta\text{OCH}_3)^1$	147.55	144.43	144.48	144.32	147.40	146.54	147.59	147.43
$\tau\text{O-CH}_3 + \tau\text{Ph}$	182.03	169.41	169.46	169.51	179.55	182.97	181.73	180.59
$\gamma\text{HC=O} + \tau\text{Ph}$	195.27	195.81	195.83	195.83	196.33	174.72	195.01	196.33
$(\delta\text{HC=O} + \delta\text{OCH}_3)^2$	238.10	231.28	233.41	231.15	236.76	237.18	232.98	237.38
$\tau\text{O-CH}_3 + \tau\text{HC=O}$	248.86	240.26	234.08	240.36	247.43	245.76	248.85	247.87
$(\delta\text{C-OCH}_3 + \delta\text{C-CHO} + \delta\text{C-OH})^1$	327.07	322.01	325.16	322.08	326.31	327.03	320.86	326.70
$\tau\text{Ph}$	363.31	364.57	364.48	364.51	364.73	351.79	452.79	452.79
$(\nu^{\text{as}}\text{Ph}^1 + \nu\text{C-CHO})$	401.39	399.91	400.79	399.94	400.68	396.28	351.79	354.25
$\gamma\text{Ph}^1$	443.50	445.45	445.63	445.45	413.36	444.89	396.28	398.94
$\gamma\text{C-OH} + \nu\text{O-H}$	452.84	452.83	452.82	452.83	452.64	452.79	444.89	445.30
$(\delta\text{C-OCH}_3 + \delta\text{C-CHO} + \delta\text{C-OH})^2 + \delta\text{Ph}$	523.69	522.28	528.21	522.27	522.90	525.16	515.55	521.18
$\delta\text{Ph} + \delta\text{C-O-CH}_3$	528.06	526.75	517.31	526.75	524.87	526.86	528.60	523.77
$\gamma\text{Ph}^2$	571.12	572.16	572.12	572.14	566.47	567.04	571.77	528.64
$\delta\text{Ph}$	608.72	613.82	613.48	613.82	612.83	609.56	612.89	609.99
$\gamma\text{Ph}^3$	711.07	710.84	711.61	711.53	661.76	710.32	711.51	695.82
$[\delta\text{Ph} + (\delta\text{C-O-CH}_3 + \tau\text{C-CHO})]^1$	710.84	711.07	707.34	717.38	713.37	703.63	716.00	712.88
$[\delta\text{Ph} + (\delta\text{C-O-CH}_3 + \tau\text{C-CHO})]^2$	794.25	793.87	793.23	793.87	744.49	790.88	788.05	715.16
$(\nu^{\text{Hydrogen}}\text{Ph} + \delta^{\text{Hydrogen}}\text{Ph})^1$	801.75	805.29	805.30	805.29	805.31	794.50	804.73	783.97
$(\nu^{\text{Hydrogen}}\text{Ph} + \delta^{\text{Hydrogen}}\text{Ph})^2$	864.87	864.81	864.60	864.80	748.05	918.77	864.88	862.30

$(\nu^{\text{Hydrogen}}\text{Ph} + \gamma^{\text{Hydrogen}}\text{Ph})$	910.18	914.19	914.20	931.10	913.59	838.19	914.19	873.27
$(\nu^{\text{as}}\text{Ph} + \delta\text{Ph})$	936.50	931.12	901.02	914.19	866.06	915.22	921.63	875.62
$\gamma\text{O-C-H}$	984.44	1138.80	984.45	1138.80	1231.34	882.23	1216.92	1132.10
$(\nu^{\text{as}}\text{Ph} + \delta\text{Ph}) + \nu\text{O-CH}_3$	1017.96	936.53	1029.40	936.55	978.40	1020.14	953.23	931.04
$(\delta^{\text{Hydrogen}}\text{Ph} + \delta\text{Ph}) + \tau\text{C-OH}$	1102.65	984.46	992.92	984.46	983.22	1237.35	984.46	981.95
$(\tau\text{C-OCH}_3 + \tau\text{C-CHO} + \tau\text{C-OH})$	1132.28	1025.21	1106.22	1025.25	1049.66	1027.23	1024.65	1025.44
$(\tau\text{C-CH}_3 + \nu^{\text{as}}\text{C-H}_3)$	1143.34	1106.24	1096.55	1106.23	1103.54	1143.34	1113.93	1143.34
$[(\tau\text{C-CH}_3 + \tau\text{C-OH}) + \delta^{\text{Hydrogen}}\text{Ph}]^1$	1165.31	1111.87	1139.20	1111.85	1143.28	1106.16	1133.52	1162.63
$[(\tau\text{C-CH}_3 + \tau\text{C-OH}) + \delta^{\text{Hydrogen}}\text{Ph}]^2$	1190.64	1176.78	1175.64	1176.78	1157.73	1145.35	1143.30	1190.68
$\delta\text{Ph} + \delta\text{C-O-H} + \delta^{\text{Hydrogen}}\text{Ph}$	1231.97	1231.61	1232.15	1231.60	1182.44	1172.82	1184.32	1201.62
$\nu^{\text{Sym}}\text{Ph} + \delta^{\text{Hydrogen}}\text{Ph}$	1255.68	1254.70	1257.90	1254.70	1219.35	1191.39	1252.55	1251.57
$\nu\text{Ph} + \delta\text{C-O-H}$	1268.41	1272.95	1270.63	1272.95	1271.21	34.00	1267.27	1263.71
$\delta\text{C-O-H} + \delta^{\text{Hydrogen}}\text{Ph}$	1365.50	1308.13	1290.74	1308.04	1364.98	1261.94	1384.76	1385.11
$(\delta\text{C-O-H} + \delta^{\text{Hydrogen}}\text{Ph} + \nu^{\text{as}}\text{Ph})^1$	1387.29	1338.46	1366.36	1338.42	1387.59	1377.23	1330.98	1354.01
$(\delta\text{C-O-H} + \delta^{\text{Hydrogen}}\text{Ph} + \nu^{\text{as}}\text{Ph})^2$	1419.39	1393.30	1343.08	1393.31	1417.08	1417.54	1417.14	1410.35
$(\nu\text{O-CH}_3 + \delta\text{C-O-CH}_3 + \nu^{\text{sym}}\text{C-H}_3 + \delta\text{C-CH}_3)$	1446.54	1366.52	1427.89	1366.54	1444.03	1446.40	1446.67	1442.61
$\nu^{\text{as}}\text{CH}_3^1$	1458.65	1427.26	1392.35	1427.28	1458.45	1458.65	1458.65	1458.65
$\nu^{\text{as}}\text{CH}_3^2$	1467.51	1456.21	1460.12	1456.37	1468.04	1468.19	1468.12	1468.05
$(\nu^{\text{as}}\text{Ph} + \delta\text{Ph} + \nu\text{C-OH} + \delta\text{C-O-H} + \nu\text{O-CH}_3 + \delta\text{C-O-CH}_3 + \nu^{\text{as}}\text{C-H}_3 + \delta\text{C-CH}_3)$	1484.00	1490.96	1492.31	1490.96	1476.25	1491.95	1492.27	1484.00
$[\nu^{\text{as}}\text{Ph} + (\delta\text{C-OH} + \delta\text{C-CHO} + \delta^{\text{Hydrogen}}\text{Ph})]^1$	1574.24	1583.23	1582.96	1583.23	1574.32	1582.39	1583.74	1573.24

$\delta\text{C-O-H} +$ $\nu^{\text{as}}\text{H-C=O} +$ $\nu^{\text{as}}\text{Ph}$	1581.13	1586.81	1586.86	1586.81	1584.45	1586.67	1575.65	1583.83
$[\nu^{\text{as}}\text{Ph} +$ $(\delta\text{C-OH} + \delta\text{C-CHO}$ $+ \delta^{\text{Hydrogen}}\text{Ph})]^2$	1694.79	1695.24	1695.24	1695.24	1694.95	1681.80	1695.24	1695.04
$\nu\text{H-CO}$	2800.87	2800.87	2800.87	2800.87	3092.24	2066.08	3101.60	3601.99
$\nu^{\text{sym}}\text{CH}_3$	2927.96	2174.03	2227.15	2173.98	2291.03	2927.96	2621.21	2266.90
$\nu^{\text{as}}\text{CH}_3^3$	2992.05	2959.60	2943.92	2959.68	2800.88	2992.05	2800.88	2800.93
$\nu^{\text{as}}\text{CH}_3^4$	3048.36	3044.72	2991.81	3044.71	2928.06	3048.36	2927.96	2927.96
$\nu^{\text{Hydrogen}}\text{Ph}^1$	3064.73	3065.71	3065.71	3065.71	2992.05	3065.66	2992.05	2992.05
$\nu^{\text{Hydrogen}}\text{Ph}^2$	3083.27	3092.21	3092.21	3092.21	3048.42	3092.21	3048.36	3048.36
$\nu^{\text{Hydrogen}}\text{Ph}^3$	3101.58	3101.54	3101.56	3101.54	3065.71	3101.59	3065.71	3090.28
$\nu\text{O-H}$	3601.99	3601.99	3601.99	3601.99	3601.99	3601.99	3092.21	3101.60

*Table 3b-12b: Simulated vibrational wavenumbers for all isotopically substituted variants of B3LYP +d for Structure 001, with associated description of the matching vibrational mode. Wavenumber values are scaled by a factor of 0.967.*

	B3LYP +d Structure 001 Vibrational Mode and Calculated Vibrational Wavenumber (W, cm <sup>-1</sup> ) for each Isotopic Substitution						
Vibrational Mode	16	17	18	19	20	21	22
$\tau\text{CH}_3$	71.49	71.48	71.64	71.81	71.10	71.43	71.74
$\tau\text{CH}_3 + \tau\text{Ph}^1$	98.84	98.67	98.16	98.20	98.40	97.43	97.49
$(\delta\text{HC=O} + \delta\text{OCH}_3)^1$	147.54	147.44	145.64	147.58	147.27	143.79	147.56
$\tau\text{O-CH}_3 + \tau\text{Ph}$	181.06	181.45	182.21	181.99	180.68	182.14	181.70
$\gamma\text{HC=O} + \tau\text{Ph}$	194.41	196.34	195.78	195.73	196.34	195.29	195.19
$(\delta\text{HC=O} + \delta\text{OCH}_3)^2$	237.91	237.89	237.19	236.25	237.60	236.29	234.36
$\tau\text{O-CH}_3 + \tau\text{HC=O}$	248.24	247.80	248.94	248.88	246.79	248.94	248.82
$(\delta\text{C-OCH}_3 + \delta\text{C-CHO} + \delta\text{C-OH})^1$	326.69	325.71	326.37	324.21	324.35	325.63	321.58
$\tau\text{Ph}$	362.43	364.55	364.89	364.26	364.21	364.85	363.64
$(\nu^{\text{as}}\text{Ph}^1 + \nu\text{C-CHO})$	401.62	401.39	399.24	399.52	401.02	396.85	397.31
$\gamma\text{Ph}^1$	417.73	445.44	445.62	445.53	445.26	445.61	445.40
$\gamma\text{C-OH} + \nu\text{O-H}$	452.84	452.83	452.84	451.83	452.82	452.84	450.98
$(\delta\text{C-OCH}_3 + \delta\text{C-CHO} + \delta\text{C-OH})^2 + \delta\text{Ph}$	515.38	527.81	529.33	528.77	527.02	529.23	528.13
$\delta\text{Ph} + \delta\text{C-O-CH}_3$	527.14	521.15	526.42	525.29	514.82	525.93	523.79
$\gamma\text{Ph}^2$	572.31	571.89	572.30	572.22	571.50	572.28	572.13
$\delta\text{Ph}$	599.72	613.62	610.69	611.64	613.41	607.86	609.54
$\gamma\text{Ph}^3$	640.00	711.46	711.61	711.42	711.33	711.60	711.26
$[\delta\text{Ph} + (\delta\text{C-O-CH}_3 + \tau\text{C-CHO})]^1$	706.33	715.22	717.20	717.68	713.03	716.78	717.67
$[\delta\text{Ph} + (\delta\text{C-O-CH}_3 + \tau\text{C-CHO})]^2$	793.74	795.11	795.24	789.73	794.82	795.07	784.56
$(\nu^{\text{Hydrogen}}\text{Ph} + \delta^{\text{Hydrogen}}\text{Ph})^1$	744.21	805.29	805.28	805.18	805.28	805.26	805.07
$(\nu^{\text{Hydrogen}}\text{Ph} + \delta^{\text{Hydrogen}}\text{Ph})^2$	1227.10	864.85	864.91	864.94	864.78	864.88	864.94

$(\nu^{\text{Hydrogen}}\text{Ph} + \gamma^{\text{Hydrogen}}\text{Ph})$	851.26	914.20	914.18	914.18	914.20	914.16	914.17
$(\nu^{\text{as}}\text{Ph} + \delta\text{Ph})$	863.16	934.29	936.79	936.85	931.72	936.69	936.79
$\gamma\text{O-C-H}$	875.51	984.46	983.65	984.46	984.46	982.94	984.46
$(\nu^{\text{as}}\text{Ph} + \delta\text{Ph}) + \nu\text{O-CH}_3$	960.38	1012.88	1020.97	1020.96	1004.85	1020.97	1020.94
$(\delta^{\text{Hydrogen}}\text{Ph} + \delta\text{Ph}) + \tau\text{C-OH}$	984.32	1104.06	1106.23	1106.06	1101.80	1106.20	1105.88
$(\tau\text{C-OCH}_3 + \tau\text{C-CHO} + \tau\text{C-OH})$	1033.77	1129.88	1133.35	1133.39	1127.03	1133.16	1133.24
$(\tau\text{C-CH}_3 + \nu^{\text{as}}\text{C-H}_3)$	1143.34	1141.75	1143.34	1143.34	1140.35	1143.34	1143.34
$[(\tau\text{C-CH}_3 + \tau\text{C-OH}) + \delta^{\text{Hydrogen}}\text{Ph}]^1$	1123.00	1166.80	1168.09	1167.59	1165.73	1168.05	1167.06
$[(\tau\text{C-CH}_3 + \tau\text{C-OH}) + \delta^{\text{Hydrogen}}\text{Ph}]^2$	1148.99	1187.14	1191.15	1191.04	1183.65	1191.14	1190.94
$\delta\text{Ph} + \delta\text{C-O-H} + \delta^{\text{Hydrogen}}\text{Ph}$	1182.33	1230.81	1232.61	1228.91	1229.48	1232.57	1224.75
$\nu^{\text{Sym}}\text{Ph} + \delta^{\text{Hydrogen}}\text{Ph}$	1256.82	1257.18	1258.24	1254.48	1256.38	1258.19	1251.94
$\nu\text{Ph} + \delta\text{C-O-H}$	1262.89	1273.59	1273.88	1273.10	1273.32	1273.80	1272.48
$\delta\text{C-O-H} + \delta^{\text{Hydrogen}}\text{Ph}$	1355.44	1365.40	1364.14	1364.76	1365.31	1362.59	1364.07
$(\delta\text{C-O-H} + \delta^{\text{Hydrogen}}\text{Ph} + \nu^{\text{as}}\text{Ph})^1$	1389.23	1388.74	1387.44	1389.12	1388.30	1385.75	1388.99
$(\delta\text{C-O-H} + \delta^{\text{Hydrogen}}\text{Ph} + \nu^{\text{as}}\text{Ph})^2$	1414.33	1423.41	1422.65	1423.16	1423.19	1421.74	1422.73
$(\nu\text{O-CH}_3 + \delta\text{C-O-CH}_3 + \nu^{\text{sym}}\text{C-H}_3 + \delta\text{C-CH}_3)$	1446.63	1445.77	1446.85	1446.85	1444.87	1446.83	1446.83
$\nu^{\text{as}}\text{CH}_3^1$	1458.65	1458.57	1458.65	1458.65	1458.50	1458.65	1458.65
$\nu^{\text{as}}\text{CH}_3^2$	1465.81	1467.78	1468.19	1468.15	1467.44	1468.18	1468.10
$(\nu^{\text{as}}\text{Ph} + \delta\text{Ph} + \nu\text{C-OH} + \delta\text{C-O-H} + \nu\text{O-CH}_3 + \delta\text{C-O-CH}_3 + \nu^{\text{as}}\text{C-H}_3 + \delta\text{C-CH}_3)$	1475.96	1491.76	1492.30	1491.42	1491.28	1492.23	1490.63
$[\nu^{\text{as}}\text{Ph} + (\delta\text{C-OH} + \delta\text{C-CHO} + \delta^{\text{Hydrogen}}\text{Ph})]^1$	1580.26	1583.10	1583.22	1583.23	1582.95	1583.11	1583.19

$\delta\text{C-O-H} +$ $\nu^{\text{as}}\text{H-C=O} +$ $\nu^{\text{as}}\text{Ph}$	1577.48	1586.93	1586.30	1586.48	1586.91	1585.55	1586.08
$[\nu^{\text{as}}\text{Ph} +$ $(\delta\text{C-OH} + \delta\text{C-CHO}$ $+ \delta^{\text{Hydrogen}}\text{Ph})]^2$	1695.06	1695.25	1678.55	1695.24	1695.25	1664.26	1695.23
$\nu\text{H-CO}$	3067.75	2800.87	2800.86	2800.87	2800.87	2800.86	2800.87
$\nu^{\text{sym}}\text{CH}_3$	2285.49	2927.95	2927.96	2927.96	2927.93	2927.96	2927.96
$\nu^{\text{as}}\text{CH}_3^3$	2800.87	2992.05	2992.05	2992.05	2992.05	2992.05	2992.05
$\nu^{\text{as}}\text{CH}_3^4$	2927.96	3048.36	3048.36	3048.36	3048.36	3048.36	3048.36
$\nu^{\text{Hydrogen}}\text{Ph}^1$	2992.05	3065.71	3065.71	3065.71	3065.71	3065.71	3065.71
$\nu^{\text{Hydrogen}}\text{Ph}^2$	3048.36	3092.21	3092.21	3092.21	3092.21	3092.21	3092.21
$\nu^{\text{Hydrogen}}\text{Ph}^3$	3101.57	3101.60	3101.60	3101.60	3101.60	3101.60	3101.60
$\nu\text{O-H}$	3601.99	3601.99	3601.99	3595.90	3601.99	3601.99	3590.52

*Table 3b-12c: Simulated vibrational wavenumbers for all isotopically substituted variants of B3LYP +d for Structure 001, with associated description of the matching vibrational mode. Wavenumber values are scaled by a factor of 0.967.*

	B3LYP +d Structure 011 Vibrational Mode and Calculated Vibrational Wavenumber (W, cm <sup>-1</sup> ) for each Isotopic Substitution							
Vibrational Mode	00	01	02	03	04	05	06	07
$\tau\text{CH}_3$	69.04	68.26	68.80	68.87	69.01	69.02	69.04	68.97
$\tau\text{CH}_3 + \tau\text{Ph}^1$	95.91	95.91	95.64	95.89	95.90	95.51	95.91	95.43
$(\delta\text{HC=O} + \delta\text{OCH}_3)^1$	158.56	216.21	158.31	158.46	215.25	216.21	216.13	216.17
$\tau\text{O-CH}_3 + \tau\text{Ph}$	153.07	153.07	152.92	153.04	152.20	153.02	153.06	152.63
$\gamma\text{HC=O} + \tau\text{Ph}$	216.21	156.83	215.91	215.91	158.25	158.35	158.42	158.32
$(\delta\text{HC=O} + \delta\text{OCH}_3)^2$	230.43	228.98	230.02	230.24	230.38	229.79	230.42	229.92
$\tau\text{O-CH}_3 + \tau\text{HC=O}$	271.61	271.59	269.56	271.33	270.56	270.82	271.50	271.53
$(\delta\text{C-OCH}_3 + \delta\text{C-CHO} + \delta\text{C-OH})^1$	329.63	326.43	329.37	329.32	329.40	329.18	329.53	329.26
$\tau\text{Ph}$	333.81	333.81	333.68	332.79	333.71	331.57	331.94	331.67
$(\nu^{\text{as}}\text{Ph}^1 + \nu\text{C-CHO})$	386.60	386.27	386.52	386.25	383.56	385.65	385.29	385.60
$\gamma\text{Ph}^1$	448.44	448.44	441.84	440.97	442.87	442.86	441.62	442.80
$\gamma\text{C-OH} + \nu\text{O-H}$	442.90	442.90	446.72	446.38	448.36	448.18	446.06	448.21
$(\delta\text{C-OCH}_3 + \delta\text{C-CHO} + \delta\text{C-OH})^2 + \delta\text{Ph}$	498.69	497.88	534.68	496.85	497.95	537.53	496.44	534.33
$\delta\text{Ph} + \delta\text{C-O-CH}_3$	537.63	536.07	498.58	535.54	537.42	498.12	536.73	498.12
$\gamma\text{Ph}^2$	568.48	568.47	567.39	565.18	568.40	560.62	567.24	565.53
$\delta\text{Ph}$	628.92	628.26	759.41	628.85	627.12	626.44	626.64	626.47
$\gamma\text{Ph}^3$	707.82	707.82	707.10	700.07	707.78	706.01	698.49	705.92
$[\delta\text{Ph} + (\delta\text{C-O-CH}_3 + \tau\text{C-CHO})]^1$	761.14	760.81	625.00	760.89	749.79	759.41	760.96	758.78
$[\delta\text{Ph} + (\delta\text{C-O-CH}_3 + \tau\text{C-CHO})]^2$	781.90	781.86	772.66	779.44	781.27	781.79	781.60	779.63
$(\nu^{\text{Hydrogen}}\text{Ph} + \delta^{\text{Hydrogen}}\text{Ph})^1$	818.82	818.82	818.75	818.63	818.74	818.42	816.06	816.43
$(\nu^{\text{Hydrogen}}\text{Ph} + \delta^{\text{Hydrogen}}\text{Ph})^2$	836.89	836.89	829.37	835.63	836.61	836.65	836.89	836.88

$(\nu^{\text{Hydrogen}}\text{Ph} + \gamma^{\text{Hydrogen}}\text{Ph})$	937.44	937.44	937.30	937.39	936.54	937.42	906.83	897.75
$(\nu^{\text{as}}\text{Ph} + \delta\text{Ph})$	907.71	905.23	901.13	905.14	905.32	906.02	937.37	932.97
$\gamma\text{O-C-H}$	986.27	986.27	986.08	986.27	973.23	983.43	986.26	985.80
$(\nu^{\text{as}}\text{Ph} + \delta\text{Ph}) + \nu\text{O-CH}_3$	1023.94	1014.23	1020.54	1019.52	1023.93	1023.91	1023.72	1021.33
$(\delta^{\text{Hydrogen}}\text{Ph} + \delta\text{Ph}) + \tau\text{C-OH}$	1100.82	1098.87	1097.70	1100.56	1100.74	1099.18	1098.43	1099.05
$(\tau\text{C-OCH}_3 + \tau\text{C-CHO} + \tau\text{C-OH})$	1143.11	1140.66	1142.89	1139.95	1141.06	1134.74	1142.44	1141.58
$(\tau\text{C-CH}_3 + \nu^{\text{as}}\text{C-H}_3)$	1143.42	1135.48	1143.42	1143.42	1143.42	1143.42	1143.42	1143.42
$[(\tau\text{C-CH}_3 + \tau\text{C-OH}) + \delta^{\text{Hydrogen}}\text{Ph}]^1$	1169.55	1165.61	1169.46	1169.42	1168.48	1164.91	1165.78	1169.50
$[(\tau\text{C-CH}_3 + \tau\text{C-OH}) + \delta^{\text{Hydrogen}}\text{Ph}]^2$	1190.73	1186.33	1189.74	1189.52	1190.73	1190.72	1188.64	1190.56
$\delta\text{Ph} + \delta\text{C-O-H} + \delta^{\text{Hydrogen}}\text{Ph}$	1227.74	1227.21	1225.27	1215.67	1227.45	1222.19	1218.09	1225.88
$\nu^{\text{sym}}\text{Ph} + \delta^{\text{Hydrogen}}\text{Ph}$	1269.02	1268.51	1266.85	1263.40	1268.65	1265.31	1256.73	1265.11
$\nu\text{Ph} + \delta\text{C-O-H}$	1279.21	1278.94	1278.86	1274.30	1277.57	1266.83	1278.79	1279.19
$\delta\text{C-O-H} + \delta^{\text{Hydrogen}}\text{Ph}$	1366.89	1366.65	1363.26	1363.09	1363.76	1359.47	1359.18	1361.32
$(\delta\text{C-O-H} + \delta^{\text{Hydrogen}}\text{Ph} + \nu^{\text{as}}\text{Ph})^1$	1377.31	1376.99	1374.68	1369.16	1376.08	1376.92	1376.16	1372.54
$(\delta\text{C-O-H} + \delta^{\text{Hydrogen}}\text{Ph} + \nu^{\text{as}}\text{Ph})^2$	1422.48	1421.46	1419.74	1416.72	1422.22	1413.59	1419.49	1419.25
$(\nu\text{O-CH}_3 + \delta\text{C-O-CH}_3 + \nu^{\text{sym}}\text{C-H}_3 + \delta\text{C-CH}_3)$	1445.85	1441.66	1445.21	1443.49	1445.71	1443.61	1445.52	1445.01
$\nu^{\text{as}}\text{CH}_3^1$	1459.44	1457.46	1459.44	1459.44	1459.44	1459.44	1459.44	1459.44
$\nu^{\text{as}}\text{CH}_3^2$	1468.70	1467.07	1468.53	1468.25	1468.70	1468.63	1468.37	1468.63
$(\nu^{\text{as}}\text{Ph} + \delta\text{Ph} + \nu\text{C-OH} + \delta\text{C-O-H} + \nu\text{O-CH}_3 + \delta\text{C-O-CH}_3 + \nu^{\text{as}}\text{C-H}_3 + \delta\text{C-CH}_3)$	1497.41	1497.36	1490.76	1490.58	1497.08	1492.92	1486.39	1495.74
$[\nu^{\text{as}}\text{Ph} + (\delta\text{C-OH} + \delta\text{C-CHO} + \delta^{\text{Hydrogen}}\text{Ph})]^1$	1575.05	1575.03	1570.43	1565.66	1591.38	1585.70	1585.70	1559.72

$\delta\text{C-O-H} +$ $\nu^{\text{as}}\text{H-C=O} +$ $\nu^{\text{as}}\text{Ph}$	1591.40	1591.36	1581.10	1585.54	1573.03	1568.10	1568.10	1589.57
$[\nu^{\text{as}}\text{Ph} +$ $(\delta\text{C-OH} + \delta\text{C-CHO}$ $+ \delta^{\text{Hydrogen}}\text{Ph})]^2$	1702.61	1702.61	1702.28	1702.17	1663.95	1701.71	1702.41	1702.06
$\nu\text{H-CO}$	2780.95	2780.95	2780.95	2780.95	2773.01	2780.94	2780.95	2780.95
$\nu^{\text{sym}}\text{CH}_3$	2922.62	2919.54	2922.62	2922.62	2922.62	2922.62	2922.62	2922.62
$\nu^{\text{as}}\text{CH}_3^3$	2984.45	2973.14	2984.45	2984.45	2984.45	2984.45	2984.45	2984.45
$\nu^{\text{as}}\text{CH}_3^4$	3046.73	3035.95	3046.69	3046.73	3046.73	3046.73	3046.73	3046.73
$\nu^{\text{Hydrogen}}\text{Ph}^1$	3100.05	3100.05	3100.05	3100.05	3100.05	3100.05	3100.04	3094.43
$\nu^{\text{Hydrogen}}\text{Ph}^2$	3085.81	3078.14	3085.81	3085.81	3085.81	3085.81	3085.80	3081.60
$\nu^{\text{Hydrogen}}\text{Ph}^3$	3078.17	3085.81	3068.67	3078.16	3078.17	3078.17	3078.17	3078.10
$\nu\text{O-H}$	3605.54	3605.54	3605.54	3605.54	3605.54	3605.54	3605.53	3605.54

Table 3b-13a: Simulated vibrational wavenumbers for all isotopically substituted variants of B3LYP +d for Structure 011, with associated description of the matching vibrational mode. Wavenumber values are scaled by a factor of 0.967.

	B3LYP +d Structure 011 Vibrational Mode and Calculated Vibrational Wavenumber (W, cm <sup>-1</sup> ) for each Isotopic Substitution							
Vibrational Mode	08	09	10	11	12	13	14	15
$\tau\text{CH}_3$	68.94	66.36	67.64	66.36	68.42	68.69	69.04	68.73
$\tau\text{CH}_3 + \tau\text{Ph}^1$	95.70	95.60	95.81	95.60	95.64	95.40	95.10	95.26
$(\delta\text{HC=O} + \delta\text{OCH}_3)^1$	216.21	196.51	195.67	196.62	215.48	156.60	216.17	215.71
$\tau\text{O-CH}_3 + \tau\text{Ph}$	152.77	149.52	151.19	149.58	152.40	144.61	151.44	151.81
$\gamma\text{HC=O} + \tau\text{Ph}$	158.38	156.32	155.02	156.18	158.28	207.19	158.42	158.13
$(\delta\text{HC=O} + \delta\text{OCH}_3)^2$	230.18	265.81	226.36	229.08	229.60	229.88	226.42	229.06
$\tau\text{O-CH}_3 + \tau\text{HC=O}$	271.36	229.11	265.31	265.79	269.29	259.72	271.48	269.33
$(\delta\text{C-OCH}_3 + \delta\text{C-CHO} + \delta\text{C-OH})^1$	329.55	324.26	327.54	324.40	329.07	329.54	447.15	328.54
$\tau\text{Ph}$	331.30	333.52	333.18	333.40	333.42	329.15	318.04	326.14
$(v^{\text{as}}\text{Ph}^1 + v\text{C-CHO})$	385.95	385.60	386.09	385.60	385.17	381.74	329.54	385.74
$\gamma\text{Ph}^1$	442.03	442.79	442.90	442.80	412.80	448.36	381.74	448.24
$v\text{C-OH} + v\text{O-H}$	447.45	448.38	448.42	448.38	444.24	442.84	442.84	442.90
$(\delta\text{C-OCH}_3 + \delta\text{C-CHO} + \delta\text{C-OH})^2 + \delta\text{Ph}$	534.81	491.88	532.47	491.87	533.85	536.92	528.37	524.42
$\delta\text{Ph} + \delta\text{C-O-CH}_3$	498.32	537.22	491.40	537.22	495.97	497.35	498.04	532.04
$\gamma\text{Ph}^2$	567.25	568.31	568.30	568.31	563.70	562.53	568.16	497.17
$\delta\text{Ph}$	622.26	760.90	628.69	627.93	620.50	626.87	624.66	621.29
$\gamma\text{Ph}^3$	707.07	707.07	707.82	707.75	648.67	706.63	707.72	707.75
$[\delta\text{Ph} + (\delta\text{C-O-CH}_3 + \tau\text{C-CHO})]^1$	754.91	627.93	752.70	760.90	818.82	734.62	760.86	775.28
$[\delta\text{Ph} + (\delta\text{C-O-CH}_3 + \tau\text{C-CHO})]^2$	780.13	780.31	776.51	780.30	739.48	780.30	777.27	714.49
$(v^{\text{Hydrogen}}\text{Ph} + \delta^{\text{Hydrogen}}\text{Ph})^1$	814.84	818.81	818.81	818.80	735.83	802.60	818.33	743.96
$(v^{\text{Hydrogen}}\text{Ph} + \delta^{\text{Hydrogen}}\text{Ph})^2$	836.88	836.81	836.56	836.81	763.21	942.22	836.84	836.78

$(\nu^{\text{Hydrogen}}\text{Ph} + \gamma^{\text{Hydrogen}}\text{Ph})$	933.83	1146.55	937.44	1146.55	937.14	827.42	937.44	883.99
$(\nu^{\text{as}}\text{Ph} + \delta\text{Ph})$	907.12	931.14	883.39	907.12	871.76	891.71	893.05	880.38
$\gamma\text{O-C-H}$	986.21	907.13	1031.45	931.13	1238.41	871.68	1216.33	1138.52
$(\nu^{\text{as}}\text{Ph} + \delta\text{Ph}) + \nu\text{O-CH}_3$	1020.61	937.45	984.94	937.45	944.52	1022.63	949.54	897.61
$(\delta^{\text{Hydrogen}}\text{Ph} + \delta\text{Ph}) + \tau\text{C-OH}$	1098.85	986.27	986.28	986.27	984.95	1232.76	986.27	983.31
$(\tau\text{C-OCH}_3 + \tau\text{C-CHO} + \tau\text{C-OH})$	1141.57	1027.95	1100.78	1027.99	1042.31	1032.83	1028.90	1028.93
$(\tau\text{C-CH}_3 + \nu^{\text{as}}\text{C-H}_3)$	1143.42	1100.82	1098.08	1100.82	1102.13	1143.42	1107.49	1169.00
$[(\tau\text{C-CH}_3 + \tau\text{C-OH}) + \delta^{\text{Hydrogen}}\text{Ph}]^1$	1167.03	1112.01	1147.41	1111.98	1143.38	1102.42	1143.42	1143.42
$[(\tau\text{C-CH}_3 + \tau\text{C-OH}) + \delta^{\text{Hydrogen}}\text{Ph}]^2$	1189.92	1179.29	1177.83	1179.29	1159.17	1150.82	1143.34	1188.99
$\delta\text{Ph} + \delta\text{C-O-H} + \delta^{\text{Hydrogen}}\text{Ph}$	1227.19	1227.10	1227.18	1227.09	1223.07	1176.06	1182.05	1210.32
$\nu^{\text{Sym}}\text{Ph} + \delta^{\text{Hydrogen}}\text{Ph}$	1263.99	1265.47	1267.66	1265.46	1183.56	1190.73	1267.06	1251.21
$\nu\text{Ph} + \delta\text{C-O-H}$	1276.35	1277.08	1278.04	1277.08	1273.26	34.00	1269.16	1369.19
$\delta\text{C-O-H} + \delta^{\text{Hydrogen}}\text{Ph}$	1366.56	1308.71	1290.66	1308.62	1364.75	1269.69	1376.54	1267.10
$(\delta\text{C-O-H} + \delta^{\text{Hydrogen}}\text{Ph} + \nu^{\text{as}}\text{Ph})^1$	1374.28	1339.47	1369.30	1339.42	1374.94	1369.69	1327.36	1360.23
$(\delta\text{C-O-H} + \delta^{\text{Hydrogen}}\text{Ph} + \nu^{\text{as}}\text{Ph})^2$	1420.15	1380.31	1340.79	1380.32	1415.19	1411.95	1416.52	1412.57
$(\nu\text{O-CH}_3 + \delta\text{C-O-CH}_3 + \nu^{\text{sym}}\text{C-H}_3 + \delta\text{C-CH}_3)$	1445.76	1369.44	1425.88	1369.47	1443.42	1444.86	1445.68	1442.93
$\nu^{\text{as}}\text{CH}_3^1$	1459.44	1425.65	1378.08	1425.67	1459.26	1459.44	1459.44	1459.44
$\nu^{\text{as}}\text{CH}_3^2$	1468.22	1455.82	1461.58	1455.98	1468.48	1468.66	1468.57	1468.54
$(\nu^{\text{as}}\text{Ph} + \delta\text{Ph} + \nu\text{C-OH} + \delta\text{C-O-H} + \nu\text{O-CH}_3 + \delta\text{C-O-CH}_3 + \nu^{\text{as}}\text{C-H}_3 + \delta\text{C-CH}_3)$	1487.59	1496.23	1497.35	1496.22	1478.32	1497.00	1497.24	1488.50
$[\nu^{\text{as}}\text{Ph} + (\delta\text{C-OH} + \delta\text{C-CHO} + \delta^{\text{Hydrogen}}\text{Ph})]^1$	1581.35	1575.04	1574.92	1591.21	1584.11	1590.58	1587.88	1565.41

$\delta\text{C-O-H} +$ $\nu^{\text{as}}\text{H-C=O} +$ $\nu^{\text{as}}\text{Ph}$	1569.74	1591.21	1591.20	1575.04	1570.81	1575.01	1567.53	1588.42
$[\nu^{\text{as}}\text{Ph} +$ $(\delta\text{C-OH} + \delta\text{C-CHO}$ $+ \delta^{\text{Hydrogen}}\text{Ph})]^2$	1702.48	1702.61	1702.61	1702.61	1702.39	1689.48	1702.56	1702.15
$\nu\text{H-CO}$	2780.95	2780.95	2780.95	2780.95	3100.05	2050.65	3100.05	3078.21
$\nu^{\text{sym}}\text{CH}_3$	2922.62	2168.83	2226.84	2168.77	2272.99	2922.62	2623.84	2288.69
$\nu^{\text{as}}\text{CH}_3^3$	2984.45	2953.37	2937.46	2953.47	2780.97	2984.45	2780.95	2780.95
$\nu^{\text{as}}\text{CH}_3^4$	3046.73	3043.28	2984.18	3043.26	2922.77	3046.73	2922.63	2922.63
$\nu^{\text{Hydrogen}}\text{Ph}^1$	3098.16	3100.05	3100.05	3100.05	2984.45	3100.05	2984.45	2984.45
$\nu^{\text{Hydrogen}}\text{Ph}^2$	3078.82	3085.81	3085.81	3085.81	3046.84	3085.81	3085.81	3046.73
$\nu^{\text{Hydrogen}}\text{Ph}^3$	3077.12	3078.08	3078.10	3078.08	3085.72	3078.14	3078.17	3089.83
$\nu\text{O-H}$	3605.54	3605.54	3605.54	3605.54	3605.54	3605.54	3046.73	3605.54

*Table 3b-13b: Simulated vibrational wavenumbers for all isotopically substituted variants of B3LYP +d for Structure 011, with associated description of the matching vibrational mode. Wavenumber values are scaled by a factor of 0.967.*

	B3LYP +d Structure 011 Vibrational Mode and Calculated Vibrational Wavenumber (W, cm <sup>-1</sup> ) for each Isotopic Substitution						
Vibrational Mode	16	17	18	19	20	21	22
$\tau\text{CH}_3$	68.62	68.57	69.00	69.03	68.13	68.97	69.03
$\tau\text{CH}_3 + \tau\text{Ph}^1$	95.72	95.81	94.76	95.49	95.72	93.71	95.09
$(\delta\text{HC=O} + \delta\text{OCH}_3)^1$	216.13	216.19	216.02	216.18	216.18	215.85	216.15
$\tau\text{O-CH}_3 + \tau\text{Ph}$	152.49	152.20	152.89	152.03	151.40	152.73	151.09
$\gamma\text{HC=O} + \tau\text{Ph}$	158.34	158.46	157.00	158.41	158.37	155.54	158.27
$(\delta\text{HC=O} + \delta\text{OCH}_3)^2$	229.82	230.29	228.99	228.69	230.14	227.66	226.98
$\tau\text{O-CH}_3 + \tau\text{HC=O}$	268.87	270.39	271.51	271.57	269.30	271.41	271.54
$(\delta\text{C-OCH}_3 + \delta\text{C-CHO} + \delta\text{C-OH})^1$	328.88	328.17	329.05	326.83	326.76	328.46	324.33
$\tau\text{Ph}$	328.13	333.50	333.79	333.03	333.22	333.78	332.32
$(\nu^{\text{as}}\text{Ph}^1 + \nu\text{C-CHO})$	386.29	386.15	383.37	384.81	385.69	380.35	383.02
$\gamma\text{Ph}^1$	421.65	448.29	448.42	447.66	448.15	448.41	447.09
$\gamma\text{C-OH} + \nu\text{O-H}$	445.28	442.87	442.89	442.47	442.85	442.89	441.98
$(\delta\text{C-OCH}_3 + \delta\text{C-CHO} + \delta\text{C-OH})^2 + \delta\text{Ph}$	531.51	535.03	498.05	536.20	532.90	625.43	494.03
$\delta\text{Ph} + \delta\text{C-O-CH}_3$	492.00	493.52	537.52	628.24	628.72	537.42	534.95
$\gamma\text{Ph}^2$	568.36	568.07	568.47	568.35	567.72	568.45	568.23
$\delta\text{Ph}$	620.49	628.82	627.08	496.31	488.29	497.48	760.25
$\gamma\text{Ph}^3$	645.15	707.69	707.82	707.61	707.58	707.82	707.43
$[\delta\text{Ph} + (\delta\text{C-O-CH}_3 + \tau\text{C-CHO})]^1$	770.73	759.65	759.89	760.81	758.16	758.82	627.59
$[\delta\text{Ph} + (\delta\text{C-O-CH}_3 + \tau\text{C-CHO})]^2$	742.65	780.70	781.81	776.02	779.75	781.73	770.93
$(\nu^{\text{Hydrogen}}\text{Ph} + \delta^{\text{Hydrogen}}\text{Ph})^1$	747.65	818.81	818.81	818.71	818.81	818.80	818.62
$(\nu^{\text{Hydrogen}}\text{Ph} + \delta^{\text{Hydrogen}}\text{Ph})^2$	836.87	836.80	836.86	836.89	836.73	836.83	836.89

$(\nu^{\text{Hydrogen}}\text{Ph} + \gamma^{\text{Hydrogen}}\text{Ph})$	1222.85	937.44	937.38	937.43	937.44	937.33	937.42
$(\nu^{\text{as}}\text{Ph} + \delta\text{Ph})$	839.98	905.43	907.47	907.44	903.37	907.25	907.21
$\gamma\text{O-C-H}$	900.94	986.27	985.48	986.27	986.27	984.79	986.27
$(\nu^{\text{as}}\text{Ph} + \delta\text{Ph}) + \nu\text{O-CH}_3$	952.58	1015.90	1023.93	1023.92	1007.64	1023.93	1023.90
$(\delta^{\text{Hydrogen}}\text{Ph} + \delta\text{Ph}) + \tau\text{C-OH}$	985.71	1097.54	1100.79	1100.61	1094.59	1100.76	1100.41
$(\tau\text{C-OCH}_3 + \tau\text{C-CHO} + \tau\text{C-OH})$	1036.07	1139.90	1143.01	1142.97	1137.36	1142.91	1142.83
$(\tau\text{C-CH}_3 + \nu^{\text{as}}\text{C-H}_3)$	1143.42	1141.83	1143.42	1143.42	1140.42	1143.42	1143.42
$[(\tau\text{C-CH}_3 + \tau\text{C-OH}) + \delta^{\text{Hydrogen}}\text{Ph}]^1$	1117.29	1168.16	1169.50	1168.91	1166.92	1169.47	1168.28
$[(\tau\text{C-CH}_3 + \tau\text{C-OH}) + \delta^{\text{Hydrogen}}\text{Ph}]^2$	1160.97	1187.26	1190.72	1190.50	1184.32	1190.71	1190.28
$\delta\text{Ph} + \delta\text{C-O-H} + \delta^{\text{Hydrogen}}\text{Ph}$	1180.21	1225.94	1227.69	1223.79	1224.65	1227.64	1219.86
$\nu^{\text{sym}}\text{Ph} + \delta^{\text{Hydrogen}}\text{Ph}$	1267.88	1267.48	1268.99	1265.11	1266.34	1268.96	1262.26
$\nu\text{Ph} + \delta\text{C-O-H}$	1258.96	1279.02	1279.10	1278.86	1278.88	1278.99	1278.55
$\delta\text{C-O-H} + \delta^{\text{Hydrogen}}\text{Ph}$	1360.69	1366.60	1366.01	1365.91	1366.36	1364.88	1365.04
$(\delta\text{C-O-H} + \delta^{\text{Hydrogen}}\text{Ph} + \nu^{\text{as}}\text{Ph})^1$	1376.88	1376.78	1375.89	1377.26	1376.35	1374.69	1377.23
$(\delta\text{C-O-H} + \delta^{\text{Hydrogen}}\text{Ph} + \nu^{\text{as}}\text{Ph})^2$	1417.22	1422.22	1420.78	1422.05	1421.99	1419.17	1421.67
$(\nu\text{O-CH}_3 + \delta\text{C-O-CH}_3 + \nu^{\text{sym}}\text{C-H}_3 + \delta\text{C-CH}_3)$	1445.58	1444.75	1445.59	1445.83	1443.85	1445.37	1445.81
$\nu^{\text{as}}\text{CH}_3^1$	1459.44	1459.37	1459.44	1459.44	1459.30	1459.44	1459.44
$\nu^{\text{as}}\text{CH}_3^2$	1466.82	1468.34	1468.70	1468.66	1468.05	1468.70	1468.62
$(\nu^{\text{as}}\text{Ph} + \delta\text{Ph} + \nu\text{C-OH} + \delta\text{C-O-H} + \nu\text{O-CH}_3 + \delta\text{C-O-CH}_3 + \nu^{\text{as}}\text{C-H}_3 + \delta\text{C-CH}_3)$	1478.29	1496.78	1497.38	1496.53	1496.29	1497.35	1495.80
$[\nu^{\text{as}}\text{Ph} + (\delta\text{C-OH} + \delta\text{C-CHO} + \delta^{\text{Hydrogen}}\text{Ph})]^1$	1586.17	1591.32	1591.35	1591.13	1591.26	1591.30	1590.90

$\delta\text{C-O-H} +$ $\nu^{\text{as}}\text{H-C=O} +$ $\nu^{\text{as}}\text{Ph}$	1567.50	1574.97	1574.37	1574.79	1574.89	1573.59	1574.55
$[\nu^{\text{as}}\text{Ph} +$ $(\delta\text{C-OH} + \delta\text{C-CHO}$ $+ \delta^{\text{Hydrogen}}\text{Ph})]^2$	1702.48	1702.60	1685.84	1702.60	1702.60	1671.45	1702.58
$\nu\text{H-CO}$	3078.25	2780.95	2780.94	2780.95	2780.95	2780.93	2780.95
$\nu^{\text{sym}}\text{CH}_3$	2285.00	2922.61	2922.62	2922.62	2922.60	2922.62	2922.62
$\nu^{\text{as}}\text{CH}_3^3$	2780.95	2984.45	2984.45	2984.45	2984.45	2984.45	2984.45
$\nu^{\text{as}}\text{CH}_3^4$	2922.63	3046.73	3046.73	3046.73	3046.73	3046.73	3046.73
$\nu^{\text{Hydrogen}}\text{Ph}^1$	2984.45	3100.05	3100.05	3100.05	3100.05	3100.05	3100.05
$\nu^{\text{Hydrogen}}\text{Ph}^2$	3096.11	3085.81	3085.81	3085.81	3085.81	3085.81	3085.81
$\nu^{\text{Hydrogen}}\text{Ph}^3$	3046.73	3078.17	3078.17	3078.17	3078.17	3078.17	3078.17
$\nu\text{O-H}$	3605.54	3605.54	3605.54	3599.45	3605.54	3605.54	3594.05

*Table 3b-13c: Simulated vibrational wavenumbers for all isotopically substituted variants of B3LYP +d for Structure 011, with associated description of the matching vibrational mode. Wavenumber values are scaled by a factor of 0.967.*

	B3PW91 +d Structure 001 Vibrational Mode and Calculated Vibrational Wavenumber (W, cm <sup>-1</sup> ) for each Isotopic Substitution							
Vibrational Mode	00	01	02	03	04	05	06	07
$\tau\text{CH}_3$	72.35	71.60	72.30	72.25	72.34	72.32	72.34	72.09
$\tau\text{CH}_3 + \tau\text{Ph}^1$	98.77	98.71	98.29	98.56	98.77	98.46	98.75	98.62
$(\delta\text{HC=O} + \delta\text{OCH}_3)^1$	145.51	143.91	145.38	145.48	145.29	145.39	145.49	145.39
$\tau\text{O-CH}_3 + \tau\text{Ph}$	182.65	182.65	181.45	182.58	182.64	182.36	182.61	182.39
$\gamma\text{HC=O} + \tau\text{Ph}$	196.01	196.01	195.92	195.88	193.66	195.93	195.90	195.93
$(\delta\text{HC=O} + \delta\text{OCH}_3)^2$	235.47	233.96	234.89	234.95	235.44	234.86	235.32	235.06
$\tau\text{O-CH}_3 + \tau\text{HC=O}$	249.77	249.75	248.46	249.75	249.58	249.06	249.75	249.73
$(\delta\text{C-OCH}_3 + \delta\text{C-CHO} + \delta\text{C-OH})^1$	324.86	321.87	324.75	324.45	324.54	324.54	324.60	324.52
$\tau\text{Ph}$	364.44	364.44	364.31	363.14	363.72	362.40	362.22	361.83
$(\nu^{\text{as}}\text{Ph}^1 + \nu\text{C-CHO})$	398.96	398.32	397.54	398.67	396.22	397.72	397.49	398.75
$\gamma\text{Ph}^1$	443.67	443.67	441.25	439.75	443.66	443.21	440.23	443.25
$\gamma\text{C-OH} + \nu\text{O-H}$	457.72	457.72	457.71	457.71	457.72	457.69	457.67	457.72
$(\delta\text{C-OCH}_3 + \delta\text{C-CHO} + \delta\text{C-OH})^2 + \delta\text{Ph}$	526.00	525.45	523.52	527.52	527.63	528.06	525.98	528.18
$\delta\text{Ph} + \delta\text{C-O-CH}_3$	528.79	526.93	527.89	523.95	525.78	524.96	525.35	522.65
$\gamma\text{Ph}^2$	568.41	568.40	567.19	565.31	568.30	560.35	567.45	565.28
$\delta\text{Ph}$	611.92	611.92	611.61	611.61	608.58	610.18	611.29	607.43
$\gamma\text{Ph}^3$	709.14	709.14	708.40	700.89	709.08	707.61	700.11	707.10
$[\delta\text{Ph} + (\delta\text{C-O-CH}_3 + \tau\text{C-CHO})]^1$	716.88	715.97	713.43	716.79	711.02	715.94	715.11	714.71
$[\delta\text{Ph} + (\delta\text{C-O-CH}_3 + \tau\text{C-CHO})]^2$	795.23	795.20	788.15	792.60	793.19	794.70	795.10	789.84
$(\nu^{\text{Hydrogen}}\text{Ph} + \delta^{\text{Hydrogen}}\text{Ph})^1$	800.84	800.84	800.77	800.55	800.70	800.64	797.62	798.43

$(\nu^{\text{Hydrogen}}\text{Ph} + \delta^{\text{Hydrogen}}\text{Ph})^2$	857.77	857.77	850.35	856.66	857.51	857.52	857.76	857.73
$(\nu^{\text{Hydrogen}}\text{Ph} + \gamma^{\text{Hydrogen}}\text{Ph})$	908.70	908.70	908.41	908.60	908.39	908.68	908.56	904.86
$(\nu^{\text{as}}\text{Ph} + \delta\text{Ph})$	941.05	938.71	931.19	938.63	936.30	940.48	940.61	934.94
$\gamma\text{O-C-H}$	980.67	980.67	980.55	980.67	967.18	977.94	980.66	980.27
$(\nu^{\text{as}}\text{Ph} + \delta\text{Ph}) + \nu\text{O-CH}_3$	1029.83	1020.30	1026.89	1024.60	1029.81	1029.82	1029.48	1027.61
$(\delta^{\text{Hydrogen}}\text{Ph} + \delta\text{Ph}) + \tau\text{C-OH}$	1103.15	1102.05	1100.65	1102.98	1103.14	1102.60	1101.25	1100.73
$(\tau\text{C-OCH}_3 + \tau\text{C-CHO} + \tau\text{C-OH})$	1137.29	1130.84	1136.44	1134.99	1134.37	1126.08	1136.92	1136.57
$(\tau\text{C-CH}_3 + \nu^{\text{as}}\text{C-H}_3)$	1138.91	1133.86	1138.91	1138.91	1138.91	1138.91	1138.91	1138.91
$[(\tau\text{C-CH}_3 + \tau\text{C-OH}) + \delta^{\text{Hydrogen}}\text{Ph}]^1$	1164.90	1161.19	1164.68	1164.56	1164.40	1162.42	1160.55	1164.71
$[(\tau\text{C-CH}_3 + \tau\text{C-OH}) + \delta^{\text{Hydrogen}}\text{Ph}]^2$	1187.74	1182.94	1186.71	1186.51	1187.52	1186.95	1185.85	1187.55
$\delta\text{Ph} + \delta\text{C-O-H} + \delta^{\text{Hydrogen}}\text{Ph}$	1236.15	1235.33	1234.03	1226.00	1236.01	1230.12	1228.57	1235.39
$\nu^{\text{Sym}}\text{Ph} + \delta^{\text{Hydrogen}}\text{Ph}$	1257.49	1257.10	1256.84	1251.70	1257.40	1252.50	1251.90	1255.36
$\nu\text{Ph} + \delta\text{C-O-H}$	1284.69	1284.19	1283.15	1279.25	1283.64	1276.85	1277.30	1282.34
$\delta\text{C-O-H} + \delta^{\text{Hydrogen}}\text{Ph}$	1362.26	1362.25	1361.27	1362.22	1358.08	1358.87	1358.41	1358.11
$(\delta\text{C-O-H} + \delta^{\text{Hydrogen}}\text{Ph} + \nu^{\text{as}}\text{Ph})^1$	1395.22	1394.28	1391.01	1385.27	1394.18	1388.42	1388.98	1389.87
$(\delta\text{C-O-H} + \delta^{\text{Hydrogen}}\text{Ph} + \nu^{\text{as}}\text{Ph})^2$	1421.19	1418.78	1418.84	1417.47	1421.15	1414.35	1419.00	1417.76
$(\nu\text{O-CH}_3 + \delta\text{C-O-CH}_3 + \nu^{\text{sym}}\text{C-H}_3 + \delta\text{C-CH}_3)$	1442.77	1440.20	1441.25	1437.03	1442.35	1437.41	1442.38	1439.63
$\nu^{\text{as}}\text{CH}_3^1$	1448.55	1446.73	1448.55	1448.55	1448.55	1448.55	1448.55	1448.55
$\nu^{\text{as}}\text{CH}_3^2$	1459.69	1458.37	1459.50	1458.78	1459.66	1459.43	1459.55	1459.38
$(\nu^{\text{as}}\text{Ph} + \delta\text{Ph} + \nu\text{C-OH} + \delta\text{C-O-H} + \nu\text{O-CH}_3 + \delta\text{C-O-CH}_3 + \nu^{\text{as}}\text{C-H}_3 + \delta\text{C-CH}_3)$	1497.80	1497.75	1490.26	1490.34	1497.49	1493.41	1484.61	1496.81

$[\nu^{\text{as}}\text{Ph} + (\delta\text{C-OH} + \delta\text{C-CHO} + \delta^{\text{Hydrogen}}\text{Ph})]^1$	1592.54	1592.52	1581.82	1580.47	1594.49	1592.21	1592.21	1576.72
$\delta\text{C-O-H} + \nu^{\text{as}}\text{H-C=O} + \nu^{\text{as}}\text{Ph}$	1595.83	1595.80	1591.58	1590.79	1592.25	1582.62	1582.62	1594.36
$[\nu^{\text{as}}\text{Ph} + (\delta\text{C-OH} + \delta\text{C-CHO} + \delta^{\text{Hydrogen}}\text{Ph})]^2$	1708.23	1708.23	1707.88	1708.11	1669.17	1707.55	1707.98	1707.95
$\nu\text{H-CO}$	2795.62	2795.62	2795.62	2795.62	2787.50	2795.61	2795.62	2795.62
$\nu^{\text{sym}}\text{CH}_3$	2920.02	2917.01	2920.01	2920.01	2920.02	2920.02	2920.02	2920.02
$\nu^{\text{as}}\text{CH}_3^3$	2989.78	2978.44	2989.78	2989.78	2989.78	2989.78	2989.78	2989.78
$\nu^{\text{as}}\text{CH}_3^4$	3046.03	3035.09	3046.01	3046.03	3046.03	3046.03	3046.03	3046.03
$\nu^{\text{Hydrogen}}\text{Ph}^1$	3060.84	3060.84	3060.83	3060.84	3060.84	3060.83	3060.84	3051.67
$\nu^{\text{Hydrogen}}\text{Ph}^2$	3089.14	3092.80	3089.14	3089.14	3089.14	3089.14	3089.12	3088.56
$\nu^{\text{Hydrogen}}\text{Ph}^3$	3092.81	3089.14	3092.80	3092.79	3092.81	3092.81	3092.81	3092.81
$\nu\text{O-H}$	3605.15	3605.15	3605.15	3605.15	3605.15	3605.15	3605.14	3605.15

*Table 3b-14a: Simulated vibrational wavenumbers for all isotopically substituted variants of B3PW91 +d for Structure 001, with associated description of the matching vibrational mode. Wavenumber values are scaled by a factor of 0.963.*

<b>Vibrational Mode</b>	<b>B3PW91 +d Structure 001 Vibrational Mode and Calculated Vibrational Wavenumber (W, cm<sup>-1</sup>) for each Isotopic Substitution</b>							
	<b>08</b>	<b>09</b>	<b>10</b>	<b>11</b>	<b>12</b>	<b>13</b>	<b>14</b>	<b>15</b>
$\tau\text{CH}_3$	72.21	69.75	71.13	69.75	72.13	72.06	72.21	71.63
$\tau\text{CH}_3 + \tau\text{Ph}^1$	98.77	98.35	98.49	98.35	98.04	98.58	97.88	98.65
$(\delta\text{HC=O} + \delta\text{OCH}_3)^1$	145.46	142.55	142.50	142.47	145.30	144.43	145.50	145.33
$\tau\text{O-CH}_3 + \tau\text{Ph}$	182.37	170.03	170.67	170.10	179.82	183.09	181.99	180.93
$\gamma\text{HC=O} + \tau\text{Ph}$	194.95	195.37	195.42	195.40	195.97	174.51	194.73	196.00
$(\delta\text{HC=O} + \delta\text{OCH}_3)^2$	235.39	229.66	230.62	229.55	234.04	234.49	230.30	234.69
$\tau\text{O-CH}_3 + \tau\text{HC=O}$	249.68	239.17	234.21	239.26	248.46	246.62	249.66	248.74
$(\delta\text{C-OCH}_3 + \delta\text{C-CHO} + \delta\text{C-OH})^1$	324.81	319.80	322.91	319.88	324.04	324.78	318.56	324.43
$\tau\text{Ph}$	362.72	364.05	363.94	363.99	364.06	351.17	457.70	353.59
$(\nu^{\text{as}}\text{Ph}^1 + \nu\text{C-CHO})$	398.59	397.16	397.98	397.19	397.86	393.48	351.17	396.05
$\gamma\text{Ph}^1$	441.72	443.46	443.66	443.46	411.55	443.02	393.48	443.48
$\gamma\text{C-OH} + \nu\text{O-H}$	457.70	457.69	457.70	457.70	457.59	457.70	443.02	457.69
$(\delta\text{C-OCH}_3 + \delta\text{C-CHO} + \delta\text{C-OH})^2 + \delta\text{Ph}$	523.90	520.76	528.05	520.76	521.88	524.24	515.73	522.53
$\delta\text{Ph} + \delta\text{C-O-CH}_3$	526.27	526.48	516.18	526.48	524.00	526.28	526.89	520.76
$\gamma\text{Ph}^2$	567.14	568.23	568.18	568.22	562.90	563.31	567.87	525.79
$\delta\text{Ph}$	606.59	611.88	611.62	611.88	610.72	607.80	610.99	608.11
$\gamma\text{Ph}^3$	708.57	708.57	709.14	709.04	659.19	707.94	709.04	690.45
$[\delta\text{Ph} + (\delta\text{C-O-CH}_3 + \tau\text{C-CHO})]^1$	710.20	710.20	706.18	716.57	713.08	701.77	715.08	714.31
$[\delta\text{Ph} + (\delta\text{C-O-CH}_3 + \tau\text{C-CHO})]^2$	794.03	793.66	792.62	793.65	740.95	791.31	787.97	783.22
$(\nu^{\text{Hydrogen}}\text{Ph} + \delta^{\text{Hydrogen}}\text{Ph})^1$	797.30	800.83	800.84	800.83	800.85	790.59	800.26	711.34
$(\nu^{\text{Hydrogen}}\text{Ph} + \delta^{\text{Hydrogen}}\text{Ph})^2$	857.70	857.62	857.36	857.62	741.93	917.47	857.71	854.99

$(\nu^{\text{Hydrogen}}\text{Ph} + \gamma^{\text{Hydrogen}}\text{Ph})$	904.79	908.69	908.70	929.37	908.00	833.72	908.69	867.85
$(\nu^{\text{as}}\text{Ph} + \delta\text{Ph})$	940.76	929.35	902.70	908.69	863.40	876.16	921.43	869.84
$\gamma\text{O-C-H}$	980.65	1142.32	980.66	1142.32	1236.71	913.01	1221.96	1135.30
$(\nu^{\text{as}}\text{Ph} + \delta\text{Ph}) + \nu\text{O-CH}_3$	1026.48	940.50	1040.59	940.49	985.81	1242.68	953.92	934.29
$(\delta^{\text{Hydrogen}}\text{Ph} + \delta\text{Ph}) + \tau\text{C-OH}$	1099.92	980.67	990.68	980.67	979.51	1021.80	980.67	978.24
$(\tau\text{C-OCH}_3 + \tau\text{C-CHO} + \tau\text{C-OH})$	1136.38	1033.02	1103.40	1033.06	1055.19	1029.83	1035.82	1138.91
$(\tau\text{C-CH}_3 + \nu^{\text{as}}\text{C-H}_3)$	1138.91	1102.79	1090.35	1102.80	1100.50	1138.91	1108.98	1161.82
$[(\tau\text{C-CH}_3 + \tau\text{C-OH}) + \delta^{\text{Hydrogen}}\text{Ph}]^1$	1162.48	1105.19	1143.25	1105.15	1138.85	1103.31	1137.27	1035.77
$[(\tau\text{C-CH}_3 + \tau\text{C-OH}) + \delta^{\text{Hydrogen}}\text{Ph}]^2$	1187.33	1175.15	1173.67	1175.14	1157.93	1148.20	1138.87	1187.57
$\delta\text{Ph} + \delta\text{C-O-H} + \delta^{\text{Hydrogen}}\text{Ph}$	1234.95	1233.75	1235.78	1233.75	1181.63	1169.06	1180.07	1198.84
$\nu^{\text{sym}}\text{Ph} + \delta^{\text{Hydrogen}}\text{Ph}$	1256.92	1254.38	1256.37	1254.37	1219.08	1188.79	1243.72	1252.08
$\nu\text{Ph} + \delta\text{C-O-H}$	1276.65	1283.34	1279.83	1283.33	1284.22	34.00	1279.07	1277.09
$\delta\text{C-O-H} + \delta^{\text{Hydrogen}}\text{Ph}$	1362.20	1303.12	1284.66	1303.04	1362.06	1263.16	1383.29	1391.09
$(\delta\text{C-O-H} + \delta^{\text{Hydrogen}}\text{Ph} + \nu^{\text{as}}\text{Ph})^1$	1393.57	1331.36	1362.29	1331.35	1394.51	1387.07	1341.13	1355.22
$(\delta\text{C-O-H} + \delta^{\text{Hydrogen}}\text{Ph} + \nu^{\text{as}}\text{Ph})^2$	1417.40	1398.69	1335.45	1398.70	1415.12	1417.37	1415.49	1410.63
$(\nu\text{O-CH}_3 + \delta\text{C-O-CH}_3 + \nu^{\text{sym}}\text{C-H}_3 + \delta\text{C-CH}_3)$	1441.52	1362.38	1431.62	1362.38	1439.49	1441.84	1442.73	1435.46
$\nu^{\text{as}}\text{CH}_3^1$	1448.55	1428.21	1398.39	1428.27	1448.33	1448.55	1448.55	1448.55
$\nu^{\text{as}}\text{CH}_3^2$	1459.12	1449.04	1450.88	1449.16	1459.41	1459.63	1459.58	1459.29
$(\nu^{\text{as}}\text{Ph} + \delta\text{Ph} + \nu\text{C-OH} + \delta\text{C-O-H} + \nu\text{O-CH}_3 + \delta\text{C-O-CH}_3 + \nu^{\text{as}}\text{C-H}_3 + \delta\text{C-CH}_3)$	1489.26	1496.73	1497.68	1496.73	1483.09	1497.32	1497.56	1490.36
$[\nu^{\text{as}}\text{Ph} + (\delta\text{C-OH} + \delta\text{C-CHO} + \delta^{\text{Hydrogen}}\text{Ph})]^1$	1584.42	1592.54	1592.36	1592.54	1585.29	1591.55	1594.31	1583.00

$\delta\text{C-O-H} +$ $\nu^{\text{as}}\text{H-C=O} +$ $\nu^{\text{as}}\text{Ph}$	1589.02	1595.66	1595.61	1595.66	1592.34	1595.75	1584.04	1593.50
$[\nu^{\text{as}}\text{Ph} +$ $(\delta\text{C-OH} + \delta\text{C-CHO}$ $+ \delta^{\text{Hydrogen}}\text{Ph})]^2$	1707.81	1708.22	1708.22	1708.22	1707.96	1694.66	1708.22	1708.05
$\nu\text{H-CO}$	2795.62	2795.62	2795.62	2795.62	3089.22	2063.25	3092.81	3046.03
$\nu^{\text{sym}}\text{CH}_3$	2920.02	2170.67	2223.92	2170.63	2285.11	2920.02	2623.50	2263.75
$\nu^{\text{as}}\text{CH}_3^3$	2989.78	2954.32	2937.99	2954.40	2795.63	2989.78	2795.62	2795.65
$\nu^{\text{as}}\text{CH}_3^4$	3046.03	3042.06	2989.55	3042.04	2920.09	3046.03	2920.02	2920.02
$\nu^{\text{Hydrogen}}\text{Ph}^1$	3059.99	3060.84	3060.84	3060.84	2989.78	3060.80	2989.78	2989.78
$\nu^{\text{Hydrogen}}\text{Ph}^2$	3080.09	3089.14	3089.14	3089.14	3046.09	3089.14	3046.03	3087.29
$\nu^{\text{Hydrogen}}\text{Ph}^3$	3092.75	3092.76	3092.77	3092.76	3060.85	3092.80	3060.84	3092.80
$\nu\text{O-H}$	3605.15	3605.15	3605.15	3605.15	3605.15	3605.15	3089.14	3605.15

Table 3b-14b: Simulated vibrational wavenumbers for all isotopically substituted variants of B3PW91 +d for Structure 001, with associated description of the matching vibrational mode. Wavenumber values are scaled by a factor of 0.963.

	B3PW91 +d Structure 001 Vibrational Mode and Calculated Vibrational Wavenumber (W, cm <sup>-1</sup> ) for each Isotopic Substitution						
Vibrational Mode	16	17	18	19	20	21	22
$\tau\text{CH}_3$	71.97	71.97	72.12	72.28	71.60	71.89	72.22
$\tau\text{CH}_3 + \tau\text{Ph}^1$	98.63	98.46	97.97	98.00	98.18	97.26	97.29
$(\delta\text{HC=O} + \delta\text{OCH}_3)^1$	145.45	145.35	143.55	145.49	145.18	141.71	145.47
$\tau\text{O-CH}_3 + \tau\text{Ph}$	181.34	181.76	182.56	182.33	180.93	182.48	182.01
$\gamma\text{HC=O} + \tau\text{Ph}$	194.14	195.99	195.45	195.43	195.98	194.96	194.94
$(\delta\text{HC=O} + \delta\text{OCH}_3)^2$	235.20	235.18	234.53	233.56	234.90	233.69	231.71
$\tau\text{O-CH}_3 + \tau\text{HC=O}$	249.04	248.72	249.77	249.71	247.80	249.77	249.66
$(\delta\text{C-OCH}_3 + \delta\text{C-CHO} + \delta\text{C-OH})^1$	324.39	323.47	324.14	321.97	322.12	323.43	319.35
$\tau\text{Ph}$	361.60	364.05	364.39	363.79	363.71	364.35	363.20
$(\nu^{\text{as}}\text{Ph}^1 + \nu\text{C-CHO})$	398.84	398.61	396.48	396.76	398.26	394.12	394.59
$\gamma\text{Ph}^1$	416.64	443.45	443.66	443.49	443.25	443.65	443.31
$\gamma\text{C-OH} + \nu\text{O-H}$	457.65	457.72	457.72	456.71	457.71	457.72	455.86
$(\delta\text{C-OCH}_3 + \delta\text{C-CHO} + \delta\text{C-OH})^2 + \delta\text{Ph}$	514.84	527.75	528.66	527.99	526.99	528.55	527.31
$\delta\text{Ph} + \delta\text{C-O-CH}_3$	526.00	519.75	525.48	524.52	513.53	524.99	523.10
$\gamma\text{Ph}^2$	568.41	567.96	568.39	568.31	567.57	568.37	568.22
$\delta\text{Ph}$	597.61	611.71	608.72	609.81	611.54	605.87	607.82
$\gamma\text{Ph}^3$	637.20	708.98	709.14	708.94	708.84	709.13	708.77
$[\delta\text{Ph} + (\delta\text{C-O-CH}_3 + \tau\text{C-CHO})]^1$	705.16	714.32	716.37	716.88	712.03	715.92	716.87
$[\delta\text{Ph} + (\delta\text{C-O-CH}_3 + \tau\text{C-CHO})]^2$	792.91	794.85	795.05	789.51	794.53	794.89	784.32
$(\nu^{\text{Hydrogen}}\text{Ph} + \delta^{\text{Hydrogen}}\text{Ph})^1$	740.54	800.83	800.82	800.71	800.82	800.80	800.60
$(\nu^{\text{Hydrogen}}\text{Ph} + \delta^{\text{Hydrogen}}\text{Ph})^2$	1229.46	857.68	857.74	857.77	857.60	857.71	857.76

$(\nu^{\text{Hydrogen}}\text{Ph} + \gamma^{\text{Hydrogen}}\text{Ph})$	846.52	908.70	908.68	908.68	908.69	908.66	908.66
$(\nu^{\text{as}}\text{Ph} + \delta\text{Ph})$	855.90	938.83	940.94	940.99	936.69	940.84	940.93
$\gamma\text{O-C-H}$	870.31	980.67	979.86	980.67	980.67	979.14	980.67
$(\nu^{\text{as}}\text{Ph} + \delta\text{Ph}) + \nu\text{O-CH}_3$	968.59	1022.49	1029.83	1029.79	1015.02	1029.83	1029.75
$(\delta^{\text{Hydrogen}}\text{Ph} + \delta\text{Ph}) + \tau\text{C-OH}$	980.56	1101.38	1103.12	1103.00	1099.57	1103.08	1102.87
$(\tau\text{C-OCH}_3 + \tau\text{C-CHO} + \tau\text{C-OH})$	1037.37	1133.23	1137.11	1137.19	1129.74	1136.94	1137.09
$(\tau\text{C-CH}_3 + \nu^{\text{as}}\text{C-H}_3)$	1138.91	1137.31	1138.91	1138.91	1135.90	1138.91	1138.91
$[(\tau\text{C-CH}_3 + \tau\text{C-OH}) + \delta^{\text{Hydrogen}}\text{Ph}]^1$	1130.17	1163.18	1164.86	1164.39	1161.87	1164.82	1163.89
$[(\tau\text{C-CH}_3 + \tau\text{C-OH}) + \delta^{\text{Hydrogen}}\text{Ph}]^2$	1146.42	1183.35	1187.73	1187.59	1179.53	1187.72	1187.45
$\delta\text{Ph} + \delta\text{C-O-H} + \delta^{\text{Hydrogen}}\text{Ph}$	1177.47	1233.43	1236.09	1233.10	1231.46	1236.04	1229.33
$\nu^{\text{Sym}}\text{Ph} + \delta^{\text{Hydrogen}}\text{Ph}$	1255.72	1257.09	1257.41	1253.64	1256.78	1257.34	1251.05
$\nu\text{Ph} + \delta\text{C-O-H}$	1274.82	1283.71	1284.66	1282.70	1283.02	1284.63	1281.28
$\delta\text{C-O-H} + \delta^{\text{Hydrogen}}\text{Ph}$	1354.63	1362.24	1360.01	1361.82	1362.23	1357.70	1361.42
$(\delta\text{C-O-H} + \delta^{\text{Hydrogen}}\text{Ph} + \nu^{\text{as}}\text{Ph})^1$	1393.98	1394.83	1394.04	1394.86	1394.49	1392.96	1394.55
$(\delta\text{C-O-H} + \delta^{\text{Hydrogen}}\text{Ph} + \nu^{\text{as}}\text{Ph})^2$	1413.42	1420.92	1420.55	1420.71	1420.70	1419.99	1420.31
$(\nu\text{O-CH}_3 + \delta\text{C-O-CH}_3 + \nu^{\text{sym}}\text{C-H}_3 + \delta\text{C-CH}_3)$	1441.95	1441.58	1442.72	1442.72	1440.58	1442.68	1442.69
$\nu^{\text{as}}\text{CH}_3^1$	1448.55	1448.46	1448.55	1448.55	1448.38	1448.55	1448.55
$\nu^{\text{as}}\text{CH}_3^2$	1458.90	1459.04	1459.68	1459.65	1458.55	1459.67	1459.62
$(\nu^{\text{as}}\text{Ph} + \delta\text{Ph} + \nu\text{C-OH} + \delta\text{C-O-H} + \nu\text{O-CH}_3 + \delta\text{C-O-CH}_3 + \nu^{\text{as}}\text{C-H}_3 + \delta\text{C-CH}_3)$	1481.89	1497.06	1497.71	1496.58	1496.48	1497.61	1495.57
$[\nu^{\text{as}}\text{Ph} + (\delta\text{C-OH} + \delta\text{C-CHO} + \delta^{\text{Hydrogen}}\text{Ph})]^1$	1590.63	1592.42	1595.20	1592.34	1592.31	1592.46	1592.14

$\delta\text{C-O-H} +$ $\nu^{\text{as}}\text{H-C=O} +$ $\nu^{\text{as}}\text{Ph}$	1585.59	1595.72	1592.51	1595.54	1595.64	1594.47	1595.31
$[\nu^{\text{as}}\text{Ph} +$ $(\delta\text{C-OH} + \delta\text{C-CHO}$ $+ \delta^{\text{Hydrogen}}\text{Ph})]^2$	1708.07	1708.23	1691.12	1708.22	1708.22	1676.41	1708.21
$\nu\text{H-CO}$	3062.83	2795.62	2795.61	2795.62	2795.62	2795.61	2795.62
$\nu^{\text{sym}}\text{CH}_3$	2283.76	2920.00	2920.02	2920.02	2919.99	2920.02	2920.02
$\nu^{\text{as}}\text{CH}_3^3$	2795.62	2989.78	2989.78	2989.78	2989.78	2989.78	2989.78
$\nu^{\text{as}}\text{CH}_3^4$	2920.02	3046.03	3046.03	3046.03	3046.03	3046.03	3046.03
$\nu^{\text{Hydrogen}}\text{Ph}^1$	2989.78	3060.84	3060.84	3060.84	3060.84	3060.84	3060.84
$\nu^{\text{Hydrogen}}\text{Ph}^2$	3046.03	3089.14	3089.14	3089.14	3089.14	3089.14	3089.14
$\nu^{\text{Hydrogen}}\text{Ph}^3$	3092.73	3092.81	3092.81	3092.81	3092.81	3092.81	3092.81
$\nu\text{O-H}$	3605.15	3605.15	3605.15	3599.06	3605.15	3605.15	3593.68

*Table 3b-14c: Simulated vibrational wavenumbers for all isotopically substituted variants of B3PW91 +d for Structure 001, with associated description of the matching vibrational mode. Wavenumber values are scaled by a factor of 0.963.*

	<b>B3PW91 +d Structure 011 Vibrational Mode and Calculated Vibrational Wavenumber (W, cm<sup>-1</sup>) for each Isotopic Substitution</b>							
<b>Vibrational Mode</b>	<b>00</b>	<b>01</b>	<b>02</b>	<b>03</b>	<b>04</b>	<b>05</b>	<b>06</b>	<b>07</b>
$\tau\text{CH}_3$	69.39	68.62	69.15	69.22	69.36	69.37	69.39	69.32
$\tau\text{CH}_3 + \tau\text{Ph}^1$	96.02	96.02	95.75	96.01	96.01	95.62	96.02	95.53
$(\delta\text{HC=O} + \delta\text{OCH}_3)^1$	155.96	217.49	155.72	155.87	216.50	217.49	217.42	217.45
$\tau\text{O-CH}_3 + \tau\text{Ph}$	152.14	152.13	151.99	152.10	151.27	152.09	152.12	151.71
$\gamma\text{HC=O} + \tau\text{Ph}$	217.49	154.32	217.17	217.21	155.66	155.74	155.82	155.72
$(\delta\text{HC=O} + \delta\text{OCH}_3)^2$	227.64	226.13	227.23	227.45	227.59	227.01	227.62	227.15
$\tau\text{O-CH}_3 + \tau\text{HC=O}$	271.45	271.43	269.46	271.20	270.43	270.58	271.36	271.38
$(\delta\text{C-OCH}_3 + \delta\text{C-CHO} + \delta\text{C-OH})^1$	327.47	324.33	327.21	327.16	327.26	327.03	327.38	327.11
$\tau\text{Ph}$	333.08	333.08	332.90	332.10	333.00	330.87	331.30	330.91
$(\nu^{\text{as}}\text{Ph}^1 + \nu\text{C-CHO})$	384.08	383.80	384.01	383.73	381.07	383.11	382.74	383.09
$\gamma\text{Ph}^1$	444.23	444.23	441.72	440.38	444.13	451.49	440.87	443.97
$\gamma\text{C-OH} + \nu\text{O-H}$	451.54	451.54	451.32	451.32	451.53	444.01	451.13	451.52
$(\delta\text{C-OCH}_3 + \delta\text{C-CHO} + \delta\text{C-OH})^2 + \delta\text{Ph}$	497.06	496.22	534.34	495.17	496.32	537.36	494.82	534.01
$\delta\text{Ph} + \delta\text{C-O-CH}_3$	537.48	536.04	496.94	535.32	537.26	496.52	536.65	496.52
$\gamma\text{Ph}^2$	564.64	564.63	563.49	561.50	564.56	556.79	563.53	561.61
$\delta\text{Ph}$	624.62	623.91	759.33	624.55	622.83	622.22	622.30	622.37
$\gamma\text{Ph}^3$	705.11	705.10	704.40	697.21	705.07	703.40	695.69	703.22
$[\delta\text{Ph} + (\delta\text{C-O-CH}_3 + \tau\text{C-CHO})]^1$	760.47	760.17	620.85	760.33	748.95	758.67	760.29	758.02
$[\delta\text{Ph} + (\delta\text{C-O-CH}_3 + \tau\text{C-CHO})]^2$	783.27	783.20	773.55	780.83	782.92	783.15	782.89	780.98
$(\nu^{\text{Hydrogen}}\text{Ph} + \delta^{\text{Hydrogen}}\text{Ph})^1$	813.88	813.88	813.79	813.68	813.81	813.51	811.06	811.54
$(\nu^{\text{Hydrogen}}\text{Ph} + \delta^{\text{Hydrogen}}\text{Ph})^2$	829.46	829.46	822.13	828.24	829.20	829.25	829.46	829.46

$(\nu^{\text{Hydrogen}}\text{Ph} + \gamma^{\text{Hydrogen}}\text{Ph})$	931.08	931.08	930.92	931.01	930.33	931.06	910.68	901.26
$(\nu^{\text{as}}\text{Ph} + \delta\text{Ph})$	911.52	909.43	904.74	909.45	909.11	909.78	931.02	926.69
$\gamma\text{O-C-H}$	982.07	982.07	981.89	982.07	968.87	979.27	982.06	981.66
$(\nu^{\text{as}}\text{Ph} + \delta\text{Ph}) + \nu\text{O-CH}_3$	1032.12	1022.94	1028.64	1026.75	1032.11	1032.11	1031.60	1029.85
$(\delta^{\text{Hydrogen}}\text{Ph} + \delta\text{Ph}) + \tau\text{C-OH}$	1098.54	1096.45	1096.09	1098.31	1098.53	1097.66	1097.03	1096.82
$(\tau\text{C-OCH}_3 + \tau\text{C-CHO} + \tau\text{C-OH})$	1144.17	1140.68	1143.93	1142.11	1142.10	1134.89	1143.64	1143.21
$(\tau\text{C-CH}_3 + \nu^{\text{as}}\text{C-H}_3)$	1138.84	1130.79	1138.84	1138.84	1138.84	1138.84	1138.84	1138.84
$[(\tau\text{C-CH}_3 + \tau\text{C-OH}) + \delta^{\text{Hydrogen}}\text{Ph}]^1$	1166.00	1161.73	1165.88	1165.91	1165.12	1162.43	1162.54	1165.96
$[(\tau\text{C-CH}_3 + \tau\text{C-OH}) + \delta^{\text{Hydrogen}}\text{Ph}]^2$	1186.92	1182.79	1185.99	1185.87	1186.90	1186.83	1184.38	1186.67
$\delta\text{Ph} + \delta\text{C-O-H} + \delta^{\text{Hydrogen}}\text{Ph}$	1235.13	1234.34	1232.68	1223.16	1234.80	1230.80	1225.48	1233.39
$\nu^{\text{sym}}\text{Ph} + \delta^{\text{Hydrogen}}\text{Ph}$	1270.89	1283.30	1270.65	1279.40	1283.79	1277.51	1267.50	1268.69
$\nu\text{Ph} + \delta\text{C-O-H}$	1283.84	1270.53	1281.26	1265.45	1269.07	1261.59	1275.89	1282.02
$\delta\text{C-O-H} + \delta^{\text{Hydrogen}}\text{Ph}$	1364.89	1364.80	1363.35	1373.35	1383.77	1359.64	1361.12	1363.73
$(\delta\text{C-O-H} + \delta^{\text{Hydrogen}}\text{Ph} + \nu^{\text{as}}\text{Ph})^1$	1383.80	1383.19	1379.68	1363.86	1360.04	1378.96	1377.66	1374.57
$(\delta\text{C-O-H} + \delta^{\text{Hydrogen}}\text{Ph} + \nu^{\text{as}}\text{Ph})^2$	1419.74	1417.52	1417.33	1415.00	1419.65	1412.63	1417.01	1416.76
$(\nu\text{O-CH}_3 + \delta\text{C-O-CH}_3 + \nu^{\text{sym}}\text{C-H}_3 + \delta\text{C-CH}_3)$	1440.17	1437.22	1439.00	1435.44	1439.95	1436.14	1439.51	1438.20
$\nu^{\text{as}}\text{CH}_3^1$	1449.21	1447.34	1449.20	1449.20	1449.21	1449.20	1449.20	1449.21
$\nu^{\text{as}}\text{CH}_3^2$	1459.78	1458.39	1459.64	1459.16	1459.78	1459.64	1459.67	1459.62
$(\nu^{\text{as}}\text{Ph} + \delta\text{Ph} + \nu\text{C-OH} + \delta\text{C-O-H} + \nu\text{O-CH}_3 + \delta\text{C-O-CH}_3 + \nu^{\text{as}}\text{C-H}_3 + \delta\text{C-CH}_3)$	1501.77	1501.74	1494.48	1494.72	1501.41	1497.18	1489.43	1500.19
$[\nu^{\text{as}}\text{Ph} + (\delta\text{C-OH} + \delta\text{C-CHO} + \delta^{\text{Hydrogen}}\text{Ph})]^1$	1583.63	1583.60	1579.63	1573.62	1600.35	1594.85	1594.85	1568.48

$\delta\text{C-O-H} +$ $\nu^{\text{as}}\text{H-C=O} +$ $\nu^{\text{as}}\text{Ph}$	1600.39	1600.36	1589.31	1594.09	1581.85	1575.98	1575.98	1598.49
$[\nu^{\text{as}}\text{Ph} +$ $(\delta\text{C-OH} + \delta\text{C-CHO}$ $+ \delta^{\text{Hydrogen}}\text{Ph})]^2$	1715.60	1715.60	1715.32	1715.20	1676.37	1714.79	1715.41	1715.12
$\nu\text{H-CO}$	2775.51	2775.51	2775.51	2775.51	2767.54	2775.50	2775.51	2775.51
$\nu^{\text{sym}}\text{CH}_3$	2914.77	2911.71	2914.77	2914.77	2914.77	2914.77	2914.77	2914.77
$\nu^{\text{as}}\text{CH}_3^3$	2982.31	2971.03	2982.31	2982.31	2982.31	2982.31	2982.31	2982.31
$\nu^{\text{as}}\text{CH}_3^4$	3044.47	3033.65	3044.40	3044.47	3044.47	3044.47	3044.47	3044.47
$\nu^{\text{Hydrogen}}\text{Ph}^1$	3095.37	3095.37	3095.37	3095.37	3095.37	3095.37	3095.36	3090.52
$\nu^{\text{Hydrogen}}\text{Ph}^2$	3081.65	3070.31	3081.64	3081.64	3081.64	3081.64	3081.64	3076.61
$\nu^{\text{Hydrogen}}\text{Ph}^3$	3070.35	3081.64	3060.83	3070.33	3070.34	3070.34	3070.34	3070.31
$\nu\text{O-H}$	3610.04	3610.04	3610.04	3610.04	3610.04	3610.04	3610.03	3610.04

Table 3b-15a: Simulated vibrational wavenumbers for all isotopically substituted variants of B3PW91 +d for Structure 011, with associated description of the matching vibrational mode. Wavenumber values are scaled by a factor of 0.963.

	B3PW91 +d Structure 011 Vibrational Mode and Calculated Vibrational Wavenumber (W, cm <sup>-1</sup> ) for each Isotopic Substitution							
Vibrational Mode	08	09	10	11	12	13	14	15
$\tau\text{CH}_3$	69.29	66.79	67.85	66.79	68.75	69.03	69.39	69.07
$\tau\text{CH}_3 + \tau\text{Ph}^1$	95.81	95.71	95.94	95.70	95.76	95.54	95.21	95.35
$(\delta\text{HC=O} + \delta\text{OCH}_3)^1$	217.49	197.22	197.14	197.32	216.65	153.98	217.47	216.96
$\tau\text{O-CH}_3 + \tau\text{Ph}$	151.85	148.56	150.49	148.66	151.47	143.63	150.48	150.91
$\gamma\text{HC=O} + \tau\text{Ph}$	155.79	154.08	152.58	153.90	155.68	208.04	155.83	155.50
$(\delta\text{HC=O} + \delta\text{OCH}_3)^2$	227.40	265.40	223.41	226.37	226.80	227.11	223.71	226.29
$\tau\text{O-CH}_3 + \tau\text{HC=O}$	271.16	226.39	264.92	265.39	269.34	259.68	271.27	269.28
$(\delta\text{C-OCH}_3 + \delta\text{C-CHO} + \delta\text{C-OH})^1$	327.40	322.16	325.39	322.30	326.91	327.27	318.97	326.40
$\tau\text{Ph}$	330.52	332.71	332.36	332.60	332.51	328.95	445.19	325.19
$(\nu^{\text{as}}\text{Ph}^1 + \nu\text{C-CHO})$	383.43	383.21	383.65	383.21	382.57	379.23	328.95	383.21
$\gamma\text{Ph}^1$	442.56	444.02	444.22	451.54	410.95	444.05	379.23	451.44
$\gamma\text{C-OH} + \nu\text{O-H}$	451.49	451.54	451.52	444.03	450.61	451.53	444.05	444.19
$(\delta\text{C-OCH}_3 + \delta\text{C-CHO} + \delta\text{C-OH})^2 + \delta\text{Ph}$	534.73	490.02	532.52	490.01	533.54	536.75	528.33	521.66
$\delta\text{Ph} + \delta\text{C-O-CH}_3$	496.68	537.10	489.78	537.11	494.25	495.79	496.44	531.87
$\gamma\text{Ph}^2$	563.34	564.45	564.44	564.45	560.02	558.83	564.35	495.59
$\delta\text{Ph}$	617.85	760.28	624.30	623.59	616.27	622.60	620.32	616.76
$\gamma\text{Ph}^3$	704.39	704.39	705.11	705.02	645.68	704.00	705.00	704.56
$[\delta\text{Ph} + (\delta\text{C-O-CH}_3 + \tau\text{C-CHO})]^1$	754.29	623.60	752.67	760.28	813.88	733.36	760.03	776.99
$[\delta\text{Ph} + (\delta\text{C-O-CH}_3 + \tau\text{C-CHO})]^2$	781.40	781.55	776.64	781.54	739.04	782.23	778.66	710.04
$(\nu^{\text{Hydrogen}}\text{Ph} + \delta^{\text{Hydrogen}}\text{Ph})^1$	809.91	813.87	813.88	813.87	730.15	798.32	813.38	741.87
$(\nu^{\text{Hydrogen}}\text{Ph} + \delta^{\text{Hydrogen}}\text{Ph})^2$	829.46	829.37	829.06	829.37	761.69	935.51	829.41	829.31

$(\nu^{\text{HydrogenPh}} + \gamma^{\text{HydrogenPh}})$	927.57	1147.73	931.08	1147.74	930.76	821.35	931.07	877.62
$(\nu^{\text{asPh}} + \delta^{\text{Ph}})$	911.05	928.93	885.56	911.06	869.12	893.58	895.17	874.35
$\gamma^{\text{O-C-H}}$	982.03	911.07	1041.16	928.91	1240.22	866.77	1222.29	1138.84
$(\nu^{\text{asPh}} + \delta^{\text{Ph}}) + \nu^{\text{o-CH}_3}$	1028.48	931.12	982.53	931.11	947.81	1238.70	947.95	900.72
$(\delta^{\text{HydrogenPh}} + \delta^{\text{Ph}}) + \tau^{\text{C-OH}}$	1096.78	982.07	982.03	982.07	980.79	1026.60	982.07	979.34
$(\tau^{\text{C-OCH}_3} + \tau^{\text{C-CHO}} + \tau^{\text{C-OH}})$	1143.21	1035.16	1098.94	1035.20	1050.02	1032.23	1039.94	1165.77
$(\tau^{\text{C-CH}_3} + \nu^{\text{asC-H}_3})$	1138.84	1098.37	1091.88	1098.38	1098.07	1138.84	1103.02	1039.06
$[(\tau^{\text{C-CH}_3} + \tau^{\text{C-OH}}) + \delta^{\text{HydrogenPh}}]^1$	1163.87	1104.53	1148.60	1104.50	1138.79	1099.24	1144.42	1142.29
$[(\tau^{\text{C-CH}_3} + \tau^{\text{C-OH}}) + \delta^{\text{HydrogenPh}}]^2$	1186.16	1177.27	1175.48	1177.27	1158.67	1152.61	1138.80	1186.13
$\delta^{\text{Ph}} + \delta^{\text{C-O-H}} + \delta^{\text{HydrogenPh}}$	1234.34	1233.92	1234.53	1233.92	1230.85	1173.82	1177.09	1209.74
$\nu^{\text{SymPh}} + \delta^{\text{HydrogenPh}}$	1276.75	1282.04	1279.77	1282.02	1181.42	1187.09	1256.85	1252.47
$\nu^{\text{Ph}} + \delta^{\text{C-O-H}}$	1269.80	1266.06	1270.43	1266.06	1282.28	1269.66	1281.40	1375.54
$\delta^{\text{C-O-H}} + \delta^{\text{HydrogenPh}}$	1363.77	1303.93	1284.26	1303.85	1362.91	1287.47	1375.10	1278.13
$(\delta^{\text{C-O-H}} + \delta^{\text{HydrogenPh}} + \nu^{\text{asPh}})^1$	1381.44	1332.66	1365.66	1332.63	1383.04	1380.00	1339.86	1363.06
$(\delta^{\text{C-O-H}} + \delta^{\text{HydrogenPh}} + \nu^{\text{asPh}})^2$	1417.25	1365.59	1427.66	1386.89	1412.94	1413.02	1413.89	1410.96
$(\nu^{\text{O-CH}_3} + \delta^{\text{C-O-CH}_3} + \nu^{\text{symC-H}_3} + \delta^{\text{C-CH}_3})$	1439.63	1386.89	1332.84	1365.60	1437.54	1438.08	1440.15	1434.97
$\nu^{\text{asCH}_3}{}^1$	1449.21	1425.69	1385.74	1425.74	1449.00	1449.21	1449.20	1449.20
$\nu^{\text{asCH}_3}{}^2$	1459.45	1447.46	1452.11	1447.61	1459.63	1459.69	1459.62	1459.56
$(\nu^{\text{asPh}} + \delta^{\text{Ph}} + \nu^{\text{C-OH}} + \delta^{\text{C-O-H}} + \nu^{\text{O-CH}_3} + \delta^{\text{C-O-CH}_3} + \nu^{\text{asC-H}_3} + \delta^{\text{C-CH}_3})$	1492.09	1500.83	1501.67	1500.83	1484.43	1501.31	1501.47	1493.82
$[\nu^{\text{asPh}} + (\delta^{\text{C-OH}} + \delta^{\text{C-CHO}} + \delta^{\text{HydrogenPh}})]^1$	1589.92	1583.61	1583.50	1600.22	1593.49	1599.65	1597.43	1575.31

$\delta\text{C-O-H} +$ $\nu^{\text{as}}\text{H-C=O} +$ $\nu^{\text{as}}\text{Ph}$	1578.60	1600.22	1600.18	1583.61	1579.77	1583.58	1576.41	1597.32
$[\nu^{\text{as}}\text{Ph} +$ $(\delta\text{C-OH} + \delta\text{C-CHO}$ $+ \delta^{\text{Hydrogen}}\text{Ph})]^2$	1715.47	1715.60	1715.60	1715.60	1715.42	1702.31	1715.56	1715.20
$\nu\text{H-CO}$	2775.51	2775.51	2775.51	2775.51	3095.37	2047.70	3095.37	3070.37
$\nu^{\text{sym}}\text{CH}_3$	2914.77	2165.53	2223.68	2165.49	2267.79	2914.77	2627.06	2285.04
$\nu^{\text{as}}\text{CH}_3^3$	2982.31	2948.26	2931.59	2948.34	2775.51	2982.31	2775.51	2775.52
$\nu^{\text{as}}\text{CH}_3^4$	3044.47	3040.67	2982.05	3040.65	2914.87	3044.47	2914.77	2914.77
$\nu^{\text{Hydrogen}}\text{Ph}^1$	3092.99	3095.37	3095.37	3095.37	2982.31	3095.37	2982.31	2982.31
$\nu^{\text{Hydrogen}}\text{Ph}^2$	3070.23	3081.64	3081.64	3081.64	3044.59	3081.64	3081.64	3044.47
$\nu^{\text{Hydrogen}}\text{Ph}^3$	3074.20	3070.26	3070.25	3070.26	3081.59	3070.32	3070.35	3086.51
$\nu\text{O-H}$	3610.04	3610.04	3610.04	3610.04	3610.04	3610.04	3044.47	3610.04

Table 3b-15b: Simulated vibrational wavenumbers for all isotopically substituted variants of B3PW91 +d for Structure 011, with associated description of the matching vibrational mode. Wavenumber values are scaled by a factor of 0.963.

	B3PW91 +d Structure 011 Vibrational Mode and Calculated Vibrational Wavenumber (W, cm <sup>-1</sup> ) for each Isotopic Substitution						
Vibrational Mode	16	17	18	19	20	21	22
$\tau\text{CH}_3$	68.96	68.93	69.35	69.38	68.49	69.31	69.38
$\tau\text{CH}_3 + \tau\text{Ph}^1$	95.81	95.92	94.88	95.59	95.82	93.84	95.19
$(\delta\text{HC=O} + \delta\text{OCH}_3)^1$	217.40	217.46	217.30	217.47	217.43	217.13	217.44
$\tau\text{O-CH}_3 + \tau\text{Ph}$	151.59	151.25	151.95	151.11	150.44	151.78	150.18
$\gamma\text{HC=O} + \tau\text{Ph}$	155.73	155.86	154.39	155.82	155.77	152.93	155.69
$(\delta\text{HC=O} + \delta\text{OCH}_3)^2$	227.05	227.50	226.27	225.95	227.35	225.01	224.29
$\tau\text{O-CH}_3 + \tau\text{HC=O}$	268.51	270.29	271.35	271.41	269.26	271.26	271.37
$(\delta\text{C-OCH}_3 + \delta\text{C-CHO} + \delta\text{C-OH})^1$	326.63	326.02	326.94	324.66	324.61	326.40	322.14
$\tau\text{Ph}$	327.38	332.75	333.06	332.32	332.46	333.04	331.64
$(\nu^{\text{as}}\text{Ph}^1 + \nu\text{C-CHO})$	383.76	383.68	380.88	382.29	383.28	377.87	380.48
$\gamma\text{Ph}^1$	420.67	451.51	451.54	444.20	443.93	451.54	444.17
$\nu\text{C-OH} + \nu\text{O-H}$	451.30	444.07	444.21	450.31	451.47	444.19	449.23
$(\delta\text{C-OCH}_3 + \delta\text{C-CHO} + \delta\text{C-OH})^2 + \delta\text{Ph}$	531.48	534.95	496.38	536.03	532.85	621.07	492.65
$\delta\text{Ph} + \delta\text{C-O-CH}_3$	490.33	491.89	537.38	623.99	624.37	537.28	534.77
$\gamma\text{Ph}^2$	564.57	564.22	564.62	564.50	563.86	564.61	564.39
$\delta\text{Ph}$	615.91	624.49	622.75	494.80	486.70	495.78	759.12
$\gamma\text{Ph}^3$	642.04	704.97	705.10	704.88	704.84	705.10	704.69
$[\delta\text{Ph} + (\delta\text{C-O-CH}_3 + \tau\text{C-CHO})]^1$	771.51	759.15	759.25	759.95	757.82	758.18	623.38
$[\delta\text{Ph} + (\delta\text{C-O-CH}_3 + \tau\text{C-CHO})]^2$	738.72	781.89	783.17	777.60	780.78	783.08	772.77
$(\nu^{\text{Hydrogen}}\text{Ph} + \delta^{\text{Hydrogen}}\text{Ph})^1$	746.42	813.87	813.87	813.77	813.87	813.86	813.67
$(\nu^{\text{Hydrogen}}\text{Ph} + \delta^{\text{Hydrogen}}\text{Ph})^2$	829.44	829.37	829.43	829.46	829.29	829.41	829.46

$(\nu^{\text{Hydrogen}}\text{Ph} + \gamma^{\text{Hydrogen}}\text{Ph})$	1228.27	931.08	931.03	931.07	931.07	930.99	931.06
$(\nu^{\text{as}}\text{Ph} + \delta\text{Ph})$	836.10	909.43	911.28	911.27	907.53	911.06	911.06
$\gamma\text{O-C-H}$	894.78	982.07	981.28	982.07	982.07	980.57	982.07
$(\nu^{\text{as}}\text{Ph} + \delta\text{Ph}) + \nu\text{O-CH}_3$	959.06	1025.27	1032.12	1032.07	1018.02	1032.12	1032.02
$(\delta^{\text{Hydrogen}}\text{Ph} + \delta\text{Ph}) + \tau\text{C-OH}$	981.60	1095.55	1098.52	1098.41	1092.76	1098.51	1098.28
$(\tau\text{C-OCH}_3 + \tau\text{C-CHO} + \tau\text{C-OH})$	1038.63	1140.28	1144.06	1144.08	1137.02	1143.94	1143.98
$(\tau\text{C-CH}_3 + \nu^{\text{as}}\text{C-H}_3)$	1138.84	1137.23	1138.84	1138.84	1135.81	1138.84	1138.84
$[(\tau\text{C-CH}_3 + \tau\text{C-OH}) + \delta^{\text{Hydrogen}}\text{Ph}]^1$	1124.75	1164.30	1165.96	1165.48	1162.81	1165.92	1164.96
$[(\tau\text{C-CH}_3 + \tau\text{C-OH}) + \delta^{\text{Hydrogen}}\text{Ph}]^2$	1157.66	1183.15	1186.90	1186.63	1180.02	1186.88	1186.36
$\delta\text{Ph} + \delta\text{C-O-H} + \delta^{\text{Hydrogen}}\text{Ph}$	1174.55	1232.65	1235.10	1230.75	1230.83	1235.08	1226.38
$\nu^{\text{sym}}\text{Ph} + \delta^{\text{Hydrogen}}\text{Ph}$	1278.39	1282.63	1270.84	1281.27	1281.81	1283.68	1279.55
$\nu\text{Ph} + \delta\text{C-O-H}$	1257.39	1270.33	1362.70	1269.11	1269.84	1270.78	1267.60
$\delta\text{C-O-H} + \delta^{\text{Hydrogen}}\text{Ph}$	1360.53	1364.83	1283.75	1364.42	1364.77	1360.47	1363.99
$(\delta\text{C-O-H} + \delta^{\text{Hydrogen}}\text{Ph} + \nu^{\text{as}}\text{Ph})^1$	1382.75	1383.25	1383.41	1383.38	1382.79	1383.07	1383.03
$(\delta\text{C-O-H} + \delta^{\text{Hydrogen}}\text{Ph} + \nu^{\text{as}}\text{Ph})^2$	1414.41	1419.47	1418.74	1419.30	1419.25	1417.76	1418.93
$(\nu\text{O-CH}_3 + \delta\text{C-O-CH}_3 + \nu^{\text{sym}}\text{C-H}_3 + \delta\text{C-CH}_3)$	1439.66	1438.95	1439.67	1440.12	1437.94	1439.23	1440.08
$\nu^{\text{as}}\text{CH}_3^1$	1449.20	1449.12	1449.21	1449.21	1449.04	1449.21	1449.21
$\nu^{\text{as}}\text{CH}_3^2$	1459.18	1459.27	1459.77	1459.75	1458.88	1459.75	1459.72
$(\nu^{\text{as}}\text{Ph} + \delta\text{Ph} + \nu\text{C-OH} + \delta\text{C-O-H} + \nu\text{O-CH}_3 + \delta\text{C-O-CH}_3 + \nu^{\text{as}}\text{C-H}_3 + \delta\text{C-CH}_3)$	1484.04	1501.00	1501.72	1500.64	1500.41	1501.68	1499.71
$[\nu^{\text{as}}\text{Ph} + (\delta\text{C-OH} + \delta\text{C-CHO} + \delta^{\text{Hydrogen}}\text{Ph})]^1$	1595.44	1600.28	1600.36	1600.15	1600.19	1600.33	1599.95

$\delta\text{C-O-H} +$ $\nu^{\text{as}}\text{H-C=O} +$ $\nu^{\text{as}}\text{Ph}$	1576.12	1583.54	1583.00	1583.35	1583.47	1582.28	1583.11
$[\nu^{\text{as}}\text{Ph} +$ $(\delta\text{C-OH} + \delta\text{C-CHO}$ $+ \delta^{\text{Hydrogen}}\text{Ph})]^2$	1715.49	1715.59	1698.41	1715.58	1715.59	1683.60	1715.57
$\nu\text{H-CO}$	3070.40	2775.51	2775.50	2775.51	2775.51	2775.49	2775.51
$\nu^{\text{sym}}\text{CH}_3$	2282.99	2914.76	2914.77	2914.77	2914.75	2914.77	2914.77
$\nu^{\text{as}}\text{CH}_3^3$	2775.51	2982.31	2982.31	2982.31	2982.31	2982.31	2982.31
$\nu^{\text{as}}\text{CH}_3^4$	2914.77	3044.47	3044.47	3044.47	3044.47	3044.47	3044.47
$\nu^{\text{Hydrogen}}\text{Ph}^1$	2982.31	3095.37	3095.37	3095.37	3095.37	3095.37	3095.37
$\nu^{\text{Hydrogen}}\text{Ph}^2$	3090.60	3081.65	3081.64	3081.64	3081.65	3081.64	3081.64
$\nu^{\text{Hydrogen}}\text{Ph}^3$	3044.47	3070.35	3070.35	3070.35	3070.35	3070.34	3070.35
$\nu\text{O-H}$	3610.04	3610.04	3610.04	3603.94	3610.04	3610.04	3598.55

*Table 3b-15c: Simulated vibrational wavenumbers for all isotopically substituted variants of B3PW91 +d for Structure 011, with associated description of the matching vibrational mode. Wavenumber values are scaled by a factor of 0.963.*

### 3b-3: Conclusions and Application to Experimental Systems

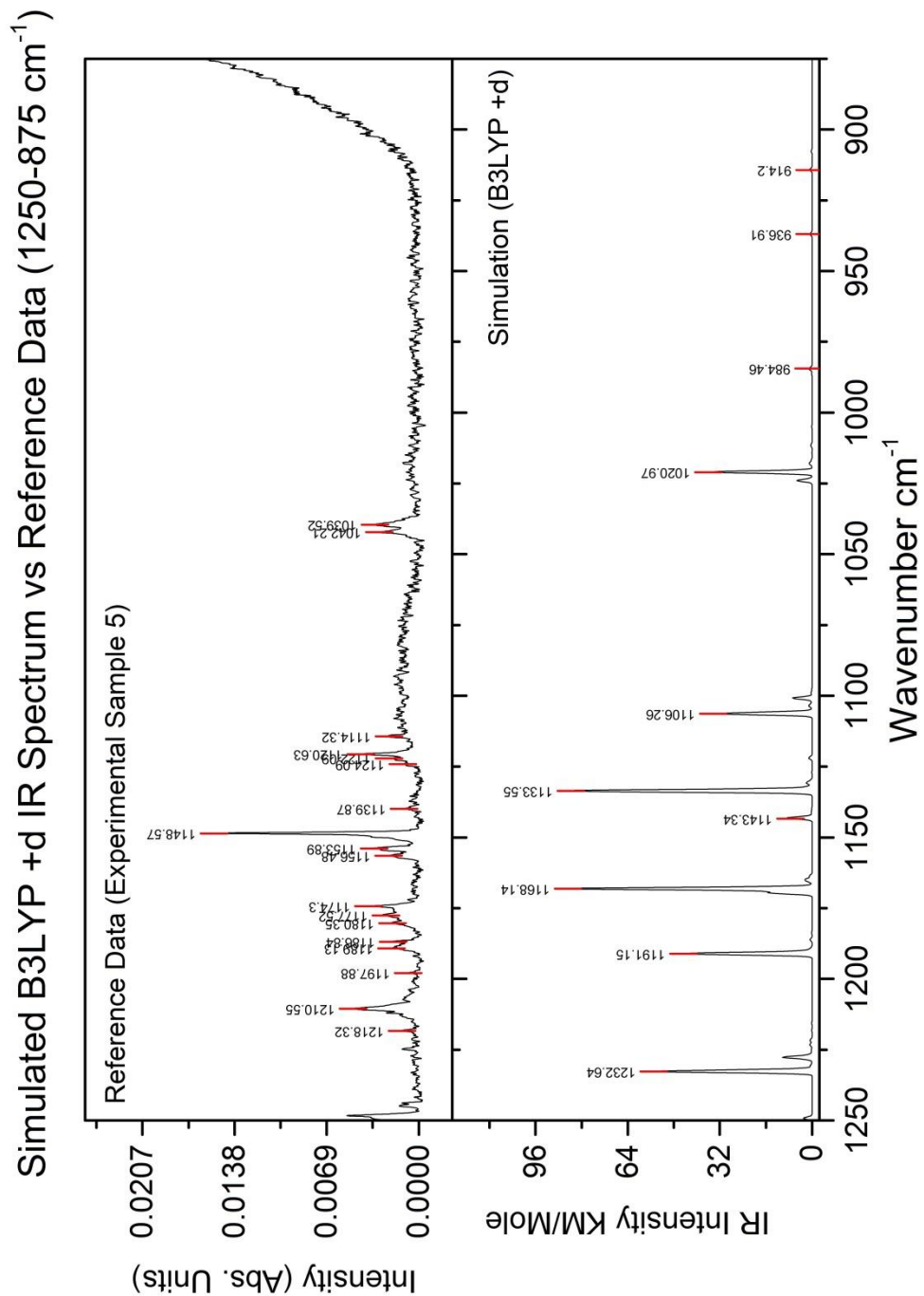


*Figure 3b-12a: Reference Sample Spectrum 5 (top) of vanillin isolated in a solid argon matrix versus final B3LYP +d simulated IR spectrum (bottom) over the  $1250\text{-}875\text{ cm}^{-1}$  range. Sample signal peaks are marked with centre bars and data points; simulations include data points for most abundant (i.e. the ‘zeroth’ spectra for structure 001) simulated peaks.*

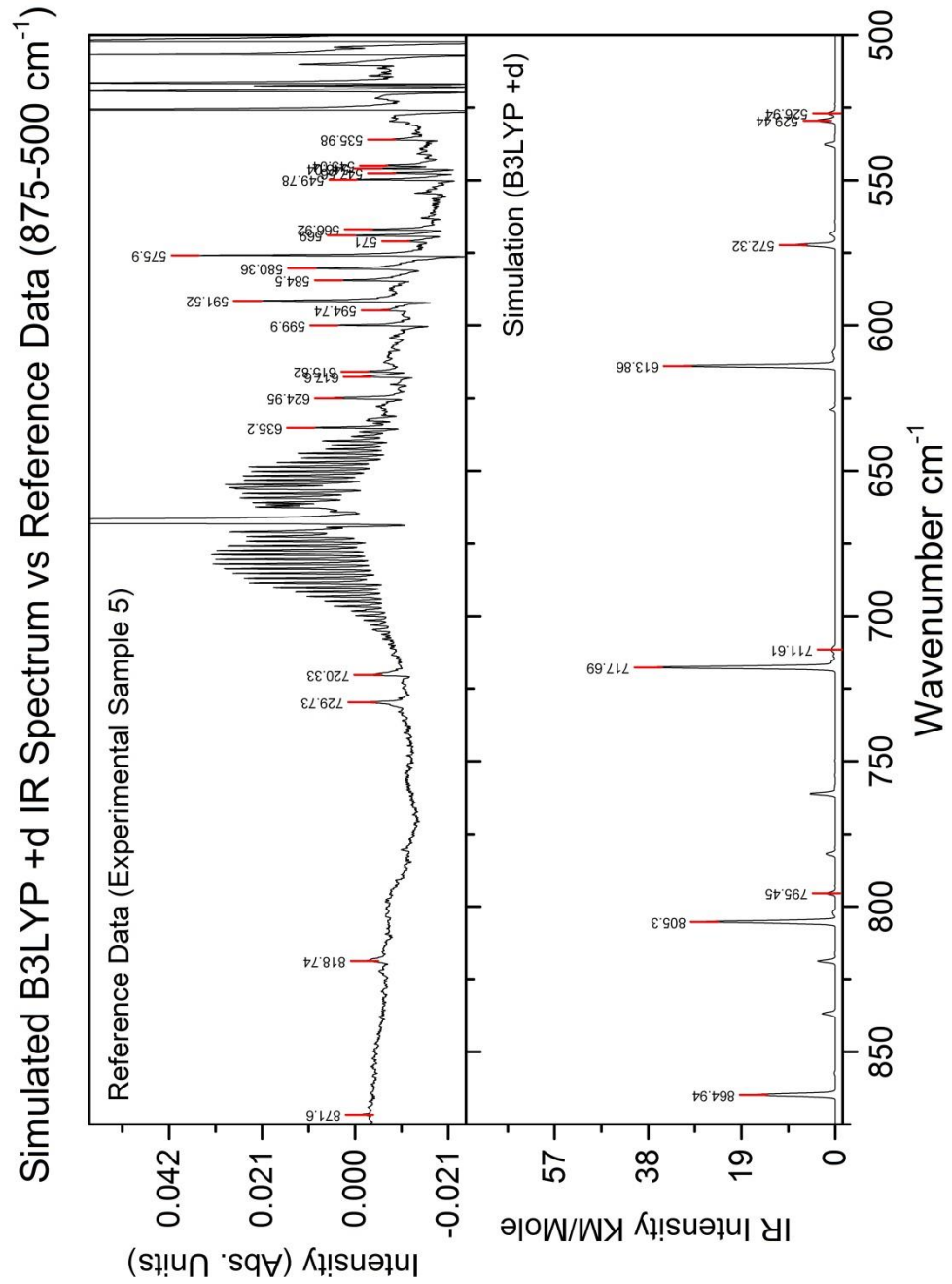


*Figure 3b-12b: Reference Sample Spectrum 5 (top) of vanillin isolated in a solid argon matrix versus final B3LYP +d simulated IR spectrum (bottom) over the  $875\text{-}500\text{ cm}^{-1}$  range. Sample signal peaks are marked with centre bars and data points; simulations include data points for most abundant (i.e. the ‘zeroth’ spectra for structure 001) simulated peaks. Range has been flattened by further baseline subtraction for display.*

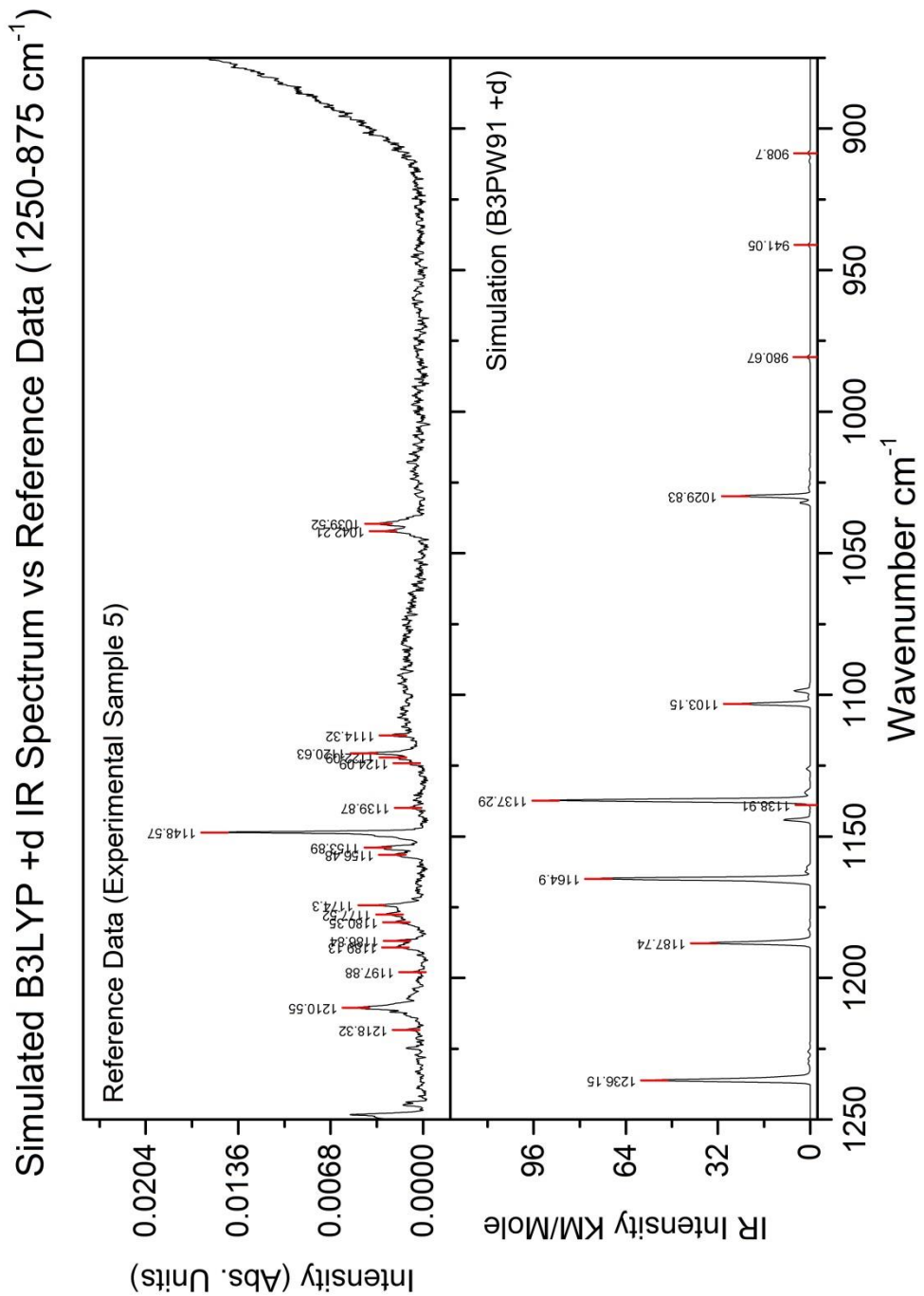


*Figure 3b-13a: Reference Sample Spectrum 5 (top) of vanillin isolated in a solid argon matrix versus final B3PW91 +d simulated IR spectrum (bottom) over the  $1250\text{-}875\text{ cm}^{-1}$  range. Sample signal peaks are marked with centre bars and data points; simulations include data points for most abundant (i.e. the ‘zeroth’ spectra for structure 001) simulated peaks.*

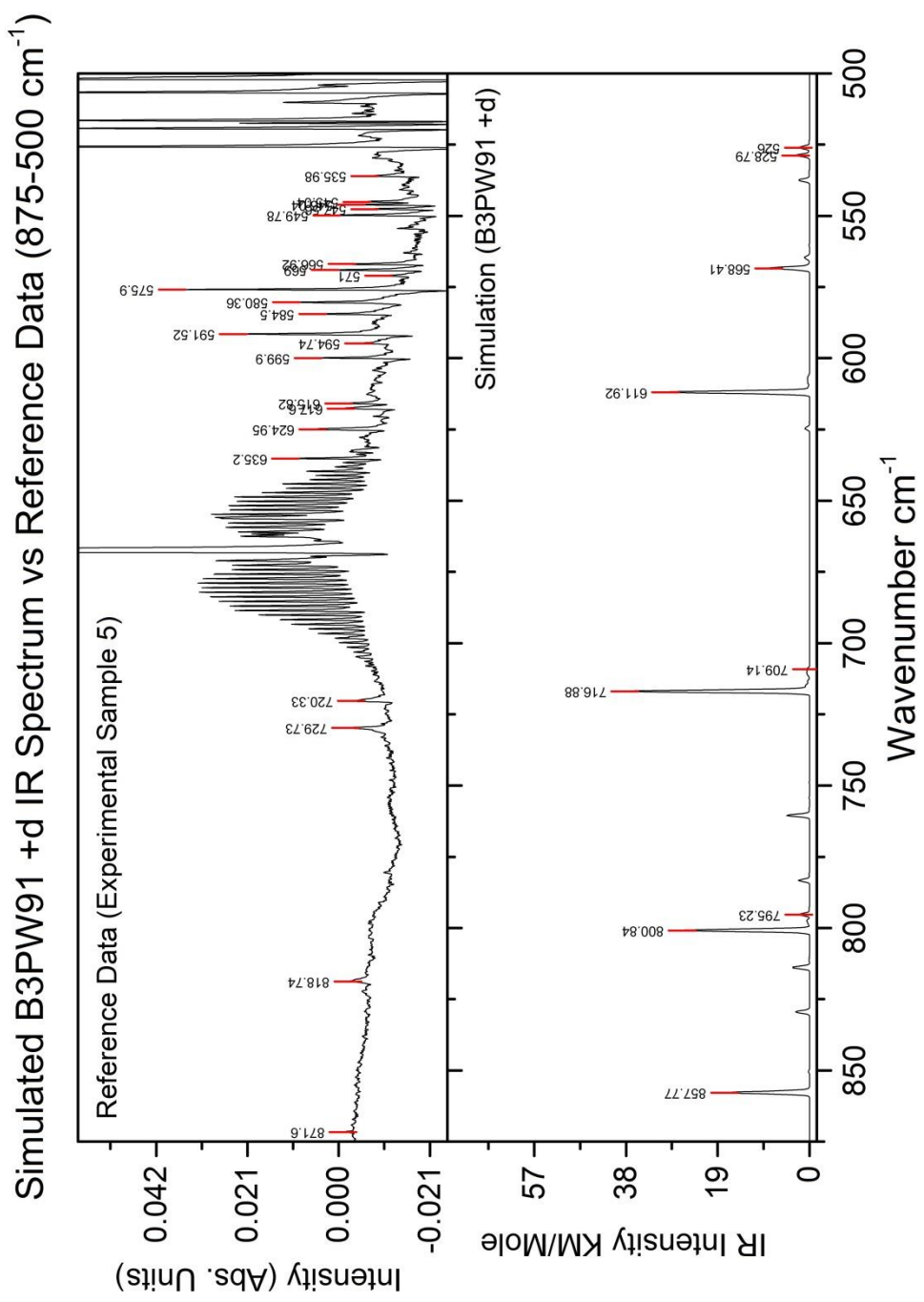


*Figure 3b-13b: Reference Sample Spectrum 5 (top) of vanillin isolated in a solid argon matrix versus final B3PW91 +d simulated IR spectrum (bottom) over the 875-500 cm<sup>-1</sup> range. Sample signal peaks are marked with centre bars and data points; simulations include data points for most abundant (i.e. the ‘zeroth’ spectra for structure 001) simulated peaks. Range has been flattened by further baseline subtraction for display.*

The main aim of this work was to assess the practicality of using Density Functional Theory to simulate the isotopic splitting effects found in vibrational spectra, as a potential method of extracting isotopic data from experimental data. The resulting simulated spectra (combining conformers 001 and 011, the two ‘zeroth’ spectra for B3LYP +d and B3PW91 +d) combining conformers 001 and 011 but without any isotopic substitutions, resemble the distribution of the experimentally obtained data from *Chapter 1* quite closely, but it is apparent that these single-isotope contributions do not produce enough distinct peaks in the visible regions to account for all of the signals observed; this is particularly obvious in the lower wavenumber range ( $\sim 700\text{ cm}^{-1}$  and below) when comparing *Figures 3b-8* and *3b-10* to the data shown in Sample 5 (*Figures 1-11 a to h*). Comparing sample data and simulated values over the relatively narrow, flat  $1250\text{-}500\text{ cm}^{-1}$  range as seen in *Figures 3b-12* and *3b-13 a and b* shows that the calculated bands lay very close (typically within  $\sim 20\text{ cm}^{-1}$ ) to the closest signals observed in the practical results. Given that there are also a number of regions in the experimental samples where any sample peaks that are present are obscured by contamination (as seen in the background spectra included in *Figures 1-11 a to h*) it is not possible to make a direct 1:1 assignment of equivalent signals between the calculated and observed spectra, but the similarity in position, intensity and relative density of peaks observed in these two simulations gives an approximation of the character of the peaks observed in the practical experiment (little is seen out of the ordinary in this case, but such may be applicable to the assignment of unusually shifted vibrational peaks in other molecular species).

When making the comparison between the simulations (with the full range of possible isotopic substitutions) and the reference data from Sample 5 seen in *Figures 3b-12* and *3b-13 a and b*, the addition of further isotopically substituted simulated spectra increases the number of peaks present. However, the expected weighting of intensity by natural abundance suggests that these species are difficult to observe, and highly unlikely to be in such concentrations as to produce the number of peaks (of comparable intensity) seen in Sample 5: by comparing the full  $4000\text{-}500\text{ cm}^{-1}$  range shown in *Figures 3b-5* and *3b-10*, the unsubstituted (*3b-5*) and fully substituted (*3b-10*) simulations are very difficult to distinguish.

There is little evidence for the presence of the H-CO stretching mode calculated at  $\sim 2800\text{ cm}^{-1}$  in each simulation in any but the two most concentrated sample spectra (*Figures 1-7* and *1-8, a to h*); if present, it is of much lower intensity than the calculations would suggest. Over the  $1250\text{-}700\text{ cm}^{-1}$  range where the best reference data exists, good agreement can be seen in *Figures 3b-12* and *3b-13 a and b* between the strongest peaks in both the calculations and the reference data, though the calculated peaks for both B3LYP +d and B3PW91 +d between  $1250\text{ cm}^{-1}$  and  $1100\text{ cm}^{-1}$  are notably more widely spread in wavenumber than in the experimental data. Compared to the calculated spectra data, the relative intensity observed for these peaks is lower than expected (although this may partially be explained by the relatively high degree of splitting of these peaks), as it is also for the peaks observed below  $\sim 700\text{ cm}^{-1}$ . Between  $1250\text{ cm}^{-1}$  and  $1100\text{ cm}^{-1}$  the modes involved appear to be primarily dominated by ring torsional modes, while almost all of the modes below  $\sim 700\text{ cm}^{-1}$  involve stretching and deformation transitions (both in and out of the plane of the molecule) of the oxygen-containing side groups; more than the peaks found in the intermediate range, these two bands (which are calculated as being ring hydrogen stretching and deformation modes) show relatively large atomic displacement.

It is worth remarking that there is a significant intensity of hydrogen bonding interactions present in the experimental samples. The fact that the peaks seen in these two regions are of similar width and show no apparent broadening effects relative to other bands suggests that there is little interaction between the polar side groups of vanillin and water contamination in the matrix. The peak attributed to the OH stretch at  $\sim 3550\text{ cm}^{-1}$  at first appears to show a significant broadening effect (and some such effects may indeed be present, as the OH would be expected to interact strongly with any neighbouring H<sub>2</sub>O contamination), but upon closer examination in Sample 4 (*Figures 1-10 a to h*) this peak can be seen to be a number of narrower, poorly resolved peaks of equivalent intensity very close together.

The larger number of peaks seen in these two ranges is not adequately explained by only the principle components described earlier: additional structure is seen that suggests either (or both) the presence of site-splitting of the bands described, or additional conformers of significant enough intensity to be visible at approximately the same intensity as the primary contributors. It seems highly improbable that the other conformers of vanillin would exist at such a similar energy level should the conformation occupied and deposition process of vanillin/ Ar gas be entirely diffusion controlled: the energy level evaluation performed in *Section 3b-1* suggests that there is a difference of  $\sim 4.85 \text{ kJmol}^{-1}$  between conformer 011 and the next most populous at 298K, conformer 051. The calculated population ratio between these two structures is approximately 48:1, and for them to exist in equivalent populations would imply that the matrix material had a drastically greater effect on some structures than others. Given that the Ar atoms are expected to show no chemical interaction with the vanillin molecule other than van der Waals forces during the packing process<sup>51</sup>, such a biased effect on the conformers seems very unlikely. If isotopic splitting effects cannot be considered a probable source for the extra structure seen in the sample spectra (in particular Sample 5) then the most logical explanation is that some additional weighting of vanillin structural conformations takes place during the condensation process, and that the condensation is not as instantaneous as first assumed.

The final simulated spectra presented above also include the predicted intensity contributions from isotopic substitutions, and the additional peaks that they would be expected to show in the infrared. If these signals are truly of intensity similar to the calculated values it is not possible to distinguish them from background noise in the present reference spectra with the equipment available during this investigation. Even with the relative similarity in size between argon atoms and the vanillin molecule (see *Chapter 1, Section 1-1-4*), it appears that the most significant effects are caused in the matrix isolated vibrational spectra by the packing properties of the gas atoms around the molecule, and the additional peaks seen in the experimental spectra are instead of physical origin, not isotopic.

## **Part Three:**

**Neutron Compton Profiles of Hydrogen and Deuterium  
through Inelastic Neutron Scattering on the VESUVIO  
Instrument**

# **Chapter 4: Neutron Compton Scattering of the Poly-N-Isopropyl Acrylamide Co-Nonsolvancy Effect**

## **4-1: Introduction**

### **4-1-1: Neutron Scattering on Solvated Systems**

Other than potential differences in magnetic properties the main variation between isotopes of a species is mass, due to the different numbers of neutrons present in the nucleus. As a result of this, isotopic labelling has a variety of potential applications for any technique that relies on the mass of the sample molecule species involved- including other, non-traditional techniques, as well as the more commonly used vibrational spectroscopy and Mass Spectrometry. One potential technique that may make use of isotopic labelling is Neutron Compton Scattering (NCS), performed on the VESUVIO Inverse Geometry electron Volt Spectrometer (eVS) instrument at the ISIS facility at Rutherford Appleton Laboratories in Oxfordshire, England. In this technique the sample is bombarded with a stream of high-energy neutrons; after striking and scattering/ deflecting from the atoms in the sample species, this instrument can thus be used to measure the resulting transfer in momentum between the colliding particles. At these high energies, between 5 and 150eV, the scattering process may be studied using the Impact Approximation. The momentum distribution of the atomic species thus obtained is the Fourier Transform of the wave function of the atomic nucleus which is targeted. Interpretation of this momentum data for the total population of a given atomic species can allow for the determination of structural properties, such as the degree (i.e. strength) of bonding interactions that population experiences in the sample material(s)<sup>9,10</sup>.

It is possible to use Neutron Compton Scattering to observe changes in a system under a variety of conditions such as temperature and pressure. The output of the VESUVIO instrument gives a series of fitted Gaussian distributions to express the momentum transferred between the incoming neutrons and the sample for each atomic species present. Given that the output of VESUVIO is a measure of homogeneity of environment over the entire population of a given species, a broadening effect would be expected with an increase in disorder in the system, either from an increase in temperature leading to a phase change, such as major structural changes due to precipitation of a solute molecule. This may therefore be used effectively as a measure of energetic and structural homogeneity in the sample; a strongly bound atom in a simple repeating lattice would be expected to give a much narrower distribution than for example a hydrogen bonding atom in the liquid state.

No prior literature of a precisely similar subject exists at the time of writing: to the best of this author's knowledge VESUVIO (and NCS) have never before been used to probe atomic momentum distributions of multiple atomic species during significant change in bulk phase properties, making this investigation a novel application of the technique. Similar application can be found, though, in the study of published by *Pantalei, et al*, published in 2011, detailing the probing of the mechanism of hydration of silanol groups in mesoporous silica. Although the silica structure presents the water with a very large interfacial surface, during the hydration process the silanol groups bind in a very specific 1:1 ratio to the water molecules, allowing for the calculation of significant data on the changes in the momentum distributions of hydrogen found in the bulk water over a given timescale. The pNIPAAm case is further complicated by the three-component system used, and to compensate deuterium labelling has been applied to give separate signals for the sites that are expected to interact in the mixture. Because of the potential data that may be extracted, Neutron Compton Scattering was chosen as a technique to study the actions of the Co-Nonsolvency phenomenon in pNIPAAm in mixed H<sub>2</sub>O/ CH<sub>3</sub>OH systems at specific concentrations and temperatures, and to analyse it and to attempt to construct a model for its behaviour under a wider range of conditions.

## 4-1-2: The Lower Critical Solution Temperature and the Co-Nonsolvency Effect

The family of polymer structures to which pNIPAAm belongs show a great deal of promise for both industrial and medical applications; unmodified pNIPAAm (that is to say pure pNIPAAm without copolymerisation with related species such as N-hydroxymethyl acrylamide) is fully soluble in methanol ( $\text{CH}_3\text{OH}$ ) under standard conditions, but shows a clear ‘cloud point’ or Lower Critical Solution Temperature (LCST) in pure water ( $31.76^\circ\text{C}$  for the unmodified polymer); as noted earlier, the polymer is solvated at low temperatures but precipitates out spontaneously with heating. Mixtures of these solvents produce an unexpected non-linear dependence of the LCST, i.e. in the case of pNIPAAm the mixture of water and methanol makes for a poorer solvent than either one alone (*Winnik, et al.*). This is believed to occur because the solvation of pNIPAAm by water is thermodynamically unstable: when the thermal energy of the system overcomes the weak polar bonds holding the polymer in the solvated ‘coil’ phase, a spontaneous process occurs in which the entire polymer population switches to the more favourable internal bonding structure of the ‘globule’ phase (i.e. a coil-globule transition) and precipitates out in a gel form<sup>66</sup>. By comparison, methanol solvation is believed to be stabilised by additional non-polar interactions with the polymer backbone and side groups. Varying degrees of copolymerisation have also been demonstrated to produce ‘tunable’ cloud points under the same conditions leading to an interesting range of possible chemical applications when combined with the other interactive properties of the molecule, particularly in such areas regarding temperature-dependent release of active reagents into a dynamic system such as industrial processes and/ or biological tissue (including the targeted delivery of therapeutic drugs, hormones and proteins for localised disease treatment and even regenerative therapy)<sup>23,24,66-72</sup>.

pNIPAAm is able to form an extended hydrogen bonding network (see *Section 4-1-3*), and forms a loose hydrogel structure in aqueous conditions. The molecule is also able to form non-polar interactions through its side-chains (hence its

superior solubility in methanol), and copolymer sub-units may have additional active functional groups made accessible in a solvated state by lowering the temperature through the LCST. This opens possibilities for the use of these species as either transport molecules, or as environmentally activated reagents or catalysts. For example, in an industrial process in aqueous solution the polymer (along with a copolymerised unit carrying a reagent or catalytic unit) may be introduced at a temperature just above the LCST where the collapsed structure of the hydrogel sterically blocks its activity, then lowered during a later phase to free the side-chain and complete the reaction without breaking open the vessel. Such specific uses are not yet practically applicable, of course, but such an example shows how the co-nonsolvency effect may prove exceptionally useful as a delivery system. As noted, the actual value of the LCST varies with the composition of the solvent mixture and is found to be depressed (i.e. the polymer precipitates at a lower temperature) relative to one pure solvent with the addition of a fraction of the other. The LCST for a water/ methanol mixture is observed at a minimum when the concentration of  $\text{H}_2\text{O}$  is at a mole fraction of 0.35, a temperature of -7°C.

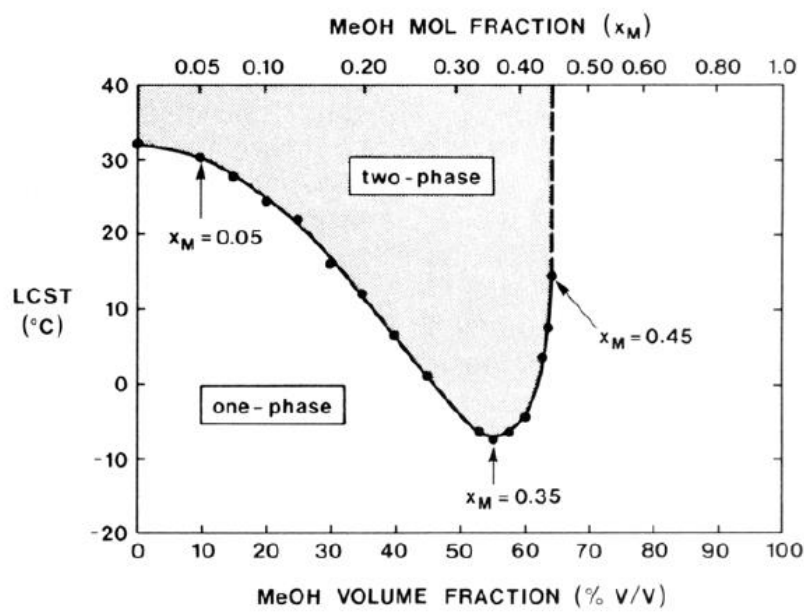


Figure 4-1: Plot of the Lower Critical Solution Temperature for a mixture of water and methanol by MeOH mole fraction (top axis) and volume fraction (bottom axis).

Image reproduced from F. Winnik, et al, *Macromolecules*, 1990, 23, p2415-2416.

The depression of the LCST, called the Co-Nonsolvency Effect, has been ascribed to the optimum concentrations for the formation of extended aggregate structures within the solvents. H<sub>2</sub>O is believed to form regions of extended hydrogen-bonding networks (as studied by *Flory, Soper et al.*), while CH<sub>3</sub>OH forms clusters according to a similar principle to the micelle formation observed in surfactant systems. This solvent system, however, is not completely understood, and yet has a great deal of impact on the LCST of the polymer (again, please see *Section 4-1-3*).

As part of this study into the behaviour of the pNIPAAm co-nonsolvancy system, we have attempted to use VESUVIO and the Neutron Compton Scattering effect to study changes in the momentum distribution of atoms expected to undergo hydrogen bonding interactions (labelled with deuterium) as the system passes through the LCST. Using this data, we have subsequently attempted to construct a simple statistical model to describe and predict the changes in the deuterium momentum distribution in polymer/ solvent mixtures over a range of concentrations for the three components (pNIPAAm, D<sub>2</sub>O and MeOD).

### 4-1-3: Water-Methanol Systems

Water and methanol, at first glance, would seem to be a system of fully miscible liquids well described by standard solution theory under standard conditions. In practice however, the mixture shows anomalous results that do not fit the classical approach, particularly in mixtures of methanol mole fraction  $\sim 0.3 \leq x \leq \sim 0.5$ , thanks to the tendency towards forming a self-assembled system of clusters and extended structures. The entropy of a pair of fully mixed liquids will naturally be higher than the combined entropy of the pure liquids before mixing; mixed water and methanol systems, however, display entropy values far lower than would be expected for fully miscible species<sup>21</sup>, implying some form of de-mixing process is taking place.

In an aqueous solution, the long-standing belief has been that the extant hydrogen-bonded structure of the molecules is *enhanced* by the presence of a hydrophobic species (for example the CH<sub>3</sub> group of methanol), in order to account for these lower entropy values; the polar water molecules would form an ice-like ‘cage’ structure about the polar end of the molecule, extending out into the bulk of the water population. Recent studies of the last  $\sim 10$  years (in particular the neutron diffraction studies published by *Soper, et al*) suggest that there is no clear evidence for extended structure enhancement, and that the presence of near equal mole fractions of water and methanol instead promotes the formation of clusters of each species<sup>73</sup>. At higher alcohol concentrations non-polar micelle structure is favoured by this process, while at very low concentrations the water-ice structure is dominant with only a slight shortening of the nearby O~H hydrogen bonding distance.

At middle concentrations (the  $\sim 0.3 \leq x \leq \sim 0.5$  noted above) a compromised structure is formed with regions of ‘micro-segregated’, partially demixed pure liquids, bordered by regions of interacting polar groups. These regions are significantly smaller than their equivalents in the (near) pure species, typically

70% of these clusters only containing 1 to 3 methanol molecules or ~5 water molecules, but do show significant percolation of single molecules of each species through these structures.

This evidence suggests that the solvation of pNIPAAm is not a simple case of solvation in a single environment, but that there are two distinct types of solvent-polymer interaction to consider. Further evidence for this can be seen in the effects of ionic contamination in a pure water solvation system: the presence of strongly solvated anions has a distinct depressive effect on the observed LCST for any given system (the presence of 0.5 mole concentration NaCl is observed to reduce the LCST by approximately 7°C, while the introduction of 0.5 mole Na<sub>2</sub>S<sub>2</sub>O<sub>3</sub> reduces the value by 25°C); this is believed to be caused by the solvation of the ions causing a reduction in the water molecules locally available for solvation of the polymer, making it yet more energetically favourable for the pNIPAAm to precipitate. By contrast, ions such as SCN<sup>-</sup> that typically behave as hydrophobic species are observed to raise the observed LCST by (it is believed) interacting with the hydrophobic elements of the polymer, as well as disrupting the aggregate water-water structure and freeing more molecules for solvation.

## 4-2: The VESUVIO Spectrometer

### 4-2-1: The Impulse Approximation and the Neutron Compton Scattering Profile

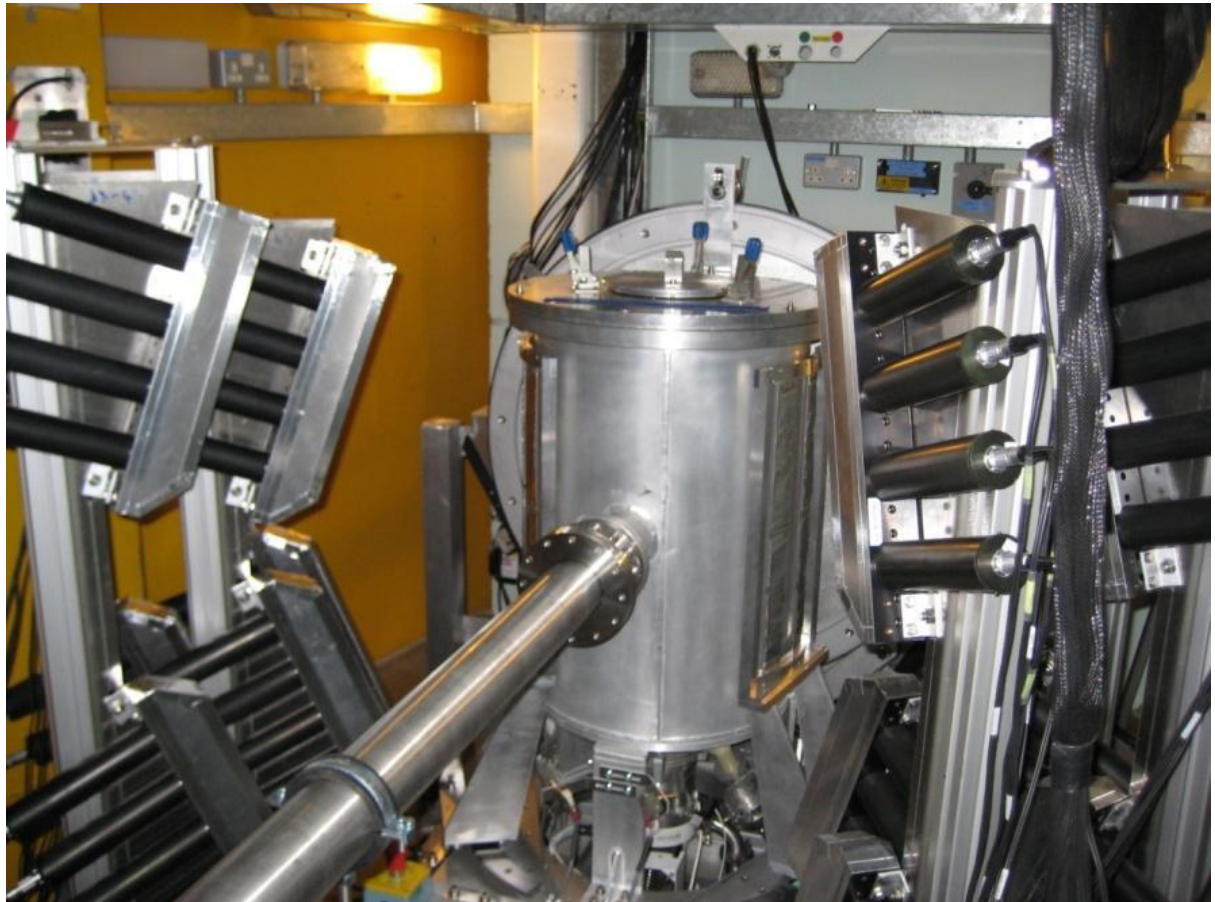


*Figure 4-2: An exterior photograph of the VESUVIO spectrometer, clearly showing the arrangement of the forward detector banks (see later). This view is not typically available during the operation of the instrument, and normal access is only available through a panel in the walkway directly above the instrument; samples are lowered into the central chamber vertically through the vacuum-sealed lid visible here on the top of the device.*

*Note: The topics discussed in this chapter, in particular the mathematical derivations presented, draw extensively on literature sources describing the construction and operation of the VESUVIO spectrometer as well as further literature describing neutron spectroscopy in general, the most significant of which can be found in references<sup>9-14</sup>.*

The VESUVIO electron Volt Spectrometer (eVS) is an inverse geometry device that uses a filter difference mechanism to measure the single atom properties of condensed matter systems. This is done using Neutron Compton Scattering (NCS), otherwise known as Deep Inelastic Neutron Scattering (DINS). The VESUVIO spectrometer operates, as one would expect, on the collision of neutrons with the target sample. Where VESUVIO differs from normal neutron instruments, however, is in that the neutrons used are of an unusually high energy for such a scattering spectrometer; neutrons entering the instrument have been measured as having energies of between 5-150 eV. Using these energies allows for the direct measurement of the atomic momentum distribution  $n(\mathbf{p})$  and mean kinetic energies of single particles in a molecular system.

VESUVIO uses such high energy neutrons in order to take advantage of the Impulse Approximation (IA). The IA is a quantum mechanical assumption that states that any Van der Waals forces between two scattering bodies, in this case the incident neutrons and the atomic nuclei in the sample molecules, can be neglected when calculating transfer of energy and momentum between them during collision. This is, as stated, an assumption, and not strictly true- however, the greater the energy of the incident particle the more closely applicable the Impulse Approximation is to the reality of the system. The VESUVIO spectrometer operates at a sufficiently high energy that the IA is considered to be true for the determination of energy and momenta. Because of relatively small particle sizes and the IA consideration during collisions, during the operation of VESUVIO each incident neutron may be considered as striking only a single atom in the sample; this does not take into consideration the possibility of the neutron undergoing more than one

collision during its path through the sample- this multiple scattering is accounted for statistically and will be explained later.

If the Impulse Approximation is considered in the classical form, with the assumption of conservation of momentum and energy we can write:

$$p_0 + A_0 = p_1 + A_1$$

Or:

$$\frac{p_0^2}{2m} + \frac{A_0^2}{2M} = \frac{p_1^2}{2m} + \frac{A_1^2}{2M}$$

*Equations 4-1 and 4-2*

Where  $p_0$  is the momentum of the neutron before collision and  $p_1$  the momentum afterward,  $A_0$  is the momentum of the atomic nucleus before collision and  $A_1$  the momentum afterward,  $M$  is the mass of the neutron and  $m$  the mass of the atomic nucleus.

The Impulse Approximation, when formally written, shows that the Dynamic Structure Factor (also called the Response Function) for atoms of mass  $M$  is:

$$S(\mathbf{q}, \omega) = \int n_m(\mathbf{p}) \delta\left(\omega + \frac{A^2}{2M} - \frac{(\mathbf{p} + \mathbf{q})^2}{2M}\right) d\mathbf{p}$$

*Equation 4-3*

Where  $n_m(\mathbf{p})$  is the atomic momentum distribution for particles of mass  $M$ ,  $\omega$  is the frequency of the energy transfer of the interaction ( $E_0 - E_1$ ),  $A$  the atomic

momentum,  $\mathbf{p}$  the neutron momentum, and  $\mathbf{q}$  the momentum transfer in the collision. If we also assume that the momentum component for the neutrons after collision is given in y-space by:

$$y_M = \frac{M}{q} \left( \omega - \frac{q^2}{2M} \right)$$

*Equation 4-4*

And that the probability distribution of the momentum component of mass  $M$  along  $\hat{\mathbf{q}}$  is given by:

$$J_M(y_M, \hat{\mathbf{q}}) = \int n_M(\mathbf{p}) \delta(y_M - \mathbf{p} \cdot \hat{\mathbf{q}}) d\mathbf{p}$$

*Equation 4-5*

$\hat{\mathbf{q}}$  is the unit vector in the direction of momentum transfer (a single dimension), and  $\mathbf{q}$  the momentum transfer along it.  $q$  is a single term for momentum transfer in a collision (a scalar unit, not a vector). Where  $\hat{\mathbf{q}} = \mathbf{q}/q$ , this then gives us the term:

$$S_M(\mathbf{q}, \omega) = \frac{M}{q} J_M(y_M, \hat{\mathbf{q}})$$

*Equation 4-6*

$J_M(y_M, \hat{\mathbf{q}})$  is a particularly important term for us- the **Neutron Compton Profile** (so called because it can be considered analogous to the Compton Profile measured in Compton scattering of photons from electrons). In isotropic samples such as liquids all directions are equivalent and the dependence upon the vector dimension  $\hat{\mathbf{q}}$  can be ignored. Finally, the Impulse Approximation as used above assumes that momentum and energy transfer values are potentially infinite, and thus a correction factor must be applied to the IA to account for the non-infinite values of momentum transfer and energy transfer in the experimental system. This correction consists of an extensive series of terms that rapidly become vanishingly small with increasing iterations; as a result, VESUVIO only makes use of the first two terms in the series:

$$J(y) = J_{IA}(y) - \left( \frac{M\langle \nabla^2 V \rangle}{36\hbar^2 q} \frac{d^3 J_{IA}(y)}{dy^3} \right) + \left( \frac{M^2 \langle F^2 \rangle}{72\hbar^4 q^2} \frac{d^4 J_{IA}(y)}{dy^4} \right) + \dots$$

*Equation 4-7*

Where  $J_{IA}(y)$  is the initial Impulse Approximation result,  $\langle \nabla^2 V \rangle$  is the mean value for the Laplacian of the potential energy of the atom, and  $F$  is the force on the atom; given a sufficiently large value of  $q$  all terms other than  $J_{IA}(y)$  could be neglected. In the VESUVIO data analysis routines, only the first and second terms on the right are included in the analysis- the third term is too small to give a statistically significant measurement at present. The term  $\langle \nabla^2 V \rangle$  is fitted as part of the Final State Effects stage of the analysis routine and subtracted from the output data. Experimental testing by the operators of VESUVIO has demonstrated that this correction factor produces values within the expected error range consistent with *Equation 4-7*. It is conventionally assumed that transfer of energy and momenta occur *from* the incoming neutron *to* the stationary atom due to the large gradient between them. In practice, however, there is nothing to prevent transfer in either direction, meaning that scattered neutrons may have either less or more energy/ momentum at the point of detection than at entry to the spectrometer.

The ISIS facility at Rutherford Appleton Laboratories produces a variety of high energy particles in its synchrotron radiation source(s). By accelerating H<sup>-</sup> ions to a velocity of ~0.84c in a 163 metre circumference synchrotron, these ions (produced in cycled pulses around the device) are used to bombard a tungsten block target. This triggers a nuclear spallation process that gives off the high-energy neutrons used for this type of experiment. These pulses of neutrons are then channelled to the two Target Stations- one pulse in five being diverted to Target Station 2. The VESUVIO spectrometer, which is positioned in Target Station 1, therefore receives 80% of the neutron intensity generated while it has access to the beam. It is of note that the use of a carbon target instead generates *pions* which then decay to *muons*, chemically analogous to protons but at 1/9th the mass. These form the basis of muon spectroscopy, another major technique used at ISIS<sup>78-80</sup>.

#### 4-2-2: Neutron Detection on VESUVIO

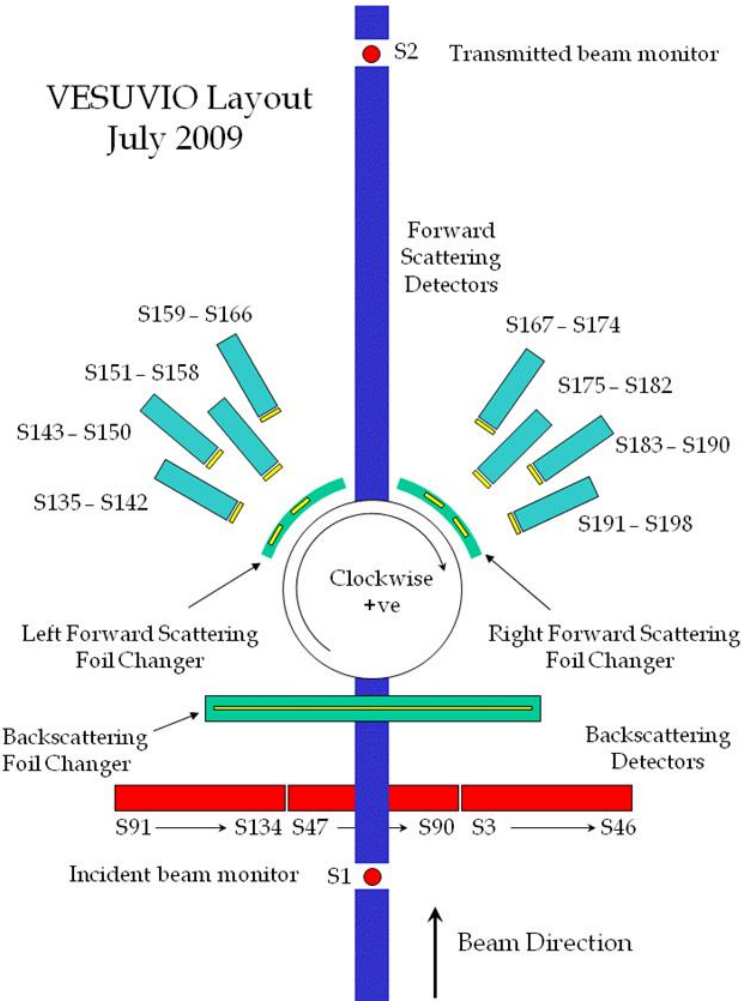


*Figure 4-3: Schematic diagram of the VESUVIO spectrometer, originally presented in system documents for instrument written by Dr. J. Mayers at the ISIS facility at Rutherford Appleton Laboratories (this image specifically taken from the Analysis of VESUVIO Data manual, undergoing revision during 2010).*

Upon reaching the spectrometer the incident neutron beam is directed to strike the target sample. The surface of the aluminium container in the beam path is thin enough (again, approximately 1mm in thickness) to be penetrated by a large proportion of the incoming neutrons. Each atomic species in the beam path scatters the neutrons that strike it, and a representative proportion of these scattered neutrons

continue on to strike one of the array of detectors arranged around the sample chamber; the population fraction that strikes the container and is scattered by the aluminium present is mathematically isolated from the detected population and disregarded, in a similar manner to a conventional infrared background. VESUVIO has an array of 196 detectors arranged about the sample chamber at a range of distances (subject to available space: obviously a significantly large opening is left at the rear of the chamber to admit the neutron beam). 64 detectors are situated in the angular positions to detect forward scattering of neutrons, and 132 in the angles to detect backward scattering. The positions of these detectors do not cover all of the possible scattering angles, but with their exact distance, location and area of coverage known from the construction of the system they allow for the detection of a representative fraction of the scattered neutron density and for an extrapolation of the overall population (see later).

VESUVIO does not directly measure the energy and momentum of each neutron it detects. Instead, each detector in each of the two arrays (132  $^6\text{Li}$ -doped glass scintillator elements in the back angles, and 64 Yttrium Aluminium Perovskite [YAP] doped  $\gamma$ - ray detectors in the forward ones) is covered with a gold foil; this foil absorbs energy from any incident neutron with 4.9eV of energy ( $+/- 0.14\text{eV}$ ) then undergoes a resonant emission of a  $\gamma$ -particle (photon). It is this emitted photon which is then registered by the detector (though the foil does not actually stop neutrons from passing through it, beyond the normal scattering effects). The VESUVIO detectors effectively only measure the **population** and **flight time** of neutrons with **this specific energy**; the rest of the neutrons remain undetected, and are assumed to be distributed about this value.

The VESUVIO system uses two different methods of detection (calibrated to give equivalent results to one another): in the back scattering detectors an older ‘double-difference’ (DD) method is used, where three count measurements are taken for each ‘cycle’, one with no foil (i.e. a ‘zero’ reading with only background  $\gamma$  counts), one with a single foil (foil thickness  $t_1$  and transmission  $T_1$ ), and a third with *two* (foil thickness  $t_2$ and transmission  $T_2$ ). The energy resolution ( $R$ ) of the

spectrometer in a single difference measurement (i.e. one-foil verses no-foil background) is defined by:

$$R_1(E) = 1 - T_1(E) = 1 - \exp(-Nt\sigma(E))$$

*Equation 4-8*

Where  $T(E)$  is the foil transmission at energy  $E$ ,  $N$  is the number of atoms per unit volume, and  $t$  is the thickness of the gold foil used.  $\sigma(E)$ , the nuclear resonance cross sections, have a natural line shape in the form of a Breit-Wigner distribution, which includes Lorentzian wings that make analysis difficult and reduce resolution. With the double-difference technique, the three measurements are assumed to have the relationship:

$$R_2(E) = [1 - T_2(E)] + [\frac{t_1}{t_2}(1 - T_2(E))]$$

*Equation 4-9*

This double-difference technique relies upon the fact that when  $\sigma(E)$  is small:

$$1 - T_1(E) = 1 - \exp[-Nt_1\sigma(E)] \sim Nt_1\sigma(E)$$

*Equation 4-10*

And similarly for the second difference:

$$1 - T_2(E) = 1 - \exp[-Nt_2\sigma(E)] \sim Nt_2\sigma(E)$$

*Equation 4-11*

This means that when the nuclear resonance cross section  $\sigma(E)$  is small,  $R_2(E) = 0$  and the Lorentzian wings of the resolution distribution can be removed from the single difference measurements. The Lorentzian components of the resulting energy resolution functions have a half width at half maximum value of ~0.18 eV.

The second detector set-up, used in the forward scattering angles, makes use of the newer Yttrium Aluminium Perovskite detectors in conjunction with a foil cycling (single difference in-out) method to achieve a similar level of resolution.

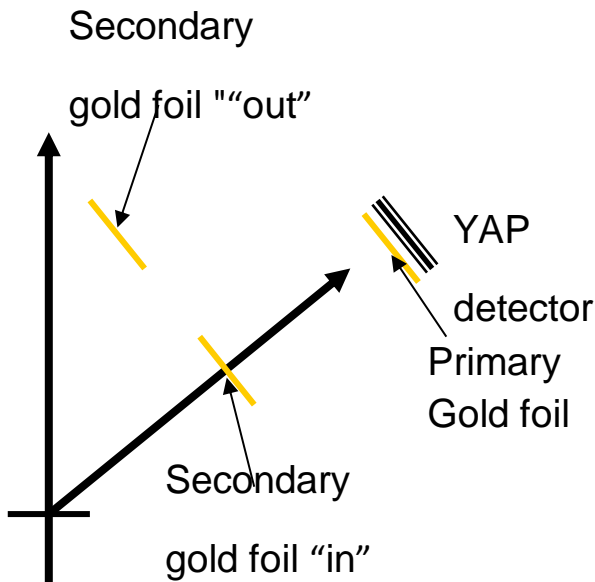


*Figure 4-4: Illustration of the process of cycling the secondary gold foil through the 'in/out' positions. This is repeated many times over a data collection period and helps to correct for detector drift. (This image specifically taken from the Analysis of VESUVIO Data manual, undergoing revision during 2010).*

Similarly to the backward scattering angles, in the forward direction the neutrons must either pass through either one or two gold resonator foils before counting. Without the second foil, neutron detection counts can be calculated as:

$$Y_{out}(E_0, E_1, \theta_1) = Y(E_0, E_1, \theta_1)\mathbf{P}(E_1)\eta + B_{out}(E_0, E_1, \theta_1)$$

*Equation 4-12*

Where  $E_0$  is the energy of neutrons incident to the sample,  $E_1$  is the energy of the scattered neutrons absorbed by the foil, and  $\theta_1$  is the scattering angle. The term  $Y(E_0, E_1, \theta_1)$  is the rate at which scattered neutrons are incident to the primary foil;  $Y(E_0, E_1, \theta_1)$  therefore depends entirely on the incident neutron spectrum; the properties of this spectrum can be mathematically derived from the detected output of the spectrometer and will be discussed later in this chapter.  $\mathbf{P}(E_1)$  is the probability that a neutron of energy  $E_1$  is absorbed in the primary foil, while  $\eta$  is the probability that the subsequent  $\gamma$ -ray emission is registered by the YAP detector.  $B_{out}$  is the  $\gamma$  background count without the secondary foil in place.

The secondary foil is moved into the neutron beam path for the ‘foil-in’ measurement so that the neutrons must pass through both. This secondary foil is also of the same thickness as the primary. As a result, the count rate is reduced by a factor of  $1 - \mathbf{P}(E_1)$ :

$$Y_{in}(E_0, E_1, \theta_1) = Y(E_0, E_1, \theta_1)[1 - \mathbf{P}(E_1)]\mathbf{P}(E_1)\eta + B_{in}(E_0, E_1, \theta_1)$$

*Equation 4-13*

As a result, the **difference** between the two counts (the raw data output from VESUVIO) is:

$$(Y_{out} - Y_{in}) = Y\eta\mathbf{P}^2 + (B_{out} - B_{in})$$

*Equation 4-14*

This data is never actually seen by the user during the operation of VESUVIO, remaining as distinct data files for each detector before being summed and weighted by the system to produce the angle-dependant time-of-flight plots that

are ‘initially’ obtained from VESUVIO. Following this single-difference foil cycling process it can be seen that the majority of the background noise is removed from the  $\gamma$ -ray peak. Using *Equations 4-3 to 4-6* it can be seen that the energy resolution with the YAP detectors approaches a Gaussian line shape, and that the peak has a half width at half maximum value of  $\sim 0.10$  eV.

#### **4-2-3: Generating the Time of Flight Count Data**

The number of neutrons that are registered by the detector subtending (covering) the solid angle (spherical segment)  $d\Omega$  can be calculated from *Equation 4-15*:

$$Y_D(E_0, E_1)dE_0dE_1 = I(E_0)D(E_1) \frac{d^2\sigma(E_0, E_1, \theta_1)}{d\Omega dE_1} d\Omega dE_0 dE_1$$

*Equation 4-15*

This equation describes the number of detected neutrons of a specific energy range. For the purposes of these experiments, the two ranges are between  $E_0$  and  $E_0 + dE_0$  for the incident neutrons at the sample (detected upon entry to the spectrometer), and  $E$  to  $E_1 + dE_1$  at the detector array (the  $4.9 \pm 0.14$ eV neutrons that trigger the resonance in the gold foils). Because detector response is not perfect the actual incident neutron count per unit area is given by the term  $I(E_0)D(E_1)$  to which the registered count is proportionate- the probability of a neutron of energy  $E_1$ . It is known that:

$$\frac{d^2\sigma(E_0, E_1, \theta_1)}{d\Omega dE_1} = |b|^2 \sqrt{\frac{E_1}{E_0}} S(q, \omega)$$

*Equation 4-16*

Where  $S(\mathbf{q}, \omega)$  is defined as the Dynamic Structure Factor as in *Equation 4-3*,  $b$  is the nuclear scattering length and  $\theta$  is once again the scattering angle.  $\omega$  has already been defined as the energy transfer of the collision (essentially the same as  $E_0 - E_1$ ) and the momentum transfer  $q$  can be defined as:

$$q = \sqrt{2m}(E_0 + E_1 - 2\sqrt{E_0 E_1} \cos\theta_1)^{1/2}$$

*Equation 4-17*

Because the particles involved are treated as discrete force fields about a given locus with no interaction or overlap during collisions VESUVIO also makes another fundamental assumption- this time based on classical mechanics: that since all of the neutrons and atoms involved can be treated as hard spheres during collisions in the same manner as in classical mechanics due to the impulse approximation, each particle scatters independently (incoherently). Because it is assumed that no attractive or repulsive forces exist between the neutron and the atom during the high-energy collision, the energy and momentum of the system will therefore be conserved through the impact- a typical ‘classical’ analogy is to describe the neutrons and atoms as ‘billiard balls’, striking one another.

For particles (neutrons) of momentum  $p_0$  before collision,  $p_1$  afterwards, neutron mass  $m$ , atomic mass  $M$ , neutron scattering angle  $\theta_1$ , atomic recoil angle  $\theta_2$  and atomic momenta  $A_0$  and  $A_1$  before and after collision, this conservation of energy and momentum means that the relationship between these properties before and after the collision can therefore be written as:

$$A_1 \cos \theta_1 + p_1 \cos \theta_1 = p_0$$

$$p_1 \sin \theta_1 = A_1 \sin \theta_2$$

$$\frac{p_0^2}{2m} = \frac{A_1^2}{2M} + \frac{p_1^2}{2m}$$

*Equations 4-18, 4-19 and 4-20*

$\theta_0$ , the incident angle of the neutron beam, is by definition zero. The velocity of the outgoing neutrons after scattering,  $v_1$ , compared to the incident velocity  $v_0$  depends on the atomic recoil angle  $\theta_2$ :

$$\frac{p_1}{p_0} = \frac{\cos \theta_1 + \sqrt{(\frac{M}{m})^2 - \sin^2 \theta_1}}{\frac{M}{m} + 1} = \frac{v_1}{v_0}$$

*Equation 4-21*

From these equations we can see that the larger the neutron scattering angle  $\theta_1$ , the greater the momentum transfer to the atom. From the classical model, in the hydrogen case (where the two masses  $m$  and  $M$  are equal) scattering in the backward angles is not possible. VESUVIO is designed to record two distinct types of scattering spectra: forward scattering, where neutrons collide with and are redirected by transfer of momentum to the atoms to angles less than  $90^\circ$  from their original flight path, and back-scattering angles where deflection occurs at greater than  $90^\circ$ . Forward scattering angle detector signals are fitted to account for scattering peaks (in the time domain) caused by all atomic species in the sample, while back-scattering peaks do not include hydrogen because the hydrogen atom nucleus is the same mass as an incoming neutron and is thus unable to recoil directly backwards.

The flight velocity of the neutrons before and after scattering can be calculated as:

$$v_0 = \sqrt{2E_0/m}$$

$$v_1 = \sqrt{2E_1/m}$$

*Equations 4-22 and 4-23*

The total neutron time of flight  $t$  is therefore given by:

$$t = \frac{L_0}{v_0} + \frac{L_1}{v_1}$$

*Equation 4-24*

And the computer processing time is accounted for in the final data plot.

The energy transfer, momentum transfer and time of flight are all intimately related, and by measuring or fixing two, the third may be calculated. For a precisely designed inverse geometry spectrometer  $L_0$  (the beam path length from entering the spectrometer at time  $t_0$ ),  $L_1$  (the beam path length from scattering at the sample to the detector foil) and  $\theta_1$  (the scattering angle) are all known values from the construction of the instrument, meaning that the flight times of the neutrons entering the spectrometer may be precisely calculated (the Time of Flight data, plotted in the time domain against the y-axis **Count Rate at a given time  $Y(t)$** ).

In addition, with the gold foil resonance process functioning as an energy selector only neutrons with the specific energy  $E_R$  are detected ( $D(E_R)$ ). This

definition of energy is why the resolution functions defined by *Equations 4-12 and 4-13* are important, and means that the momentum transfer may be precisely calculated:

$$D(E_1) = D(E_R)\delta(E_1 - E_R)$$

*Equation 4-25*

Since the number of detected neutrons between time  $t$  and time  $t + dt$  may be expressed as:

$$Y(t)dt = \left[ \int Y_D[E_0(t, E_1), E_1] \frac{dE_0(t, E_1)}{dt} dE_1 \right] dt$$

*Equation 4-26*

This may be related back to *Equation 4-15* in the form:

$$Y(t) = 2 \left( \frac{2}{m} \right)^{1/2} \frac{E_0^{3/2}}{L_0} I(E_0) D(E_R) N \frac{d^2\sigma}{d\Omega dE_1} d\Omega$$

*Equation 4-27*

Where  $m$  is the neutron mass,  $N_M$  is the number of atoms of mass  $M$ , and  $\frac{d^2\sigma_M}{d\Omega dE_1}$  is the partial differential cross section for mass  $M$ .

As noted above, in the VESUVIO system it is assumed that (because the neutron wavelength is so much smaller than inter-atomic spacing and because of the neutrons' extremely high energy) the neutrons and atoms can be treated as hard

spheres that collide and scatter incoherently in much the same way they would in conventional mechanics. The number of neutrons detected at a given time  $Y_t$  will be affected if atoms of different mass  $M$  are present in the sample, and the **absolute** count rate can therefore be described by the sum total of the populations of all masses.

#### 4.2.4: Predictions for the Neutron Compton Scattering Profile in the Poly-N-Isopropyl Acrylamide Co-Nonsolvency System

The VESUVIO spectrometer measures the momentum distribution of atoms by "neutron Compton scattering" (NCS): as noted above, the Neutron Compton Profile ( $J_M(y_M, \hat{\mathbf{q}})$ ) is the probability distribution of the momentum component of mass  $M$  along the vector  $\hat{\mathbf{q}}$ ) and is analogous to the Compton Profile measured in Compton scattering of photons from electrons. All samples used in this project were in the liquid state, and are considered to be isotropic in structure (all directions are equivalent in the sample) and the dependence upon  $\hat{\mathbf{q}}$  can be ignored.

It can be expected that a more homogeneous structure in the sample (such as extensive hydrogen bonding) will cause a narrowing in the spread of momentum transfer (i.e. a narrowing of the Neutron Compton Profile for the sample) relative to the same elemental composition in a different, more heterogeneous state. For example, by labelling the sites in our three species expected to undergo hydrogen-bonding with D, we would expect to see significant changes in the momentum distribution for D as the system passes through the Lower Critical Solution Temperature; as the system passes through the LCST and the pNIPAAm precipitates out into its collapsed globule form, the disparity in environment between the deuterium atoms in the polymer (those involved in cluster formation in the CH<sub>3</sub>OD, and those forming the 'hydrogen-bonding' network in the D<sub>2</sub>O) increases. The deuterium in the system has become less structurally homogeneous, and the width of

the momentum distributions is expected to increase as the range of momentum transfer becomes broader. Conversely, the H signal is expected to remain quite similar, as little change is expected in the interactions it experiences during the process of polymer collapse into the globular state. A second experiment would reverse this isotopic labelling and would be expected to show a reversal of these trends, with D remaining largely unchanged and H showing a greater dynamic range, confirming their roles in the mechanism.

The materials used for this experiment were therefore not simply water, methanol and pNIPAAm, but rather H<sub>2</sub>O, D<sub>2</sub>O, CH<sub>3</sub>OD, CD<sub>3</sub>OH and D-pNIPAAm, giving us a variety of target sites of isotopic substitution which may be observed.

# **Chapter 5: Results of Neutron Compton Scattering Study of Mixed Water, Methanol and Poly-N-Isopropyl Acrylamide Systems**

## **5-1: Introduction**

This project consisted of two experimental sessions on the VESUVIO instrument, operated by the ISIS facility at the Rutherford Appleton Laboratory site in Oxfordshire, England, and the analysis and conclusions drawn from those two sets of data. It is noteworthy that, due to a re-evaluation of certain aspects of the data processing procedure, the results initially obtained for the first experiment were later recalculated to give different values.

The procedures described below follow the project in chronological order, and show the actions, results obtained and conclusions drawn at each step. As a result, this chapter is split into three sections: first, the initial experimental procedure, data analysis and modelling from the first experiment (*Section 5-2*), next the equivalent from the second (*Section 5-3*, this time using the refined method of calculation), and third the re-calculated results of the first experiment (*Section 5-4*). The chapter ends with a discussion of the overall conclusions that have been drawn from this work (*Section 5-5*).

## **5-2: Experiment I: Neutron-Scattering Momentum Distribution Study of Deuterated Poly-N-Isopropyl Acrylamide Displaying the Co-Nonsolvency Effect in Mixed D<sub>2</sub>O and CH<sub>3</sub>OD Solvents**

### **5-2-1: The Poly-N-Isopropyl Acrylamide Co-Nonsolvency System**

To briefly summarise the properties of the target system, poly-N-isopropyl acrylamide is part of a class of materials that show an unusual maximum temperature critical value below which they are solvated by aqueous systems (rather counterintuitively referred to as the Lower Critical Solution Temperature, or LCST) above which it spontaneously precipitates out into a collapsed hydrogel structure; conversely, these species are easily solvated by pure methanol at all observable temperatures. It is also observed that the critical temperature is lowered relative to pure water in the presence of a mixed solvent system (i.e. mixed water and methanol are a poorer solvent of pNIPAAm than either one alone), and that this co-nonsolvency effect is observed to reach a minimum temperature value of -7°C at a methanol mole fraction of ~0.35.

Because the unusual behaviour of this system is believed to be the result of competition between the solvating effects of both polar and non-polar clustered groups in the solvent system, a study was made using the VESUVIO inelastic neutron scattering spectrometer to measure the momentum distributions of hydrogen and deuterium populations in this system to see how they change as this system goes through its LCST. More information on this system can be found in *Chapter 4*, along with a description of the predicted polymer interaction with the two solvents.

## 5-2-2: Experimental I

Poly-N-isopropyl acrylamide was synthesised and ion-exchanged (for deuterium at the amide group) by Dr. A. Saeed, working as part of the research group of Dr. A. Mayes at the University of East Anglia.

Samples were prepared for scan time on VESUVIO in the laboratory provided on-site at the ISIS department of the Rutherford Appleton Laboratories facility. Polymer samples were mixed with appropriate quantities of solvent(s) to produce the concentrations listed in *Table 5-1*:

	D <sub>2</sub> O Content	CH <sub>3</sub> OD Content	pNIPAAm Content	
Sample	Mole Fraction	Mole Fraction	Mole Fraction	Temperature of Study (°C)
1	1	0	0	25
2	0	1	0	25
3	0.65	0.35	0	25
4	0.98	0	0.02	25
5	0.98	0	0.02	40
6	0	0.96	0.04	25
7	0.637	0.343	0.02	25
8	0.637	0.343	0.02	-15

*Table 5-1: Mole fractions of components used in production of experimental mixtures for Experiment I*

For those samples that were to be studied below the Lower Critical Solution Temperature, refrigeration was provided by an on-site freezer unit (c.a. -20°C) during short-term storage, and an ice-salt bath while being transported in the sample can (see below) quickly to the instrument.

The samples to be studied were held in a sealed aluminium container, in a square cell of 1mm path length (thickness) and 5ml capacity (sample solutions were injected until overflow in each case). This aluminium case was affixed to the end of a cryostat (~1m in length) and placed in the VESUVIO sample chamber through the access port on the top of the device (the entire spectrometer is held on the ground level, while control, access and operation take place on a first-floor walkway; the sample chamber was vacuum sealed and raised/ lowered to the desired temperature if necessary. Main safety interlocks are operated at the device, but primary computer control is performed from the VESUVIO control cabin some 10m away on the upper floor- this station is able to control the internal environment of the instrument, and shows a real-time plot of data collection as a Time of Flight plot.

A statistically significant result was considered to be obtained after total neutron counts exceeded a combined 900-1000MeV; this process took a period of approximately 18 hours for each sample studied.

### **5-2-3: Results and Analysis I**

Fitting the output of VESUVIO in momentum space involves the deconvolution of several poorly separated time-domain peaks separated by a scale factor of  $\sim 1/\text{Mass}$ , and as a result only the Hydrogen (H) and Deuterium (D) peaks observed are well resolved enough to be considered truly reliable.

Time of Flight results are presented by the system in the form of an x/y plot of time (defined by *Equations 4-22 to 4-24* in *Chapter 4*) verses neutron count intensity (given by *Equations 4-14* and *4-25*) at a specific energy (with the resolution of that energy value defined by *Equations 4-12* and *4-13*, and their equivalents for the forward scattering detectors) of  $4.9 \pm 0.14\text{eV}$ . Data is generated for each of the detectors, weighted for relative intensity, and then combined into the data plots presented here. Since the centre point for the Time of Flight distribution for each atomic species is known from its mass, the data includes fitted distributions for each atomic species present in the sample (defined as part of the input file for the analysis process).

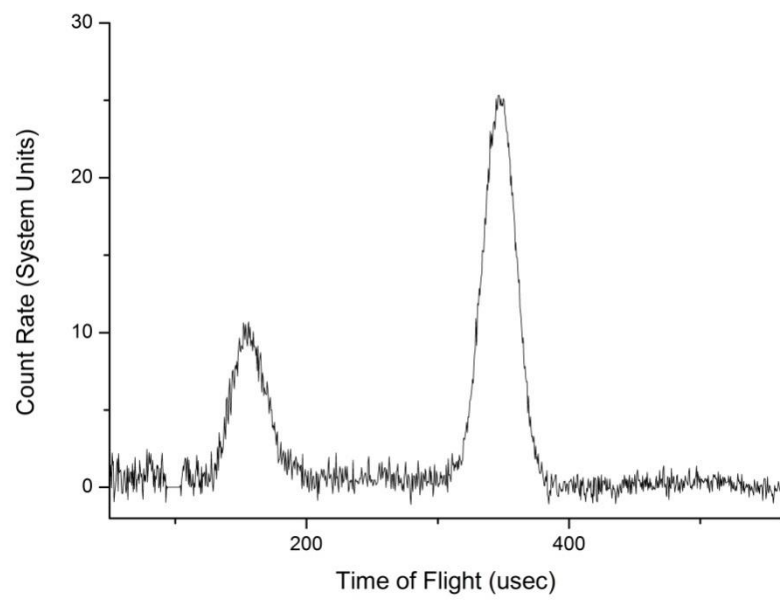


*Figure 5-1: Example raw output for Time of Flight data for backward scattering detectors for pure D<sub>2</sub>O.*

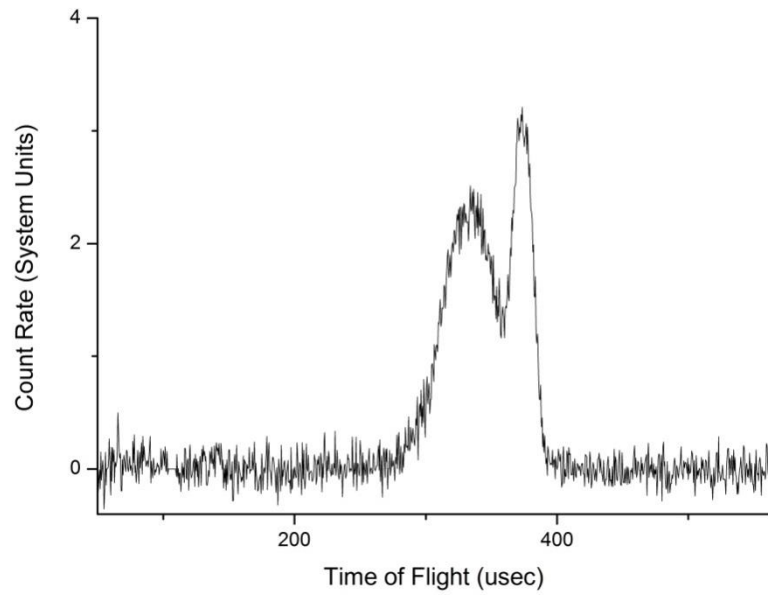


*Figure 5-2: Example raw output for Time of Flight data for forward scattering detectors for pure D<sub>2</sub>O.*

Data, fit and individual components

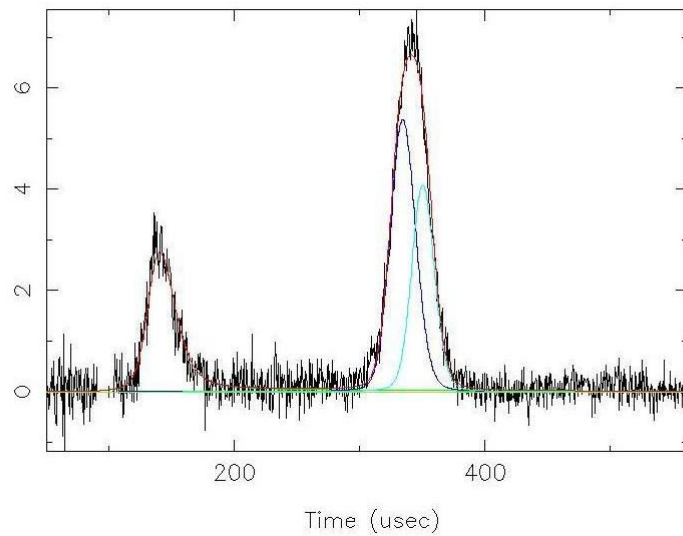


Figure 5-3: Fitted output for Time of Flight data for backward scattering detectors for pure  $D_2O$ . From left to right, peaks are fitted for Deuterium, Oxygen and Aluminium.

Data, fit and individual components

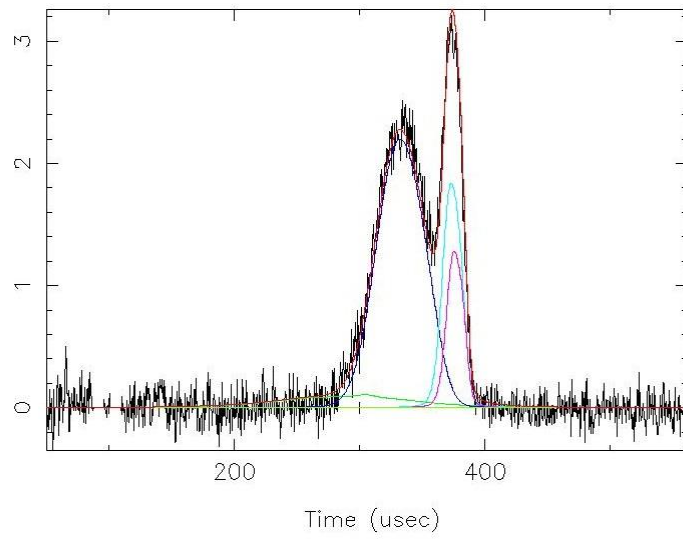


Figure 5-4: Fitted output for Time of Flight data for forward scattering detectors for pure  $D_2O$ . From left to right, peaks are fitted for Hydrogen (which is of negligibly low intensity in this data set), Deuterium, Oxygen and Aluminium.

In order to practically fit the Time of Flight data in the momentum domain, a number of assumptions are required: Firstly, though we have assumed above that terms such as  $L_0$ ,  $L_1$ ,  $\theta_1$  and  $E_1$  are already precisely known from the construction of the instrument, what we actually have is a probability function (i.e. each detector has approximately  $x$  value for each of the four terms). In order to reduce the necessary processing time (as this would require the calculation of a four dimensional integral), the measured neutron count rate is considered as a single resolution function  $R_M(t)$  for each mass:

$$Y_m(t) = \left[ \frac{E_0 I(E_0)}{q} \right] \sum_M A_M M J_M(y_M) \otimes R_M(t)$$

*Equation 5-1.*

The second approximation of the data analysis is that  $J_M(y_M)$  is assumed to have a normalised Gaussian form:

$$J_M(y_M) = \frac{1}{\sqrt{2\pi w_M^2}} \exp\left(\frac{-y_M^2}{2w_M^2}\right)$$

*Equation 5-2.*

*Equations 5-1* and *5-2* define the fitting expression used to fit data in time of flight. The parameters fitted are  $A_M$  (the amplitudes of scattering from each peak), and  $w_M$  (which defines the width of each peak in momentum space ( $y_M$ )). Several of these values can be fixed manually as part of the fitting process (in particular, the amplitudes of the heavy atoms can be fixed by reference to the neutron scattering cross section of the species included in the sample multiplied by their relative population); this produces a more accurate fit for the remaining data peaks in momentum space (hydrogen and deuterium):

Mole Fraction			Temperature (K)	Hydrogen HWHM (Å <sup>-1</sup> )	Hydrogen HWHM Error (+/-Å <sup>-1</sup> )	Deuterium HWHM (Å <sup>-1</sup> )	Deuterium HWHM Error (+/-Å <sup>-1</sup> )
D <sub>2</sub> O	CH <sub>3</sub> OD	pNIPAAm					
1	0	0	298	n/a	n/a	5.376	0.774
0	1	0	298	4.706	0.889	14.196	0.672
0.65	0.35	0	298	4.52	0.756	6.378	0.007
0.98	0	0.02	298	4.4	0.368	5.676	0.173
0.98	0	0.02	313	4.845	0.392	5.364	0.421
0	0.96	0.04	298	4.686	0.87	17.456	0.388
0.637	0.343	0.02	298	4.646	0.889	11.482	0.16
0.637	0.343	0.02	258	4.598	0.796	5.014	0.142

Table 5-2: Experimentally measured widths and errors for momentum distributions of hydrogen and deuterium in each sample.

Gaussian peak Half-Widths can be converted into variance values for the distribution by dividing by  $\sim 1.1775$  ( $\sqrt{2\ln 2}$  to be exact, but this is an irrational number and the approximate value is in common use).

Further analysis of these results, together with how a statistical model was applied to predict their behaviour at different concentrations, is presented below. Following the results presented for Experiment II, however, a modification was proposed to the analysis routine that gives significantly different values for the above Experiment I (presented in *Section 5-3* below), and it is from those results that the final conclusions for this chapter have been drawn.

#### 5-2-4: Analysis and Conclusions I

Our current understanding of the solvated polymer system suggests that as it passes through the Lower Critical Solution Temperature phase change point, the energy of the system overcomes the weak polar bonds holding it in the solvated ‘coil’ phase and causes it to instead switch to the more favourable internal bonding structure of the polymer’s ‘globule’ phase (i.e. undergoing a coil to globule transition)<sup>72</sup>. As a result of this transition, the polymer can no longer be adequately

solvated and precipitates out of solution. The present understanding of the water methanol mixtures demands at least three main environments for the H and D nuclei (pure deuterated water clusters undergoing only polar interactions, pure deuterated methanol clusters undergoing both polar and non-polar interactions, and the aggregate structure(s) that form as they are mixed). Due to the small range of data obtained for the range of samples, it is necessary to use only a single term to describe the resulting Neutron Compton Scattering profile experimentally determined for each of these regions in each of the mixtures; the variance of each momentum distribution  $J_M(y_M)$  (which is assumed to be normally distributed, as noted in *Chapter 4*) was used for this purpose.

By statistical modelling of these momentum distributions, we have derived terms to describe each component region in each mixture. In our experimental data, relative intensity can be calculated from the simple multiplication of the number of atoms per ‘molecular unit’; since the resulting distribution is represented with a Gaussian line shape, the only remaining variable to describe this distribution is its variance (itself a function of the distribution’s width). By considering the system as a combination of variance values, the expected *resulting* variance can theoretically be calculated for any given mixture from the variances of its components, working from the assumption that there is a characteristic variance value for each species on its own. This can be illustrated by considering a two-part mixture in a quadratic form:

$$x^2 + y^2 + 2xy$$

*Equation 5-3.*

Where  $x$  and  $y$  are the two components, weighted for relative mole fraction, each involved in two different environments:  $x^2$  and  $y^2$  where the components are interacting only among themselves (i.e. regions of pure solvent and/ or pure polymer self-interactions), and  $2xy$  for the regions in which the two components are interacting with each other (i.e. the resulting variance values from the standard deviations  $x$  and  $y$  of those regions  $x^2$ ,  $y^2$  and  $xy$ )- further to this, a correlation coefficient ( $\rho$ ) is included in the mixed term as a measure of the relative strength of

the interaction between the two species involved. In the example above,  $\rho$  is considered as having a value of 1 (i.e. the components are governed solely by diffusion and interact freely). In a real system, however, this may not be the case as some interactions may be helped or hindered by the electrostatic potentials and/ or the physical dynamics of the species involved (for example, the collapsed polymer is believed to at least partially exclude methanol in preference to the smaller water molecules). For this reason, each interaction term is also weighted to represent the degree of interaction that occurs.

Obviously these values will be different for each atomic species, but our primary interest is in the deuterium values obtained from each experimental case. The variance of the interacting molecules in the pure solvent cases (pure D<sub>2</sub>O and pure CH<sub>3</sub>OD) is simply a function ( $\frac{2(HWFM)}{2.355}$ ) of the width of the resulting momentum distribution: no significant hydrogen signal exists in D<sub>2</sub>O to measure, but the deuterium variance observed is 4.566. The equivalent values for CH<sub>3</sub>OD are 3.997 and 12.056 respectively.

If we consider a mixture of deuterated water and deuterated methanol at mole fractions of  $C_w$  and  $C_m$  respectively, the observed total variance of the momentum distribution for an atomic nucleus could be represented as a sum of the variances of the individual sites as follows:

$$S_{wm}^2 = C_w^2 S_w^2 + C_m^2 S_m^2 + 2\rho_{wm} C_w C_m S_{wm}^2$$

*Equation 5-4.*

Where  $S_w^2$ ,  $S_m^2$  and  $S_{wm}^2$  are the variances of the water methanol mixture, pure water, methanol and the water/methanol interface, respectively.  $\rho_{wm}$  is a correlation coefficient representing the strength of the dimeric interactions (i.e. hydrogen-bonding between water and methanol molecules).

By writing the results from the experimental reference samples in the quadratic format, we can derive the values for the  $\rho$  correlation coefficients for each interaction:

$$1. \quad S_{wm1}^2 = C_{w1}^2 S_w^2 + C_{m1}^2 S_m^2 + 2\rho_{wm} C_{w1} C_{m1} S_w^2 S_m^2$$

$$2. \quad S_{wp2}^2 = C_{w2}^2 S_w^2 + C_{p2}^2 S_p^2 + 2\rho_{wp} C_{w2} C_{p2} S_w^2 S_p^2$$

$$3. \quad S_{mp3}^2 = C_{m3}^2 S_m^2 + C_{p3}^2 S_p^2 + 2\rho_{mp} C_{m3} C_{p3} S_m^2 S_p^2$$

*Equations 5-5, 5-6 and 5-7.*

The additional terms are subscripted  $p$  to refer to the polymer contribution, and mole fraction values and final variances are subscripted to distinguish their mixture of origin;  $S_w^2$  and  $S_m^2$  are assumed to be known from the experimental values of the pure solvents, and variance values for the sample mixtures can be calculated from the observed HWHM of the VESUVIO output, which is noted in *Chapter 4* as being plotted by the instrument as a Gaussian curve function.

The assumption is made in the calculation of these unknown terms that the  $\rho$  values for each pair of interacting species **remain the same no matter the environment, concentration of components or temperature in which they are found**, allowing them to be considered equivalent across the full range of mixtures. In the case of a mixture of three components, as in the mixture of water, methanol and polymer, the variance of the final distribution  $S_{wmp}^2$  may be written as;

$$4. \quad S_{wmp4}^2 = C_{w4}^2 S_w^2 + C_{m4}^2 S_m^2 + C_{p4}^2 S_p^2 + 2\rho_{wm} C_{w4} C_{m4} S_w S_m + \\ 2\rho_{wp} C_{w4} C_{p4} S_w S_p + 2\rho_{mp} C_{m4} C_{p4} S_m S_p$$

*Equation 5-8.*

By subtracting *Equations 5-6* and *5-7* from *Equation 5-8* we are left with a series of terms that can be expressed in the form  $aS_p^2 + bS_p + c = 0$ , and the value of  $S_p$  solved using the quadratic formula  $S_p = \frac{-b \pm \sqrt{b^2 - 4ac}}{2a}$  where:

- $a = C_{p4}^2 - C_{p2}^2 - C_{p3}^2$
- $b = 2([C_{m4}C_{p4}S_m\rho_{mp}] - [C_{m3}C_{p3}S_m\rho_{mp}] + [C_{w4}C_{p4}S_w\rho_{wp}] - [C_{w2}C_{p2}S_w\rho_{wp4}])$
- $c = (S_w^2[C_{w4}^2 - C_{w2}^2]) + (S_m^2[C_{m4}^2 - C_{m3}^2]) + 2(C_wC_mS_wS_m\rho_{dm}) - (S_{wmp4}^2) + (S_{wp2}^2) + (S_{mp3}^2)$

*Equation 5-9.*

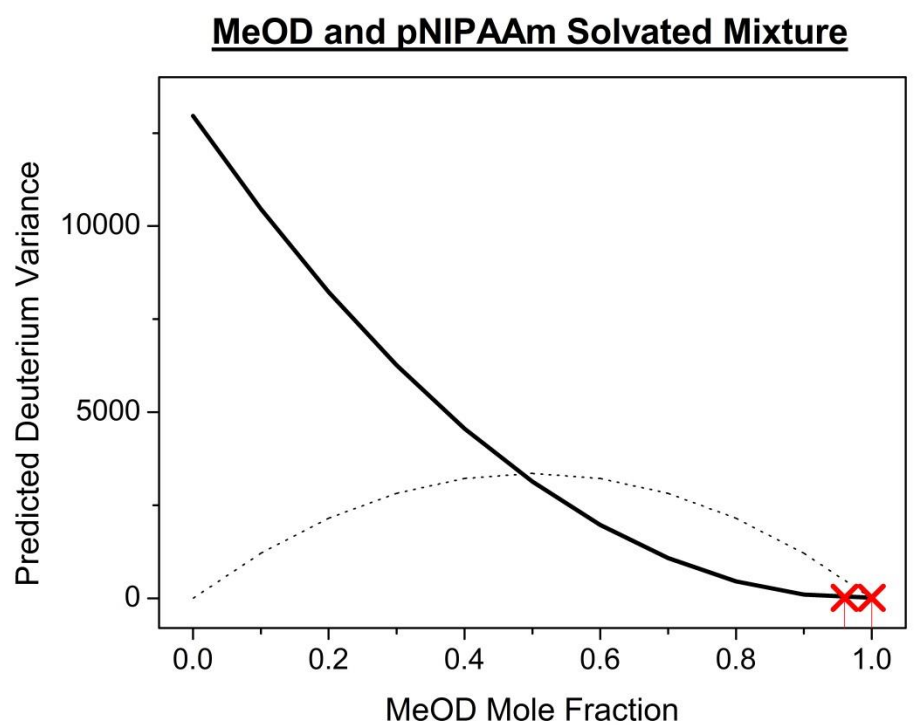
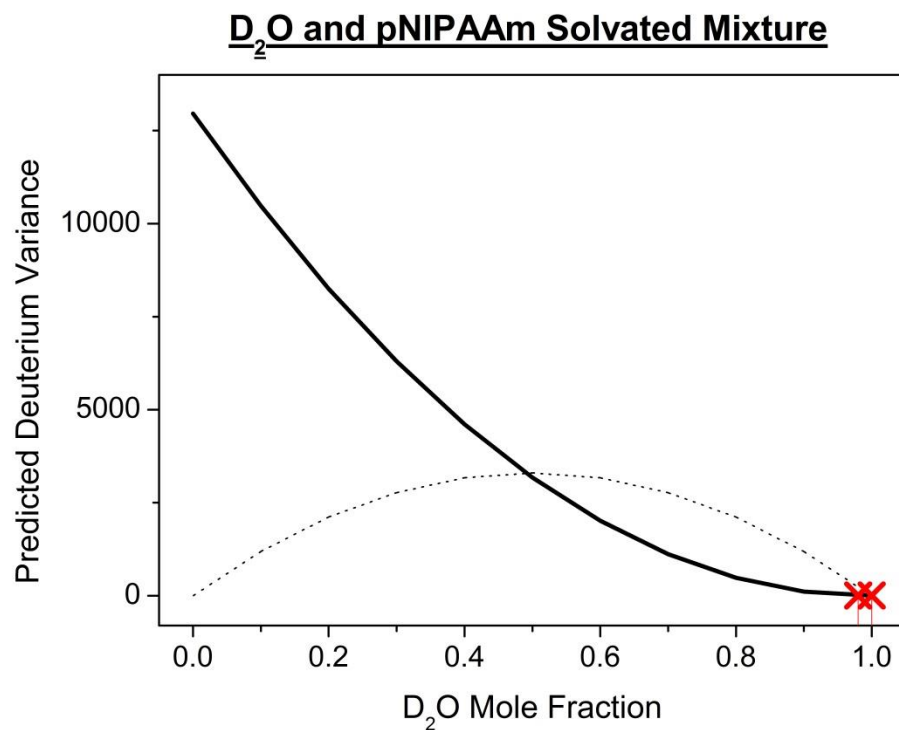
This value can then be re-inserted back into the earlier equations to calculate values for the other correlation coefficients:  $\rho_{wm} = 0.596$ ,  $\rho_{wp} = -0.498$  and  $\rho_{mp} = -0.561$ . That these correlation coefficient values are non-zero implies that a two-population model is insufficient to describe these systems accurately: where populations are completely independent (i.e. there is no mixing between them) one would expect coefficients of zero, while for fully mixed populations one would expect coefficients of 1.

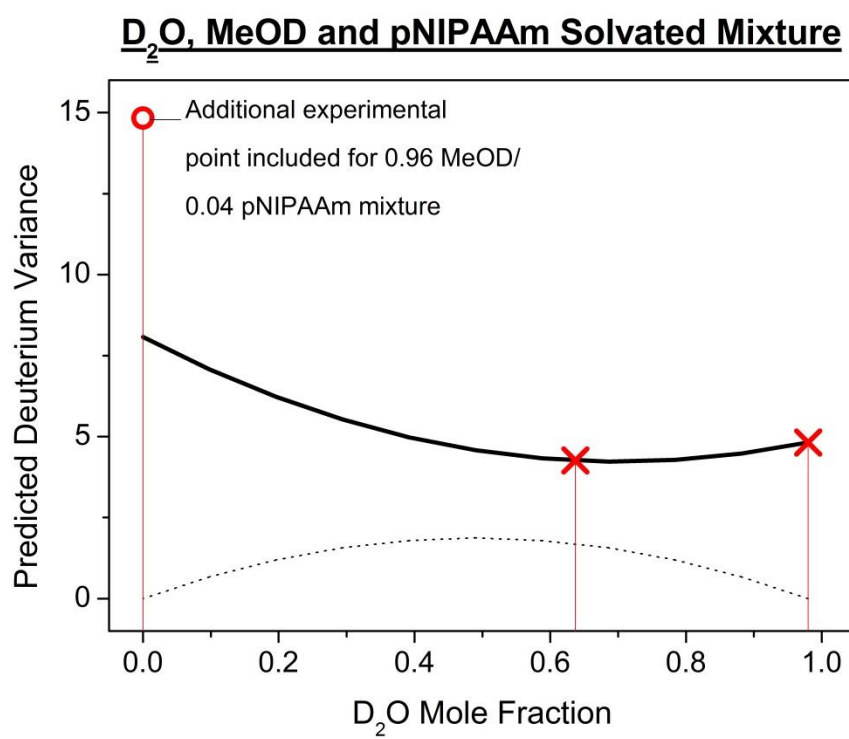
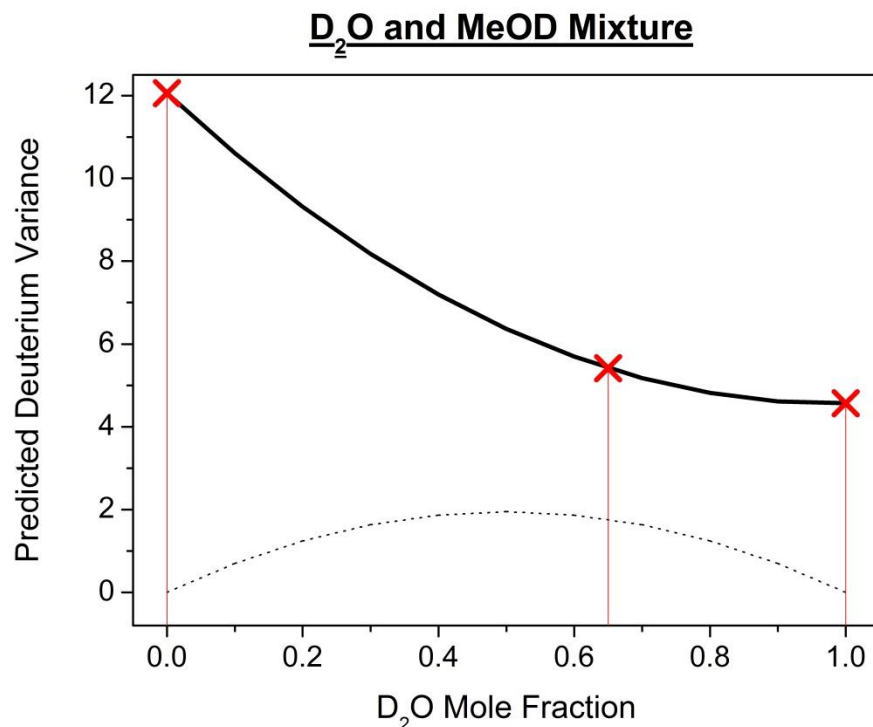
NOTE: It is important to remember that these values cannot be calculated for the non-solvated final mixture, due to the lack of equivalent reference data for non-solvated pNIPAAm.

The observed  $\rho$  values imply that there is a strong (approximately 25%) interdependence between the variances of two interacting species, likely due to the changes caused in the potential wells by heteromolecular (H-D) hydrogen bonding.

The results plotted below in *Figures 5-5 to 5-8* are fitted with quadratic best fit lines: given that pNIPAAm was a minor component, it was initially believed that the behaviour of the system would be dependent primarily on the interactions of the two-component solvent mixture, and these lines were applied to predict its behaviour of the system. In the case of precipitated pNIPAAm (in the two part mixture at

higher temperatures), a departure from the predicted curve was expected with an increase of D<sub>2</sub>O concentration (while the solvated mixture was expected to continue to follow the established trend), though insufficient data points were collected to construct an equivalent plot for the precipitated mixture to test this theory.





*Figures 5-5, 5-6, 5-7 and 5-8: Predicted deuterium momentum variances for component concentrations, experimental points superimposed as crosses. Difference from linear behaviour is shown by the dotted line. Equations of prediction lines are (13208.95x<sup>2</sup> - 26166.47x + 12962.09), (13417.505x<sup>2</sup> - 26367.534x +*

$12962.087)$ ,  $(7.784x^2 - 15.275x + 12.057)$  and  $(7.784x^2 - 10.948x + 8.075)$   
*respectively*

With an increase in the understanding of the dependence of the NCS distribution on the interacting populations in a sample (and with a sufficiently large data set), this technique may be expanded to study more complicated systems such as protein interactions in solvated systems. With this in mind, a second experiment was planned using the inverse labelling of the equivalent molecules to examine the mechanism of solvation and build up a ‘reference library’ of characteristic momentum distribution widths for hydrogen and deuterium in different states of solvation.

## **5-3: Experiment II: Neutron-Scattering Momentum Distribution Study of Deuterated Solvent-Only Systems (Inverse Labelling)**

### **5-3-1: Samples used in Experiment II**

The small number of measurements made in Experiment I limit the ‘characteristic variances’ that can be calculated for each of the components in the solvent-polymer system. In particular, with no equivalent value for  $\text{CD}_3\text{OH}$  (hydrogen bonding to the methanol through hydrogen itself, not deuterium) not enough data was obtained to calculate the equivalent values for hydrogen in the system.

In order to compensate for this limited amount of data the liquid samples chosen for the second experiment deliberately excluded the polymer, instead focusing our efforts on deriving as much information as possible from the solvent mixture(s) themselves. The mixtures used here therefore are those labelled at sites expected to interact as hydrophobic clusters ( $\text{H}_2\text{O}$  and  $\text{CD}_3\text{OH}$ ). By repeating the measurement of  $\text{CH}_3\text{OD}$  from the first experiment a measure of experimental reliability should also be implied (see later), and using additional mixtures of  $\text{D}_2\text{O}$  and  $\text{CH}_3\text{OD}$  allow for the testing of the model proposed in *Section 5-2*.

### **5-3-2: Experimental and Results II**

A further seven solutions were prepared and scanned in VESUVIO using the same method described in *Section 5-2* above. As a complimentary exercise to the first, the solutions this time were produced using a variety of isotopically labelled water ( $\text{H}_2\text{O}$  and  $\text{D}_2\text{O}$ ) and methanol ( $\text{CH}_3\text{OD}$  and  $\text{CD}_3\text{OH}$ ). Unlike the first

experiment, none of these samples required refrigeration since all samples are fully miscible at room temperature and were recorded at a controlled 298K; the only significant difference between Experiments I and II lies in the calculation and subtraction of the multiple scattering effects from the time-of-flight data. Multiple scattering is a significant contributor to the observed signal strength in the VESUVIO system, and is simply the additional signal observed by the detector array caused by neutrons that have scattered from more than one atomic body in the sample: with the assumption of only one scattering event, this then gives a ‘false’ increase in signal intensity at a given time which can then greatly impact the momentum distribution calculated from that time-of-flight data.

The VESUVIO system uses a Monte-Carlo process to calculate the multiple scattering effects in the sample for removal; this means that an iterative process is used to calculate the best fit to the observed data for the contribution in the signal from the multiple scattering effects, and is an entirely mathematical process based on previously observed phenomena (not the sample being studied). Where this becomes important is in the re-examination of data from the first experiment:

- The results reported and analysed in *Section 5-2* were calculated using a series of 10 iterations- typical for most solid crystal samples, and initially expected to be sufficient for this system.
- The results reported and analysed here in *Section 5-3* were calculated using a series of 1000 iterations- 100 times greater than the first.

It is suspected that the use of the faster iterative process incorrectly calculated some of the multiple scattering contributions to be subtracted and inflated a number of the calculated hydrogen and deuterium momentum distribution widths during analysis, leading to inappropriate conclusions.

Other than the use of a longer iterative process to calculate the momentum distributions of each atomic population in the samples, all other procedures were identical to Experiment I:

Sample	Mole Fraction				Temperature of Study (°C)
	D <sub>2</sub> O	H <sub>2</sub> O	CH <sub>3</sub> OD	CD <sub>3</sub> OH	
9	0	0	1	0	25
10	0.25	0	0.75	0	25
11	0.75	0	0.25	0	25
12	0	0	0	1	25
13	0	0.25	0	0.75	25
14	0	0.5	0	0.5	25
15	0	0.75	0	0.25	25

Table 5-3: Mole fractions of components used in production of experimental mixtures for Experiment II.

### 5-3-3: Analysis and Conclusions

Given that the same analysis method is used here (other than the changes noted for the multiple scattering contribution calculation) the results of this second experiment are as follows in *Table 5-4*:

Mole Fraction				Temperature (K)	Hydrogen HWHM (Å <sup>-1</sup> )	Hydrogen HWHM Error (+/- Å <sup>-1</sup> )	Deuterium HWHM (Å <sup>-1</sup> )	Deuterium HWHM Error (+/- Å <sup>-1</sup> )
D <sub>2</sub> O	H <sub>2</sub> O	CH <sub>3</sub> OD	CD <sub>3</sub> OH					
0	0	1	0	298	4.768	0.017	7.136	0.285
0.25	0	0.75	0	298	4.871	0.017	6.305	0.243
0.75	0	0.25	0	298	4.761	0.018	6.198	0.072
0	0	0	1	298	4.685	0.032	6.319	0.071
0	0.25	0	0.75	298	4.613	0.023	6.267	0.087
0	0.5	0	0.5	298	4.670	0.017	6.415	0.128
0	0.75	0	0.25	298	4.683	0.016	6.967	0.233

Table 5-4: Results of Experiment II generated using the revised data analysis process.

As can be seen in *Table 5-4*, the calculated momentum peak widths are significantly different for the pure CH<sub>3</sub>OD sample (Sample 9) from the original value (retroactively labelled Sample 2 in *Table 5-2*). The resulting deuterium variance is calculated (using the procedure described in *Section 5-2-4*) as 6.060, less than half the equivalent value from the first experiment's results. The model

developed to describe the results of *Section I* of this chapter predicts a deuterium variance of 4.98 for a D<sub>2</sub>O mole fraction of 0.75, and 8.74 for a mole fraction of 0.25 when the solvent is mixed only with CH<sub>3</sub>OD (based on the experimental points for pure D<sub>2</sub>O, pure CH<sub>3</sub>OD and the 0.65 D<sub>2</sub>O mole fraction mixture). The results shown in *Table 5-4* are within the cumulative experimental error for the measurement of the 0.75 sample (a prediction of ~5.01 compared to an experimental value of 4.894), but significantly different from the experimental value for the 0.25 mole fraction mixture (8.76 compared to 5.355).

This difference in the observed values for deuterium in CH<sub>3</sub>OD under ostensibly the same conditions implies that either the data treatment process used was insufficient, or there is too great a degree of experimental uncertainty to produce a repeatable measurement (the calculated experimental error value remains an unknown quantity if this is true). Before attempting to extract further ‘characteristic variances’ from this data, the decision was made to re-examine the obtained momentum peak widths from Experiment I using the same revised analysis procedure used for the results of Experiment II to see if the resulting peak widths for the two CH<sub>3</sub>OD samples were in fact within experimental error margins of each other.

## 5-4: Re-analysis of Data from Experiment I Using the Revised Multiple Scattering Calculation

### 5-4-1: Results and Analysis

With the revision of the multiple scattering correction process, the time-of-flight data from Experiment I was re-examined at the same time as the equivalent processing was performed:

Mole Fraction			Temperature (K)	Hydrogen HWHM (Å <sup>-1</sup> )	Hydrogen HWHM Error (+/- Å <sup>-1</sup> )	Deuterium HWHM (Å <sup>-1</sup> )	Deuterium HWHM Error (+/- Å <sup>-1</sup> )
D <sub>2</sub> O	CH <sub>3</sub> OD	pNIPAAm					
1	0	0	298	-	-	5.829	0.042
0	1	0	298	4.772	0.016	5.987	0.360
0.65	0.35	0	298	4.721	0.019	5.777	0.126
0.98	0	0.02	298	4.646	0.080	5.766	0.068
0.98	0	0.02	313	4.697	0.089	5.779	0.069
0	0.96	0.04	298	4.807	0.014	4.730	0.510
0.637	0.343	0.02	258	4.728	0.017	5.584	0.133
0.637	0.343	0.02	298	4.771	0.018	5.706	0.133

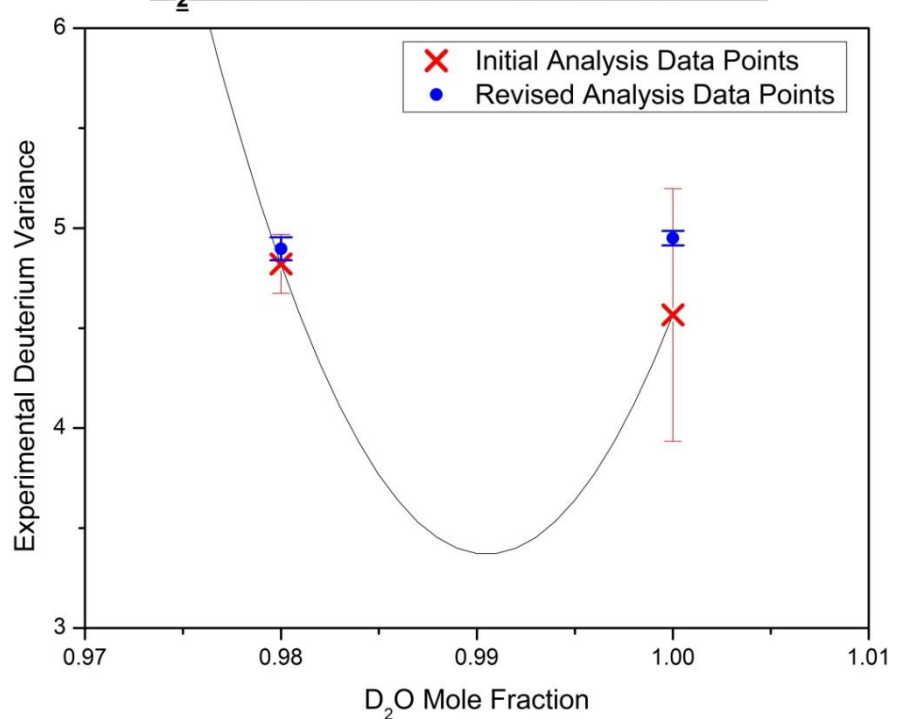
*Table 5-5: Results of Experiment I re-analysed using the revised data analysis process.*

As can be seen from *Tables 5-4* and *5-5*, a significant difference is seen between the calculated momentum distribution widths for deuterium in CH<sub>3</sub>OD in the two experiments. With the recalculation of the multiple scattering effects these two values should theoretically be identical; in experimental practice each should fall within the quoted error value for the other. *Figures 5-9, 5-10, 5-11* and *5-12* show the recalculated variance values (using the revised method) for the samples from Experiment I plotted on the same scales as the original calculated values from *Section 5-2-3* along with the original predicted fit lines first shown above. *Figures 5-13, 5-14, 5-15* and *5-16* show the variance values calculated from the results of

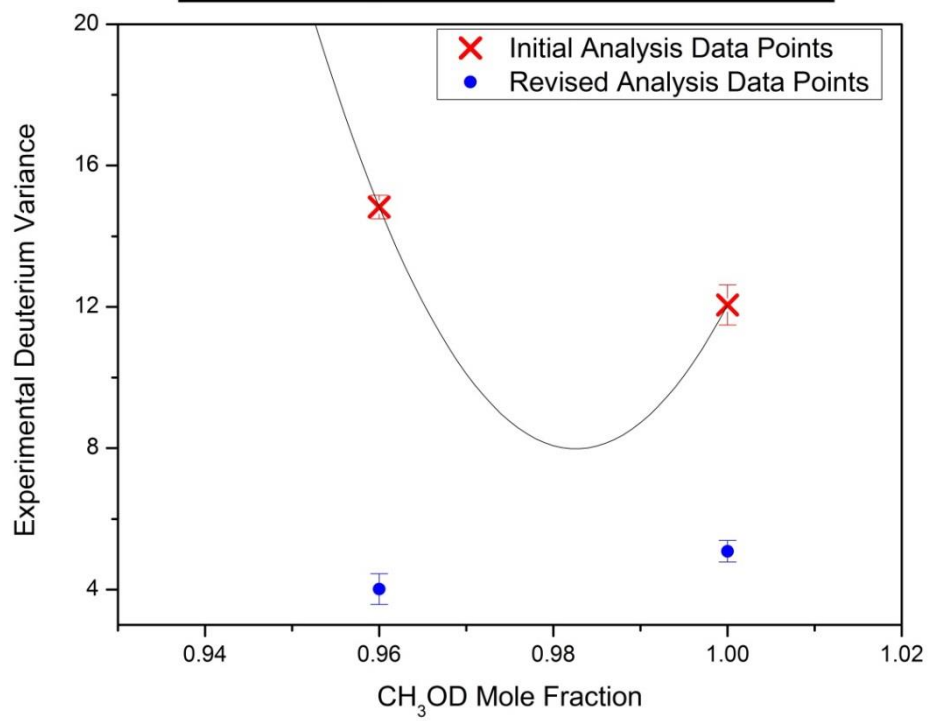
Experiment II only (again, using the revised method); these points are fitted with quadratic best-fit curves (weighted by error, in the cases where more than three points are present) to show the apparent trends in the data.

Were the data completely reproducible (see below), and if the system displayed the expected behaviour of hydrogen bonding interactions, we would expect to see similar behaviour in the best-fit lines for the hydrogen and deuterium signals in opposite sample sets (i.e. the –OH samples' hydrogen would be expected to display similar behaviour to the –OD samples' deuterium distribution); the fact that this similarity is not obvious between the data sets implies that either the system is not at all well represented by the quadratic model we have attempted to use, or that the measured data is inconsistent.

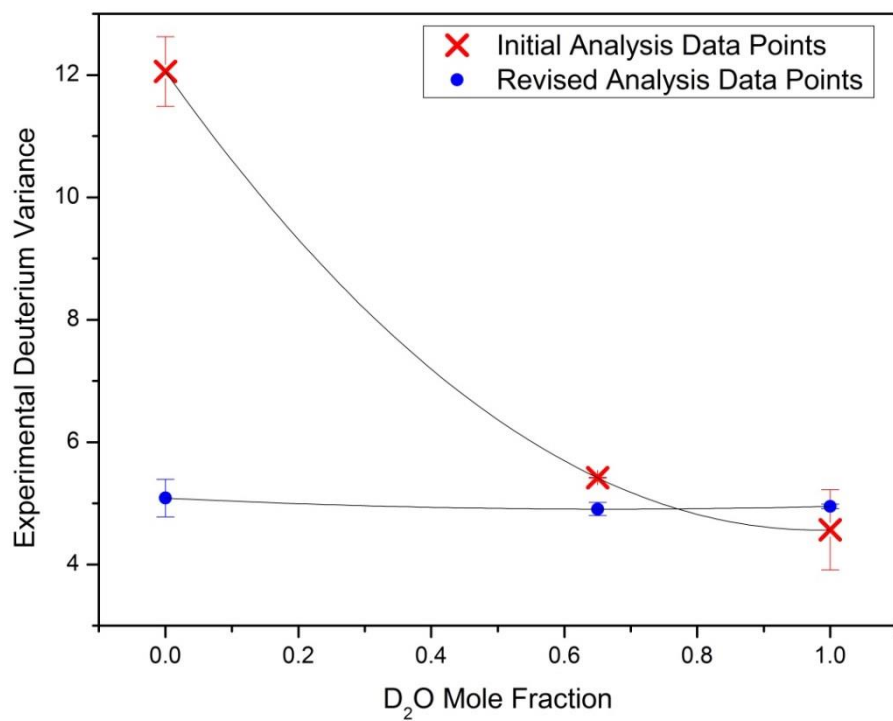
### D<sub>2</sub>O and pNIPAAm Solvated Mixture



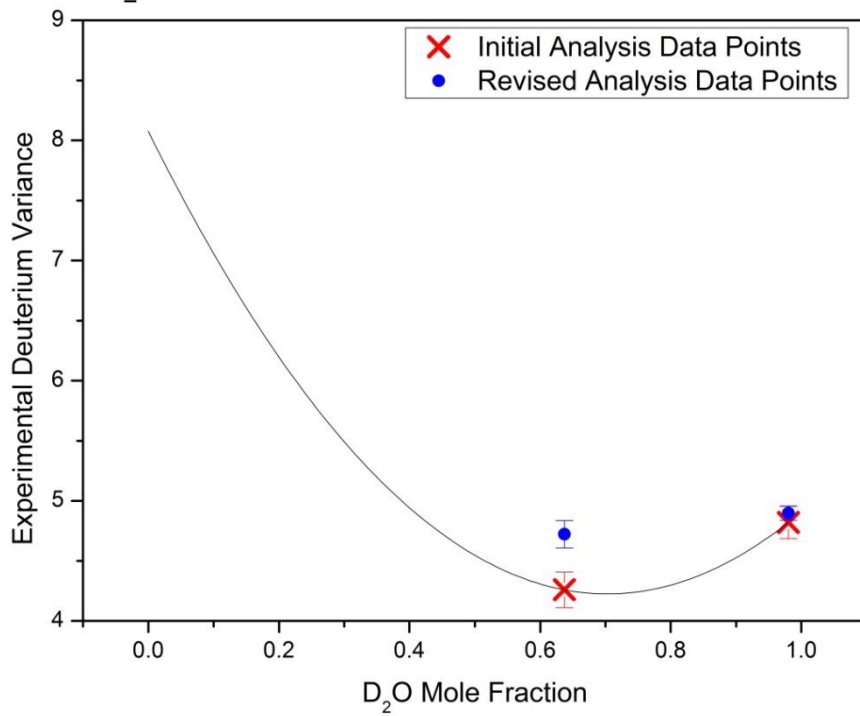
### MeOD and pNIPAAm Solvated Mixture



### D<sub>2</sub>O and MeOD Mixture



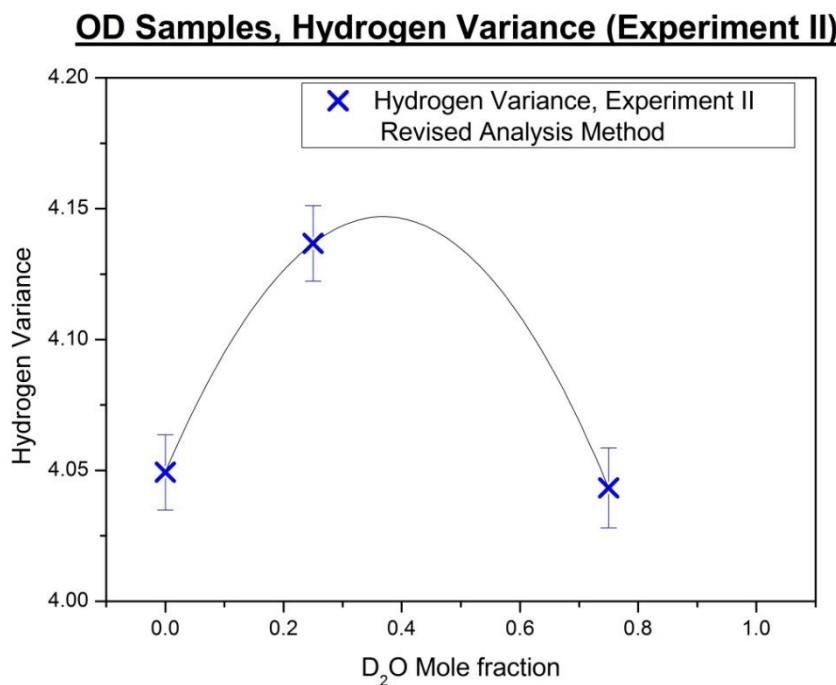
### D<sub>2</sub>O, MeOD and pNIPAAm Solvated Mixture



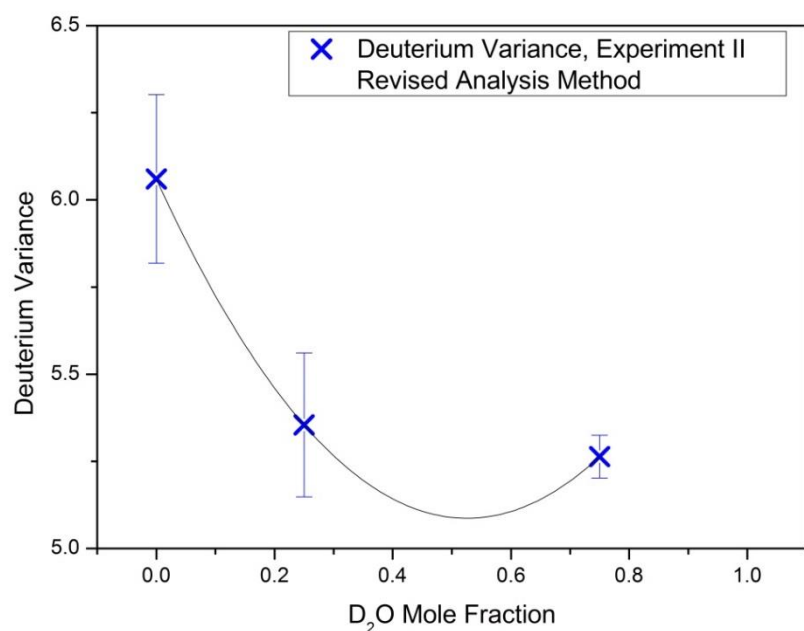
Figures 5-9, 5-10, 5-11 and 5-12: Revised data points for the deuterium variances calculated from Experiment I. Predicted deuterium momentum variances from the original model are displayed to show deviation from the expected values (these prediction curves have the same parameters described in Figures 5-5 to 5-8 earlier).

As before, the data points displayed on *Figures 5-9* to *5-12* above are a quadratic fit to the experimental data points (the first four also reproduce the fit lines and data from *Figures 5-5* to *5-8*). These plots illustrate the differences observed between the initial and re-analysed data for the first experiment.

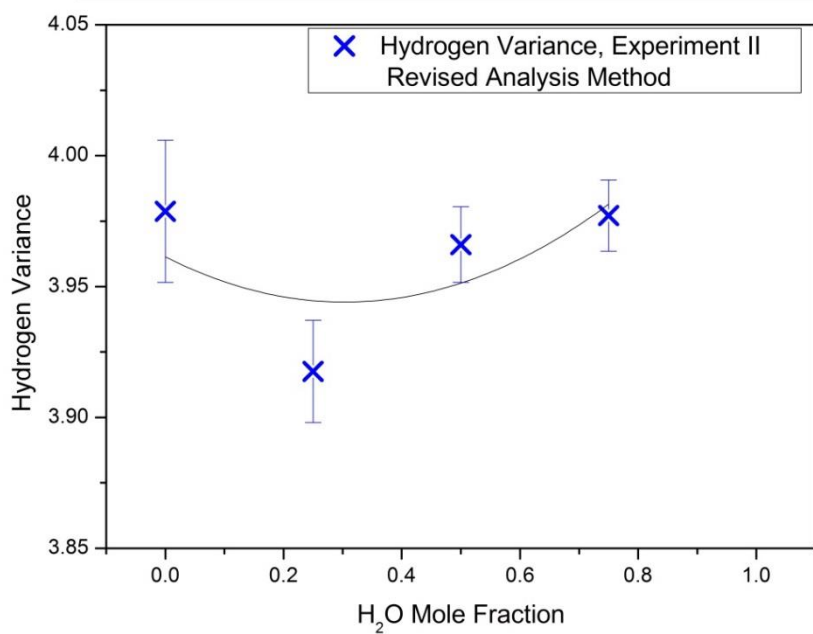
The second set of four figures (*Figures 5-13* to *5-16*) display equivalent data from the water-methanol only mixtures used in the second experiment, both deuterium and hydrogen signals. Properly confirmed, these quadratic relationships should form the ‘baseline’ data from which the momentum distributions observed in the co-nonsolvancy system deviate.



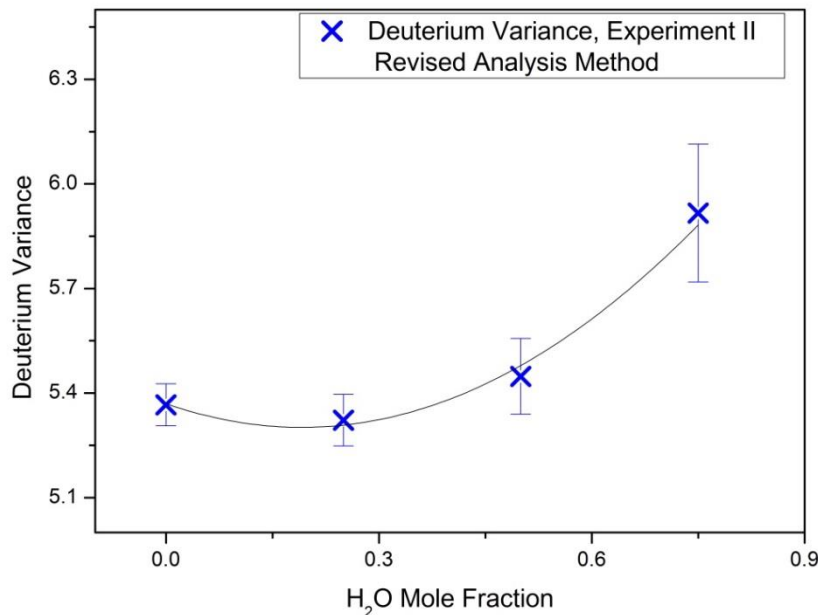
### OD Samples, Deuterium Variance (Experiment II)



### OH Samples, Hydrogen Variance (Experiment II)



## OH Samples, Deuterium Variance (Experiment II)



*Figures 5-13, 5-14, 5-15 and 5-16: Data points for the hydrogen and deuterium variances calculated from the -OD and -OH samples used in Experiment II. Equations of the best-fit lines included are ( $x^2 - 26166.47x + 12962.09$ ), ( $13417.505x^2 - 26367.534x + 12962.087$ ), ( $7.784x^2 - 15.275x + 12.057$ ) and ( $7.784x^2 - 10.948x + 8.075$ ) respectively.*

### **5-4-2: Conclusions**

$\text{CH}_3\text{OD}$  samples were taken from fresh bottles ordered from the Sigma-Aldrich online catalogue for both experiments, and showed no signs of having been opened or tampered with in any way. No observable difference exists between the two sample materials or their treatment, thus the most probable source for this difference in magnitude is the data treatment process itself. As can be seen from the tables, the error values calculated for hydrogen are notably smaller than those for deuterium in the samples of lowest deuterium concentration. The calculated error depends greatly on the intensity of signal available (proportionate to the greater inelastic scattering cross section of hydrogen compared to that of deuterium), and the

fact of overlap between the two species means that the weaker is frequently swamped by intensity from the first. Although the VESUVIO system is designed to extrapolate the necessary momentum distribution data from only one side of the Gaussian curve it remains that this is effectively a reduction in available detector signal points, and one which increases the error of the calculated curve even further and has a proportionately inverse effect on the quality of the hydrogen<sup>9</sup>.

Without a well-defined, repeatable measurement for each of the samples, making statistical predictions for complex mixtures becomes a difficult prospect. This model was initially constructed based on the assumption that each species had a characteristic momentum distribution based on the environment in which it was held; without such reliable measurements accurate values for the other properties of the system cannot be calculated. Taking *Equation 5-4* and inputting the various deuterium values obtained from the re-evaluation of Experiment I only, a correlation coefficient of **0.960** is obtained.

However, using the D<sub>2</sub>O from Experiment I, CH<sub>3</sub>OD from Experiment II and the measured variances of the mixed solvent systems in Experiments I and II (revised calculation method) yields σ correlation coefficient values for D<sub>2</sub>O and CH<sub>3</sub>OD variously of **1.147** (using the variance of the 0.65 D<sub>2</sub>O mole fraction Sample 3 from Experiment I), **1.221** (using the variance of the 0.75 D<sub>2</sub>O mole fraction Sample 11 from Experiment II) and **0.842** (using the variance of the 0.25 D<sub>2</sub>O mole fraction Sample 10 from Experiment II). In the two-component system we have modelled, these correlation coefficients cannot have a magnitude greater than 1. In addition, the fact that two measurements that should be of identical material (the CH<sub>3</sub>OD) are different means we cannot be certain which of these values is appropriate, and either the model is incorrect or the data still has an unacceptable level of error.

Given the fundamental nature of these values in determining the parameters for the system, at this time we cannot determine how well the model represents the

behaviour of the species involved without data points confirmed to be more reliable for each measurement.

*Figure 5-11* shows the clear difference in the quadratic fit between the results obtained for solutions containing mixtures of D<sub>2</sub>O and CH<sub>3</sub>OD in Experiment I and Experiment II:

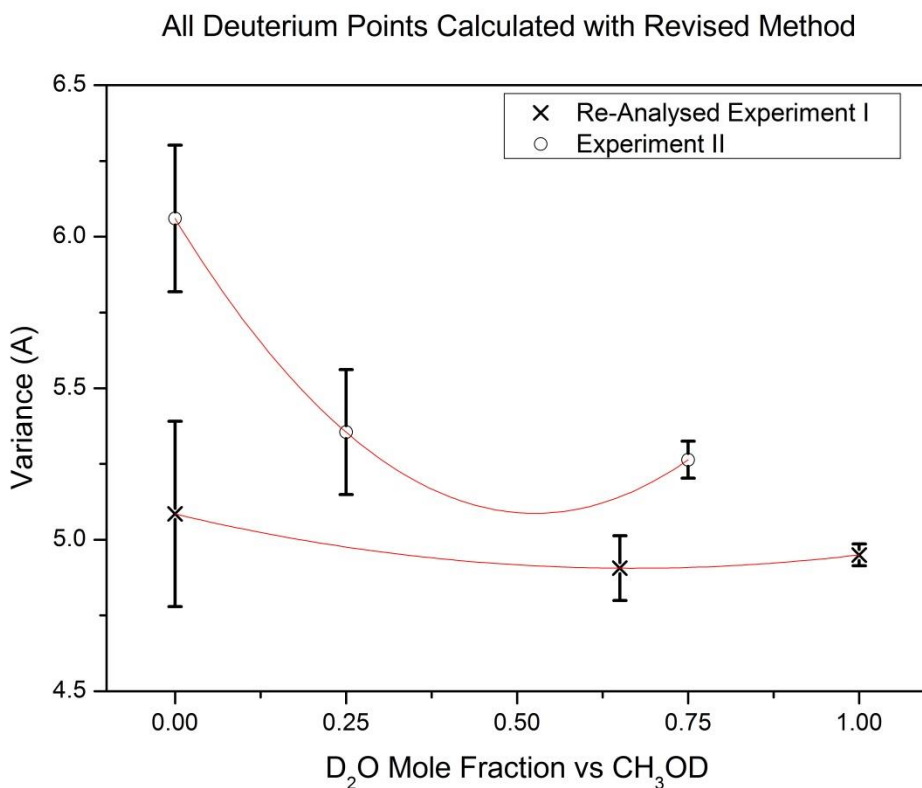


*Figure 5-17: Overlaid deuterium momentum variances (with error bars) for re-analysed Experiment I versus Experiment II. The differences between the two data sets can clearly be seen to be greater than the calculated experimental error for the system. Each data set has its own polynomial best-fit line (analogous to the predictions in Figures 5-6 to 5-9: These lines are: for the re-analysed Experiment I data ( $0.401x^2 - 0.536x + 5.085$ ); for the Experiment II data ( $3.517x^2 - 3.699x + 6.06$ ).*

With regard to the co-nonsolvency properties of the system explored in experiment I, it can be seen from the deuterium results for the 0.02 mole fraction pNIPAAm in D<sub>2</sub>O and for the final mixture of all three components that no significant change is observed with the crossing of the LCST value in the first experiment outside of the quoted experimental error values. Conversely, the hydrogen signal in the final mixture (which is expected to change less than the deuterium) *does* show a slight broadening. It appears that the error introduced in each step of the calculation process results in an unacceptably high degree of uncertainty in these measurements, and a categorical determination of whether the phase change caused by the co-nonsolvency effect has a visible effect on the Neutron Compton Scattering Profile cannot be made at this time.

In theory, this experimental procedure would still be effective in cases where large proportions of the hydrogen positions in a sample are labelled with deuterium, for example if you were to examine CD<sub>3</sub>OH mixed with either H<sub>2</sub>O or D<sub>2</sub>O across a range of concentrations. The decreased deuterium concentration in H<sub>2</sub>O-dominated samples would increase the error, but by maximising the exposure time for each sample this could be minimised to practical levels.

## **5-5: Final conclusions about the system and future development on VESUVIO.**

This investigation consists of two experiments, but *three* discrete sets of data analysis. After extensive consultation with the instrument scientists in charge of the VESUVIO system refinements were made to the analysis process that improved upon the reliability of the calculated results, which provoked the re-examination of the data from our first experiment (these results are thus also presented below). This new data does not directly support our original model; however neither does it disprove our predictions. Rather, it strongly suggests that the experimental accuracy/reliability of the VESUVIO system is not yet at a level where the desired measurements can be made accurately enough to distinguish changes in bulk properties of the magnitude we would expect to see.

The VESUVIO system has been reported as giving very precise measurements to within a small experimental error value for solid crystal systems, but from the results obtained differences observed between the two experiments detailed here imply that the reproducibility of such measurements on liquid systems (particularly those containing mixed signals from both hydrogen and deuterium) is much lower. This is a case of the classic difference between accuracy (small experimental error) and reliability (small spread of results): though the system may quote a relatively small experimental error, the actual value obtained may not be properly reproducible. Although the principle of measuring the change in momentum distribution through inelastic neutron scattering is theoretically sound, what is required to make such measurements on the VESUVIO instrument practical is a series of repeated measurements to quantify the reproducibility of results for such samples, and an attempt to improve the system stability as much as possible before this technique is attempted on a larger scale. Until reliable measurements can be made, the changes in atomic momentum distribution are not yet possible to effectively predict for solvated systems with very low concentrations of isotopic species, making the targeted labelling of specific sites impractical but not

impossible. Proposed changes for the VESUVIO system include updating the remaining detector array to include more YAP units<sup>81</sup>, increasing the number of signal counts proportionately, but such changes carry a significant financial weight and have yet to be implemented. Our beamtime for these experiments at the Rutherford Appleton Laboratory facility was limited, and in an effort to make the best use of it a wide variety of samples were exposed to neutron counts perhaps more suited to solid crystal samples. By taking the combined two weeks of beam access and dividing it between just four samples with three to four times the exposure time (instead of the fifteen that were studied here), a far more robust and reliable data set might be achieved over a smaller range (for example, the D<sub>2</sub>O and CH<sub>3</sub>OD mixtures).

This study demonstrates well that although the determination of detailed structural properties of complex interacting molecular systems (such as the solvation of pNIPAAm by deuterated methanol and water) is a difficult undertaking using the VESUVIO instrument, the data obtained by the measurement of the momentum distributions of labelled sites/ species in the system is potentially very rewarding. It can also be seen, however, that the data obtained exposes certain issues of practical reproducibility in the instrument when attempting to observe changes in small momentum values in such heterogeneous liquids. Such problems must be resolved before Neutron Compton Scattering as performed on VESUVIO can be properly employed to describe the interactions of the components of the solvated system, or for study to move on to even more complex systems such as solvated proteins (which share many of the same chemical characteristics as the pNIPAAm system, albeit on a much larger scale).

**Part Four:**  
**Conclusions**

## Chapter 6: Final Conclusions

The key feature of isotopic labelling, seen in both the simulated data predictions for the infrared spectra described in *Chapters 3a* and *3b*, and in the experimental results of the Neutron Compton Scattering work detailed in *Chapter 5*, is the ability to distinguish populations of atoms that would otherwise be identical to most common forms of interrogation without making significant chemical changes to the species involved. At its most basic level, labelling compounds with isotopic species is an extremely robust method of analytical science with many advantages in the way that such atoms can be introduced (either during synthesis or by later exchange processes) into the target molecules. These labels can be used to derive structural information, not just in examination of the stable species but also by allowing the observer to follow reaction pathways in a system.

As with all spectroscopic signals, the effectiveness of isotopes in distinguishing labelled signals depends greatly on the detection limits, resolution and reproducibility of the results produced by the instrument. Even when artificially introduced into a system however isotopes may still have a relatively low abundance; when the detection of an isotopic population in a sample relies on the natural intensity of such species it is entirely possible that the signals they generate will approach the limit of detection for the instrument being used. This can be seen to have a significant impact on the results of the co-nonsolvency investigation described in *Chapter 5*, where the limit in signal strength and overlap in the Time-of-Flight data of hydrogen and deuterium contributes directly to the uncertainty of the measurement at the neutron count levels used. Concurrently, it is not expected that the labelling of species with isotopes of heavier atoms (i.e.  $^{13}\text{C}$  or  $^{18}\text{O}$ ) would produce useful results: with the increase in mass of the bodies from which they scatter, the detection times of the selected-energy neutrons converge, and the overlap of such peaks in the Time-of-Flight data would render them near indistinguishable.

Assignment of isotopic effects can be difficult, particularly in systems that show multiple signal splitting effects from other sources (such as the expected splitting of signal intensity in the Matrix Isolated Infrared spectra, both experimental and simulated in *Chapters 1, 3a* and *3b*). Locating the source of fine structure arising from multiple splittings is largely a matter of patience, changing single variables in the system until the exact structure is known. Relative noise in a spectrum competes with the intensity of many of the weaker signal peaks in the isolated phase, making a longer scan time (to minimise noise as far as possible) desirable. The determination of matrix packing effects on the system has been considerably more difficult than first anticipated: it was originally believed that the comparatively large size of vanillin relative to the single argon atoms used to form the matrix would limit the impact of such effects, but the results of *Chapter 1* strongly suggest that this is not the case. The full determination of such properties in the matrix isolation work presented here was not possible with the time and resources available to this project, but now that the experimental method has been refined to the level where isolated species can be reliably produced, such isotopic labels may be introduced in various positions and population levels to determine the ‘ownership’ of fine structure in the resulting spectra, be it due to isotopic species or matrix packing effects.

Though beyond the scope of the investigation presented in this work, the use of Matrix Isolation also offers the possibility of using the physical properties of the matrix to control reactions and transformations within it<sup>82</sup>. In principle, it is entirely possible to add an isotopic marker to a functional group on one of two reactive analytes held in a matrix, and use a temperature-controlled annealing process to allow them to react while physically limiting the rate at which they do so; the ability to re-solidify the matrix would allow the detailed monitoring of the reaction process (identifying possible transition states and the like), while the isotopic label would provide the ability to track specific atoms through the reaction scheme. Clearly, though, this matrix would need to be one of sufficiently high reactant concentration for the two to interact chemically in significant proportion- not a true case of Matrix

Isolation, but another application of similar principles. Regardless, the use of annealing to allow limited diffusion of analyte through the matrix is a useful property, and whether or not one observes changes in the IR spectra upon heating can support (or deny) the assertion that a true isolated state has been obtained.

Reliability is the key in regard to the future development of Neutron Compton Profile studies on the VESUVIO instrument<sup>81</sup>. Up until now the VESUVIO system has been used to only a limited degree on liquid samples, or on simple samples containing both hydrogen and deuterium signals- the water, methanol and pNIPAAm system has both attributes, making it a much more complicated case.. As the system stands now, our data is not sufficiently reproducible to draw any significant conclusions about the change in momentum distribution width as the system passes through the polymer phase change temperature, but even if there is no actual change in the Compton Profiles of the hydrogen and deuterium with precipitation of the polymer (an extremely unlikely conclusion, given the predicted changes in inter/ intramolecular binding interactions), with more reliable measurements this technique promises interesting applications with the labelling of species even in static solutions of mixed labels.

In order for the techniques discussed in this work to be effective, reliability is paramount. This means that, in addition to the improvement of detector sensitivity and resolution, the most important factor in the improvement of quality of results is the increase of relative scan time to minimise uncertainty in the final measured value. Should this be accomplished, the way will be open for the prediction and measurement of a wide variety of targeted properties in systems.

## References

Below is presented a complete list of all sources referenced during the production of this thesis, whether or not directly linked to the main text:

1. E. Tenailleau, et al., *Anal. Chem.* 2004, 76, 3818-3825
2. N. Acquista, E. Pyler, *Journal of the Optical Society of America*, 43, 11, 1953
3. Chemical Summary for Vanillin, CAS No. 121-33-5, 1996
4. L. Jiang, Q. Xu, *J. Phys. Chem. A*, 2009, 113 (13), 3121-3126
5. Vibrational Analysis in Gaussian- J. Ochterski, 1999
6. DFT Basics, New Trends and Applications- Kohanoff and Gidopoulos, *Handbook of Molecular Physics and Quantum Chemistry, Volume 2, Part 5, Chapter 26, pp 532–568, John Wiley & Sons, Ltd, Chichester, 2003*
7. The Fundamentals of Density Functional Theory (revised and extended version)- H. Eschrig, *Institute for Solid State and Materials Research Dresden and University of Technology Dresden*.
8. T Egawa , A Kameyama, H Takeuchi, *Journal of Molecular Structure* 794 (2006) 92–102
9. J. Mayers, *Analysis of VESUVIO Data Manual*
10. VESUVIO Instrument Paper- J Mayers and G Reiter
11. VESUVIO Project Final Report, 2002
12. W. Marshall, S. W. Lovesey, *Theory of Thermal Neutron Scattering, Oxford Clarendon Press 1971*
13. S. Lovesey, *Theory of Neutron Scattering from Condensed Matter Vol. 1, Oxford Clarendon Press 1984*
14. S. Lovesey, *Theory of Neutron Scattering from Condensed Matter Vol. 2, Oxford Clarendon Press 1984*
15. A. Giuliani, et al., *Phys. Rev. Lett.* 106, 2011
16. A. Giuliani, et al., *Physical Review B* 86, 104308 (2012)
17. Pietropaolo, et al., *Phys. Rev. Lett.* 100, 127802 (2008)
18. A. Soper, C. Benmore, *Phys. Rev. Lett.* 101, 2008
19. F. Winnik, et al., *Macromolecules* 1992, 25, 6007-6017
20. Erbil, E. Kazancioglu, N. Uyanik, *European Polymer Journal* 40 (2004) 1145-1154
21. Soper, et al., *J. Phys. Chem. B* 2006, 110, 3472-3476
22. A. Soper, K. Weckstrom, *Biophysical Chemistry* 124 (2006) 180-191
23. D. Kuckling, et al., *Macromol. Chem. Phys.* 201, No. 2 (2000) 273-280
24. D. Kuckling, et al., *Polymer*, 44 (2003) 4455-4462

25. Blostein, *et al.*, Critique on the measurement of neutron cross-sections by the Deep Inelastic Neutron Scattering technique, 2006
26. D.Griffith, G. Schuster, *Journal of Atmospheric Chemistry* 5 (1987), 59 -81
27. D. Anderson, J. Winn, *J. Phys. Chem. A* 2000, 104, 3472-3480
28. G. Pollack, *Physical Review A*, Vol. 23, 5, 1981
29. D. Dows, *Journal of Chemical Physics*, Vol 26, 4, 1957, 745-747
30. G. Selwyn, H Johnston, *J. Chem Phys* 74 (7), 1981
31. H. Valds, J. Sordo, *J. Phys. Chem. A*, 2004, 108 (11), 2062-2071
32. H. Waechter, M. Sigrist, *Appl. Phys. B* 87, 539–546 (2007)
33. K. Hiraoka, *et al.*, *J. Phys. Chem.*, 1994, 98 (34), 8295-8301
34. M. Bahou, *et al.*, *Chemical Physics Letters* 265 (1997) 145-153
35. M. Solimannejad, I.Alkorta, and J. Elguero, *J. Phys. Chem. A*, 2007, 111 (11), 2077-2083
37. N. Yamasaki, *et al.*, *J. Phys. Chem.* 93, 1989, 2204-2209
38. Preparation of Novel Polyazetes, Final Technical Report, Patent and Fiscal Report- J. Radziszewski, 2002
39. Qian, 1997, *Journal of Molecular Spectroscopy*
40. S Toyoda and N Yoshida, *Anal. Chem.* 1999, 71, 4711-4718
41. S. Kudoh, K. Onoda, M. Takayanagi, M. Nakata, *Journal of Molecular Structure* 524 (2000) 61–68
42. Stable Isotope Investigations of Atmospheric Nitrous Oxide- J.Kaiser, Dissertation, 2002
43. Steven S. Cliff, and Mark H. Thiemens, *Anal. Chem.*, 1994, 66 (17), 2791-2793
44. T. Rockmann, *et al.*, *Journal of Geophysical Research*, Vol. 106, No. D10, p10403-10410, 2001
45. W. Guillory, C. Hunter, *Journal of Chemical Physics*, Vol. 50, No. 8, 1969
46. W. Herrebout, *et al.*, *Journal of Molecular Spectroscopy* 189, 235–243 (1998)
47. George C. Pimentel Papers, BANC MSS 90/139 c, The Bancroft Library, University of California, Berkley
48. I. Harris, *et al.*, *Phys. Rev. Lett.* Vol.53, No.25, 1984
49. J. Farges, *et al.*, *J. Chem. Phys.* 78, 5067 (1983)
50. O. Peterson, D. Batchelder, R. Simmons, *Physical Review*, Vol. 150, 2, 1966
51. The Crystal Structure of the Group 0 Elements- J. Cuthbert and J. W. Linnett, *Inorganic Chemistry Laboratory, Oxford*, 1957
52. The Solid State of Rare Gases- G. L. Pollack
53. J. L. Finney, *Proc. R. Soc. Lond. A* 1970 319, 479-493
54. A. Longares-Patron, M. Canizares-Mac'ias, *Talanta* 69 (2006) 882–887
55. J. Perdew, Y Wang, *Physical Review B* Vol 45, 23, 1992
56. J. Perdew, *et al.*, *J. Chem. Phys.* 105 (22), 1996
57. A. Becke, *J. Chem. Phys.* 98 (7), 1993
58. A. Becke, *J. Chem. Phys.* 104 (3), 15 January 1996
59. M. Govindajaran, *et al*, *Spectrochimica Acta Part A* 76 (2010) 12-21

60. A Guide to Molecular Mechanics and Quantum Chemical Calculations- W. Hehre, 2003 by Wavefunction, Inc
61. Conceptual DFT- Geerlings, DeProft and Langenaeker, *Chem. Rev.*, 103, 1793-1873, 2003
62. ORTEP-3 for Windows- L. J. Farrugia (2012) *J. Appl. Cryst.* 45, 849-854
63. E. Cocinero, *et al*, *Phys. Chem. Chem. Phys.*, 2010, 12, 12486-12493
64. E. Davidson and D. Feller, *Chem. Rev.* 1988, 86, p661-696
65. J. Stride, U. Jayasooriya, I. Reid, *J. Phys. Chem. A* 2002, 106, 244-250
66. G. Graziano, *International Journal of Biological Macromolecules* 27 (2000) 89-97
67. D. Kuckling *et al.*, *Polymer* 44 (2003) 4455-4462
68. F. Winnik, H. Ringsdorf, J. Venzmer, *Macromolecules* 1990, 23, 2415-2416
69. F. Winnik *et al.*, *Macromolecules* 1992, 25, 6007-6017
70. F. Winnik *et al.*, *Macromolecules* 1993, 26, 4577-4585
71. F. Winnik, *Macromolecules* 1990, 23, 233-242
72. G. Graziano, *International Journal of Biological Macromolecules* 27 (2000) 89-97
73. S. Dixit *et al.*, *Letters to Nature*, *Nature* 416, 2002, 829-832
74. G. Watson, Neutron Compton Scattering, 1996
75. C. Lemon, PhD Thesis, 2009
76. J Mayers and T Abdul-Redah, *J. Phys. Condens. Matter* 16 (2004) 4811-4832
77. J. Mayers *et al.*, *Physica B* 350 (2004) 659-662
78. J. Stride, U. Jayasooriya, I. Reid, *J. Phys. Chem. A* 2002, 106, 244-250
79. V. Oganesyan, *et al.*, *J. Phys. Chem. A* 2004, 108, 1860-1866
80. M. Probert and A. Fisher, *J.Phys. Condens. Matter* 9 (1997) 3241-3257
81. Autrans Conference Report, 1996
82. L. Jiang and Q. Xu, *J. Phys. Chem. A*, 2009, 113 (13), 3121-3126

### Additional Sources of Information

Though these documents were not specifically referenced in the text, they have nonetheless been very useful throughout the production of this thesis; these references are not listed in any specific order, and should all be given weight as sources of background information on Matrix Isolation, Density Functional Theory, the Deep Inelastic Neutron Scattering mechanism employed in the VESUVIO instrument, or on a related field of study.

83. Soper, M. Ricci, *Phys. Rev. Lett.* 84, No. 13 (2000) 2881-2884
84. Soper, *Pure Appl. Chem.*, Vol 82, No. 10, 1855-1867, 2010
85. K. Gierszal *et al.*, *J. Phys. Chem. Lett.* 2011, 2, 2930-2933

86. S. Dixit *et al.*, *Europhys. Lett.*, 59 (3), 377-383 (2002)
87. Raymond *et al.*, *J. Phys. Chem. B* 2003, 107, 546-556
88. G. Graziano, *J. Chem. Soc., Faraday Trans.*, 1998, 94, 3345-3352
89. S. Dixit *et al.*, *Letters to Nature, Nature* 416, 2002, 829-832
90. Soper, J. Finney, *Phys. Rev. Lett.* Vol. 71, No. 26 (1993) 4346-4349
91. L. Dougan *et al.*, *J. Chem. Phys.* 122 (2005) 17514(1-7)
92. Frank, M Evans, *J. Chem. Phys.* 13, No. 11 (1945) 507-532
93. Pantalei *et al.*, *Phys. Rev. Lett.* Vol. 100, No. 17 (2008) 177801(1-4)
94. R. Senesi *et al.*, *Phys. Rev. Lett.* Vol. 98, No. 13 (2007) 138102(1-4)
95. Mizuno, T. Ochi, Y. Shindo, *J. Chem. Phys.* 109, No. 21 (1998) 9502-9507
96. P. Flory, *J. Chem. Phys.* 10 (1942) 51-61
97. Lee, *J. Chem. Phys.* 83 (1985) 2421-2425
98. Dougan *et al.*, *J. Chem. Phys.* 121 (2004) 6456-6462
99. S. Dixit *et al.*, *Europhys. Lett.*, 59 (3), 377-383 (2002)
100. Water's Hydrogen Bond Strength- M. Chaplin, London South Bank University
101. S. Dixit *et al.*, *Letters to Nature, Nature* 416, 2002, 829-832
102. Soper, J. Finney, *Phys. Rev. Lett.* Vol. 71, No. 26 (1993) 4346-4349
103. L. Dougan *et al.*, *J. Chem. Phys.* 122 (2005) 17514(1-7)
104. H. Frank, M Evans, *J. Chem. Phys.* 13, No. 11 (1945) 507-532
105. Pantalei *et al.*, *Phys. Rev. Lett.* Vol. 100, No. 17 (2008) 177801(1-4)
106. Senesi *et al.*, *Phys. Rev. Lett.* Vol. 98, No. 13 (2007) 138102(1-4)
107. K. Mizuno, T. Ochi, Y. Shindo, *J. Chem. Phys.* 109, No. 21 (1998) 9502-9507
108. P. Flory, *J. Chem. Phys.* 10 (1942) 51-61
109. Lee, *J. Chem. Phys.* 83 (1985) 2421-2425
110. L. Dougan, *et al.*, *J. Chem. Phys.* 121 (2004) 6456-6462
111. Soper *et al.*, *J. Phys. Chem. B* 2006, 110, 3472-3476
112. Soper, K. Weckstrom, *Biophysical Chemistry* 124 (2006) 180-191
113. Soper, M. Ricci, *Phys. Rev. Lett.* 84, No. 13 (2000) 2881-2884
114. Soper, *Pure Appl. Chem.*, Vol. 82, No. 10, 1855-1867, 2010
115. K. Gierszal *et al.*, *J. Phys. Chem. Lett.* 2011, 2, 2930-2933
116. S. Dixit, *et al.*, *Europhys. Lett.*, 59 (3), 377-383 (2002)
117. Soper *et al.*, *J. Phys. Chem. B* 2006, 110, 3472-3476
118. G. Graziano, *J. Chem. Soc., Faraday Trans.*, 1998, 94, 3345-3352
119. Saeed, D. Georget, A. Mayes, *Reactive & Functional Polymers* 70 (2010) 230-237
120. G. Zhang, C. Wu, *J. Am. Chem. Soc.* 2001, 123, 1376-1380
121. H. Fredrickson, A. Liu, F. Bates, *Macromolecules*, 1994, 27, 2503-2511
122. Y. Gao, *et al.*, *J. Macromol. Sci. Phys.*, B36(3), 417-422 (1997)
123. Y. Zhang, *et al.*, *J. Am. Chem. Soc.* 2005, 127, 14505-14510
124. Z. Liu, *et al.*, *Chem. Commun.*, 2011, 47, 12283-12285
125. Wu, S. Zhou, *Macromolecules*, 1995, 28, 8381-8387

- 126.Kuckling, *et al.*, *Macromol. Chem. Phys.* 201, No. 2 (2000) 273-280
- 127.Kuckling, *et al.*, *Polymer* 44 (2003) 4455-4462
- 128.Tiktopulo, *et al.*, *Macromolecules*, 1994, 27, 2879-2882
- 129.Fredrickson, A. Liu, F. Bates, *Macromolecules*, 1994, 27, 2503-2511
- 130.Zhang, C. Wu, *J. Am. Chem. Soc.* 2001, 123, 1376-1380
- 131.Fredrickson, A. Liu, F. Bates, *Macromolecules*, 1994, 27, 2503-2511
- 132.Schild, M. Muthukumar, D. Tirrell, *Macromolecules*, 1991, 24, 948-952
- 133.Kubota, S Fujishige, I. Ando, *J. Phys. Chem.* 1990, 94, 5154-5158
- 134.Kanazawa, *et al.*, *Anal. Chem.* 1996, 68, 100-105
- 135.M. Shibayama, T. Tanaka, C. Han, *J. Chem. Phys.* 97, No. 9 (1992) 6829-6841
- 136.M. Shibayama, T. Tanaka, *J. Chem. Phys.* 102 (23), 1995 9392-9400
- 137.M. Yoo *et al.*, *Polymer* 38 (1997) 2759-2765
- 138.M. Yoo *et al.*, *Polymer* 41 (2000) 5713-5719
- 139.N. Morimoto *et al.*, *Macromol. Rapid Commun.* 2008, 29, 672-676
- 140.R. Stile, W. Burghardt, K. Healy, *Macromolecules* 1999, 32, 7370-7379
- 141.S. Fujishige, K. Kubota, I. Ando, *J. Phys. Chem.* 1989, 93, 3311-3313
- 142.T. Park, A. Hoffman, *Macromolecules* 1993, 26, 5045-5048
- 143.T. Tokuhiro et al., *Macromolecules* 1991, 24, 2936-2943
- 144.X. Wang, X. Qiu, C. Wu, *Macromolecules* 1998, 31, 2972-2976
- 145.Y. Gao *et al.*, *J. Macromol. Sci.- Phys.*, B36(3), 417-422 (1997)
- 146.Y. Maeda, T. Higuchi, I. Ikeda, *Langmuir* 2000, 16, 7503-7509
- 147.Y. Okada, F. Tanaka, *Macromolecules* 2005, 38, 4465-4471
- 148.Y. Takei *et al.*, *Bioconjugate Chem.*, Vol. 5, No. 6, 1994 577-582
- 149.Y. Zhang *et al.*, *J. Am. Chem. Soc.* 2005, 127, 14505-14510
- 150.Z. Liu *et al.*, *Chem. Commun.*, 2011, 47, 12283-12285
- 151.Fielding, J. Mayers, *Nuclear Instruments and Methods in Physics Research A* 480 (2002) 680-689
- 152.Pietropaolo, *et al.*, *Institute of Physics Publishing and SISSA*, 2006
- 153.C A Chatzidimitriou-Dreismann and M Krzystyniak, *J. Phys. Condens. Matter* 18 (2006) 4741-4749
- 154.Chatzipidimitriou-Dreismann, *et al.*, *Phys. Rev. B* 72, 054123 2005
- 155.F. Bruni, *et al.*, *J. Phys. Chem. Lett.* 2012, 3, 2594-2597
- 156.K. Morrone *et al.*, *J. Chem. Phys.* 126, 234504 (2007)
- 157.J. Morrone, R. Carr, *Phys. Rev. Lett.* 101, 017801 (2008)
- 158.S. Gunasekaran, S. Ponnusamy, *Indian Journal of Pure and Applied Physics* Vol. 43, 2005, 838-843
- 159.V. Kannan, *et al.*, *phys. stat. sol. (a)* 203, No. 10, 2488-2495 (2006)
- 160.The Solid State of Rare Gases- G. L. Pollack
- 161.W. Rodney, *Journal of the Optical Society of America*, Vol. 45, No. 11, 1955
- 162.T Egawa , A Kameyama, H Takeuchi, *Journal of Molecular Structure* 794 (2006) 92-102

- 163.P. Geerlings, F. De Proft, and W. Langenaeker, *Chem. Rev.* 2003, 103, 1793-1873
- 164.R. Armiento, Master's Thesis, Theory of Materials, Department of Physics Royal Institute of Technology, SE-100 44 Stockholm, Sweden, Stockholm, 2000
- 165.Y. Imamura, R. Kobayashi and H Nakai, *Journal of Chemical Physics* 134, 124113 (2011)
- 166.Scott and L. Radom, *J. Phys. Chem.* 1996, 100, 16502-16513
- 167.Salavati-Niasari, et al., *Journal of Structural Chemistry*. Vol. 51, No. 3, pp. 437-443, 2010
- 168.Wong, *Chemical Physics Letters* 256 (1996) 391-399
- 169.Bytheway, M. Wong, *Chemical Physics Letters* 282 (1998) p219–226
- 170.Quantum Mechanics for Engineers (Website), Leon van Dommelen, Version 5.56 alpha
- 171.Exploring Chemistry With Electronic Structure Methods, 2nd Edition- J. Foresman, A. Frisch, *Gaussian, Inc.*
- 172.P. Shreiner, et al., *Organic Letters*, Vol. 8, No. 17, 3635-3638
- 173.H. Sabzyan, Z. Kalantar, *Journal of Molecular Structure (Theochem)* 663 (2003) 149–157
- 174.Hutter, et al., *J. Am. Chem. Soc.* 1994, 114, 750-156
- 175.Kubelka and T. Keiderling, *J. Phys. Chem. A* 2001, 105, 10922-10928
- 176.University of East Anglia, School of Chemistry, CHE-M3OY (Computational Chemistry) Module Manual, 2009-2010
- 177.S. Kong, et al., *J. Phys. Chem. A* 2010, 114, 2393–2399
- 178.E. Velcheva , B. Stamboliyska, P. Boyadjieva, *Journal of Molecular Structure* 963 (2010) 57–62
- 179.E. Velcheva, B. Stamboliyska, *Spectrochimica Acta Part A* 60 (2004) 2013–2019
- 180.S. Andrade, L. Gonçalves, F. Jorge, *Journal of Molecular Structure (Theochem)* 864 (2008) 20–25
- 181.H. Arslan, Ö. Algül, *Int. J. Mol. Sci.* 2007, 8, 760-776
- 182.G. Rauhut and P. Pulay, *J. Phys. Chem.* 1995, 99, 3093-3100